Towards photon FLASH radiotherapy

Edward Rupert James Finbow Taylor

Supervisors:

Dr Kristoffer Petersson

Dr Geoffrey Higgins

St Edmund Hall

Department of Oncology

University of Oxford

A thesis submitted for the degree of

Doctor of Philosophy

Trinity Term 2025

This thesis is dedicated to James Whitbourn 1963-2024

Acknowledgements

First and foremost, I would like to thank my supervisors. Kristoffer Petersson, for guiding me and encouraging me throughout my DPhil. I am very grateful for your insightful contributions, your unrelenting effort and your feedback. Geoffrey Higgins, for sharing your extensive clinical knowledge and being a supportive mentor throughout. Salomé Paillas, and Jia-Ling for your hard work and significant contribution to enabling all the preclinical investigations. I have thoroughly enjoyed collaborating on these interdisciplinary projects with you both. Abdallah Reza, Daniel Long, and Felix Hoffman for your help with all the material science elements and for being there to answer all my questions. John Prentice and Kyle Hallett from the Department of Oncology Mechanical Workshop for helping to turn all the designs into reality.

I would also like to extend my thanks also to Christian, Sovan, Nathalie, Michele, Janielle, and Mark for being such supportive friends, mentors and colleagues throughout my academic journey. To my friends; Cyril, Nick, Madi, Vasily, Zoe, Francesca, Natalie, Luke, Daniel, Vicky, Luke, David, Michael, Mario, and Conor I can only hope to mirror the kindness and support you have given me throughout these years.

My warmest and grateful thanks to my flatmates and friends over these years; Theana, Boris, Momo, Alex, Casey, Maike, Raphael, Hannah, Archie, Kira, Verena, Camille, Mohammad, Poppy, and Julien. I would like to thank you for being such an integral part of my life over this time and for being there through thick and thin. The choir of St Edmund Hall and to James Whitbourn, for masterfully conducting for so many wonderful years. I would also like to thank my college and all those who have worked tirelessly to make the community at Teddy Hall so welcoming, warm, and friendly. The Oxford city squash team, Martin, DQ, Jamie, Miles, Ben, Sam, James, Francois, Charlie, Andy, James, Sam. I have loved spending an evening each week in your company, and I look forward to seeing you soon. To Aymeric, Gus and Ary and the touch rugby team, thank you for rekindling my love for rugby and helping me carry it on injury free. To my girlfriend Ruirui Dong, for being so loving and encouraging along the way.

To my parents Anne and Myles. I am grateful for the love, support and opportunities you have provided me in my life and I appreciate the sacrifices you made for me to

have these. To my sister Georgina, thank you for supporting and housing me. To the dog Tilly, for being a calming presence and a fluffy companion.
I would also like to thank the funding bodies which have supported my work including Cancer Research UK—RadNet (C6078/A28736), the National Cancer Institute/NIH/DHHS (1P01CA257904), and the Medical Research Council with the Programme grant (MR/X006611/1) and funding for my studentship.

Abstract

FLASH radiotherapy is a promising treatment modality that employs ultra-high dose rates ($\gtrsim$40 Gy/s) and short delivery times (<1 s) to achieve enhanced normal tissue sparing while maintaining equivalent tumour control compared to conventional radiotherapy. Since most clinical treatments worldwide are delivered with photon beams from linear accelerators, the most feasible route toward widespread clinical adoption of FLASH lies in photon-based implementations. However, the majority of preclinical studies demonstrating normal tissue sparing at ultra-high dose rates have been performed with electron beams. Delivering photon beams to sufficient depths at high rates requires overcoming significant technological challenges in irradiation platform design and dosimetry. Expanding preclinical irradiation capabilities to accommodate beams with varying types and parameters is therefore essential to improve understanding of the underlying biological mechanisms and clinical potential of FLASH.

Spatially fractionated radiation therapy (SFRT) represents a paradigm shift in treatment philosophy, intentionally introducing spatial dose heterogeneity within both tumours and normal tissues. Although SFRT has shown clinical promise, achieving effective tumour control with reduced toxicity, its biological mechanisms remain poorly understood. The full potential of SFRT alone, or in combination with other modalities, remains largely unexplored, motivating further preclinical investigation to identify and predict scenarios where enhanced therapeutic outcomes can be achieved.

This thesis focuses on the development of a preclinical platform capable of delivering megavoltage (MV) photon beams at ultra-high dose rates, enabling future in vivo FLASH studies. Because the implementation of MV photon FLASH irradiations poses thermo-mechanical challenges to maintain target integrity under increased beam power, this work also compares temperature rise, fatigue lifetime, and photon dose rate production from thin tungsten targets in air using a preclinical electron linear accelerator. It is hypothesised that increasing the beam exit window–target separation, separating target and backer materials, and using air-cooled target configurations can both enable photon FLASH irradiations and reduce target heating to extend operational lifetimes.

Using this platform, an in vivo study was conducted to investigate radiation-induced

skin toxicity from photon and electron irradiations delivered at comparable doses and dose rates. These results provide insight into how existing electron FLASH data can inform future MV photon applications.

This body of work also introduces preclinical setups for SFRT using electron beams delivered at conventional and ultra-high dose rates. These include adaptable collimator systems that allow systematic exploration of spatial fractionation parameters to assess their influence on tumour control and normal tissue toxicity. In a tumour growth assay, the difference between homogeneous and spatially fractionated electron irradiations with partial tumour coverage is demonstrated.

Together, the developments outlined in this thesis provide platforms for future preclinical studies aimed at advancing the understanding and combined application of FLASH and SFRT.

Original papers

This thesis is based on work from the following papers:

i. **Taylor ERJF**, Vojnovic B, Petersson K. *Megavoltage photon FLASH for preclinical experiments.* Med Phys. 2025; 10.1002/mp.17891

ii. Paillas S, **Taylor ERJF**, Lövgren N, Petersson K. *Quantifying the FLASH effect and its dependence on average dose rate in vivo for 6 MeV electron and 6 MV photon beams.* CTRO. 2025; 10.1016/j.ctro.2025.101052

iii. **Taylor ERJF**, Ruan JL, Paillas S, Higgins G, Petersson K. *A preclinical setup for spatially fractionated radiotherapy.* Med Phys. (under review) 2025

iv. **Taylor ERJF**, Long DJ, Reza A, Hoffman F, Petersson K.*Managing bremsstrahlung target heating in megavoltage photon FLASH radiotherapy.* Med Phys. (under review) 2025

Contributions to papers

i. I contributed to the planning, writing, measurements and analysis of the paper, preparing all manuscripts and data. I was the first author.

ii. I performed dosimetric analysis used in the supplementary materials. I helped plan the beamline setup and procedures. I rewrote, edited and provided feedback on the submitted manuscript and was second author.

iii. I contributed to the planning, writing, measurements and analysis of the paper, preparing all manuscripts and data. I was the first author.

iv. I contributed to the planning, writing, measurements and analysis of the paper, preparing all manuscripts and data. I was the first author.

Contents

List of Figures

List of Tables

List of Abbreviations

AAPM . . . . American Association of Physics in Medicine

ALARA . . . . As Low As Reasonably Achievable

AMC . . . . . Advanced Markus® ionisation chamber

ARC . . . . . Advanced Research Computing

Co . . . . . Cobalt

CPU . . . . . Central Processing Unit

CSDA . . . . . Continuous Slowing Down Approximation

CT . . . . . Computed Tomography

CTV . . . . . Clinical Target Volume

ctc . . . . . Centre-to-Centre

DNA . . . . . Deoxyribonucleic Acid

DPA . . . . . Displacement Per Atom

DSB . . . . . Double Strand Break

DVH . . . . . Dose Volume Histogram

EBRT . . . . . External Beam Radiation Therapy

EM . . . . . Electromagnetic

EQD . . . . . Equivalent Dose

EUD . . . . . Equivalent Uniform Dose

eV . . . . . Electronvolts

FE . . . . . Finite Element

FFF . . . . . Flattening Filter Free

FS . . . . . Field Size

FP . . . . . Frenkel Pair

FWHM . . . . Full Width at Half Maximum

Geant4 . . . . GEometry ANd Tracking

GPU . . . . . Graphical Processing Unit

GTV . . . . . Gross Tumour Volume

Gy . . . . . Gray (unit of dose)

HDR . . . . . High Dose Rate

HF . . . . . Hypofractionation

HFF . . . . . Heat Flux Factor

HWHM . . . . Half Width at Half Maximum

IAEA . . . . . International Atomic Energy Agency

ICRP . . . . . International Commission on Radiological Protection

ICRU . . . . . International Commission on Radiation Units and Measures

IDR . . . . . Instantaneous Dose Rate

IGRT . . . . . Image Guided Radiation Therapy

IMRT . . . . . Intensity Modulated Radiation Therapy

IORT . . . . . Intraoperative Radiation Therapy

IR . . . . . Irradiation

ISL . . . . . Inverse Square Law

KERMA . . . Kinetic Energy Released per unit MAss

LDR . . . . . Low Dose Rate

LET . . . . . Linear Energy Transfer

linac . . . . . Linear Accelerator

LRT . . . . . Lattice Radiation Therapy

MBRT . . . . . Minibeam Radiation Therapy

MC . . . . . Monte Carlo

MCNP . . . . Monte Carlo N-Particle

MLC . . . . . Multi-Leaf Collimator

MPI . . . . . Message Passing Interface

MRI . . . . . Magnetic Resonance Imaging

MRT . . . . . Microbeam Radiation Therapy

MT . . . . . Multi-threading

MU . . . . . Monitor Unit

MV . . . . . Megavoltage

NCRP . . . . . National Council on Radiation Protection and Measurements

NIST . . . . . National Institute of Standards and Technology

NPL . . . . . National Physical Laboratory

NTCP . . . . . Normal Tissue Complication Probability

OAR . . . . . Organ-at-risk

OD . . . . . Optical Density

OER . . . . . Oxygen Enhancement Ratio

PB . . . . . Pencil Beam

PDD . . . . . Percentage Depth-Dose

PFN . . . . . Pulse Forming Network

PI . . . . . Post Irradiation

PKA . . . . . Primary Knock-on Atom

PMMA . . . . Polymethyl Methacrylate

PSD . . . . . Phase Space Distribution

PSDL . . . . . Primary Standard Dosimetry Laboratory

PTV . . . . . Planning Target Volume

PVDR . . . . . Peak to Valley Dose Ratio

QA . . . . . Quality Assurance

RBE . . . . . Relative Biological Effect

RF . . . . . Radio Frequency

RMS . . . . . Root Mean Square

SAD . . . . . Source to Axis Distance

SCD . . . . . Source-Chamber Distance

SD . . . . . Standard Deviation

SDD . . . . . Source to Detector Distance

SDOM . . . . . Standard Deviation of the Mean

SFRT . . . . . Spatially Fractionated Radiation Therapy

SLURM . . . . Simple Linux Utility for Resource Management

SPR . . . . . Stopping Power Ratio

SSB . . . . . Single Strand Break

SSD . . . . . Source-to-Surface Distance

SSDL . . . . . Secondary Standard Dosimetry Laboratory

SW . . . . . Standing Wave

TCP . . . . . Tumour Control Probability

TIFF . . . . . Tagged Image File Format

TMR . . . . . Tissue Maximum Ratio

TPS . . . . . Treatment Planning System

TW . . . . . Travelling Wave

UHDR . . . . Ultra-High Dose Rate

UTS . . . . . Ultimate Tensile Strength

VMAT . . . . Volumetric Modulated Arc Therapy

VPDR . . . . . Valley to Peak Dose Ratio

Z . . . . . Atomic Number

List of Symbols

$D_{w,Q}^{-}$	Absorbed dose to water at reference depth z_{ref} in a water phantom irradiated by a beam of quality Q, Gy
$\bar{E}_0$	Mean Energy, MeV
$\frac{d\Phi}{dt}$	Fluence rate $m^{-2}s^{-1}$
Γ_a	Energy Spread
d_{80}	Depth of 80% dose, cm
d_{max}	Depth of dose maximum, cm
D_m	Maximum Dose level, Gy
D_x	X-ray Dose background along the central axis, Gy
$E_{m,a}$	Maximum Energy, MeV
$E_{p,0}$	Modal Energy, MeV
$E_{p,a}$	Most probable energy in front of vacuum exit window, MeV
G	Dose Gradient
k_p	Coverage factor to calculate expanded uncertainty for a confidence level p
k_{TP}	Factor to correct for temperature and pressure differences between standard reference laboratory and user facility
$P_{80/20}$	Penumbra between the 80% and 20% dose levels
Q	Quality of radiation beam

R_p Practical Range, cm

R_q Depth where tangent at the inflection point intersects the maximum dose level, cm

R_t Therapeutic range, cm

$TPR_{20,10}$ Tissue-Phantom ratio in water at depths of 20 and 10 $g\,cm^{-2}$ for a field size of 10 cm $\times$ 10 cm and a SCD of 100 cm, it is used as a measure of beam quality in high-energy photon radiation

z_{max} Depth of maximum dose, $g\ cm^{-2}$

z_{ref} Reference depth for phantom measurements, $g\ cm^{-2}$

E_z Mean Energy at depth z, MeV

Nevertheless, scientific method is not the same as the scientific spirit. The scientific spirit does not rest content with applying that which is already known, but is a restless spirit, ever pressing forward towards the regions of the unknown, and endeavouring to lay under contribution for the special purpose in hand the knowledge acquired in all portions of the wide field of exact science. Lastly, it acts as a check, as well as a stimulus, sifting the value of the evidence, and rejecting that which is worthless, and restraining too eager flights of the imagination and too hasty conclusions.

— Sir Archibald Garrod

1 Introduction

Contents

1.1 Cancer treatment

Cancer is the leading cause of death globally, with incidence rates increasing and nearly one in two of us predicted to develop the disease in our lifetime. World Health Organization figures indicate that by 2040 cancer cases will increase by 89.1% in Africa, 65.6% in Latin America and the Caribbean, 59.2% in Asia, 47.8% in Oceana, 37.9% in North America, and 21% in Europe. Cancer is a complex disease defined by the division of cells in an unregulated way with an ability to spread and become invasive in other parts of the body. Preventative measures to lessen the risk of disease occurrence can be achieved with lifestyle choices to avoid risk factors such as; smoking, obesity, high UV exposure, alcohol consumption, diet, and physical inactivity [1].

Huge progress has been made in improving treatment techniques and introducing early screening programs. In the past 40 years in the UK, these new treatment technologies and interventions have reduced the proportion of the population dying from cancer by 22%, despite life expectancy increases and age providing a substantive risk factor [1]. For some, complete remission can be achieved. However, the long term impact of treatment on patients cannot be neglected. In the UK alone, at least one in four people living with cancer face poor health or disability following treatment. A significant proportion will also suffer long-term treatment induced physical difficulties, such as incontinence, sexual dysfunction, fatigue or an increased risk of secondary cancers elsewhere as well as the psychosocial issues that result from these [2]. Therefore treatments must minimise impact to normal tissues to prevent these secondary effects. Improvements in treatments for patients have occurred across three main types of cancer treatment: surgery, chemotherapy and radiotherapy.

Surgery can be safely performed when tumours are small, confined and when there is little risk of damage to vital adjacent organs/vessels. It can also be used when debulking is required, or when symptoms cause pain or pressure elsewhere in the body. Surgery either involves open surgery; in which a large incision is performed and the tumour, alongside adjacent healthy tissue, is removed. Or minimally

invasive surgery in which a few specialised surgery tools enable the removal of tumours with laparoscopic equipments. As well as treatment, surgery can be used for classification of tumour type and stage. However, for some tumours, their positioning or shape makes complete surgical removal impossible, while tumour metastases may reduce the impact of local tumour control measures.

For most cancers chemotherapy is effective at targeting rapidly growing tumour cells with cytotoxic drugs to cause DNA damage, hereby exploiting the ineffectiveness of cancer cells to repair damage relative to normal tissues. However, the normal tissue damage can lead to a number of unwanted side effects including: an immunocompromised patient state throughout treatment, the potential for secondary cancers, as well as poor quality of life throughout treatment. Here, most chemotherapy forms are systemic, moving through the body to reach cancer cells.

Radiotherapy remains an important component of cancer treatment with ∼50% of cancer patients receiving radiation therapy as part of their treatment; it contributes to ∼40% of curative treatments [3]. Globally there are 155 countries with radiotherapy facilities with 17,092 MV therapy, 133 light ion therapy, and 3355 brachytherapy centres ([4],as of September 2025). Accessibility currenly stands in direct constrast to demand where, scored by facilities per million people, Africa has 0.078-1.151, Latin America and the Caribbean has 1.247-2.803, Asia has 0.44-1.86, Oceana has 6.053, North America has 11.36, while Europe has 3.015-6.927 [5]. Therefore, novel personalised radiation therapies with fast, reliable and inexpensive equipment is needed to successfully manage increased therapeutic demand.

1.2 History of radiotherapy

The foundations of radiotherapy were laid in November 1895, with the discovery of X-rays by Wilhelm Conrad Röntgen at the University of Würzburg [6]. Naming them "X-rays" to denote their unknown nature, Röntgen quickly discovered their insensitivity to magnetic fields, and attenuation properties through different materials. In doing so, he performed the first ever radiograph of the bones of his wife's hand

[7]. Soon after, in January 1896, just 82 days after Röntgen's discovery, physicians utilised X-rays to visualize skeletal injuries and investigate diseases of the lungs and other organs [8]. Having claimed to have suffered burns from exposing his hand repeatedly in x-ray experiments, Emil H. Grubbé, a medical student, noticed potential therapeutic applications and in 1896 treated a woman with recurrent breast cancer [1]. Though ultimately unsuccessful, this definitively linked exposure and tissue damage, paving the way for further treatments [9].

In Vienna, Leopold Freund successfully used X-rays to treat a large hairy nevus in a young girl with the first example of fractionated radiotherapy. Other treatments soon followed with applications for pathological conditions, as well as stomach, skin, breast, carcinoma and pharyngeal cancers [10], with the first public clinic established soon after in Hamburg, Germany.

Similarly, after the isolation of radium by Marie and Pierre Curie, Henri Becquerel famously also suffered a radiation burn after carrying a radium vial in his pocket, an incident that kickstarted the use of radium for therapeutic applications [11].

However, technical limitations hindered early radiotherapy. Crookes tubes, the primary radiation source at the time, generated low-energy X-rays, requiring long exposures that only deposited energy superficially. A breakthrough came in 1913 with William D. Coolidge's invention of the hot cathode X-ray tube, which used a heated wire filament to release electrons via thermionic emission [12]. This invention provided higher stable output at voltages up to 200 kV, which enabled the treatment of deeper seated tumours [13].

In the 1920s, deeper treatment became possible with the introduction of "deep therapy" units operating at higher energies 120–300 kVp, later known as orthovoltage machines. By the 1930s, the push for even higher energy machines led to the creation of "supervoltage" X-ray units, reaching up to 1000 kVp. To create compact machines with even higher energies, the Van de Graaff generator was adapted for therapy

[1] "Grubbé's story is so implausible, so lacking of contemporary corroboration, and in such irreconcilable conflict with readily provable facts, and Grubbe's untruthfulness in other respects is so readily demonstrable, as to warrant the inclusion of his claims in this postscript, rather than in the body of a history of American radiology." A History of Radiology in the United States and Canada by F. Brecher

in the late 1930s [14] which enabled multidirectional and eventually rotational megavoltage X-ray treatment, though it lacked reliability and stability [15]. The first linear accelerators (linacs) emerged, following wartime advances in microwave cavity technology, as well as the development of the klystron and magnetron tubes [12]. The first medical linac was utilised in London in 1953, while the first successful treatment of a paediatric ocular tumour with a linac occurred at Stanford in 1956 [15]. Early linacs ranged from 0.5-4 MeV, while Cobalt-60 teletherapy units also emerged which utilized the gamma rays emitted by the radioactive decay of cobalt-60 isotopes. These γ-rays had effective energies around 1.17 and 1.33 MeV, offering greater tissue penetration and improved dose distributions for deep tumours [16]. Cobalt-60 therapy represented the first true megavoltage (MV) modality, and it rapidly gained global adoption due to its relative simplicity, reliability, and ability to treat a broader range of cancers. Betatrons [17], and Cyclotrons soon followed [18], with the former offering higher energies (up to 24 MeV). However, their size, low X-ray output, and non-isocentric design limited long-term use. By the mid-1950s, linacs reached 6–8 MeV, and by the 1960s, isocentric and fully rotational models became standard. These linacs were travelling wave (TW) design, with microwaves travelling from one end to the other with microwaves cyclically reinjected from the downstream to upstream end. This design limited the maximum accelerator gradient. The introduction of the standing wave (SW) accelerator in the late 1960s enabled the propagation and interference of microwaves back and forth within the waveguide, enabling higher efficiency acceleration. With the introduction of side-coupled [19] and compact standing-wave designs in the 1970s, linacs became the backbone of modern high-energy X-ray therapy. Meanwhile, the notable disadvantages of Cobalt-60 units including; continuous emission of radiation, intensity decay necessitating replacement every 5 years, requirement of extensive shielding, source disposal as well as security protocols led to a gradual decline in usage [20]. By the 1970s and 1980s though other novel accelerators were introduced such as the microtron [21], linear accelerators (linacs) became the standard for external beam radiotherapy.

Today, radiotherapy is most commonly delivered with electron, proton, or photon

beams with modern linacs offering flexibility in output of electrons or photons at adjustable megavoltage energies. However, the clinical usefulness of electron beams is limited by their short penetration at clinically used energies of around 6-20 mega-electron-volts (MeV), making them appropriate to treatment of superficial sites. Proton (or ion) beam radiotherapy has the advantage of well-defined irradiation volumes, achieved through the use of spot scanning and spread-out Bragg peak energy deposition; however, this modality is reliant on access to highly complex, large and expensive installations. As a result, <1% of radiotherapy patients worldwide receive treatments with protons or heavier ions [22].

1.3 Linear accelerators

A linear accelerator transports electrons emitted from the gun along the waveguide via high-power radio waves. Emitted electrons are steered via magnets, and focused (for photon output) to hit a high proton number target causing photon emission. Output photons are then collimated and flattened with a conical flattening filter which turns the central, highly peaked photon distribution, into a usable flat top hat shape. Multi-leaf collimators (MLCs) may also be placed in the path of the beam to alter its shape to conform to a particular tumour. The components of a linac are categorised into six main systems (see Figure 1.1) [23]. These are:

- **injection system** — the injection system provides electrons from an electron gun. Two types of electron gun are used in linacs; diode and triode types. Both involve a heated cathode, from which electrons are released via thermionic emission [24]. The triode design uses a grid [23] which enables greater control of electron injection into the waveguide.

- **RF power generation system** — the RF microwave power used for acceleration of electrons is provided by the RF source and pulsed modulator. The RF source is provided by magnetrons (or klystrons - RF amplifiers [12]). The pulse-forming network (PFN) synchronises the electron bunches with the microwave phase [20].

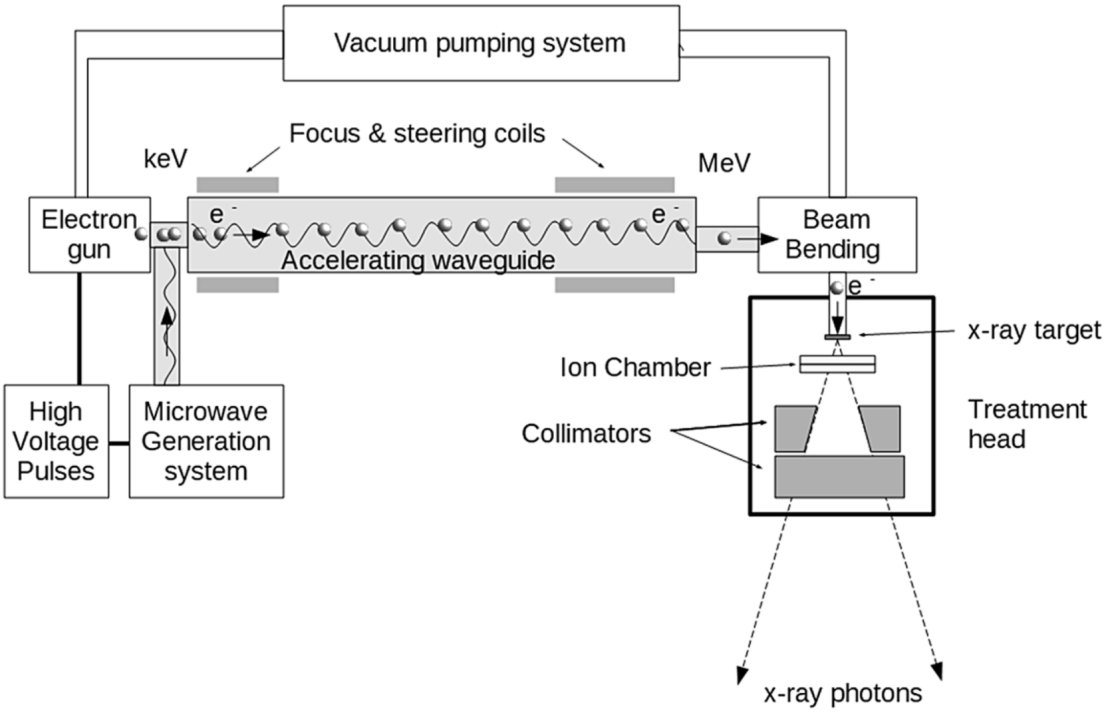

Figure 1.1: Components of a linear accelerator, from [26]

- **accelerating waveguide** — Electrons are accelerated along the waveguide in bunches via energy transfer from the RF fields inside. Here, the waveguide is comprised of a series of equally spaced coaxial resonant cylindrical cavities, separated by circular irises [25].

- **auxiliary system** — Auxiliary systems maintain linac operation with cooling, vacuum pumps, air flow control and shielding materials

- **transport systems** — Transport systems enable output of a focused beam of high energy electrons from the waveguide e.g., the bending magnet

- **treatment head** — The treatment head enables the output beams to be shaped and modified to produce a consistent and deliberate radiation field e.g., the bremsstrahlung target (photon) or scattering foil (electron), primary and secondary collimators, flattening filter, monitoring ionisation chamber, jaws, multi-leaf collimators, and wedges

Most linacs use microwaves at 3 GHz in the S-band with wavelengths of 10 cm, and cavity diameters of ~ 8 cm [27]. Typically magnetrons are used for low energy linacs (4-8 MV), or medium energy linacs (10-15 MV), while klystrons are predominantly used for 6-20 MV linacs and have longer lifespans [28–30]. Key principles of operation and design for a linac include:

- **Microwave power** — The power transferred to accelerated electrons is represented by $P = I \times E \times D$, where P is the incident power (watts, W), I is the electron current (amps, A), E is the electron energy (electronvolts, eV), and D is the duty cycle. To first approximation the power determines the beam intensity [31].

- **Shunt impedance** — Shunt impedance $P_d = \frac{V^2}{ZL}$ is a measure of the efficiency of the linear accelerator to convert microwave power into accelerating beam energy per unit length. Where Z is the shunt impedance per unit length, and L is the length of the waveguide [2].

- **Q value** — the Q value represents the dependence of the power coupling to the microwave frequency, a high Q value indicates a small change in frequency causes a large change of power efficiency to accelerate charged particles [12].

- **Beam loading** — Filament current is related to the beam current, such that a high filament current produces greater thermionic emission. When beam current is increased via increasing the number of electrons per pulse, the increased charge induced on cavity walls disrupts the flow of bunches, causing an additional resistive load in the cavities which can shift the phase and field causing a degraded electron energy output [35].

- **Electric field gradient** — RF electric breakdown occurs when high fields occur in copper cavities. The limit is known as the Kilpatrick Criterion $f = 1.64E_k^2 e^{\frac{-8.5}{E_k}}$ (with f in MHz and E_k in MeV). The factor E_k can be scaled by a 'bravery factor' b to increase the electric field acceleration.

[2] Values are typically between 86-112 $M\Omega m^{-1}$ for SW linacs [30, 32–34]

However using superconducting materials such as niobium reduces the surface resistance by a factor of $\sim 10^5$ compared to commonly utilised copper which can increase the efficiency of acceleration [35].

- **Operation** — The beam structure in a linac is provided in two types of operation; continuous wave (CW) or pulsed operation, which determines the duty cycle [36]. For the same average beam current, a low current CW operation is less power efficient than pulsed operation and can attain a lesser peak surface electric field. CW operation however reduces the effect of space charge and beam-current dependent effects at high average currents [35].

- **Microwave frequency band** — Though higher frequencies enable shorter accelerating structures, their machining tolerance makes them more expensive and difficult to build. Here, the combination of shunt impedance, RF defocusing, and maximum surface electric field become obstacles for higher frequencies, with linacs forced to become longer, occupying a greater volume, which increases their overall cost [31].

- **Emittance** — To produce a smaller focus spot and energy spread, its phase volume i.e., its emittance must be reduced. The space charge effect, which repels electrons in each bunch, limits the maximal beam intensity and causes defocusing which distorts the particle distribution [35].

1.4 Radiobiological principles

Radiotherapy treatments, using high energy accelerators, aim to cause targeted tumourcidal cell death via DNA damage, with DNA damage being at the heart of deleterious macroscopic tumour tissue damage, tumour shrinkage and eradication. These treatments aim to maximise the direct and indirect forms of DNA damage that occur in tumour cells, while minimising the normal tissue damage from ionising radiation via conformal treatments. Subsequent double-strand breaks (DSBs) are widely considered to determine the radiobiological effects in cells.

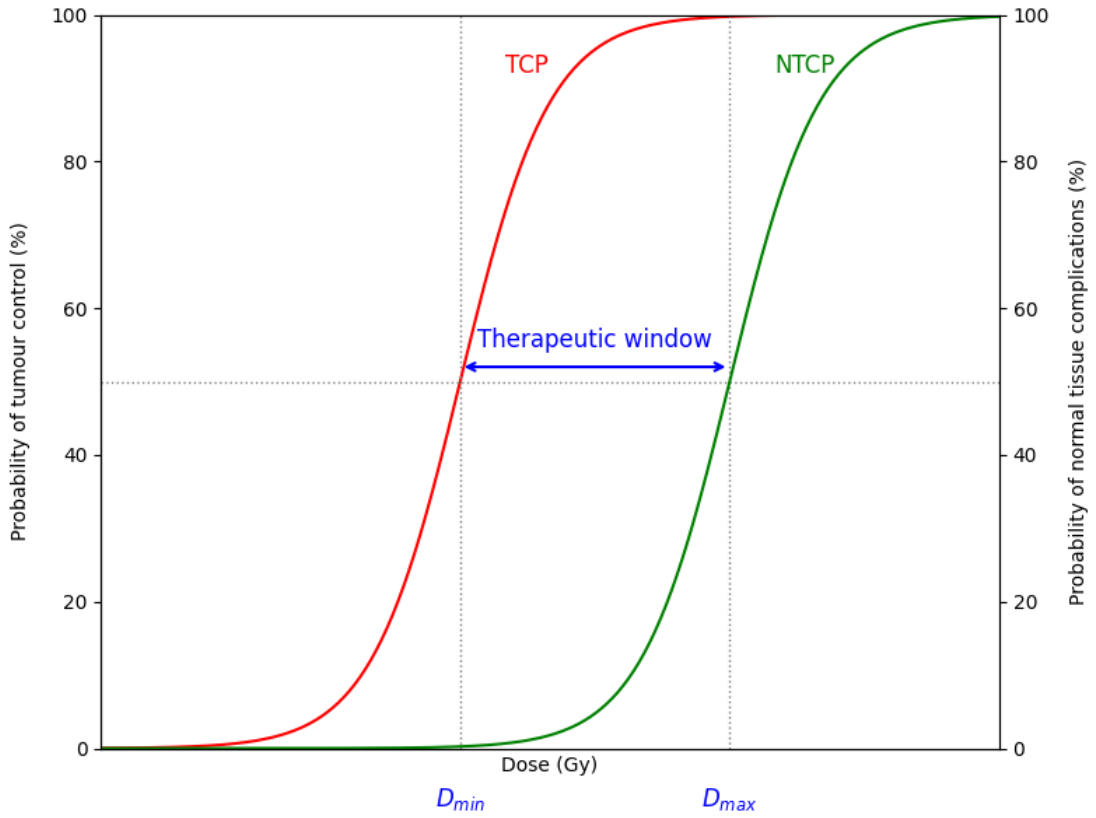

Figure 1.2: Illustrations of tumour control and normal tissue complication probability (TCP & NTCP)

1.4.1 Normal tissue complication probability & tumour control probability

The tumour control probability (TCP), and normal tissue complication probability (NTCP) follow sigmoidal curves reaching a plateau at high doses (Figure 1.2). The therapeutic index is the ratio of the maximum dose tolerated by normal tissue to the minimum dose required to control the tumour. Meanwhile, the "therapeutic window" corresponds to the range of doses for which the TCP is much higher than the NTCP. This represents the difference in dose-response between tumour and normal tissues, where radiotherapy treatment is achievable when the therapeutic window is large. To widen the therapeutic window, both deleterious tumour effects, and normal tissue tolerance need to be increased. There are many factors that affect the NTCP including; biological endpoint, tissue sensitivity and heterogeneity, fractionation effects, treatment planning and conformity, individual patient variability from

genetic predisposition, or treatment combination with a radiosensitizer or drugs [27, 37]. In addition, the TCP may depend on radiosensitivity, hypoxia, regrowth and repopulation. Here, any radiation treatment must also consider the risks and severity of treatment to normal tissues.

1.4.2 Fractionation

To minimise the NTCP, irradiations can be delivered in separated fractions. The main categories of fractionation schedules are: hyper-fractionated (<2 Gy per day), conventional fractionation (2 Gy per day & 5 treatments per week), hyper-fractionation (>2 Gy per fraction), accelerated fractionation ($>$ 10 Gy per week), and protracted/extended fractionation ($<$ 10 Gy per week over extended time periods). The choice of fractionation scheme is dependent on the differences in repair, repopulation, reoxygenation, re-assortment of cell cycle, radiosensitivity and fractionation sensitivity of normal and tumour cells. Fractionation enables repair of sub-lethal injury in the time between fractions [38], and can reduce the effect of treatment setup errors by reducing the contribution from each fraction [39].

1.4.3 5 Rs of radiobiology

The main factors which influence the effect of radiation treatments can be summarised with 5 processes and characteristics [40, 41]:

1. **Repair** — Repair can occur between fractionations and is better for normal tissues than tumours, as normal tissues can repair via a number of pathways that tumours cannot

2. **Reoxygenation** — Tumour vasculature is often weak, making many regions hypoxic. Previously hypoxic tumour cells can become exposed to oxygen following the death of adjacent radiosensitive oxygenated tumour cells, enabling formerly hypoxic cells to increase radiosensitivity prior to the next fraction

3. **Redistribution** — Some cell phase are vary radioresistant. Therefore when radiation is provided, more radioresistant cells survive which synchronises

remaining cell phases. Fractionation enables remaining cells' phases to redistribute into more sensitive phases

4. **Repopulation** — Following irradiation, surviving normal tissue and tumour cells can proliferate and repopulate. The repopulation of normal tissue cells can aid healing and reduce side effects, while tumour repopulation can mitigate radiation treatments. Here, extensions or interruptions between fractions can decrease treatment effectiveness

5. **Radiosensitivity** — Responses to radiation treatments can vary for different tumours, tissues and patients. The more radioresistant the tumour, the greater the potential dose required for treatment, and the greater the risk of normal tissue toxicity

1.4.4 DNA damage and repair

A method of targeting cancer cells with radiation is via the damage of DNA. DNA damage can be categorised into direct or indirect damage [42]. Direct damage is caused by molecular ionisation of the DNA molecules, while indirect damage to DNA is caused by free radicals generated by the ionisation of water molecules in close proximity to the DNA (such as hydroxyl radicals). Damage to DNA can be broken down into its most common forms including: base lesions, single-strand breaks (SSB) or double-strand breaks (DSB) [43]. Base lesions contribute little to cell death, while SSBs are simple to repair. By contrast, DSBs can cause a greater abundance of cell death. For each Gy of radiation, there are approximately >2000 base lesions, 1000 SSBs, and 40 DSBs. Here, the number of DSB breaks has been seen to scale linearly with dose [37]. The formation of these breaks depends on the linear energy transfer (LET) of the incident radiation, namely, the amount of energy a particle deposits throughout its track (in units of $keV/\mu m$). Electrons and photons typically have low LET values, while particle ions (e.g., carbon) have high LET values. Low-LET radiation causes sparse ionisation, while high-LET radiation is densely ionising with many ionisations along its track, which results in a higher

frequency of clustered [3] DNA damage. For particle ions, the LET is dependent on incident energy and changes with depth in tissues, reaching a maximum at the distal edge of the Bragg-peak [45]. The complex DSB damage from high LET particles is harder to repair and is therefore repaired at a slower rate than DSB damage from low LET particles [46].

A number of repair pathways can rectify DNA damage. Base damage is repaired through base excision repair (BER), while nucleotide excision repair (NER) repairs bases and strand breaks in place, and mismatch repair (MMR) repairs erroneous insertions and deletions into the DNA structure. For DSBs, there are two main repair mechanisms: non-homologous end joining (NHEJ) and homologous recombination (HR). NHEJ is more rapid and dominant, though its error-prone nature causes more frequent mutations. NHEJ is divided into classical (C-NHEJ) and alternative (A-NHEJ). C-NHEJ is the primary and efficient pathway for repairing DSBs throughout the cell cycle, restoring breaks with only minor sequence alterations and a low probability of translocations [47]. However, when C-NHEJ is impaired or overwhelmed, DNA ends undergo resection and the repair machinery shifts toward A-NHEJ [48, 49]. A-NHEJ is microhomology-mediated process that acts as a backup to reseal escaped ends. However, its tendency to generate extensive deletions, junctional mutations, and translocations makes A-NHEJ a major driver of genomic instability [47]. By contrast, HR is slower, and considered an 'error free' repair mechanism with far fewer errors, though it is less common as it is restricted to the latter stages of the cell cycle [50]. The miss-repair of different sites of DNA damage can result in chromosomal aberrations which can ultimately result in cell death particularly when asymmetric aberrations form. Whereas, cell survival and subsequent subdivision is contingent on symmetric reciprocal translations or minor deletions [51].

[3] defined as two or more lesions (strand breaks and/or base damage) within 1-2 helical turns of the DNA [44]

1.4.5 Linear quadratic model

The survival of cells following irradiation is often described by the linear-quadratic (LQ) model:

$$S(D) = e^{-\alpha D - \beta D^2} \tag{1.1}$$

where $S(D)$ is the survival fraction, at a given dose D, with the parameters α and β describing the radiosensitivity of cells [52]. Here, the survival fraction is usually shown on a semi-log plot, where for low doses the linear term dominates, and at higher doses, the quadratic term is more pronounced. The linear term α represents the lethal lesions produced from a hit by a single particle track, while the quadratic term β represents two track events. The curvature is defined by the α/β ratio, which indicates the dose at which the contributions of the parameters α and β to killing are identical. Early responding tissues typically have a high α/β ratio, while late responding tissues typically have a low α/β ratio (with late adverse events typically mitigated by increasing the number of low dose fractions used). While most tumours are rapidly growing and have high α/β values, making them sensitive to overall dose with less effect from fraction size, however some tumours, for example prostate cancer, have low α/β values. This makes them more sensitive to large fraction sizes and resistant to small fraction sizes. Here, both tumour and normal tissues can be ascribed values [53]. However, in extreme high or low dose, or hypo/hyper-fractionated scenarios, the LQ model is limited. For such cases other models have been proposed [54, 55].

A low α/β ratio (e.g., $\approx$ 3 Gy) indicates a better capacity for repair and would better suit a prolonged fractionation schedule to spare normal-tissues. Whereas, for tissues with a high α/β ratio (e.g., $\approx$ 10 Gy), tissues have limited repair capacity and respond in a similar way independent of the fractionation schedule. Here, the deviation in values between normal and tumour tissues can highlight which fractionation schedule would be most relevant for treatment. Fraction size therefore is a key parameter which determines the biological response of late responding tissues.

Here, the measure for quantifying the biological effect of different fractionation schedules is given by the biologically effective dose (BED):

$$BED = D \times \left(1 + \frac{d}{\alpha/\beta}\right) \tag{1.2}$$

where n is the number of fractions and d is the dose per fraction, such that $D = nd$ is the total dose delivered [56]. The total dose delivered can, for a given tissue or fractionation schedule, be adjusted to provide the same biological effect [57]. Because 2 Gy fractionation schedules are widely used, treatments can be compared on the basis of the equivalent dose in 2 Gy fractions (EQD2) [58] which is given by:

$$EQD2 = D \times \frac{\alpha/\beta + d}{\alpha/\beta + 2} \tag{1.3}$$

1.5 FLASH radiotherapy

FLASH radiotherapy utilizes a differential sparing effect between normal and tumour tissues to broaden the therapeutic window within the modality of external beam radiotherapy. Whilst the most pertinent choice of temporal and spatial parameters remain to be determined, average ultra-high dose rates (UHDR) of at least ∼30 Gy/s have been observed to induce this effect [59, 60]. Because of the short delivery time, UHDR radiotherapy has the potential to increase patient throughput, reduce effects of anatomical movement, and reduce uncertainties in targeting tumour volumes [34, 61] in conjunction with appropriate low latency imaging techniques.

1.5.1 History

Early ultra-high dose rate studies

From the late 1950s to the mid-1980s a number of experiments were performed at ultra-high dose rates to study their effect on bacteria, mammalian cells, and mice. One of the first high dose rate experiments was performed by Dewey and Boag in 1959 at Mount Vernon Hospital [62]. Survival of bacteria was assessed following irradiations with doses of 100-200 Gy, from 1.5 MV X-ray at 0.1 Gy/s or 1.5 MeV single pulse electron irradiations delivered in 2 μs, at 50-100 MGy/s.

When comparing survival after irradiation in different percentage nitrogen and oxygen conditions, greater oxic conditions showed higher radiation sensitivity. They hypothesised that the increased survival was caused by the removal of dissolved oxygen by radiation induced reactions, without replacement from diffusing oxygen [62]. Quickly, similar observations followed for experiments with bacteria, supporting an oxygen depletion hypothesis [63–65]. In each experiment a clear "hockey-stick" shape survival curve with increasing dose could be seen. This curve, at a given dose, broke away from the steep falloff typical of aerobic cells, to a shallower falloff typical of hypoxic cells. The diffusion time of oxygen was also inferred by Epp et al. in 1973, by separating pulses and observing changes in bacterial survival with increased inter-pulse time. At pulse separations $>10^{-4}$ s significant levels of oxygen were restored in cells via diffusion [66]. These showed that the dose at which the hypoxic effects became apparent depended on the initial oxygen concentration and the timescale over which oxygen diffusion could occur [67].

Experiments investigating the survival of mammalian cells showed a similar break-away response, supporting the oxygen depletion hypothesis [68–70]. Here, the transition was observed to occur over a narrow dose range once oxygen levels have depleted by $\sim$90% and for smaller doses than those used for bacteria [71]. However, repeated experiments did not observe a hockey-stick shape in the survival curves under aerated conditions, indicating that too low a dose was used to deplete the oxygen [72–74]. In these experiments, a breakaway was only observed when irradiating in low oxygen conditions $<$1%, indicating that only cells with partial hypoxia would show 'radiobiological hypoxia' responses [75–78]. At this time, Berry et al. highlighted that for increased dose rates, the radiobiological hypoxia (and thus protection) induced in normal tissues could be utilised to increase doses to hypoxic tumour cells [74]. Similar breaks in survival were seen in oxic conditions for x-rays and high energy electrons [79], with too low an instantaneous dose rate postulated to cause an absence of the breakaway response. Because of these contradictory observations, other hypotheses were proposed, including radical-radical interaction,

which would deplete the number of radicals that could interact with oxygen and biological targets to cause cell death [76].

Early in vivo mouse experiments exploring acute radiation lethality using electrons and X-rays from a linear accelerators at dose rates from $0.0128\dot{3} - 26.\dot{6}$ Gy/s, saw little difference in survival up to 30 days post-irradiation [80]. Later experiments with mice and dogs irradiated with x-rays and neutrons respectively, mirrored these results with acute mortality when comparing moderate dose rates of ∼0.004-0.017 Gy/s with single high-dose rate pulsed response at ∼33-167 Gy/s [81].

Sensitivity to dose rate was seen after electron and x-ray irradiations when comparing mortality in mice breathing oxygen at dose rates from 0.0033-8.3 Gy/s, with a reduced dose required for mortality at increasing dose rates up to 1 Gy/s [82]. Later studies investigating mouse survival 5 days after irradiation disagreed with these findings. Comparing dose rates of 16-83 Gy/s and low dose rates of 1 Gy/s they demonstrated a clear decrease in sensitivity at higher dose rates with oxygen breathing, and no differences in survival for irradiations of mice with nitrogen breathing [83]. Meanwhile, an effect akin to mammalian experiments was seen for in vivo cell survival with a tumour 'take' model. Here, they showed a sparing effect only in leukaemia cells irradiated at low oxygen concentrations (0.35%) [78].

Irradiations to the skin of rat feet at dose rates of 83 Gy/s were seen to exhibit a sparing effect, inducing less early and late skin reactions and deformities compared to irradiation with dose rates of 0.033 Gy/s [84]. Here they highlighted that these results may have been because of the anaesthetization, causing the feet to not become fully oxygenated in oxygen or air breathing. Similar skin sparing was seen for mice when altering the instantaneous dose rate. Significant differences in sparing was found at instantaneous dose rates between $3,800\,Gy/s$ and $\sim 10,000$ Gy/s, as well as between $3,800\,Gy/s$ and $16,000\,Gy/s$, but not between $\sim 10,000$ Gy/s and $16,000\,Gy/s$ [85]. Meanwhile, irradiations on timescales <4.5 s to mouse tails revealed resistance to epithelial necrosis from oxygen depletion of cells at oxygen concentrations of 3-6 μM at high dose rates. Here, they highlighted that

a slow rediffusion of oxygen may occur with low dose-per-pulse (DPP) / intra-pulse dose rates. In their irradiations, they varied DPPs, dose rates within pulses, irradiation times, repetition rates, and the number of applied fractions, finding that skin sparing was greatly reduced for irradiation times ≥20s, and increased for irradiation times ≤4.5s [86].

Re-emergence in the 21st century

A revitalisation of ultra-high dose rate experiments emerged following the landmark 2014 paper by Favaudon et al. [60]. The study utilised 4.5 MeV electrons to deliver 17 Gy to C57/BL6 mouse lungs with xenografted human tumours and orthotopic lung tumours, at mean dose rates of 40 Gy/s, to compare biological outcomes to those from a delivery from a ^{137}Cs X-ray source at conventional dose rates of 0.03 Gy/s. Their results highlighted a widened therapeutic window, where lung fibrosis was reduced with ultra-high dose rates, while tumour control was isoeffective for ultra-high and conventional dose rates. The differential effect seen here was coined the 'FLASH' effect. A follow up by Montay-Gruel et al. achieved normal tissue sparing from whole brain irradiation of C57BL/6J mice with 6 MeV electrons using doses of 10 Gy, at dose rates of 0.1-500 Gy/s, and a single pulses at 5.6 MGy/s. Their novel object recognition tests indicated the start of a FLASH sparing effect at 30 Gy/s, with results indistinguishable from non-irradiated controls above 100 Gy/s [59]. A study at Stanford in 2017 by Loo et al. also found greatly increased survival (90%) of C57BL/6 mice following abdominal 20 MeV electron irradiations at 70 and 210 Gy/s, compared to conventional dose rate irradiations of 0.05 Gy/s (29%). Greater survival was seen at higher dose rates indicated with the metric of dose for 50 % lethality (LD50) increasing by a factor of 1.13 & 1.19 with FLASH compared to CONV dose rates [87]. In a later study by Vozenin et al., long term (up to 48 weeks) sparing was seen after 300 Gy/s irradiations on pig skin, for doses of 28-34 Gy compared to irradiations at conventional dose rates (0.083 Gy/s) [88]. In this study, a phase I single-dose escalation trial was also conducted for cat patients with locally advanced squamous-cell carcinoma (SCC) of the nasal planum.

Here, doses of 25-41 Gy were utilised at FLASH dose rates and five of the six cats showed progression free survival (PFS) after 16 months. Meanwhile, three cats experienced no acute toxicity, three experienced acute (after <20 days) moderate mucositis, and all experienced no late effects other than depilation starting >3 weeks after FLASH treatments. However, no equivalent conventional irradiations were performed for comparison using these doses.

in vivo

Preclinical studies in vivo have attempted to demonstrate the effect in a number of animal models (Table 1.1), for a number of normal tissue (Table 1.2) and tumour sites (Table 1.3). Most have utilised mice, with normal tissue investigations most commonly assessing brain, skin, or intestinal sparing.

Table 1.1: in vivo preclinical studies by animal model.

Model	Number of studies	Representative studies
Mice	52	[59, 60, 83, 85–87, 89–134]
Zebrafish embryos	7	[135–141]
Rats	6	[142–147]
Dogs	5	[107, 148–151]
Pigs	3	[88, 152, 153]
Cats	2	[88, 152]
C. elegans	1	[154]

The vast majority of preclinical investigations in vivo have utilised electrons from linacs [161], with biological endpoints following irradiations subdivided into acute (several weeks after) and late (several months after) effects. Sensitivity to these irradiation parameters depend on tissue or tumour model [101, 162], and not all studies have included groups that were not irradiated, or were irradiated at conventional (CONV) dose rates ($\lesssim 0.03$ Gy/s [88]) to compare effects. In general, favourable outcomes comparing FLASH and CONV have been concluded when isoeffective tumour growth suppression or enhanced normal tissue sparing have been observed. Most tumour growth assays have shown isoeffective tumour responses, by measuring tumour growth delay, but have used limited numbers of animals with short follow up times. In addition, differences in efficacy may be tumour type

Table 1.2: in vivo preclinical studies by normal tissue model.

Site	Number of studies	Representative studies
Brain	15	[59, 92, 94, 95, 104, 108, 114, 120, 126, 133, 134, 136, 143, 147, 155]
Skin	15	[85, 86, 88, 99, 102, 107, 110, 116, 124, 125, 128, 142, 148, 152, 153]
Lung	11	[60, 89–91, 97, 109, 117, 134, 156–158]
Intestinal regions	11	[83, 96, 105, 109, 111, 118, 121, 126, 127, 130, 134]
Abdomen	8	[87, 93, 96, 98, 113, 118, 132, 159]
Bone marrow	1	[101]
Heart	1	[93]
Gonads	1	[160]

dependent [161]. Meanwhile, for normal tissue toxicity assays, significant sparing at ultra-high dose rates has mainly been seen for irradiations with doses >10 Gy with mammalian skin irradiations [163]. A FLASH dose modifying factor (DMF), has been calculated, which compares the isoeffective doses to obtain the same biological endpoint after ultra-high dose rate (UHDR) and CONV irradiations. Most brain, intestine, skin, and lung studies have demonstrated a DMF of $\sim 1.1 - 1.5$, though outcomes are highly dependent primarily on tissue type, as well as irradiation modality, field/volume, and irradiation schedule [105, 128, 164].

$$DMF = \frac{D_{UHDR}}{D_{CONV}} \tag{1.4}$$

Some notable exceptions which did not show a FLASH sparing effect include: Venkatesulu et al. [93], Zhang et al. [118], Smyth et al. [134], Beyreuther et al. [135], and Bley et al. [152]. In Smyth et al., average dose rates of 37-41 Gy/s were used to irradiate C57BLJ/6 mice using a scanned synchrotron beam for total body, partial abdominal and head irradiations, while conventional dose rate irradiations (at 0.05-0.06 Gy/s) utilised an X-ray tube. There were no FLASH normal sparing effects seen here, however there were notable limitations to the study, such as; a small sample size in each group utilised, inconsistent field sizes and doses with FLASH and

Table 1.3: in vivo preclinical studies by tumour model.

Site	Number of studies	Representative studies
Lung	5	[60, 122, 156–158]
Glioblastoma	5	[104, 122, 144–146]
Naturally occurring superficial malignant melanomas; oral cavity tumours, carcinomas, sarcomas, mast cell tumours	5	[88, 148–151]
Breast	4	[106, 115, 119, 131]
Pancreatic	2	[93, 96]
Head and neck	2	[122, 156]
Ovarian	2	[98, 159]
Melanoma	2	[125, 130]
Medulloblastoma	1	[108]
Diffuse midline glioma	1	[123]
Colon sarcoma	1	[156]
Osteosarcoma	1	[112]
Squamous cell carcinoma	1	[129]

CONV groups, low scanning speeds resulting in long irradiation times (>1 s) [165], and too low dose rates to elicit a normal tissue sparing effect [134]. Beyreuther et al. also found no evidence for a FLASH effect when comparing treatments of zebrafish embryos with 224 MeV proton beams, at mean dose rates of 100 Gy/s and 0.083 Gy/s. They highlighted that their proton beam quasi-continuous cyclotron delivery resulted in micro-pulse dose rates far lower than those from electron linacs, with comparatively long FLASH treatment times of up to 400 ms. For reduced medium oxygen pressures, higher mean dose rates, and shorter delivery times, a later follow up study with the same equipment saw a prominent FLASH effect [139]. Venkatesulu et al. used a 20 MeV electron beam at mean dose rates of 35 Gy/s and 0.1 Gy/s. Here, a higher normal tissue toxicity was observed for FLASH irradiations than CONV [61]. Possible explanations for the absence of an effect include; a different beam setup with higher electron energies than utilised previously, too low mean dose rate used where a higher tissue specific / structure proliferation rate specific dose rate threshold may be required to observe a FLASH effect [166]. Similarly, Bley et al. performed a phase III clinical trial with cats with locally advanced squamous

cell carcinoma (SCC) of the nasal planum, as well as toxicity measurements for pig skin irradiations. Cats irradiations with a 6,9 or 12 MeV electron beam (for 4×4 cm^2 or 6×6 cm^2 field sizes) received standard protocol treatment (10×4.8 Gy at 0.1 Gy/s) or (2.6 cm diameter field size) FLASH treatments (1×30 Gy at 1500 Gy/s). One cat in each group developed local recurrence while both groups displayed acute toxicity ranging from mild to moderate. Three of the seven cats treated with FLASH developed late high-grade toxicity, unlike any of those receiving the standard protocol treatment. The three cats treated with FLASH developed bone necrosis at 12.5 – 15.1 months causing the trial to end prematurely, and relapse was observed for one cat in both groups. Meanwhile, when 6 MeV electron irradiation fields on pig skins were broadened from 3.5×4.5 cm^2 to 8×8 cm^2 with doses of 31 Gy at 150 Gy/s, late cutaneous toxicity was increased [152]. Cat treatments highlighted an inconsistent use of fractionation for only the conventional group, as well as non-identical total doses, field sizes and incident beam directions. The skin toxicity assay also did not have a conventional group from lack of ethical approval. Zhang et al. used a proton pencil beam to deliver 228 MeV in partial (∼60% volume coverage) abdominal irradiations of C57BL/6j and immunodeficient Rag1$^{-/-}$/C57 mice with doses of 14-18 Gy. Crypt cell counts were measured 280 days after irradiation, and showed worse survival for FLASH at 112-128 Gy/s relative to CONV at 0.053-0.4 Gy/s. Reductions in circulating lymphocytes from inconsistent field positioning was proposed as a possible explanation for the absence of a sparing effect [118]. However, their results were at odds with their previous study with fewer mice and the same setup. In this earlier study, each dose-rate group was irradiated consecutively (CONV group then FLASH group) while for their newer study, mice from each cohort were irradiated in an alternating order [167].

Clinical

In 2018, the first patient received ultra-high dose rate (FLASH) treatment for a 3.5 cm CD30+ T-cell cutaneous lymphoma on the skin surface. A 5.6 MeV linac was used to prescribe 15 Gy in 90 ms (∼ 167 Gy/s), or in 2.87 minutes to a separate

lesion on the same day. Five months after treatment, a complete tumour response was observed. After 2 years, there was isoeffective tumour control, while acute and late effects to skin around the tumour (i.e., initial redness, mild epithelitis/grade 1 toxicity peaking after 3-4 weeks, and return to normal appearance after 85 days), were similar for both FLASH and CONV irradiations [168]. Other patients have been irradiated with high proton dose rates of ∼10 Gy/s, close to, but below the widely assumed threshold for FLASH ($\gtrsim$ 40 Gy/s), without a major decrease in acute and subacute toxicity [169]. A non-randomized FAST-01 clinical trial at Cincinnati Children's Hospital Medical Centre (CCHMC) Proton Therapy Centre irradiated 10 patients with severe bone metastases by providing palliative 250 MeV transmission proton beam treatments with single fraction doses of 8 Gy at 51-61 Gy/s [170]. Two patients died prior to the two month follow up, while those remaining were evaluated up to three months after treatment. Long term patient follow up was limited because of disease progression, however, treatments were well tolerated, and most patients showed minimal toxic effects with comparable pain relief to previous trials with CONV photon treatments (67% vs 65%). A phase I dose escalation trial was also performed on 8 patients with skin metastases of melanoma. Total dose was delivered in 2 Gy increments from 22-28 Gy, with 10 MeV electrons at dose rates >200 Gy/s (in 90 ms). Dose limiting toxicity was not present up to 28 Gy, and tumour sizes were reduced by an average of 41% [171].
In the near future, the FAST-02 trial hopes to build on the work of FAST-01, with the aim of palliative treatment to 10 patients with painful bone metastases in the thorax with 8 Gy FLASH doses with the same proton beam. The trial may begin to discover whether FLASH sparing effects occur in proximal sites such as the lung, spinal cord, heart and oesophagus [172]. In addition, a phase II study of FLASH is recruiting to treat 60 patients with localised Cutaneous Squamous Cell Carcinoma (CSCC) or Basal Cell Carcinoma (BCC). Single dose treatments will be delivered to small lesions (<20 mm diameter) with doses of 22 Gy at FLASH (220 Gy/s) using 9 MeV electrons, or CONV (0.03-0.13 Gy/s) using 10 MeV electrons respectively. For large lesions (>20 mm & <40 mm diameter), doses will be applied

in 5×6 Gy fractions over two weeks with FLASH and CONV. This will highlight the potential of FLASH for small and large treatment areas with fractionation, and skin toxicity up to 12 months following treatment [173].

1.5.2 Parameters

In addition to setup-specific irradiation parameters (e.g., beam energy, SSD, and setup), several other key parameters are critical for exploring the FLASH effect and understanding its mechanisms.

Timescale

FLASH irradiation timescales are typically <100 ms. A key advantage of using these short timescales is the reduction of organ motion, respiration and changes in anatomy which therefore reduces uncertainty in targeting tumour volumes [34]. This is a significant source of uncertainty in the treatment in thoracic and abdominal cancers where tumour volumes can move as much as 5 cm [16]. Treatment sessions generally last for 30 minutes or more, with the majority of time devoted to preparation and patient positioning [174, 175]. Of the remaining time, beam delivery only accounts for ∼1-5 minutes [176]. Although a shorter beam delivery will reduce treatment time, even greater savings may be derived from eliminating the need for rigid immobilization devices. Doing so would also increase patient throughput and wellbeing by reducing their times spent in such devices [30]. In addition, reduced treatment times can reduce harmful psychological effects, while treatments with fewer/single fractions can reduce travel, expense, and the risk of treatment discontinuation or prolongation [177].

Dose

Single fraction doses have generally utilised $> 8\,Gy$ to observe a FLASH effect [166], though it is still unknown whether a minimum dose is required, and clinicians may consider these high fraction doses too large as for hypofractionated treatments at conventional dose rates, there is a considerable risk of late toxicity [61]. In addition, for critical normal tissues, conformal techniques already provide steep dose gradients

aimed at minimising normal tissue doses, which may in turn reduce the potential for additional normal tissue–sparing effects [163, 178].

Spatio-temporal parameters

Parameters describing the spatial dose distribution include; the field size, the dose profile, depth-dose profile, and irradiated volume [162]. Preclinical FLASH irradiations have typically irradiated mice and zebrafish volumes of $\sim 1-2\,cm^3$ [166], cat volumes up to $\sim 12\,cm^3$ [179], and pig skin volumes up to $64\,cm^3$ [152]. It is often assumed that the FLASH effect is independent of volume, and experiments with partial volume FLASH irradiations may be needed to verify this [180]. For larger volumes, scanning may be required which may affect the FLASH effect; from reduced local oxygen consumption rates [181], prolonged irradiation time, and variable volumetric distribution of doses and dose rates below FLASH thresholds [182]. The substantial demands imposed on traditional beam sources have meant most preclinical research has irradiated small volumes with no real-time spatial adjustments because of the slow adjustment speeds of multi-leaf collimators (MLCs) ($< 10\,cm/s$ [183]) [34]. A number of studies have highlighting that to achieve an isodose effect, the dose required rises significantly when field sizes are reduced [184–187]. However, it remains to be seen how normal tissue sparing seen in in vivo single dose irradiations over small volumes would scale to clinically sized treatment volumes.

Temporal dose delivery parameters may also be of direct relevance. The temporal parameters of pulsed output of a linac, and from which other quantities are derived, include: the number and pulse repetition frequency of micro and macro pulses (f_{mic} and f_{mac}), and the dose rate within the micro pulse ($\dot{D}_{mic}$), (as seen in table 1.4). Pulse structures vary depending on the beamline system used for acceleration (see Table 1.5). Differences in temporal beam structure between quasi-continuous (cyclotron), pulsed (synchrocyclotron), and continuous (synchrotron) delivery further complicate comparisons with electron FLASH irradiations from linacs, even when similar average dose or dose-rate metrics are achieved in a given irradiation [139].

Table 1.4: Temporal parameters adapted from [165, 188–190]

Symbol	Equation	Parameter Name
n_{pmac}	-	number of macro pulses
n_{pmic}	-	number of micro pulses
t_{mic}	-	micro pulse time
t_{rmac}	$\frac{1}{f_{mac}}$	time between macro pulses
t_{rmic}	$\frac{1}{f_{mic}}$	time between micro pulses
t_{mac}	$(n_{pmic}-1)\,t_{rmic}+t_{mic}$	macro pulse time
DC_{mac}	$100\times\frac{t_{mac}}{t_{mac}+t_{rmac}}$	macro duty cycle
DC_{mic}	$100\times\frac{t_{mic}}{t_{mic}+t_{rmic}}$	micro duty cycle
$\dot{D}_{mic}$	-	dose rate in micropulse
DPP_{mic}	$\dot{D}_{mic}t_{mic}$	dose per micropulse
$\bar{\dot{D}}_{mic}$ or $\dot{D}_{mac}$	$\frac{n_{pmic}DPP_{mic}}{t_{mac}}$	mean dose rate in macropulse
DPP_{mac}	$\dot{D}_{mac}t_{mac}$	dose per macropulse
D_{totmac}	$DPP_{mac}n_{pmac}$	total dose in macropulse
D_{totmic}	$DPP_{mic}n_{pmic}$	total dose in micropulse
t_{irr}	$(n_{pmac}-1)\,t_{rmac}+t_{mac}$	total irradiation time
$\bar{\dot{D}}_{mac}$	$\frac{n_{pmac}DPP_{mac}}{t_{irr}}$	mean dose rate in irradiation

Here, the use of continuous rather than pulsed irradiation may affect biological endpoints in normal and tumour tissues [165, 191].

Average dose rate & dose-per-pulse

The first study to explore the effect of altering FLASH temporal parameters with separated two-pulse deliveries was performed by Ruan et al. Here C3H mice were

Table 1.5: Pulse parameters from common accelerator systems [166]

Type	Pulse duration	Repetition rate
Cyclotron	ns-μs	kHz-MHz
Linac	μs-ms	Hz-kHz
Synchrotron	ms	Hz

irradiated with 6 MeV electrons over the whole abdomen 33×30 mm^2 field. CONV irradiations were performed at 0.25 Gy/s, with 10 mGy/pulse while single pulses were delivered at FLASH dose rates of $2.2 - 5.9 \times 10^6$ Gy/s, with doses of 11.2 and 12.5 Gy. Comparison of FLASH and CONV revealed a dose modifying factor to achieve equal remaining crypt numbers of 1.1 for conventional doses between 7.5-12.5 Gy. For 11.2 Gy irradiations for a two-pulse delivery was varied from 3.3 ms - 30 s. As the interval was increased, and dose rate was reduced, there was decreased crypt survival, with highest survival for a single pulse irradiation [105].
At MD Anderson, Liu et al. [130] explored the effect of DPP by performing total abdominal 9 MeV electron irradiation of C57BL/6J mice. DPP was varied for 1-5.5 (11 Gy total dose), 1.3-6 Gy (12 Gy total dose), and 1.08-4.7 Gy (14 Gy total dose). DPP was varied with altering pulse width (0.6-3.6 μs), with a constant instantaneous dose rate (between 1.5-1.7 MGy/s). Mean dose rate was adjusted by altering repetition rate (5-120 Hz), for an output of 0.3-1350 Gy/s (11 Gy total dose), 0.3-1440 Gy/s (12 Gy total dose), and 0.3-830 Gy/s (14 Gy total dose). Meanwhile, conventional irradiations were performed at 0.3 Gy/s and a DPP of 10 mGy. Dose rates above 100 Gy/s showed highest sparing of intestinal crypts in highest DPP groups (5.5, 6 and 4.7 Gy/pulse for 11, 12 and 14 Gy total dose) and greatest difference to the CONV treatment for the highest dose group (14 Gy). With high DPP (>4.7 Gy/pulse), adjusting the time between two pulses (even with mean dose rates similar to CONV) did not drastically change the numbers of regenerating crypts, with all showing significant sparing relative to the CONV treatment.
Another treatment arm of Liu et al. [130] delivered 14 Gy in high (4.7 Gy/pulse) and low (0.93 Gy/pulse) DPP groups, while maintaining UHDR (104 Gy/s) or

CONV (0.3 Gy/s) dose rates (see Table 1.6). Survival after 86 days, was similar for high DPP irrespective of mean dose rate (50-60%), with UHDR irradiations at low DPP also similar (60%). Survival was much higher than for the low DPP irradiations at CONV (20%), and the standard CONV irradiations (10%).

Lastly, in Liu et al. [130], tumour growth was also monitored after 20 Gy

Table 1.6: Irradiation parameters for temporally equidistant irradiations from Liu et al. [130]

Group	Pulses in sequence	DPP (Gy)	Total Dose (Gy)	Total Time (s)	Mean dose rate (Gy/s)
High-DPP (UHDR)	3	4.7	14	0.13	104
High-DPP (CONV)	3	4.7	14	45	0.3
Low-DPP (UHDR)	15	0.93	14	0.13	104
Low-DPP (CONV)	15*	0.93	14	45	0.3
standard CONV	1356	0.01	14	45	0.3

$\star$ 3 sets of 5, with 22.5 s gaps

irradiation of mice bearing a 100 mm^3 volume subcutaneous melanoma. Three groups; a standard conventional, 6.7 Gy/pulse & 1208 Gy/s, and 6.7 Gy/pulse & 0.3 Gy/s showed no differences in tumour growth. These findings suggested that FLASH doses may be delivered in separated schedules if the DPP is high (>4 Gy/pulse). Though, when DPP is low, increasing the mean dose rate or reducing the total irradiation time highly influences biological outcomes. In addition, their findings for acute regenerating crypt numbers with lower DPPs ($\sim$1 Gy/pulse) at high mean dose rates (100 Gy/s) were not significantly different to their CONV irradiations. The authors postulated that these contradictory findings may indicate that acute and long term assays may involve biological mechanisms with different sensitivities to dosimetric parameters [130].

In Grilj et al., whole abdomen irradiations of C57BL/6 mice occurred with single doses of 17 Gy using a parameter space defined by average dose rate and DPP. Mice were irradiated with electrons with energies of 5-6 MeV. Pulse repetition rates were varied from 5-250 Hz, with pulse durations varied between 1-2.2 μs, DPPs from 0.02-2.83 Gy, and average dose rates from 0.2-340 Gy/s. This meant treatments times varied from 0.05-84.9 s. Survival and the number of regenerating crypts were

scored and monitored up to 30 days after treatment. With a repetition rate of 100 Hz, dose rate was raised from 16 to 340 Gy/s. Survival of 340 Gy/s and 106 Gy/s groups were similar at ∼90%, while 42 Gy/s showed 48%, and <16 Gy/s groups showed no significant differences (with survival at <8%). These same significant differences were also seen when counting the number of regenerating crypts. With DPP constant in 4 separate groups (0.02 to 2.83 Gy/pulse) and repetition rate altered, average dose rate was isolated as an independent variable. After 30 days, DPP led to variable survival rates. However, a much stronger correlation occurred with survival and average dose rate (independent of DPP), with those above ∼100 Gy/s providing maximal sparing, and those at ∼40 Gy/s marking the inflection point in the sigmoidal survival curve. These findings for average dose rate cannot be distinguished from the dependence of total irradiation time because of the inverse correlation and fixed overall dose. There may also be a greater dependence of DPP >2.33 Gy/pulse, and that DPP for few sparse pulses at low repetition rates is a more useful metric of comparison [127].

However, there were notable differences between these studies, such as the methodologies for counting crypt survival, anaesthesia agent [132](& absence of some control groups), weight loss criteria for euthanasia [4], mouse type, electron energy, field size, doses, instantaneous dose rates, and number of mice per group. These differences make retrospective analysis more complex, but highlight that methodologies for metrics such as crypt regeneration can be useful when correlated with clinically relevant biological endpoints such as efficacy/lethality (using overall survival), acute toxicity (using weight loss), and organ functionality (with faecal analysis).

Fractionation

In treatment plans, increasing the number of fields can often produce an improved treatment. However in FLASH, any subdivision of dose within fields may reduce the total dose in a given fraction below the threshold required to induce a sparing

[4] in Levy et al. [98] 20% weight loss in FLASH groups irradiated with 16 Gy were reversed after 15 days, while Grilj et al. euthanised mice with >15% permanent body weight loss with 17 Gy [127]

effect [178].

Hypofractionation with 10 Gy brain irradiations, using a 6 MeV electron beam, have been seen to spare normal brain tissues without compromising tumour control in orthotopic murine and human glioblastoma models up to one month after irradiation [104]. FLASH irradiations were performed with single pulses, at a mean dose rate $>2\times10^6$ Gy/s, while CONV irradiations were delivered at a mean dose rate of 0.1 Gy/s. With 2×7 Gy fractions 24 hrs apart, and 3×10 Gy fractions 48 hrs apart, mice did not experience neurocognitive decline in FLASH regimens. For the 4×3.5 Gy fractionated group (every 24 hrs), similar tumour growth delay was seen for irradiated groups with a significant delay relative the non-irradiated control. For irradiated groups, there were no differences in survival and no significant neurocognitive decline in all groups. This indicated that at low dose per fraction (and therefore DPP), no sparing was derived from FLASH. A 25 Gy irradiation over a conformal tumour bearing region was also performed. Complete tumour control was seen for irradiated groups with >25% survival. Both treatment groups showed significant control relative to non-irradiated animals, while neurocognitive function was comparable for irradiated and non-irradiated groups. This study indicated for intra-pulse/mean dose rates ($\sim2\times10^6$ Gy/s) with doses below <14 Gy, that large DPP ($\sim$7 Gy) in daily fractions could exhibit a normal tissue FLASH sparing effect, while enabling equivalent tumour control to CONV irradiations [104].

These findings were similar to Limoli et al., who performed whole brain irradiations with 6 MeV electrons over a field of 17 mm diameter. Here, 10×3 Gy was delivered at CONV (0.09 Gy/s) or single pulses at FLASH dose rates (1.6×10^6 Gy/s), with mice evaluation 4 months after irradiation using an electrophysiologic measure of synaptic plasticity called long-term potentiation (LTP). LTP, alongside other metrics, exhibited a sparing effect following irradiations with FLASH but not CONV which indicated a preservation of memory and learning processes [155].

Mascia et al. utilised a proton beam scanned at FLASH (250 MeV) field average dose rates of 100 Gy/s, and compared them to CONV (244 MeV) 1 Gy/s irradiations of C57Bl/6j mice legs, with skin toxicity scored after 7 weeks. Dose delivery was

performed with 2 minute interruptions observed between 1, 2 or 3 fractions, and total doses ranging from 30-45 Gy. For CONV irradiations, no differences were seen in toxicity between these groups. For 2×15 Gy, 3×10 Gy, and 3×11.7 Gy no noticeable difference was seen between CONV and FLASH irradiations. However, for 2×17.5 Gy there was an improvement with FLASH compared to CONV [170]. For Sørensen et al., splitting the dose (39.3 Gy) delivered with a scanned proton pencil beam (at field average dose rates[5] of 0.7-80 Gy/s, & PBS dose rates from 2 to 210 Gy/s) into a number of identical deliveries (2-6) with 2-minute pauses, reduced the FLASH skin sparing effect (after 25 days) for increased numbers of pauses (for >3 there was no sparing effect). In addition, repainting with the same field dose rate led to higher toxicity, and a diminished skin sparing effect [192].

Konradsson et al. evaluated tumour growth and survival up to 100 days after fractionated irradiations of Fisher rats with subcutaneous glioma cells with 3×[8, 12.5, or 15] Gy using 10 MeV electrons at FLASH dose rates of 70-90 Gy/s, and at CONV dose rates of 0.13 Gy/s. No significant difference was seen between FLASH and CONV in overall survival, and acute and late side effects for all dose levels. Only when comparing to the 3×8 Gy, were significant differences seen in survival between CONV groups. In addition, no severe acute toxic skin effects were seen between CONV and FLASH, and late skin toxicity increased with fraction dose. They postulated that a FLASH sparing effect may have been absent because too low doses were delivered [144].

Similar experiments were performed in Liljedahl et al., with Fischer 344 rats injected subcutaneously or intracranially with glioblastoma cells. Treatments of developed tumours were given using a 10 MeV linac in fractions of 2×8 Gy (for subcutaneous) or 2×12.5 Gy (for intracranial) at FLASH (66 Gy/s) or conventional dose rates (0.13 Gy/s). For subcutaneous irradiations at both dose rates, irradiated mice were cured and showed long-term tumour immunity, while similar increases in survival were seen for intracranial CONV and FLASH irradiations [145]. These studies highlight the potential for similar tumour control in fractionated schedules at UHDR and CONV

[5]'the total dose delivered divided by the total field duration' [192]

dose rates, and that a FLASH sparing effect may only be attainable in a fractionated schedule for a specific tissue type, dose, dose rate and DPP. However, for schedules more akin to the clinic, the number of fractions tested preclinically may need to be >3, with a more diverse array of irradiated normal tissues type, and tumour models.

1.5.3 Potential Mechanisms

The mechanisms behind the FLASH effect warrant further exploration. Leading hypotheses include; oxygen depletion, a reduced number of reactive oxygen species, reduced lipid peroxidation, free radical recombination, and reduced irradiation of circulating cells.

Oxygen depletion

The biological effectiveness of radiation in the presence of oxygen is well categorised by the oxygen enhancement ratio (OER), defined as the ratio of doses required for a biological system under hypoxic to aerobic conditions to achieve the same radiobiological effect (typically with a value of between $2.5 - 3.5$ for low-LET radiation) [37]. Here, radiosensitivity changes sharply at oxygen levels around $\sim 0.5\%$ (see Figure 1.3). Because normal tissues typically exist at relatively low oxygen tensions ($\sim 3-7\%$), even relatively small reductions in oxygen can markedly alter radiosensitivity. By contrast, for experiments in air or at higher than normoxic oxygen levels ($\sim 21\%$), comparable reductions in oxygen tension do not significantly alter radiosensitivity. The timescale over which this effect occurs was originally investigated using 'gas explosion' techniques to rapidly oxygenate mammalian cells and bacteria before or after an electron $\approx 2\mu s$) pulse from a linac [66, 71, 193, 194]. These experiments highlighted that sensitisation could occur from supplying oxygen up to a delay of a few ms after the irradiation [195]. The mechanism behind this effect is the oxygen fixation hypothesis. Here, indirect damage to DNA is caused by the reaction of free radicals (predominantly hydroxyl radicals $^{\bullet}$OH) with DNA to produce an intermediary DNA$\bullet$ radical. In the presence of oxygen, this radical can produce a non-restorable organic peroxide (DNA-$O_2\bullet$),

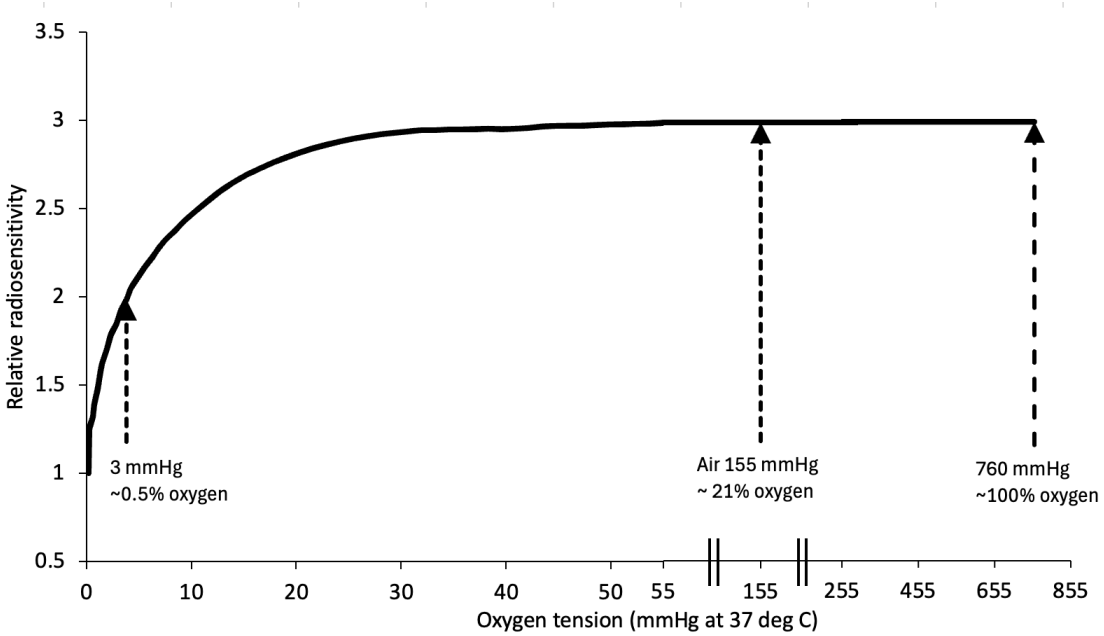

Figure 1.3: Idealised representation of relative radiosensitivity with oxygen tension, adapted from [37]

whereas, in the absence of oxygen, the damage can be restored in the presence of naturally occurring reducing species e.g., thiols via a reaction with a sulfhydryl (SH) group. The presence of molecular oxygen therefore shifts the balance of these competing reactions and 'fixes' the damage to DNA, where the organic peroxide (DNA-O_2•) can otherwise only be repaired via an enzymatic pathway from a DNA repair mechanism [37, 51]. It is also noteworthy that the reaction of hydroxyl radicals with macromolecules, such as proteins, can form additional radicals on a nanosecond timescale which can cause rapid oxygen depletion within the irradiation field. Therefore, the oxygen concentration within milliseconds of irradiation is a key driver of radiosensitivity, where a local oxygen depletion can reduce radiosensitivity to radiation. The oxygen depletion hypothesis stems from the observation that at high dose rates, radiation may deplete oxygen to a greater extent than it is restored via diffusion (typically a few microns per millisecond up to $\sim 70\mu m$) and by blood perfusion (via the circulatory system). Subsequently, normal tissue becomes hypoxic and reoxygenation will not occur during treatment, causing increased radioresistance of normal tissue. When a hypoxic tumour is surrounded by normal tissues, ultra-high dose rate will preferentially increase the radioresistance of the

normal tissues without impacting the tumour tissue, leading to a widening of the therapeutic window [196]. Evidence for this hypothesis came from experiments showing that the dose required to induce epithelial necrosis in 50% of clamped (anoxic) mouse tails was unchanged across dose rates, whereas in tails irradiated in air, the required dose increased with dose rate, demonstrating a clear sparing effect [86]. By contrast, in Montay-Gruel et al., when oxygen levels were increased above normoxic levels, this caused an abrogation of the long term FLASH sparing effect [136]. The hypothesis indicates that sparing may be derived from reduced yields of toxic reactive oxygen species (ROS) which are caused by the rapid depletion of local oxygen concentration [104]. However, it has been suggested that oxygen is unlikely to be the sole contributor to sparing as, in oxygenated pure water environments, only extremely large doses (>100 Gy) are required to elicit appreciable reductions in oxygen levels. These arguments most commonly concern fully oxygenated pure water, rather than the highly reactive intracellular environment where the lifetime of radicals is limited to nanoseconds and where small reductions in oxygen have a larger impact under the reduced oxygen concentrations typical of normal tissues [197, 198]. Similarly, it does not fully explain the equal tumour control seen in vivo even when ROS levels are decreased.

Lipid peroxidation

The lipid peroxidation hypothesis originates from evidence of decreased lipid peroxidation yields when dose rates are increased [199]. Lipid peroxidation has also been seen to persist for longer at a greater rate with CONV rather than for FLASH dose rates [200]. The hypothesis suggests that the increased labile iron pool in tumours would increase the reaction rate of Fenton chemistry to exacerbate tumour killing, with an increased free iron concentration and low pH indicative of a high yield of lipid peroxidation. Where an increased lipid peroxidation corresponds to an increase in ferroptosis [201]. Ferroptosis is therefore a unique form of programmed cell death obtainable in refractory tumours even when other forms of cellular stress response e.g., cell-cycle arrest, apoptosis and/or senescence are abrogated [202].

More recently, the effect of lipid peroxidation has been explored further, with in vivo models showing an elimination of a FLASH effect in normal tissues when iron levels were sustained at increased levels in the intestine. In these studies, tumours showed similar levels of peroxidation for FLASH and CONV dose rates [203].

Radical recombination

The free radical recombination hypothesis is obtained from the prediction that FLASH can increase instantaneously free radical numbers which can enable their recombination, thereby reducing the production of radiolytic species, and resultant damage [204]. This was supported by observations in Montay Gruel et al. with a reduction in the concentration of H_2O_2 in water with FLASH dose rates compared to CONV [136]. However, unlike water, the highly reactive environment within the cell, limits the lifetime of the radicals, such as $OH^{\bullet}$ to the order of 4–9 ns and associated diffusion distance to just 6–9 nm [205], limiting the reaction probability with other radiation induced radicals.

Circulating immune cells

Lastly, the circulating immune cell hypothesis states that the number of irradiated circulating cells is reduced. This reduction arises from the notion that lymphocyte damage is dependent on irradiated volume and exposure time, where high dose rate reduces the number of circulating blood cells irradiated, which spares the immune system to a greater extent than conventional fractionated treatments [196]. This hypothesis highlights the potential utility of constituent cells in the blood volume to mediate toxicity, whilst indicating the potential role of immune system in the mechanism [155].

1.5.4 Beamlines

Electron accelerator systems

To enable ultra-high dose rate electron output, clinical linacs have been modified with x-ray target and flattening filter removal, adjusted source separation, gun current setting, beam steering, scattering foil placement, and pulse control [206–211].

In Schüler et al. 2017 [206], 9 and 20 MeV beams were delivered with source-to-surface distances (SSD) of 100 cm to ∼5 cm, to change dose-rate settings. They demonstrated dose rates of 220 Gy/s at ∼ 12.5 cm SSD, 1 cm depth, >4 cm field size, and 90% homogeneity up to a depth of 2 cm in the irradiated volume. Here, the reduced SSD and field size restricted usage to small preclinical animal or cellular experiments [210]. For reduced separations and scattering foil thickness, beam flatness was seen to reduce but dose rates were increased [207], with linac conversion easily reversible [209]. For these beams greater output variability has been seen in warm-up periods, and at higher pulse repetition rates [207, 211]. However, these approaches have caused concerns among accelerator manufacturers. They indicate that modifications must occur on decommissioned beamlines, and if restored to clinical usage, these may cause patient harm if untrained users have pushed dose rates beyond tested limits and into operation that reduces their operational life, and causes unpredictable output variation or irrevocable failures [212]. In addition, use of beams still in clinical use have availability restricted to non-working hours. Prototype preclinical research linacs have also been used to produce UHDR beams [60, 213–215]. Output variation was also seen to depend on dose-rate, with the relative DPP (compared to a single pulse irradiation) dropping by up to ∼20% when the number of delivered pulses was increased and the repetition frequency was set to its highest setting. Beam energy with FLASH irradiations have been degraded, with energies of 4.9 MeV for FLASH compared to 6 MeV for CONV irradiations [213], with different pulse durations for these dose rates [214].

Photon accelerator systems

Many x-ray FLASH systems have relied on the use of x-ray tubes [110, 216]. In addition, small animal radiation research platforms (SARRPs) have been used to deliver kV FLASH x-rays (at ∼150-160 kVp) for preclinical research [125, 217–219]. A SARRP irradiator is an advanced, image-guided system for preclinical radiation research, enabling precise delivery of radiation to small animals to mimic human cancer therapies. It is self shielded, and integrates cone-beam CT (CBCT)

for accurate targeting, and treatment planning software to enable complex, 3D-conformal treatments (such as stereotactic radiotherapy) to be performed by controlling beam angles and field sizes with high precision, sharp penumbra, and high treatment conformality [220]. However, only higher power systems (∼6-7.5 kW) can reach FLASH dose rates, and limited filtration has only enabled FLASH dose rates to obtained in superficial sites (up to 2-3 mm) and square field sizes up to ∼20 mm. By increasing input power by a factor of ∼10, and with parallel-opposed arrangement with variable tube separations, dose rates of 40 Gy/s have been achieved at up to 10 mm depth with fluoroscopy x-ray tubes [221]. Similarly, adjustable dose rates from <1 Gy/s to 100 Gy/s (dependent on field size) have been developed with FLASH SARRP systems [219]. Here, the removal of copper filtration increased dose rates most prominently at shallow depths, and caused a reduction in flatness for increasing field size. The central axis dose rate within the fields also followed an approximately inverse square relation with depth [219]. However, these parallel-opposed systems have resulted in 30% higher entrance and exit doses than those in the centre of phantoms [217].

Synchrotron sources such as the Australian Synchrotron [134], National Synchrotron Light Source (NSLS) at Brookhaven [143, 222] or the European Synchrotron Research Facility (ESRF) [133] have been used to deliver scanned kV X-rays. These beams have short pulses at high brilliance with small beam divergence [143, 223, 224]. However, these sources suffer from high construction and maintenance costs, and limited worldwide accessibility.

To enable a clinical translation of FLASH and greater treatment access, a number of systems are being developed to deliver ultra-high dose rates. The pluridirectional high-energy agile scanning electronic radiotherapy (PHASER) system proposed by Maxim et al. [225], could enable the delivery of image-guided X-ray FLASH to deep-seated targets. Here, a new accelerating cell design was proposed to improve efficiency, and shunt impedance by ∼2.5-4× by minimizing peak surface magnetic fields, and waste heating. In each cell the power is distributed independently without cell coupling, so higher frequencies can be achieved without exciting other

accelerating modes when beam loading increases. The power source was described as multiple compact klystrons with ∼330 kW of peak RF power that can form a combined power output. This power can be rapidly distributed sequentially among 16 stationary linacs delivering non-coplanar FLASH IMRT photon beams from 16 angles. Photons are produced by scanning the electron beam across a stationary target and collimator array to generate 10 MV X-rays, mitigating target heating and eliminating the need for MLCs. Here, beam conformality is achieved with flexibly shaped channels in a downstream tungsten collimator block using 3-D printing [226]. This beamline is said to be able enable the delivery of high photon dose rates to larger volumes without gantry or collimator motion. Other beamline setups have been proposed with rotating sources with multiple MLCs [227], laser-driven plasma X-ray sources [228, 229], or developed using inverse Compton scattering [230–232]. However, only two beamlines are currently available that can deliver preclinical ultra-high dose rate MV photon beams; China Academy of Engineering Physics terahertz free electron laser (CTFEL) (Chengdu, China) [111, 113, 233], and the TRIUMF Advanced Rare Isotope Laboratory (ARIEL) (Vancouver, Canada) [234].

1.5.5 Preclinical photon FLASH

Relatively few studies have used photons at FLASH dose rates compared to electrons and protons. Kilovoltage photon FLASH investigations have included Montay-Gruel et al. where 10 Gy was delivered to mice in whole brain irradiations. Here, the ESRF was used to produce a broad 50 μm beam scanned over the target with a dose rate per slice of 12,000 Gy/s, a mean-dose rate of 37 Gy/s and total delivery time of 0.27 s ($V_{irr} < 1cm^3$) [235]. Comparing results 2 and 6 months post-irradiation, treatments with single doses at FLASH dose rates showed a large sparing effect compared to CONV, and little difference to an unirradiated control [133].

Miles et al. also utilised an orthovoltage x-ray tube system to expose the hind leg of non-tumour bearing mice to a dose of 35 or 43 Gy at FLASH (87 Gy/s) or CONV (<0.05 Gy/s) dose rates. A subcutaneous melanoma tumour growth assay was also performed, with treatments of 35 Gy at FLASH and CONV dose rates. Again, a

significant reduction in skin toxicity, inflammation and fibrosis was seen 8 weeks after irradiation for FLASH relative to CONV dose rates, while tumour growth was equivalent for these dose rates [116].

Likewise Brown et al. utilised a SARRP system to deliver kV x-rays at dose rates of 3.2 Gy/minute (CONV) and 72 Gy/s (FLASH). Mouse skin toxicity was assessed following doses for FLASH at 18.1,21.3 and 25.8 Gy, and a dose at CONV of 20.2 Gy. In addition, two pulse split dose irradiations were delivered with an 8-10s interval. Melanoma tumour growth was also assessed in a subcutaneous model. Higher doses caused greater toxicity, and a delay in the induction of skin toxicity was seen for FLASH groups (2 weeks) with the same maximum at 50 days, while CONV groups saw more fibrosis after 12 weeks, and split doses reduced sparing. Equivalent tumour control also occurred. However, their results showed sex based differences for skin toxicity potentially from variations in skin thickness. Results also highlighted the dependence of biological endpoint on their calculated DMF values (1.04±0.13 for skin toxicity & 1.75±0.52 for fibrosis). Here, tumour growth delay was not significantly different at all dose rates [125].

These kV irradiation platforms are however, limited to irradiated tissues/tumours at superficial depths so cannot be expanded to investigate other endpoints. In these investigations, platforms varied markedly in their bunched and continuos temporal structures, highlighting that mean dose rate (above a threshold dose) may be a parameter most attributable with normal tissue sparing.

Megavoltage photon FLASH investigations have been conducted at the CTFEL. In Gao et al., photon beams at 6-8 MV were produced with dose rates of >1000 Gy/s. Three experiments were performed to compare the effect of FLASH and CONV single fraction doses on mice. For whole-thorax irradiated mice, fibrosis was more severe for CONV irradiated mice after 72 hrs and survival to 60 days was 90% in the FLASH group, and 50% in the CONV group. For whole-abdomen irradiated mice, an inflammatory response was seen, and after 4-5 days FLASH and CONV groups died from radiation induced enteritis. In a repeat of thorax-irradiated mice, median survival for the FLASH group (120 days) was greater than the CONV group

(86 days). For abdominal-irradiated mice, 62.5% of mice survived to 120 days, while all CONV mice died after 7 days. They concluded that X-ray FLASH can spare normal tissue, but had no protective effect for abdominal irradiations because of differences in organ specific dose and dose rate tolerance [233].

Similarly, Shi et al., delivered doses of 10 or 13 Gy, with instantaneous dose rates of 1.85×10^5 Gy/s, and mean dose rates for FLASH at 110-120 Gy/s using the CTFEL. Meanwhile, an orthovoltage source was used at ~ 0.03 Gy/s for CONV irradiations. From irradiations of mice in vivo, and their results of intestinal crypt organoid irradiations, a mechanism for the FLASH effect was proposed that indicated that FLASH preserves DNA integrity to a greater extent than CONV irradiations and only depends on the total time for dose delivery [111].

In Zhu et al., mice were irradiated abdominally with 6 MV X-rays FLASH or CONV. In FLASH groups, mean dose rates of >150 Gy/s and instantaneous dose rate of 5.5×10^5 Gy/s were delivered. After 6 weeks, FLASH irradiated mice were seen to produce a lesser inflammatory response. Meanwhile, acute response revealed higher ROS signal intensities and reduced lipid peroxidation in the FLASH group compared to the CONV group [113].

Extending this work in Zhu et al. (2023), C57BL/6 mice were inoculated subcutaneously with xenograft breast tumour cells. For FLASH irradiations of abdominal regions, 10 Gy was delivered with 6 MV photons produced at instantaneous and mean dose rates of 4.6×10^5 Gy/s and 125 Gy/s respectively, and for CONV irradiations, 10 Gy was delivered with a 6 MV FFF X-ray beam at 0.2 Gy/s. Similar tumour growth suppressed was seen up to 30 days after irradiations with FLASH and CONV. One week post-irradiation, tumour samples were indistinguishable from controls; at two weeks, FLASH and CONV remained similar indicating comparable immune responses. By contrast, spleen analyses showed differences between FLASH and CONV, consistent with a stronger systemic immune response with FLASH. From crypt investigations, FLASH was seen to induce less intestinal inflammation. They highlighted that similar tumour control behaviour could be achieved for FLASH and CONV irradiations, but that reduced toxicity in normal tissues may occur from

altered immune response with FLASH [119].

However, these studies at CTFEL were limited by inconsistent FLASH and CONV beamlines, variable dose profile flatness, doses, and dose rates, which makes retrospective analysis more complex.

1.6 Spatially fractionated radiation therapy (SFRT)

Like FLASH radiotherapy, spatially fractionated radiation therapy (SFRT) can increase normal tissue tolerance to dose, thereby widening the therapeutic window. SFRT represents a step change from traditional approaches to radiotherapy, with the deliberate application of heterogeneous dose distributions in tumours. This method contradicts conventional wisdom, whereby all cells within the tumour volume are required to receive directly, a lethal dose for tumour control. The rationale behind this irradiation method is to kickstart anti-tumour immunological response, and exploit the benefits mediated by abscopal, bystander effects, vascular damage, perfusion, inflammatory and immunological mechanisms that occur because of heterogeneous dose delivery [236–238].

The approach may lower normal tissue toxicity, potentially enhance tumour control and thereby widen the therapeutic window, using small volume regions of higher peak doses to harness greater normal tissue tolerance by reducing deleterious dose-volume effects. SFRT treatments with high doses have potential to better target bulky (> 5 cm), and radioresistant tumours, especially those close to sensitive structures and organs at risk (OAR), where treatments often result in long-term toxicities and impairments that reduce patient quality of life [239, 240]. These include primary cancers such as head and neck, lung, breast, gynecologic and sarcomas.

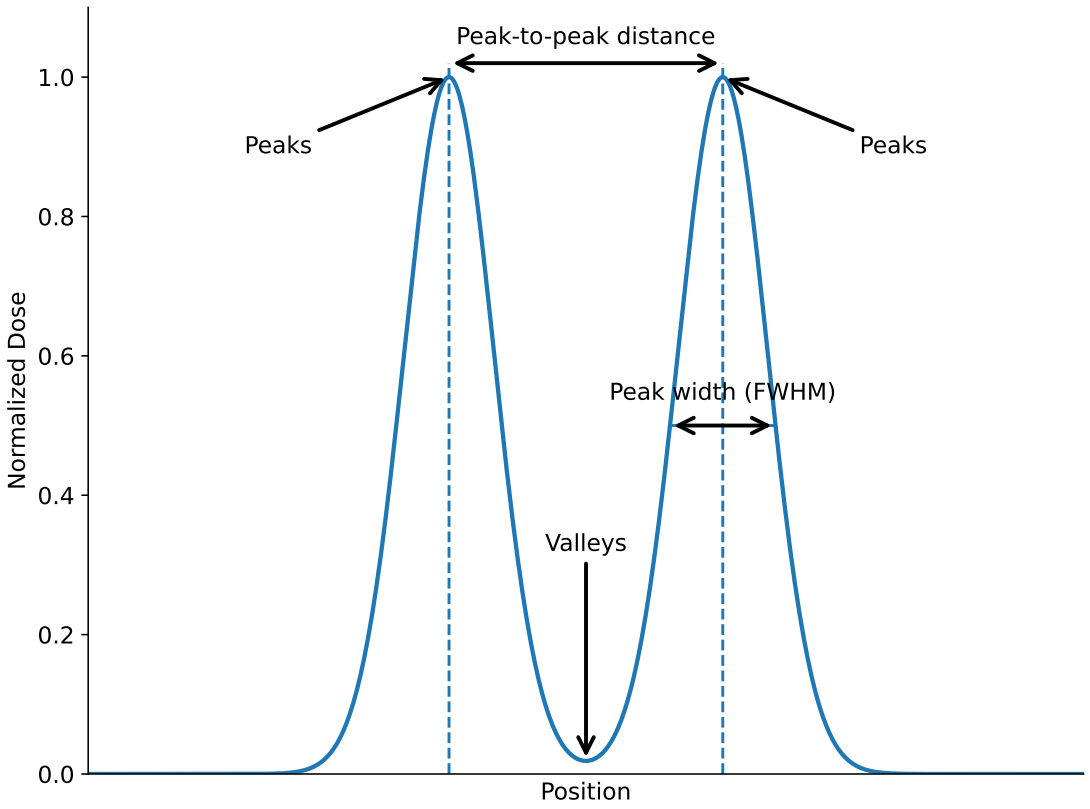

Figure 1.4: Dosimetric characteristics of SFRT parameters

1.6.1 Dosimetric characteristics

There are many metrics to categorise the heterogeneous dose patterns produced from SFRT deliveries, these include: average dose, peak dose, valley dose, peak-width, peak-to-peak distance, and peak-to-valley dose ratio (PVDR). PVDR is often believed to be of great therapeutic importance with a high value indicating potential to increase normal tissue dose tolerance (if peak and valley doses are also not excessive).

1.6.2 Techniques

Several forms of SFRT exist, with notable differences in the spatial scale of their beam modulation including; GRID therapy, Lattice therapy (LRT), Microbeam radiation therapy (MRT), and Minibeam radiation therapy (MBRT).

GRID therapy

GRID therapy utilises perforated metallic brass or Cerrobend collimators, or MLCs to produce 2D pencil beams. Its initial aim was to enable increased surface doses of orthovoltage photon beams to reduce skin toxicity to enable an increased dose to tumour volumes. In doing so, it was noted at the time that tolerable skin (peak) doses could be up to 20× those used conventionally [241]. Collimator design has typically employed a hexagonal or orthogonal pattern of peak spots of $\sim$ 1 cm diameter, with a spacing of 2 cm. The use of linacs have enabled megavoltage photon GRID therapy, with greater conformity from integration of techniques such as VMAT, FFF beams [242], or helical tomotherapy (TOMOGRID) [243]. Accommodation for the divergence of the photon beam has often been made in collimator proximal and distal hole diameters [244], where a number of collimator designs have been proposed [245]. For designs with 1-2 cm centre-to-centre hole (ctc) spacing with 6 MV beams, PVDRs have been seen to be $\sim 3.7-5.9$ [246], and to fall off slowly with depth (5.9 at 1.5 cm & 5.1 at 5 cm)[247]. These systems are however, heavy and cumbersome, therefore the use of MLCs has been used instead to better integrate with treatment planning systems, and to provide greater flexibility of collimation parameters [241, 248–251]. For electron GRID irradiations, Meigooni et al. have indicated that for energies from 6-20 MeV, Cerrobend GRID collimators would be clinically optimal $\geq$2.5 cm hole diameters, and centre-to-centre distances of 3 cm to enable the irradiation of bulky shallow tumours (at $<$ 2 cm depth) [252, 253].

Lattice radiation therapy (LRT)

Lattice radiation therapy (LRT) represents an extension to GRID in 3D, where high dose spherical regions (vertices), typically of 1-2 cm diameter, and typically 15–25 Gy each, are formed in the tumour using converging photon beams [237, 247, 249, 254–256]. LRT can be delivered with non-coplanar beams using helical tomotherapy, IMRT, VMAT [257], or CyberKnife [258] techniques [259–263]. The treatment can position vertices away from sensitive structures, avoiding normal tissue toxicity complications, and toward specific sites in tumours [239, 264–266].

An aim of LRT is to provide a dose boost; giving the highest tolerable dose to the largest tumour volume possible while minimising normal tissue dose [263].

Microbeam radiation therapy (MRT)

Microbeam radiation therapy (MRT) utilises large synchrotrons with multi-slit collimators to produce quasi-parallel arrays of high flux, kV photon beams of width 25-100 μm & 200-400 μm spacing. Radiation is often delivered at peak dose rates that are above those required to exhibit a FLASH effect with peak doses in excess of 100 Gy [267–269]. Here, the divergence of the beam is low, meaning it can deliver high spatial modulation, though only to samples at superficial depths [270]. As MRT requires synchrotron-generated X-rays, it offers limited clinical applicability due to infrastructure and dosimetry challenges [237, 265, 271].

Minibeam radiation therapy (MBRT)

Minibeam radiation therapy (MBRT) utilises beams with 0.3-1 mm widths using x-ray sources such as small animal irradiators with 1-3 mm spacing [249]. MBRT reduces the doses typically used with MRT, and so precludes the use of more accessible accelerator systems with lower doses and dose rates. The larger field size relative to MRT also reduces the effect of anatomical motion, thereby eliminating stringent positioning requirements to stop beam blurring. Because of the low penetration and dose rates at orthovoltage photon energies, linear accelerators with tungsten collimators have been developed instead to produce megavoltage photon beams with limited spatial modulation at depth [272–275]. Static collimators, however, provide limited flexibility, therefore newer alternating plate combinations have been proposed where stacking can produce different geometric outputs [276]. Proton minibeam radiation therapy (pMBRT) systems have also been developed, which improve the conformity of dose relative to x-ray systems, with magnetic scanning or dynamic scanning collimators [277, 278].

1.6.3 Clinical usage

Clinical translations have occurred with both GRID and LRT therapies, though it is worth bearing in mind that clinical evidence may be confounded by; lack of controls, different histologies, mixed tumour types, altered delivery parameters for each patient, different dose properties with depth, different follow up times for acute and late toxicity, and different treatment planning and target designation [241]. From their early uses with palliative intent and symptom management, experience has progressed to its use with curative intent for bulky, non-metastatic tumours with poor prognoses. GRID therapy has been used to treat large or recurrent advanced tumours with beneficial outcomes such as encouraging complete response rates, pain improvement, symptom relief, and few occurrences of late grade toxicity [244, 251, 279–284].

LRT can deliver higher maximum doses to the tumour [285], with treatments often provided in daily fractions, or with conventional RT. These have sometimes utilised reproducible geometric patterns of vertices, or arbitrarily positioned vertices [263]. LRT has been performed for tumours in a number of locations [254, 256, 259–261, 286–288]. Though beneficial outcomes have been seen for tumour control, the variety of tumour locations, irradiation geometries, doses, combination treatments makes it difficult to draw out one overarching factor that has improved outcomes. Beneficial outcomes attained with treatment combinations highlight that SFRT alone may not be enough to achieve tumour control [247]. Treatments have been complimented in GRID therapy; by conventional fractionated radiotherapy [251, 281, 282, 289–297], chemotherapy [283, 298–300], immunotherapy [238] or a combination of these with later surgery [283, 290, 299, 301]. These types of studies have been mirrored for LRT too with combination treatments, again with conventional fractionated radiotherapy commonly following a LRT treatment [256, 269, 287, 302], chemotherapy [260, 261, 287, 302], or immunotherapy [258]. Combination treatments have aimed to initiate tumour cell death by triggering immune responses in a vaccine-like effect [303, 304] which has been demonstrated clinically [300].

Recently MBRT has been implemented clinically to treat two patients; one with

Merkel cell carcinoma and another with squamous cell carcinoma, with an orthovoltage (180 kVp) unit using tungsten collimators with 0.5 mm slits and 1.1 mm spacings with surface PVDRs of $\sim 8-11$. Doses were delivered in two fractions with the collimator rotated by 90° in the second fraction to create a crossfire dose distribution. A reduction of pain was observed for both patients with a large long term tumour shrinkage, and modest response in the non-irradiated metastatic lesion in the first patient [305]. In Jacobson et al. MBRT was also used to treat a patient with recurrent metastatic melanoma, delivered in a series of 2-fraction treatments with PVDRs of ~ 15. A dramatic and rapid tumour response was seen over several weeks, while an abscopal response was also seen to another non-treated lesion, with minimal toxicity 6 months after treatment [306].

1.6.4 Preclinical usage

Most studies with MRT and MBRT have been preclinical, though early indications suggest that clinical translation could lead to clinical benefits. The preclinical findings of sparing from MRT irradiation of the brain [143, 275, 307–310] and spinal cord [311, 312], are of particular relevance to paediatric cases to avoid long term dysfunctional development of the central nervous system (CNS) [313].

MRT alone has increased survival of tumour bearing mice [314], with reduced tumour proliferation and markedly reduced normal tissue damage to skin compared to conventional radiotherapy [315, 316], and tolerance to high doses in lungs without acute functional deficits [317]. In these MRT studies, greater treatment efficacy has been obtained than conventional treatments [318], with a continued preservation of normal tissue even up to extremely high doses (up to ∼1 kGy) not seen in broad beam irradiations [319]. Combination treatments with chemotherapy [320, 321], or anti-inflammatory drugs in tumour bearing mice have also increased survival and slowed tumour growth [322], while immunotherapy combinations have prolonged antitumour immunity [318, 323]. Additionally, MRT treatment of dogs has yielded encouraging levels of tumour reduction (87 %) 3 months post irradiation [324]. From these positive findings, it has often been postulated that the therapeutic index

of MRT may be larger than that of broad beam therapies [223, 325].
Likewise, photon MBRT with small animal irradiator systems has reduced toxicity for non-tumour bearing mice [326], extended survival for mice with melanoma tumours [327] and for mice [328] and rats with gliomas [329, 330], and greatly reduced damage 6.5 months after rat brain irradiation compared to standard radiotherapy treatment [331]. In addition, a long term immune effect has been indicated by Betho et al. with an absence of benefit from MBRT for immunodeficient mice, and significant tumour growth suppression for MBRT treatments in immunocompetent mice [332]. With pMBRT, similar outcomes have also been achieved with decreased acute skin toxicity [333], a significant tumour control and eradication, increased survival [334], and less brain damage when treating gliomas [335–337]. However, combining MBRT with immunotherapies have not increased efficacy for the treatment of rat gliomas relative to conventional treatments, therefore further work is required to fully understand whether their combination would improve treatment efficacy [338].

1.6.5 FLASH and SFRT

It is hypothesised that the mechanisms underlying FLASH and SFRT are interlinked, especially as their radiation-induced immune responses may be similar [332, 339]. While evidence for long-term preservation of memory with FLASH alone highlights potential for combined treatments of gliomas [319]. These modalities may also be complimentary as FLASH has mostly occurred in short timescales, while SFRT has been seen be independent of irradiation timescale. In addition, SFRT utilises high peak doses, which in normal tissues may show a larger FLASH sparing effect. As SFRT reduces the volume irradiated, the technique may enable more beamlines to produce FLASH-SFRT beams without the use of scanning or imaging for motion management. However, their combination may complicate dose prescription and expand an already large parameter space [340]. Early preclinical studies at ESRF have showed some promising results when combining SFRT and FLASH. Here, a study investigating tumour growth of mammary carcinomas in mice in scanned irradiations with MRT (PVDR of ∼17-23) at peak doses of 75 or 150 Gy found a

large delay in tumour growth [341]. Meanwhile, in an MRT study with Fischer-344 mice using single fraction peak doses of 50-600 Gy to the right lung at an average dose rate of 1.4e4 Gy/s with vertical beam scanning (PVDR of $\sim$ 50), broad beam and high dose/broad peaked MRT showed lesions and fibrosis. Here, the FLASH-MRT combination improved lung tissue radioresistance by an order of magnitude more than FLASH alone [342].

1.6.6 Potential mechanisms

Immune effects

SFRT irradiations have been said to alter the tumour micro-environment (TME). Here, there are increases in the number of immune cells infiltrating tumours, as well as the number of cytokines released. Also, in high dose regions a higher release of tumour neoantigens from local tumour cell death is said to cause an activation of antigen presenting cells which can prime immune cells, creating an in-situ vaccine [241].

Bystander effects

Radiation-induced bystander effects are responses in which non-irradiated cells adjacent to irradiated cells exhibit similar cellular, genetic, or chromosomal changes [343, 344]. These effects are mediated by intercellular communication and by the release of soluble factors, with responses often depending on the cell type involved [345]. Initially observed with alpha-particle irradiation [346], bystander effects have been reported for various radiation qualities [347–349] and in in vivo models [286, 350, 351], where an effect has been dependent on parameters, including dose, dose rate, particle type, and LET [345, 352]. Bystander responses are associated with increased intercellular signalling and with the modulation of genes related to DNA repair, cell cycle arrest, oxidative stress, and apoptosis. Such effects have been proposed as possible contributors to both normal tissue sparing and tumour response in spatially fractionated radiotherapy (SFRT). The abscopal effect represents a systemic extension of the bystander response, in which the effect of

irradiation occurs outside the irradiated field. Cohort effects, by contrast, describe interactions between irradiated cells within a heterogeneously irradiated volume. Immune mechanisms are thought to play a key role in regulating abscopal responses [238, 353], which have been demonstrated in vivo when irradiation of a single tumour site induces regression of distant, non-irradiated lesions [238].

Vascular effects

It is hypothesised that the enhanced normal tissue preservation observed in SFRT results from the preservation of functional vasculature networks. Within low valley dose regions tumour vasculature can also be preserved, enabling the movement of genes and immune cells. Tumour tissues have vasculature which is often immature and more sensitive to radiation, leading to reduced perfusion, and increased tumour hypoxia with high doses causing vascular deterioration [354]. This hypothesis however, is refuted from the observation of tumour vasculature repair and reorientation following irradiation. Though it is known that the degradation of tumour vasculature can cause cascading cell death [355], can inhibit metastatic growth [241], and may be an indicator of tumour radiosensitivity [269].

Cell migration

The cell migration hypothesis states that the sparing of normal tissues stems from the proliferation of valley region cells such as stem or germ cells into peak regions following irradiation to mediate repair [356].

Oxygen-derived free radicals

Like FLASH, oxygen-derived free radicals such as hydroxyl, superoxide anion, and hydrogen peroxide have been theorised to contribute to the mechanism behind sparing effects. The hypothesis suggests that the distribution of hydrogen peroxide is a key determinant of efficacy and that ROS diffuse from peak to valley regions [357].

1.6.7 Challenges

To enable more widespread clinical adoption and investigation of SFRT techniques a number of challenges must be overcome.

Dosimetry

Dosimetric systems' resolution and dynamic ranges are often limited when regions become too highly spatially modulated [358]. Aside from Radiochromic films, few active dosimetry systems have the required spatial resolution except those such as the PTW microdiamond or solid state diodes. However, these systems may lack lateral charged particle equilibrium (LCPE), require repositioning, and have dose rate limitations. Radiochromic films also suffer from the requirement of a wait time prior to scanning. For dosimetric simulations, increasing the voxel resolution is necessary for accurate dose determination, but this substantially increases the computational time. In addition, inaccuracies of input sources can significantly alter simulated results, therefore, careful consideration and experimental measurements are required to validate and benchmark source inputs.

Collimation

There is little biological evidence to clearly indicate the benefit of a particular material/geometry for SFRT therapies. For these, suitability may depend on tumour characteristics and desired treatment outcomes. Therefore, in GRID therapy for example, the flexibility of MLC systems may be preferred over static collimators to enable faster treatments that can better avoid sensitive areas. Efforts to identify an 'optimal' GRID design have been inconclusive with MLC and static Cerrobend collimators offering similar therapeutic outcomes when different total tumour volumes were irradiated (30% - 50%) [251], worse therapeutic outcome for larger apertures (1 cm vs 2 cm) (despite a higher PVDR) [359], and no improvement in the therapeutic effects for a number of grid designs with different hole spacings (1.5 cm - 1.9 cm)[360]. LRT has similar uncertainties regarding vertex size and spacing exist though a consensus has emerged with vertex diameters of 1.0-1.5 cm

and ctc's of 2-6 cm, with larger distances causing higher dose gradients [263].
In MRT, it has been suggested that reducing the ctc can increase tumour control but can lead to greater normal tissue toxicity from higher valley doses [361, 362]. With constant valley doses, alteration of beam widths saw broadest beams provide greatest tumour control (75 μm) and narrowest beams provide greatest acute normal tissue damage (25 μm) [363]. Meanwhile, the opposite trend has been seen when comparing tumour growth suppression for 25 μm and 100 μm beam widths [364], and 50 μm and 500 μm beam widths [341]. With these same beam widths, Nakayama et al. found that increasing the ctc (from 100 - 300 μm)(and therefore PVDR), linearly increased lethal peak doses to non-tumour bearing mice brains [365]. However, conclusions must take into account the differences in tissue sites, doses used, whether radiation was delivered in an orthogonal or cross-fire method, as well as the narrow range of values explored for each parameter and their interdependence. In addition, imprecision in the positioning of collimation systems or the incident beam in the beamline may result in altered dose distributions on the patient surface [319]. Investigations with collimators for MRT and MBRT have also suggested that there may be detrimental effects on vasculature and blood perfusion when transitioning from MRT to MBRT beam widths preclinically [366].

Dose Prescription

Dose is usually prescribed at the surface or at a depth of highest dose, which remains valid only for superficial treatment depths if modulation varies significantly with depth in tissues [247]. In addition, it has been suggested that dose be defined at the prescription depth, but also to compare with homogeneous irradiations, the equivalent uniform dose (EUD) [6] should be used. However, this assumes a linear-quadratic relation for cell death, which may ignore the key intracellular mechanisms which cause differences in biological results [368]. Other reporting standards have included using the valley dose, though this oversimplification ignores peaks entirely,

[6]The concept equates two doses from their radiobiological effect (usually tumour control), independent of their distribution calculated from dose calculation points or dose-volume histograms [367]

dose prominence, or mean dose (which is dependent on the size of the irradiated region). In addition metrics such as the fractional, or percentage volume receiving dose below a threshold (e.g., 10% of the peak, or 95% of the volume of vertices for LRT [285]) have been proposed which introduce the idea of volumetric [369], rather than point dose measure [370]. Investigations attempting to identify which dose metric is most beneficial have been mixed. Mean dose has often been used to compare regimes [338, 371], while valley dose has commonly shown a strong correspondence with increased lifespan [372, 373] (for MRT /MBRT). Meanwhile, peak dose has shown greater correspondence with normal tissue sparing in MBRT [374, 375], and higher PVDR in pMBRT (through higher peak doses) has caused reduced immunosuppression and increased tumour control [334]. However, strong correlations exist between these dose prescription metrics and for biological effects such as survival, extremely high or low doses can result in mortality from normal tissue toxicity or rapid tumour growth respectively [372]. In any case, transparent reporting of doses, volumes, and collimation systems should enable retrospective analysis to better link outcomes to a given method of dose prescription, taking into account the potential effects of treatment combinations. It is also important that dose prescription separates normal tissue and tumourcidal effects as it is likely their mechanism and dependencies to a given metric will differ. Attempts to predict outcomes from one SFRT technique to another may also present challenges from their differing spatial patterns, scales, irradiation timescales, temporal fractionation [376, 377], and their relative sensitivities to these metrics for a given tissue type [375].

1.7 Motivation

FLASH radiotherapy has the potential to increase patient throughput, reduce anatomical motion, and reduced acute and long-term normal tissue toxicity. The delivery of FLASH has commonly utilised cyclotron-based proton, linear accelerator (linac)-based electron and X-ray tube-based photon beams [61, 189, 378], while conventional radiotherapy treatments have mainly utilised linac-based photon beams which is still the most accessible, and affordable treatment option worldwide [4, 22].

It is thus likely that MV photons will eventually be used for FLASH radiotherapy, if this is to become a commonplace clinical modality. However, the techniques used to achieve high conformality with MV photons rely on intensity-modulation and/or delivery from multiple beam angles, both of which are difficult to achieve within FLASH timescales as these require mechanical motion of the MLC and gantry. To achieve FLASH dose rates with MV photons, a ∼1000-fold increase in average dose rate will be required for traditional linacs [379]. Such FLASH treatments should ideally be delivered with technologies comparable to those used by current installation, albeit with a higher peak output and reduced operational duty cycles. This primarily requires confronting the inefficient bremsstrahlung process that converts electrons to photons, and causes significant heating in converter materials [103].

SFRT also has therapeutic potential to boost tumour control and reduce normal tissue toxicity. However, the optimal delivery and spatial fractionation parameters have not been deciphered and the mechanisms at play are not yet fully understood. Therefore, accessible preclinical irradiation platforms must be established which can explore the effect of delivery parameters on normal and tumour tissues alike to inform clinical treatment plans, and to examine potential mechanistic hypotheses. In doing so, it is essential to design flexible systems that enable rapid modification of dosimetric and collimation configurations for systematic experiments which directly connect preclinical findings to clinical implementations.

1.8 Aims

The principle aims of this thesis were to:

- develop a preclinical radiation platform to monitor and deliver FLASH with MV photons
- utilise this platform to compare photon and electron megavoltage FLASH irradiations in vivo at similar dose rates

- assess the impact of electron irradiations on the longevity and material properties of the bremsstrahlung target
- develop a preclinical electron SFRT platform to deliver spatially modulated beams using flexible collimation systems
- compare SFRT treatments to homogeneous irradiation deliveries in vivo

Chapter 4 details the modifications to target materials, beamline setups, and dosimetry to enable MV photons at FLASH dose rates. This setup is used in chapter 5 for a preclinical skin toxicity experiment to compare the effects of megavoltage electron and photon FLASH irradiations with comparable dose rates and doses. Chapter 6 details the brass collimation systems and beamline setup utilised for SFRT with electrons at FLASH dose rates. Here, a preliminary in vivo bladder tumour growth assay was performed to compare SFRT and homogeneous deliveries. While in chapter 7, a thermocouple setup and finite element model (FEMM) were used to measure the thermo-mechanical effects on bremsstrahlung targets during photon FLASH irradiations.

2 Theory

Contents

2.1 Electron interactions with matter

Electrons interact with matter in four main mechanisms; losses via inelastic (with atomic electrons) or elastic (with nuclei and atomic electrons) collisions, electron-positron annihilation, or radiative loss with bremsstrahlung photon emission. As electrons traverse matter, they primarily lose energy via inelastic Coulomb interactions that cause ionisations and excitations. The net energy transfer from a traversal of the electron with atomic nuclei is dependent on its categorisation as a 'soft' or 'hard' collision [23]. Here, the relative scales of the impact parameter b and the atomic radius a, determine its standing. Soft collisions are most common and transfer small amounts of energy (eV). When the electron is far from the atom ($b >> a$), the Coulomb force field distorts the whole atom, occasionally with an excitation or ionisation of a valence-shell electron. Whereas when the electron passes relatively close to the atom ($b \approx a$), a 'hard' collision results in an electron being ejected with appreciable kinetic energy (a.k.a a knock-on electron or δ-ray — usually >100 eV). Hard collisions are less frequent, but make up a similar contribution to the total electronic energy loss. If an inner-shell electron is ejected from a hard collision, the return of the atom to the ground state would lead to an emission of characteristic X-rays or Auger electrons [27].

2.1.1 Mass collision stopping power

The mass collision stopping power for collisions is combined into the form:

$$\left(\frac{dT}{\rho dx}\right)_c = 4\pi r_0^2 m_e c^2 z^2 \left(\frac{N_A Z}{A}\right)\left(\frac{1}{\beta^2}\right)\left[ln\left(\frac{2m_e v^2}{I\left(1-\beta^2\right)}\right) - \beta^2 - \frac{C}{Z}\right] \tag{2.1}$$

where m_e is the electron mass, r_0 is the classical electron radius, v is the velocity of the incident electron, c is the speed of light in vacuum, $\beta = \frac{v}{c}$ is the Lorentz factor, N_A is Avogadro's number, Z and A are the proton and atomic number of the nucleus, I is the mean excitation potential of the medium, $\frac{C}{Z}$ is the shell correction. The mass stopping power is also composed of the collisional stopping power which is the primary cause of heat generation [103]. The mass stopping power can be approximated in the form [380]

$$\left(\frac{dT}{\rho dx}\right)_c \approx \{C_1\left[1 - C_2(1+C_3T)^{-2}\right]\}^{-1} \tag{2.2}$$

where C_i for $i = 1, 2, 3$ are constants for a given material.

2.1.2 Mass radiative stopping power

Photons can be emitted from the deceleration, vibration and deflection of electrons in materials in a process called Bremsstrahlung (braking radiation)[30, 381]. Bremsstrahlung photons are produced via two primary methods, namely, electron-nucleus interaction and electron-electron interaction. The former has a higher cross section and photon energy maximum than the latter because of the energy of the recoil. In electron-nucleus bremsstrahlung, photons emitted tend to be on the same side as the outgoing decelerated electrons relative to the incident beam. The main cause of bremsstrahlung emission is therefore the Coulomb field of nuclear charge. Atomic electrons screen this Coulomb field which reduces the bremsstrahlung cross section, whilst acting as individual particles which can undergo collisions causing bremsstrahlung. Most interactions with the Coulomb force are elastic with few resulting in an inelastic radiative photon emission. Bremsstrahlung radiation is only emitted 1-5 % of the time with the other 95-99% of the incident electron energy converted to heat via ionisation and excitation in collision interactions [29, 382].

At low incident velocities ($v << c$), classically the total radiated power from an accelerating charge e moving at velocity in an electric field is given by:

$$I = \frac{e^2 a^2}{6\pi\epsilon_0 c^3} \tag{2.3}$$

where a represents the acceleration and ϵ_0 the vacuum permittivity. By considering the fields surrounding the charge at large distances, the field can be approximated as equivalent to electric dipole radiation where the angular distribution of radiation is:

$$\frac{dI}{d\Omega} \propto sin^2\theta \tag{2.4}$$

Here, θ is the emission angle relative to the dipole axis. At higher energies ($v \approx c$), the distribution becomes forward peaked for increasing incident energy. Meanwhile, for lower electron energies the angular distribution is more isotropic [383]. Photons can be emitted with a range of energies (hv) up to the incident electron energy.

$$E_{incident_{e^-}} = E_{outgoing_{e^-}} + hv \tag{2.5}$$

Radiation produced is a superposition of emitted photons from electrons at different scattering angles and is rotationally symmetric about the incident electron beam axis. The rate of bremsstrahlung production by electrons is called the mass radiative stopping power (units of $MeVcm^2/g$) described by:

$$\left(\frac{dT}{\rho dx}\right)_r = \sigma_0 \frac{N_A Z^2}{A}(T + m_e c^2)\bar{B}_r \tag{2.6}$$

where $\sigma_0 = \frac{1}{137}\left(\frac{e^2}{m_0 c^2}\right)^2$, T is the electron kinetic energy (MeV), and $\bar{B}_r$ a slowly varying function of Z and T [$\bar{B}_r = \frac{16}{3}$ for $T << 0.5MeV$, 6 for $1MeV$, 12 for $10MeV$]. For MeV energy ranges the radiative stopping power is approximately $\propto Z^2$ and T[23, 382].

2.1.3 Stopping power and range

The total mass stopping power can then be found by combining the collision and radiative stopping powers (see Figure 2.1 for tungsten):

$$\left(\frac{dT}{\rho dx}\right)_{tot} = \left(\frac{dT}{\rho dx}\right)_{r} + \left(\frac{dT}{\rho dx}\right)_{c} \tag{2.7}$$

The ratio of these terms is approximately $\frac{\left(\frac{dT}{\rho dx}\right)_r}{\left(\frac{dT}{\rho dx}\right)_c} \cong \frac{ZT}{1600 m_e c^2} \cong \frac{ZT}{800} \equiv \alpha T$. For high

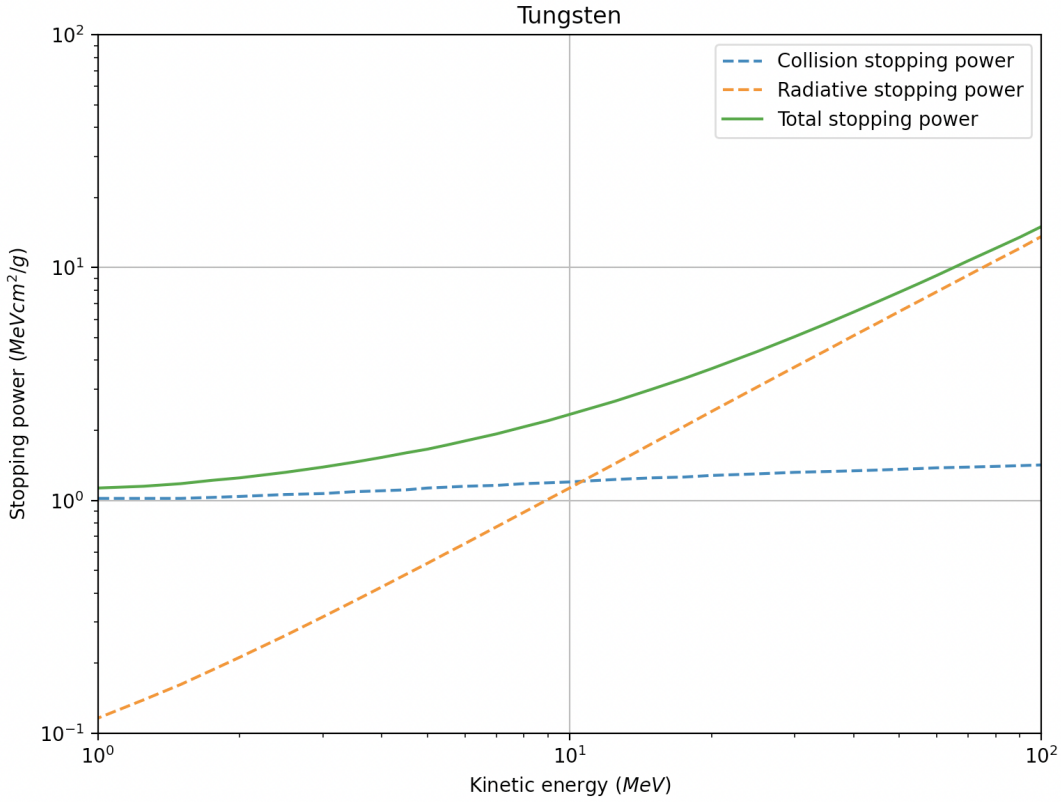

Figure 2.1: Electron stopping powers in tungsten, from [384]

Z materials this means at $\sim 10\ MeV$ the radiative and collisional components are approximately equal [385], and for $< 5\ MeV$ the ratio is ~ 0.1 [27]. The range of the electron within a material can be approximated by the continuous-slowing-down-approximation range (CSDA) given by

$$R_{CSDA} = \int_0^{T_0} \left(\frac{dT}{\rho dx}\right)_{tot}^{-1} \tag{2.8}$$

though as this is merely the path length, this overestimates the average depth reached because of the spread of electron trajectories with depth [27]. Other semi-empirical forms have been proposed [386] for both the CSDA and practical range — the thickness at which the tangent of the steepest decreasing linear portion of a transmission curve crosses zero. Here the CSDA range is

$$R_{CSDA} \simeq C_1 \left[\left(\frac{1}{\alpha} \right) ln\,(1 + \alpha T) - \frac{C_2 T}{1 + C_3 T} \right] \tag{2.9}$$

and practical range is

$$R_p = a_1 \left[\left(\frac{1}{a_2} \right) \ln(1 + a_2 \tau) - \frac{a_3 \tau}{1 + a_4 \tau^{a_5}} \right] \tag{2.10}$$

with $\tau = \frac{T}{m_e c^2}$ and coefficients of a_i, b_i, c_i and d_i, $i = 1, 2, 3, 4, 5$ described in the appendices.

2.2 Photon interactions with matter

Photon interactions occur through imparting energy to electrons, which either already exist or are created in the interaction process. The processes that occur are Compton (incoherent) scattering, Rayleigh (coherent) scattering, photoelectric absorption, and pair production each of which have a cross section dependent on the incident photon energy and the material considered [387].

2.2.1 Linear attenuation coefficient

The relative contribution of each interaction can be broken down to highlight the interaction probabilities of each mechanism, whereby the linear attenuation coefficient μ $[cm^{-1}]$ is represented by

$$\mu = N(\sigma_c + \sigma_r + \sigma_{pe} + \sigma_{pp}) \tag{2.11}$$

where N is the atomic number density $(= N_A \rho / A)$, $\sigma_c, \sigma_r, \sigma_{pe}$ and σ_{pp} are the cross sections for Compton, Rayleigh, photoelectric and pair production processes respectively, while ρ is the material density. From Figure 2.2, it is evident for soft tissues ($Z_{eff} \approx 7$) that photoelectric absorption dominates for low photon

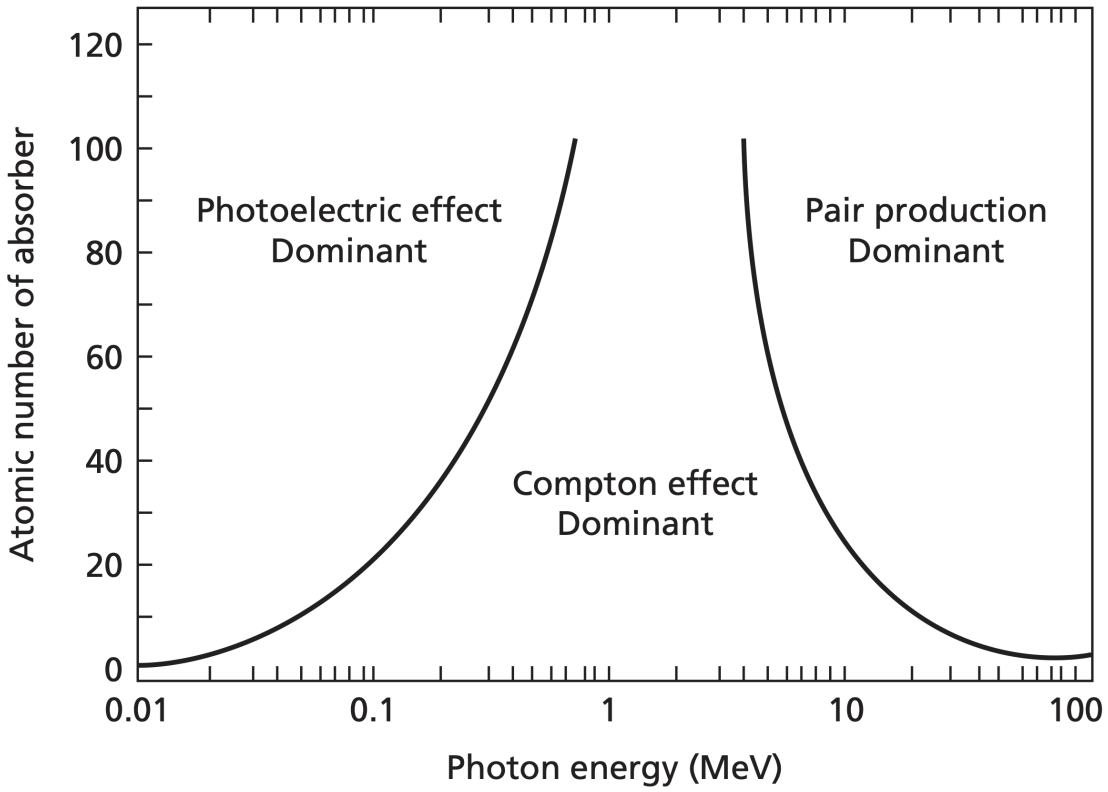

Figure 2.2: Relative weighting of interactions of photons, from [12]

energies (<26 keV), while for intermediate energies (26 keV - 30 MeV) Compton scattering becomes most significant, and at high energies (>30 MeV) pair production dominates. The breadth of dominance of the Compton effect with energies also diminishes for materials of increased atomic number. Soft tissues such as muscle, have an effective proton number similar to water, and therefore have components as seen in Figure 2.3.

2.2.2 Mean free path

The average distance traversed by the photon before interaction is known as the 'mean free path', λ_{mfp}, and is the inverse of the linear attenuation coefficient

$$\lambda_{mfp} = \frac{1}{\mu} \tag{2.12}$$

this is the thickness over which the number of photons would reduce by a factor of $e^{-1} \approx 37\%$

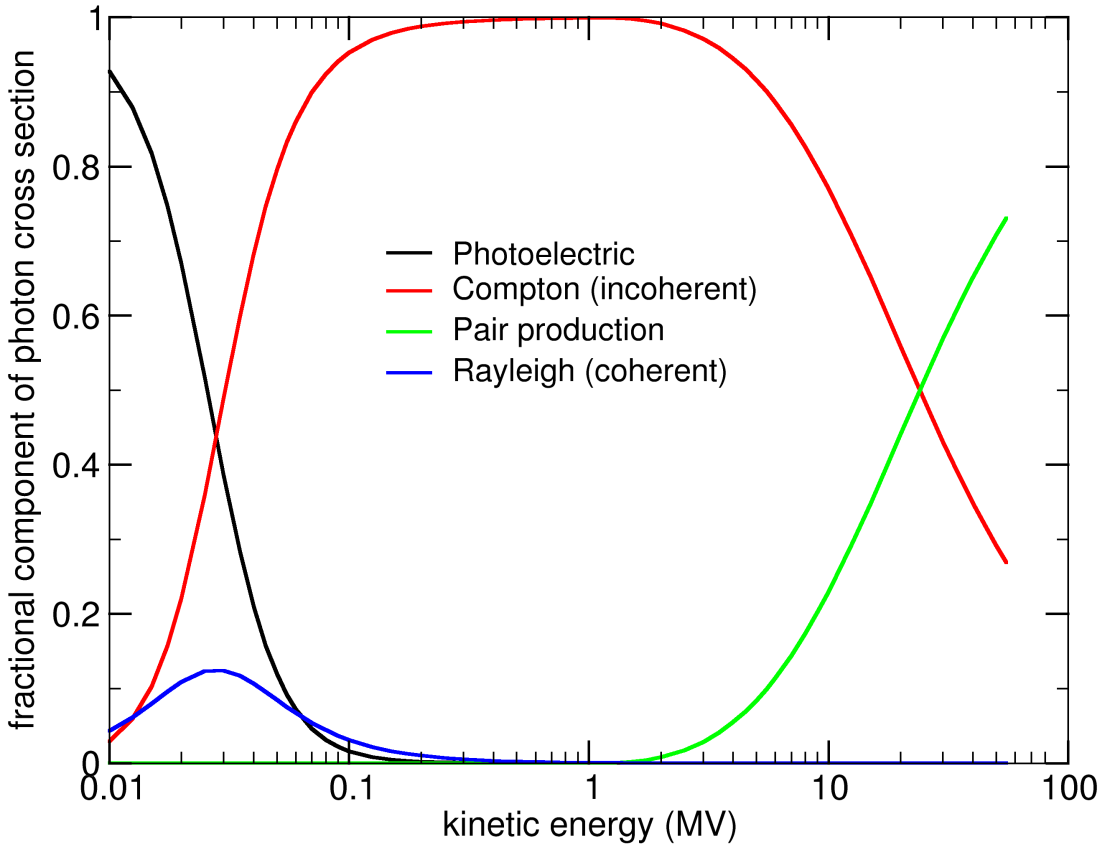

Figure 2.3: Relative fractional components of photon cross section in water

2.2.3 Mass attenuation coefficient

For a beam of monoenergetic photons with intensity I_0 penetrating a layer of material with mass thickness x and density ρ. The mass attenuation coefficient, $\frac{\mu}{\rho}$ will be:

$$\frac{\mu}{\rho} = \frac{1}{x} ln \left(\frac{I_0}{I} \right) \tag{2.13}$$

Meaning the fraction of incident photons passing through a material of thickness x can be seen as:

$$\frac{I}{I_0} = e^{-x\frac{\mu}{\rho}} \tag{2.14}$$

2.2.4 Photoelectric interactions

In the photoelectric interaction, the photon is removed, transferring its energy $h\nu$ to eject an atomic electron at energy E

$$E = h\nu - E_B \tag{2.15}$$

where its energy in the bound state is E_B. The cross section is approximately

$$\sigma_{pe} \cong \frac{kZ^4}{(h\nu)^3} \tag{2.16}$$

which implies the photoelectic interaction probability increases at low photon energies and for high proton number materials [27].

2.2.5 Compton (incoherent) interactions

Compton (incoherent) scattering occurs when a photon transfers a fraction of its energy to a loosely bound atomic electron. The interaction, and requirement of conservation of energy, results in the scatter of the incident photon by an angle which depends on the energy transferred. The energy $h\nu'$ of the scattered photon is given by the Compton equation whereby:

$$E_\gamma = h\nu' = \frac{h\nu}{1 + \alpha(1 - cos\theta)} \tag{2.17}$$

where $\alpha = \frac{h\nu}{m_e c^2}$, and the Compton wavelength is given by $\lambda_c = \frac{h}{m_e c^2}$. Here the angle between the incident photon and recoil electron is

$$cot\phi = (1 + \alpha)\ tan\frac{\theta}{2} \tag{2.18}$$

where θ is the scattering angle, and ϕ is the angle between the incident photon and recoil electron. From momentum conservation, the scattering of electrons can only occur in the forward hemisphere. When the incident photon energy is $< 0.01\ MeV$ the electron receives almost none of the incident electron energy, with most transferred to the outgoing photon. Photon backscatter occurs when $\phi = 0$ and $\theta = \pi$ [388]. The likelihood of Compton scattering is independent of Z, as the electron is assumed to be free and static before interaction, but decreases for increasing energy and, when the photon energy increases (up to $\sim 100\ MeV$), the outgoing scattered photon is also more forward peaked and the majority of energy is transferred to the outgoing electron ($> 80\%$) [23]. The differential cross

section for Compton scattering with a free electron per electron is given by the Klein-Nishina (KN) formula (Equation (2.19)) [12, 27, 388].

$$\frac{d_e\sigma_{KN}}{d\Omega} = \frac{r_e^2}{2}\left(\frac{h\nu'}{h\nu}\right)^2\left(\frac{h\nu'}{h\nu} + \frac{h\nu}{h\nu'}sin^2\theta\right) \tag{2.19}$$

where at low energies $h\nu \to 0$ this is reduced to the classical Thomson cross section.

$$\frac{d_e\sigma_{Th}}{d\Omega} = \frac{r_e^2}{2}(1 + cos^2\theta) \tag{2.20}$$

Here, the total Klein-Nishna cross section can be obtained via integration over the photon scattering solid angle Ω

$$\begin{aligned} {}_e\sigma_{KN} &= \int_\Omega \frac{d_e\sigma_{KN}}{d\Omega}\, d\Omega \\ &= 2\pi r_e^2\left\{\frac{1+\alpha}{\alpha^2}\left[\frac{2(1+\alpha)}{1+2\alpha} - \frac{\ln(1+2\alpha)}{\alpha}\right] + \frac{\ln(1+2\alpha)}{2\alpha} - \frac{1+3\alpha}{(1+2\alpha)^2}\right\} \end{aligned} \tag{2.21}$$

2.2.6 Pair production

When the photon is enveloped in a Coulomb field near to the nucleus, the photon can be annihilated and transformed into an electron-positron pair. Given the rest mass of both electron and positrons ($m_e = 0.511\ MeV$) the minimum photon energy threshold for pair production is 1.022 MeV, with the electron-positron pair sharing the rest of the available kinetic energy. Triplet production can also occur with a higher energy threshold ($4m_ec^2$) formed from Coulomb interaction in the vicinity of an atomic electron, releasing an electron and electron-positron pair. Pair production is increasingly likely for higher photon energies ($> 10MeV$), and is $\propto Z^2$ and $ln(E_\gamma)$, where E_γ is the incident photon energy. Meanwhile, triplet production is $\propto Z$, and the ratio of triplet to pair production increases with incident photon energy, and decreases for increased medium atomic number.

2.2.7 Rayleigh (coherent) interactions

Rayleigh (coherent) scattering, occurs when the photon transfers all of its energy to the atom and radiates the energy of the photon at a different angle outward

[383]. The effect is pronounced at low photon energies and in high Z materials, and therefore has little effect with radiotherapy beams and tissues with low Z [12].

2.2.8 Photo-neutron production

Photoneutron interactions (γ, n) occur between photons and the nucleus causing neutron emission. These provide significant unintended dose within treatment rooms from collimators, targets, and flattening filters as well as from activation of beamline components. Typically the threshold for production occurs between 8-10 MeV and rises rapidly, plateauing above 20 MeV [389]. In the energy range $\sim 10 - 20\ MeV$ the absorption cross section is dominated by the Giant Dipole Resonance (GDP) term. Where

$$\sigma_{GDR} = \sigma_R \frac{E_\gamma^2 \Gamma_R^2}{\left(E_R^2 - E_\gamma^2\right)^2 + E_\gamma^2 \Gamma_R^2} \tag{2.22}$$

Here, σ_R is the peak GDR cross section, E_R is the resonance energy, and Γ_R is the width of the distribution [390] (Figure 2.4). This peak features at lower energies for materials with higher Z [388], and occurs at $\sim 80 \times (A)^{-1/3}$ [391]. Neutrons produced from these interactions are fast with typical energies between 1-1.5 MeV, causing a neutron dose peak at around 4-5 cm in phantom materials [392].

2.3 Bremsstrahlung targets

Clinical linacs are designed to accelerate pulses of electrons onto a target that generates bremsstrahlung photons. The target, the electron energy, and the average beam current determine the photon beam dose rate and photon energy spectrum. In clinical linacs, the power deposited in the target is of the order of 10^3 W and the photon-generating targets are designed to run continuously, requiring appropriate target cooling. The highest photon dose rate output is ultimately determined by the peak radiofrequency power used to accelerate the electrons, by the ability to inject electrons into the accelerating waveguide structure, and by the design of the structure and by its shunt impedance [389].

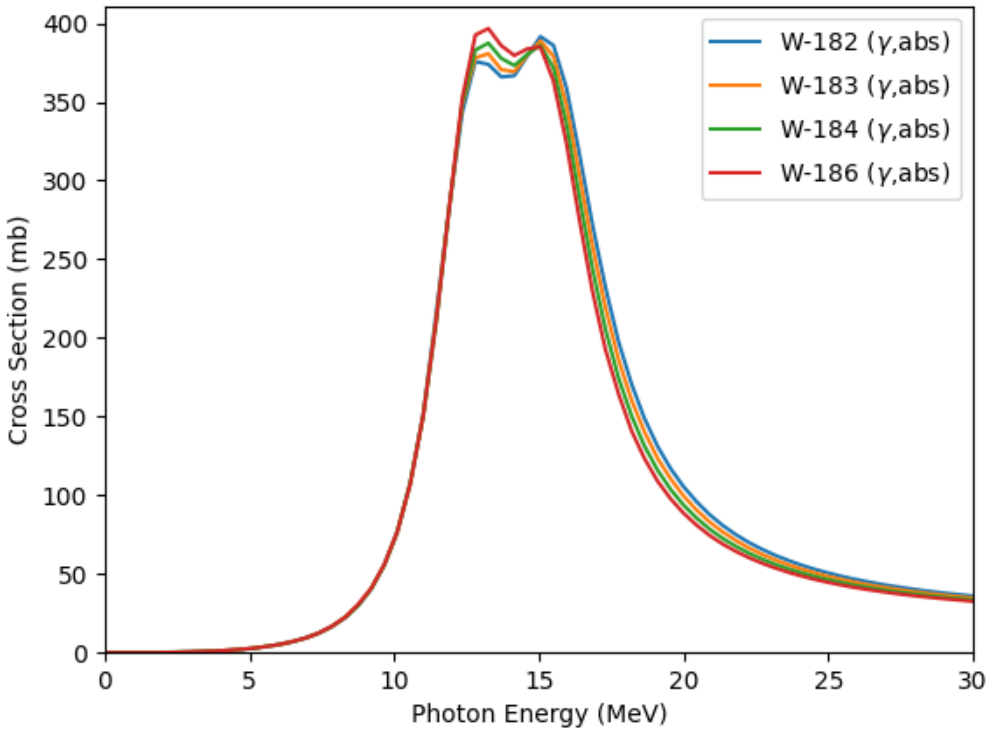

Figure 2.4: Photo-absorption cross section of the main isotopes of tungsten, from [390]

2.3.1 Target materials

Bremsstrahlung target materials, such as tungsten, are often chosen for their high melting temperature, proton numbers, electron density, density, specific heat capacity, and thermal conductivity [13, 393]. Tungsten is also commonly used as its properties include a low thermal expansion coefficient [394, 395], vapour pressure, and sputtering rate [24, 396]. Most of the incident electron energy onto the target is converted to heat which can destroy or damage the target [397]. However, tungsten also has a high capacity to withstand thermo-mechanical stresses, i.e., a high ultimate tensile strength (UTS) [398] (Figure A.22), which increases for reduced temperatures, reduced foil thicknesses [399–401], as well as for rolled samples [402]. Machining pure tungsten is challenging as it is brittle at room temperature, making tungsten carbide alloys a more preferable alternative [395, 403–405].

When the tungsten temperate is increased above the ductile-to-brittle (DBTT)

transition temperature (∼150-200°C) it becomes ductile [406, 407]. In air, at 500°C an adhesive and protective oxide layer forms slowly, and does not threaten target operation [408, 409]. Above 500°C, oxide formation rate increases rapidly and can causes swelling that leads to high stresses and crack formation [410–413]. Beyond 750°C oxide sublimation occurs, and above 1300℃ sublimation and oxide formation rates are equal. At these temperatures, creep damage [414], and recrystallisation can also cause material failure [396, 403, 415, 416]. Mechanical effects arise from circumferential compressive stress developed from thermal expansion of heated areas constrained by surrounding material [416, 417], causing localised multi-axial stresses, and strains. Thermal cycling through the DBTT can also promote fatigue cracks to propagate from the surface [418], in the plane with highest temperature gradient (usually radially) when tensile stress exceeds the UTS during cooling [419–422].

2.3.2 Target thickness

Target thickness balances key parameters such as; photon production and self-attenuation, photon energy fluence distribution as well as limiting electron fluence transmission [423, 424] (see supplementary materials Figures A.20 and A.21 and Table A.9). The optimal thickness of a thin high Z target has been found to be $\sim 1/3$ of the electron range in materials [423, 425, 426]. Here, the optimal thickness of target between 1-10 MeV is given by [397, 427] ($\sim 0.61\ cm$ at 6 MeV)

$$t_{opt}(E, \rho, Z) = \frac{0.89(E - 0.7)^{0.46}}{\rho Z^{\frac{0.17}{E^{0.2}}}}[cm] \tag{2.23}$$

where E is kinetic energy of electron (MeV), ρ is the density of the target material (gcm^{-3}), and Z is its atomic number. For target thicknesses from 0.2-1 of the electron range, measurements of photon output have been similar [30, 425]. While, decreased target thickness has also been found to result in increased surface dose rates for 0.5 mm targets compared to a 1 mm ones [428].

2.3.3 Backing material

Targets are often backed downstream by a layer of lower density, highly thermally conductive, water-cooled material to limit electron transmission and reduce peak target temperature and fluctuation. This backing material can limit the maximum dose rate achievable, as its temperature limit is reached earlier than that of the target. Contact with the backer material also risks dissimilar thermal expansion at interfaces [429, 430], and introduces stricter thermal constraints [431]. Alternatively, rotational target systems may reduce peak temperatures, however better integrability, accessibility, and affordability is generally provided by static targets [234]. The combined target and backer thickness is usually chosen to stop all incident electrons and it is well known that composite Tungsten-Copper targets are preferred when high photon outputs are required [233, 432]. The penetration of energetic electrons in conducting solids is usually defined by the continuous slowing down approximation (CSDA) of the highest energy of the incident electrons. When a combination of materials is used for targets, the condition described in equation 2.24 is fulfilled [234, 433] ($R_{CSDA_{copper}}$ ~4.5 mm at 6 MeV & $R_{CSDA_{copper}}$ ~5.3 mm at 8 MeV) therefore a 6 mm copper backer alone, ignoring any electron energy loss in the tungsten or in air, can be considered more than enough to minimize electron surface dose contamination [234, 434].

$$\frac{t_{tungsten}}{R_{CSDA_{tungsten}}\left(E_{e^-}\right)} + \frac{t_{copper}}{R_{CSDA_{copper}}\left(E_{e^-}\right)} > 1 \tag{2.24}$$

The CSDA range is known to overestimate the electron range as it assumes a straight line trajectory, though Ebert's formulation from Tabato, Iko and Okabe, can indicate combinations of materials that exceed the extrapolated range of electrons (for copper and tungsten at 6 MeV these are 2.9 mm, and 1.1 mm respectively) [386, 435].

2.3.4 Focal spot size

Using a thin tungsten target not only minimizes self-attenuation of photons generated, but also enables higher dose rate output as less energy is converted to heat, which enables the use of higher input currents [429]. Owing to a very small heat diffusion length [436] (∼0.03 mm) in tungsten relative to the electron range ($R_{CSDA_{tungsten}}$ ∼2.21 mm at 6 MeV) [437], the temperature rise of the focal spot is said to be limited by the heat capacity [438], such that the temperature rise is proportional to the incident power density and pulse length, and inversely proportional to the element mass (ρ ∼19,300 $kg \cdot m^{-3}$) and the heat capacity (c ∼133 $J \cdot kg^{-1} \cdot K^{-1}$) [436]. However, the applicability of these analytical models, established for anode targets in x-ray tubes, are limited for MeV beams; where electron transport is non-negligible with the position of maximum energy absorption at an appreciable depth (∼0.3 mm [439]) in the target (akin to a volumetric heat source) [438], irradiations utilize a pulsed rather than continuous delivery, lateral heat redistribution occurs, and thermal radiation is significant for unpolished targets [393, 440]. These models also highlight how increasing the focal spot size (e.g., achieved by moving the target some distance from the beam exit window) can reduce the incident power density, temperature increase in the focus, and increase the target lifetime without a substantial reduction in photon dose rate [234].

2.4 Dosimetric quantities

2.4.1 Fluence

The number of particles dN incident on a sphere of infinitesimal cross-sectional area da is termed fluence Φ (m^{-2}).

$$\Phi = \frac{dN}{da} \tag{2.25}$$

Planar fluence is the number of particles traversing a plane, per unit area of plane, meanwhile, it can also be defined in terms of the sum of the track lengths dl of

particles in a sphere with elemental volume dV

$$\Phi = \frac{dl}{dV} \tag{2.26}$$

2.4.2 Absorbed dose

Energy is deposited by stochastic energy deposits within a given volume. Absorbed dose is defined as the quotient of the mean energy imparted $d\bar{\varepsilon}$ by radiation to matter of a given mass dm in units of joule per kilogram ($J\ kg^{-1}$). The SI unit of absorbed dose is the gray (Gy) [441].

$$D = \frac{d\bar{\varepsilon}}{dm} \tag{2.27}$$

It is of note that the calculation is an average for a mass m and independent of the heterogeneity of energy deposition [391].

2.4.3 Field parameters

Field Size

Field size defines the dimensions or diameter of the radiation field at a measurement distance [442]. For flat beams (with a flattening filter) this is usually the full width at half maximum (FWHM). Meanwhile, for unflattened beams (flattening filter free, FFF), this can be interpreted as the distance between inflection points (IPs) in the penumbra region of the profile [443], when matched to the same levels as WFF beams [444], renormalised [445], fit to a polynomial [446], or interpolated [447].

Penumbra

The penumbra is defined as the lateral distance between the 80% to 20% positions across one side of the relative profile [448]. However, this definition is not as useful for comparison with FFF beams, as their profile is peaked along the central axis [449]. With renormalisation [444], the 80% to 20% method is valid for FFF beams [445], though other methods with relative dose values (RDV) have been proposed [447, 450].

Flatness

Flatness can be defined as the maximum difference in the field between the central 80% positions, usually taken at a depth of 10 cm or d_{max} [451]

$$Flatness = 100 \times \frac{D_{max} - D_{min}}{D_{max} + D_{min}} \tag{2.28}$$

for FFF beams this is

$$Flatness = 100 \times \frac{D_{max}}{D_{min}} \tag{2.29}$$

or the lateral distance from the central axis at 90%, 75% and 60% relative dose on either side of the beam profile [447, 452].

Symmetry

Symmetry is defined as

$$Symmetry = 100 \times \left| \frac{D_{(x)}}{D_{(-x)}} \right|_{max} \tag{2.30}$$

with $D(x)$ as a dose at a given distance from the central axis [453]

2.5 Dosimetry

2.5.1 Ionisation chambers

Absolute dosimetry uses measurements with the highest meteorological quality at a Primary Standard Dosimetry Laboratory (PSDL). Reference conditions consist of a reference quality ^{60}Co source at 100 cm SSD, with a $30 \times 30 \times 30$ cm^3 phantom, at $20°C$, 101.3 kPa, 5 gcm^{-2} depth, within a 10×10 cm^2 field size [454]. The absorbed dose to water at a reference depth z_{ref} for a reference beam quality Q_0 is

$$D_{w,Q} = M_{Q_0} N_{D,w,Q_0} \tag{2.31}$$

Where M_{Q_0} is the dosimeter reading under reference conditions used in the standards laboratory and N_{D,w,Q_0} is the calibration factor of the absorbed dose to water of the dosimeter obtained from a standards laboratory. When the actual radiation quality

Q is different from the reference beam quality Q_0 used to calibrate the ionisation chamber, another correction factor can be applied k_{Q,Q_0} to correct for the difference

$$D_{w,Q} = M_Q N_{D,w,Q_0} k_{Q,Q_0} \tag{2.32}$$

and the reading M_Q, has been corrected to the reference values of influence quantities other than beam quality. Influence quantities include: pressure, temperature and polarization voltage [455]. Also those from the dosimeter include ageing, zero drift, and warm-up. Meanwhile, those from the radiation field include: beam quality, dose rate, field size, and depth in the phantom. Influence quantities cannot all be controlled, and are assumed to be independent, such that a combined factor $\prod k_i$, can combine each factor k_i. Here the pressure and humidity factors can be combined into

$$k_{TP} = \frac{273.2 + T}{273.2 + T_0} \frac{P_0}{P} \tag{2.33}$$

where P_0 and T_0 are the reference pressure and temperatures values ($20°C$, $101.3\,kPa$), and P and T are the cavity pressure and temperature at the time of measurement. Here, humidity does not require correction k_h if the reference relative humidity was 50%, and the chamber is used in the range of 20-80%. Other factors include; k_{elec} — the electrometer calibration (unity if electrometer and chamber calibrated together), $k_{pol} = \frac{|M_+|+|M_-|}{2M}$, where $M_{+/-}$ are electrometer readings at positive/negative polarity — the value is negligible & non-negligible effects for photon and electron beams respectively, but is unity when the chamber is used at the same polarizing potential and polarity as performed in calibration, and k_s — the saturation from ion recombination in the user beam at high dose rates [454].

2.5.2 Radiochromic film

Radiochromic film dosimetry is excellent for relative dose measurements in high-energy electron and photon beams. The advantages of radiochromic film include: high spatial resolution (sub-millimeter) [456], negligible angular dependence even for films parallel to the beam axis [457], water equivalence [458], minimal energy independence in photon [456, 459, 460] or electron beams [461] at clinical energies,

independence with depth for electrons [462], dose rate independence for electron [461, 463] and photon beams [464, 465], dose-per-pulse independence for electron beams [213], ease of handling, and integration into solid water phantoms [466]. Measurement output variability can depend on processing conditions [467] such as UV light and ambient exposure [468], batch variation, scanning orientation [469], and can cause large errors for low optical density values [462]. Therefore, the response of each batch needs to be calibrated against known exposures [470]. Uncertainties of measurements with films can therefore be estimated to range from 2-5% [471, 472]. The radiation-induced opacity (optical density) of films change from polymerization of di-acetylene monomers within the active layer [459]. The polymer established has the highest absorption in the red part of the optical spectrum, at a wavelength of ∼633 nm [469]. The opacity is dependent on absorbed dose, temperature, and post-irradiation development time [464]. This long development time (typically ∼24 hrs), enables colour stabilisation on the films, but is a limiting factor as it introduces a large delay to experiments. CCD-based flatbed scanners can be used as optical densitometers to measure light transmission and opacity of irradiated films.

2.5.3 Diamond detector

Diamond detectors are a type of solid-state detector composed of semiconductor material with a high electron and positron hole mobility. Absorbed dose causes temporary changes to its electrical conductivity [473]. The detector is water equivalent [474], has minimal directional dependence, and can be used for small field dosimetry because of its small sensitive volume, high sensitivity and high spatial resolution. However, they are expensive, have variability of active layer dimension for each detector [475], and experience large differences for different dose rates / dose-per-pulses [463, 476–478]. In addition, diamond detectors require pre-irradiating to give accurate results [479].

2.6 Beam quality specifiers

2.6.1 High energy photons

The quality of a high energy photon beam can be determined using the tissue-phantom ratio TPR_{10}^{20} [454] or $\%dd(10)_x$ [1] [480, 481]. The former uses a $10 \times 10\ cm^2$ field at constant source-to-chamber distance (SCD) of 100 cm, with an ionisation chamber, where the ratio of ionisation at 20 cm depth is taken to the ionisation at 10 cm depth, whilst the latter takes the percentage depth-dose at 10 cm depth for a field size of $10 \times 10\ cm^2$ on the surface of a phantom at a SSD of 100 cm [482]. Here, the effective point of measurement (EPOM) for cylindrical ionisation chambers requires a shift upstream by $0.6r_{cav}$, where r_{cav} is the cavity radius of the ionisation chamber [454, 483]. TPR_{10}^{20} is often the preferred choice from practicality and independence from electron contamination [484]. Water-equivalent phantoms e.g., solid water, can be used for energies below 10 MeV, and should extend at least 5 cm from the edges of the beam and by at least 5 cm beyond the chamber at its maximum depth of measurement to ensure that there is no reduction in scatter [454]. The TPR_{10}^{20} method has been shown to be similar for 6 MV FFF and FF beams when tuning the linac to match their PDDs [485, 486]. TPR_{10}^{20} can be given by relations from [487], [488] and [489] (see Equation (2.34)).

$$\begin{aligned} TPR_{10}^{20} &= 1.2661 PDD_{20,10} - 0.0595 \\ &= -0.7898 + 0.0329 PDD(10) - 0.000166 PDD(10)^2 \\ &= -0.6391 + 0.029348(\%dd(10)_x) - 0.00014498(\%dd(10)_x)^2 \end{aligned} \tag{2.34}$$

Where $PDD_{20,10}$ is the ratio of the percentage depth-dose at 20 and 10 cm, whilst $PDD(10)$ is the percentage depth-dose at 10 cm. Other formulations for different non-reference equivalent square field sizes [482, 490, 491] and protocols for other SSDs have been proposed (e.g., for Tomotherapy, CyberKnife (CK) & GammaKnife)[492]. Here effective equivalent square field sizes $s_{eq,eff}$ have been calculated from circular shaped apertures of diameter $d_{eq,eff}$ such that $s_{eq,eff} = 0.9 \times d_{eq,eff}$ [493]. Typical

[1] where the subscript x indicates a pure photon beam

values for 6 MV photon beams are 67.5 and 0.677 for $PDD(10)/\%dd(10)$ and $TPR_{20,10}$ respectively [388].

2.6.2 High energy electrons

Electron beam quality is highly linked to its depth-dose characteristics (see Figure 2.5). For these measurements, phantoms should extend around 5 cm around

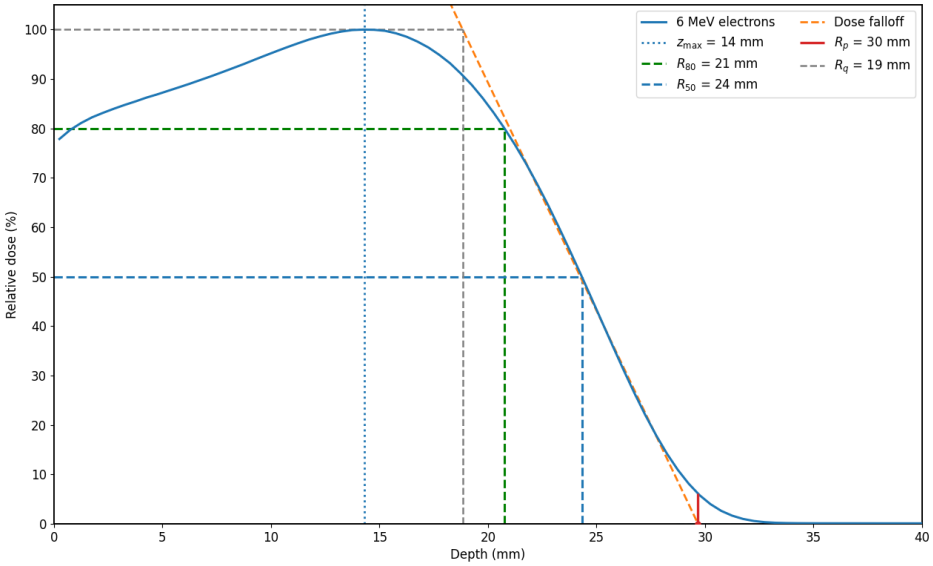

Figure 2.5: Example 6 MeV electron percentage depth-dose (PDD) curve

the field and with depth to account for beam scatter [494]. Notable parameters extracted from the depth-dose graph are; z_{max} — depth of maximum dose, R_p — the practical range, and R_{80} — the therapeutic range [2]. Here, the practical range, R_p defines the point where the tangent at which the inflection point on the descending part of the depth-dose curve meets the extrapolated bremsstrahlung background [496, 497]. Meanwhile, the therapeutic range is defined as the depth of the 80% depth-dose on the distal falloff of the curve. The modal energy or most probable energy at the surface, $E_{p,0}$ and practical range are related by:

$$E_{p,0} = C_1 + C_2 R_p + C_3 R_p^2 \tag{2.35}$$

[2]For conventional treatment units, R_{80} (cm) is $\sim E_{p,0}/3$ (MeV) [495]

Constant	Value
C_1	0.22 MeV
C_2	1.98 $MeVcm^{-1}$
C_3	0.0025 $MeVcm^{-2}$

Table 2.1: Constant values from Ding & Rogers et al. [498], for modal energy calculation in equation 2.35

where the values of constants C_{1-3} are given in Table 2.1.

The mean energy at the phantom surface, $\bar{E}_0$ is related to the half-value depth in water, R_{50} (the depth at which the absorbed dose is 50% of the maximum) [3], via the semi-empirical relation ($< 20\ MeV$) [499]:

$$C_4 = \frac{\bar{E}_0}{R_{50}} = 2.33\ MeV\ cm^{-1} \tag{2.36}$$

Here, measurements of depth-dose are taken at a constant source-to-detector distance (SDD) of 100 cm, with broad beams of field size of at least $10 \times 10\ cm^2$ [454]. For monoenergetic beams values of C_4 are between $2.34\ -2.56\ MeVcm^{-1}$, for energies of $5 - 50\ MeV$ [500]. At a constant SSD of 100 cm for ionisation curves, or depth-dose distributions, the mean energy can instead be represented for ionisation measurements as:

$$\bar{E}_0 = 0.818 + 1.935\ R^I_{50} + 0.04\left(R^I_{50}\right)^2 \tag{2.37}$$

and for depth-dose measurements with:

$$\bar{E}_0 = 0.656 + 2.059\ R^D_{50} + 0.022\left(R^D_{50}\right)^2 \tag{2.38}$$

where R^I_{50} is taken from a depth ionisation curve, and R^D_{50} is taken from a depth-dose curve [4][481, 501]. The mean energy at depth z in a phantom is given by the Harder relation [481]:

$$\bar{E}_z = \bar{E}_0\left(1 - \frac{z}{R_p}\right) \tag{2.39}$$

and the reference depth for calibration is given by

$$z_{ref} = 0.6R_{50} - 0.1\ gcm^{-2} \tag{2.40}$$

[3] $R_p = 1.271R_{50} - 0.23$ [489]
[4] $R^D_{50} = 1.029R^I_{50} - 0.064cm$ [494]

where the mean energy at the reference depth is

$$\bar{E}_{z_{ref}} = 0.07 + 1.027R_{50} - 0.0048(R_{50})^2 \tag{2.41}$$

2.7 Monte Carlo simulation

Monte Carlo techniques attempt to model the temporal evolution of particles traversing matter. All radiation transport is based on radiation transport theory which can model the behaviour, creation, deletion and interaction of particles within a given volume with the integro-differential equation called the Boltzmann transport equation (BTE). These transport equations are prohibitively complicated thereby excluding an analytical treatment except under severe approximations or for simple scenarios with few dimensions [496]. To simplify the modelling of radiation, Monte Carlo methods have been developed which can model complex geometries without unfeasible simulation time or complexity. The Monte Carlo process draws conclusions by sampling numerous times to from unbiased estimators (averages) of specific measures.

2.7.1 Random number generation

Pseudo-random number generation (RNG) lies at the heart of Monte Carlo. Here, a seed can be used to define the sequence of random numbers utilised for a given simulation. For identical seeds, simulations should yield identical results, while for different seeds, results should be statistically independent. Sequences of random numbers are long enough to avoid repetition during simulations and are distributed uniformly in multiple dimensions [502, 503].

2.7.2 Sampling

Sampling algorithms in Monte Carlo codes enable complex distributions to be sampled using a random number generated uniformly over a select number range [504]. This sampling process determines whether interactions occur, depending on the physics and transport data of the processes and materials involved [505].

Particle parameters for interactions, secondary production and deletion will be sampled from differential cross sections and probability distribution functions [503].

2.7.3 Condensed History Technique

MC employs the condensed history (CH) technique which groups interactions so their cumulative effect can be assessed by sampling energy, direction and position changes for a given interaction. The condensed history technique has two implementations. Class I regards all particles with the same grouping, and the correct number of secondary particles are setup and transported. Meanwhile, class II categorises collisions into "hard" and "soft" groups dependent on an energy threshold, where "soft" collisions employ the class I implementation and "hard" collisions use explicit analogue simulation methods [496]. The class II implementation often involves subdividing the movements of particles within tracks to increase accuracy because paths within materials are often dictated by multiple scattering. The threshold energy which determines the maximum particles range must ensure it is smaller than the spatial resolution of the geometry. A global maximum step size, material dependent step size, or maximum energy loss per step can ensure simulation times aren't prohibitively long or cause large inaccurate step sizes [503]. The parameter of step size in Monte Carlo can introduce a 'step size artefact' which can significantly change simulated results [506]. The step size must be sufficiently small relative to the dimensions of the scored region to ensure that the underlying theories and algorithms used to model particle energy loss, scattering, secondary particle production, and transport across materials and interfaces remain valid. If the step size is too large, these approximations break down because interaction cross-sections can change significantly over the step, which in turn introduces a non-physical step-size artefact that perturbs the value of scored quantities. These values converge in the limit of small step sizes, but at an increased computational cost [507–510].

2.7.4 Transport

The primary unit of simulation is the event which consists of tracks. Events input primary vertices and particles and output hits and trajectories. A track provides particle information and is composed of steps, where a start point and end point define a particle's properties as it propagates alongside a step length. Each step provides a position in the coordinate system, global and local time and details of the material that enclosing it. With each step, the physical values are updated in accordance with the track status and physics process occurring. A track status can change with each step, dependent on whether the particle comes to rest, exits the volume or is lost via an interaction. Interactions are defined by energy dependent cross sections of physical processes which can update primary particle properties and generate secondary particles to track. Overestimation of particle range and straggling can be addressed with path length (PLC) and lateral correction algorithms (LTA) [511]. The random hinge method is often utilised for problems such as the multiple scattering of electrons. This divides the step length into sub-steps with one or more random hinges between where the multiple scattering angle is sampled [503].

2.7.5 Boundary crossing

CH techniques work in large materials where the step size is less than size of the geometry. When particles come near to a material interface, the step size must be decreased. This reduction can cause prohibitively long simulations unless appropriate limits are set for the threshold separation from a boundary that a particle can reach before step sizes must be decreased.

2.7.6 Scoring

Quantities scored and averaged over a given number of histories in MC can be measurable and unmeasurable in physical experiments. These quantities are typically scored over a voxelised region whereby increased voxel size reduces runtime as well as spatial resolution [496]. Given the accuracy of a measurement is given with an uncertainty of $k\sigma/\sqrt{N}$, (where k is a constant), increasing the number of

histories or reducing the variance can reduce uncertainty [512]. Here voxel sizes, as recommended by Chetty et al. for field sizes are [496]:

$$\begin{cases} field\ size > 3 \times 3\,cm^2 & voxel\ size\ < 2 - 5\,mm \\ field\ size < 3 \times 3\,cm^2 & voxel\ size\ < 1 - 2\,mm \end{cases} \tag{2.42}$$

The decision on voxel size is a trade off between the uncertainty in each voxel relative to the spatial resolution of the measurement [513]. Phase spaces can also record particle properties at a particular plane upon entering or leaving materials. Intermediate phase-space scoring (IPSS) can be used to create a virtual linac source at different points within a linac geometry. The phase space can be sampled to model particle transport in each layer inside the linac geometry [503].

2.7.7 Uncertainty and Efficiency

The uncertainty of a measurement characterises the dispersion of values of a measurand. The expression of experimental uncertainties can be grouped into two categories: those evaluated by statistical methods, and those evaluated by other means. In the former, components are characterised by estimated variances, and the number of degrees of freedom. Meanwhile, in the latter, components are characterised by approximated variances. Uncertainty components can be grouped into two categories, based on their method of evaluation. Uncertainty for a correction of a systematic effect can be obtained by a Type A evaluation, while a Type B evaluation will characterise a random effect. Type A evaluations will result in a probability distribution from a sequence of observations, while Type B will result in an assumed probability distribution from available reliable knowledge [514]. In general, the greater the dose in a region, the lesser the fractional uncertainty there [496]. There are two common methods for calculating statistical uncertainties: the batch method and the history by history method.

Batch method

In the batch method, the sample variance (see appendix A.3.2, equation A.6), can be calculated where N is the number of independent batches and X_i is the quantity

```
if (n_hist = x_last):
    x_tmp = x_tmp + delta
else:
    x = x + x_tmp
    x_sqr = x_sqr + (x_tmp*x_tmp)
    x_tmp = delta
    x_last = n_hist
```

Figure 2.6: History by history algorithm from [515]

measured in each batch. Here, calculations rely on different phase-space inputs using a different random seed. The batch approach has a number of issues, which include large uncertainty fluctuations for small N, the ignoring of correlations between incident particles, and increased storage requirements for scored quantities [515]. The number of batches used is typically on the order of 10 - 100 [502, 512].

History by history method

The history by history method ascribes X_i as the recorded value in history i, and N the number of primary histories, such that the sample standard deviation (see appendix A.3.2, equation A.7), can be used as a representation of the standard error of the mean [496]. This method groups scored quantities to the primary histories (i.e., electrons) that generated them. Scored quantities can also be grouped by the incident particle (i.e., photons) that altered them, such that N is the number of incident particles. Here, the algorithm seen in figure 2.6 as described in Sempau et al. [516], describes the process of updating the scored quantities $\sum_{i=1}^{N} x_i$ (represented by x) and $\sum_{i=1}^{N} x_i^2$ (represented by x_sqr). In each iteration the value delta adds the contribution of the current step to the scored quantity. Also, the mean scored value, $\bar{X}$ will be calculated after n_hist reaches its final value X_last. The method therefore requires three counters for each voxel, such that the total may be huge and the execution can be slow or infeasible [517]. Here the estimated uncertainty of a scored quantity in equation A.7 in appendix A.3.2, can be rewritten as:

$$s_{\bar{x}} = \sqrt{\frac{1}{N-1}\left(\frac{\sum_{i=1}^{N} x_i^2}{N} - \left(\frac{\sum_{i=1}^{N} x_i}{N}\right)^2\right)} \tag{2.43}$$

and the covariance in A.25 in appendix A.3.6 can be rewritten as:

$$\sigma_{x,y} = \frac{1}{N}\left(\sum_{i=1}^{N} x_i y_i - \frac{\sum_{i=1}^{N} x_i \sum_{i=1}^{N} y_i}{N}\right) \tag{2.44}$$

such that the error on the output of a ratio of scored quantities e.g., $C_q = \frac{x}{y}$, then the uncertainty on a ratio of correlated quantities is:

$$s_{\bar{C}} = \bar{C}\sqrt{\left(\frac{s_{\bar{x}}}{\bar{x}}\right)^2 + \left(\frac{s_{\bar{y}}}{\bar{y}}\right)^2 - \frac{2\sigma_{xy}}{(N-1)\,\bar{x}\bar{y}}} \tag{2.45}$$

To calculate the average photon energy crossing a zone, the total photon energy and the total number of photons needs to be scored and divided by one another. These quantities are correlated, therefore to estimate the uncertainty requires using equations 2.44 and 2.45 [518].

Efficiency

The efficiency of a Monte Carlo simulation is defined as:

$$\epsilon = \frac{1}{[s(N)]^2\, T(N)} \tag{2.46}$$

where $T(N)$ is the calculation time, and $s(N)^2$ is an estimate of the true variance of the parameter of interest. For large N $[s(N)]^2 \propto 1/N$, and $T(N) \propto N$, so the efficiency is independent of N.

2.7.8 Variance reduction

Variance reduction techniques can be used to reduce the variance of an estimator without increasing the number of histories and simulation time, while keeping an unbiased estimate of the variance so that increasing the number of histories would converge to the same result. Variance reduction techniques can be categorised into real (RVRT) and approximate (AVRT), where both must not compromise accuracy, but only the former maintains an unbiased estimate of the variance.

Russian Roulette and Splitting

To reduce the variance, particle splitting can be used. The technique can be used to split a bremsstrahlung photon produced by an electron into many photons sampled from the same distribution as the original photon. Photons produced from the original electron are ascribed a weighting $w = 1/N_{split}$, where N_{split} is the particle splitting factor. These splitting factors can be modified depending on the direction of the incident electron (selective bremsstrahlung splitting), or left as equal (uniform particle splitting). By contrast, Russian Roulette methods can also reduce variance by ascribing each particle a survival probability $p_{survive}$. A random number, ε is sampled between [0,1] such that the particle is killed if $\varepsilon < p_{survive}$. The weighting of surviving particles is then increased by a factor $w = 1/p_{survive}$. A hybrid between these methods is directional bremsstrahlung splitting which defines a constant splitting factor, and analyses the photon output direction. A photon is then killed in the Russian Roulette method if it is not directed into a region of interest [519].

Range rejection

In range rejection, an electron's history is terminated when its range shorter than the shortest distance to a boundary. Range rejection is an AVRT as it ignores possible bremsstrahlung emission in the curtailed path [520].

Cross section enhancement

The interaction cross section in a given region around a scoring volume can be enhanced by an enhancement factor, with the weight of secondary particles produced decreased by this same factor [521].

History repetition

Histories can be repeated by displacing pre-calculated histories from a stored database to start at different positions in a material. Each history is repeated sequentially before considering the next stored history to eliminate restarting with the same random number sequence, which would underestimate uncertainties and

cause biased results [497]. This is an AVRT where the distance between displacement must be enough to eliminate correlations between the original and repeated history and the problem must ensure a degree of geometric symmetry. If the number of reuses of particles is high, eventually the variance will approach the latent variance of the phase space file rather than statistical variation of scored quantities [522]. Correlations in results, from recycling primary histories, can cause significant underestimation of uncertainties. The maximum recommended number of times that electron beams can be recycled is 4 [523], as beyond this value the fractional uncertainty in a scored value increases with the square root of the factor. However, compared to electrons, recycling photon sources has been seen to increase fractional uncertainties by a markedly smaller extent as multiple photons originating from a primary history have a low probability of interacting in identical voxels [515].

2.8 Radiation effects on materials

Target displacement damage can occur when energetic projectiles displace atoms from lattice sites. Primary knock on atoms (PKA) are created which can move throughout the lattice. Displaced atoms leave vacancies, and become interstitial atoms between lattice sites. The vacancy-interstitial pair is a Frenkel pair (FP) and the number of displacements is characterised by the number of displacements per atom (dpa) [524]. This quantity defines the number of times, on average, the atoms of a material have been displaced from their original sites. The dpa is directly related to the total number of defects/ Frenkel pairs N_F.

$$dpa = \frac{A}{N_A \rho} N_F \tag{2.47}$$

Where ρ is the density in g/cm^3, A the mass number, and N_A, Avogadro's number. Bombarding a crystalline solid with electrons of $>\sim 1MeV$ can cause point defects, with the displacement of atoms from their equilibrium lattice positions via elastic collisions [404]. Photons can also cause damage indirectly by producing charged particles, neutrons or ions. Pair production and bremsstrahlung also cause small

momentum transfers to targets and therefore, can generate displacement damage [525–527]. These displacements can reduce the thermal diffusivity and can be used to estimate dpa damage [408, 528]. Heating and cooling tungsten sequentially can cause annealing which can reverse dpa damage and recover the original thermal diffusivity [528]. A number of models are used to approximate the number of defects including the Norgert, Robinson and Torrens (NRT) model:

$$N_{NRT} = N_F = \kappa \frac{\xi\left(T\right) T}{2E_{th}} \tag{2.48}$$

where N_{NRT} is the number of defects, $\kappa = 0.8$ is the displacement efficiency, T is the kinetic energy of the primary knock-on atom (PKA), and $\xi\left(T\right)$ is the Lindhard partition function, and E_{th} is the displacement damage threshold. The model assumes that damage occurs in a cascade of electronic two-body collisions whereby the energy transferred to the lattice is zero. For energies below a cut-off E_c only atomic collisions take place with no electronic stopping, and above the cut-off energy E_c, no displacement occurs. The number of defects $\nu\left(T\right) = 0, 1, T/2E_{th}, E_c/2E_{th}$ in the respective ranges $0 < T \leq E_{th}, E_{th} < T \leq 2E_{th}, 2E_{th} < T \leq E_c, T > E_c$. The factor $2E_{th}$ is from the hard sphere model, which assumes energy is equally shared between two atoms on each collision. The threshold displacement energy E_{th} is the average minimum energy over all crystallographic directions to produce a defect (for Tungsten it is $70\,eV$). In FLUKA, when dpa scoring is requested a biased sampling is performed for momenta higher than an energy threshold E_{th}.

3

Materials and Methods

Contents

3.1 Physical materials and methods

3.1.1 Linear accelerator

Measurements in this work were performed using a 6 MeV electron linear accelerator (Figures 3.1 and 3.2, and Table 3.1).

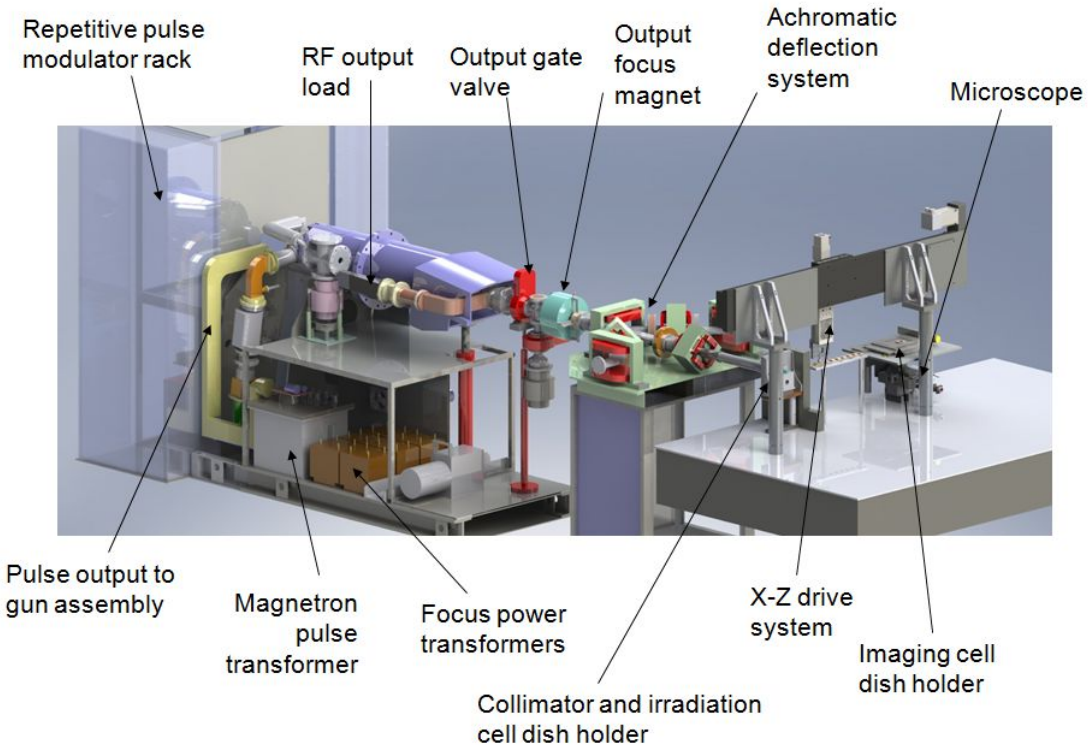

Figure 3.1: Linear accelerator SolidWorks CAD model

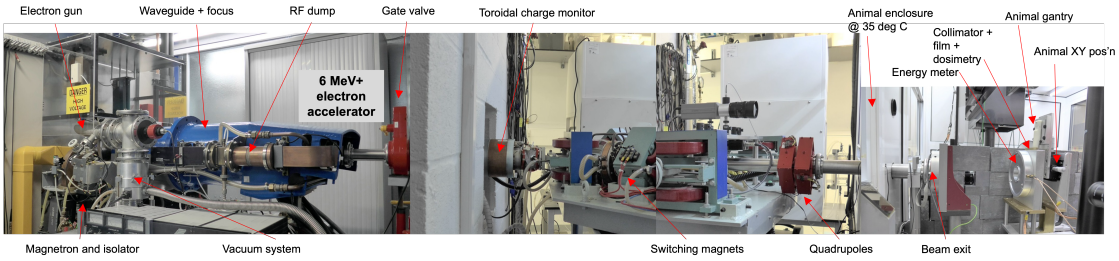

Figure 3.2: Linear accelerator irradiation bunker

The linac consisted of a waveguide, beam focus constructed from an Elekta SL75 TW waveguide and S-band RF magnetron source (Teledyne e2v-M5125 type 2.89 GHz) and thryatron (CX1140)-based modulator. The structure is housed

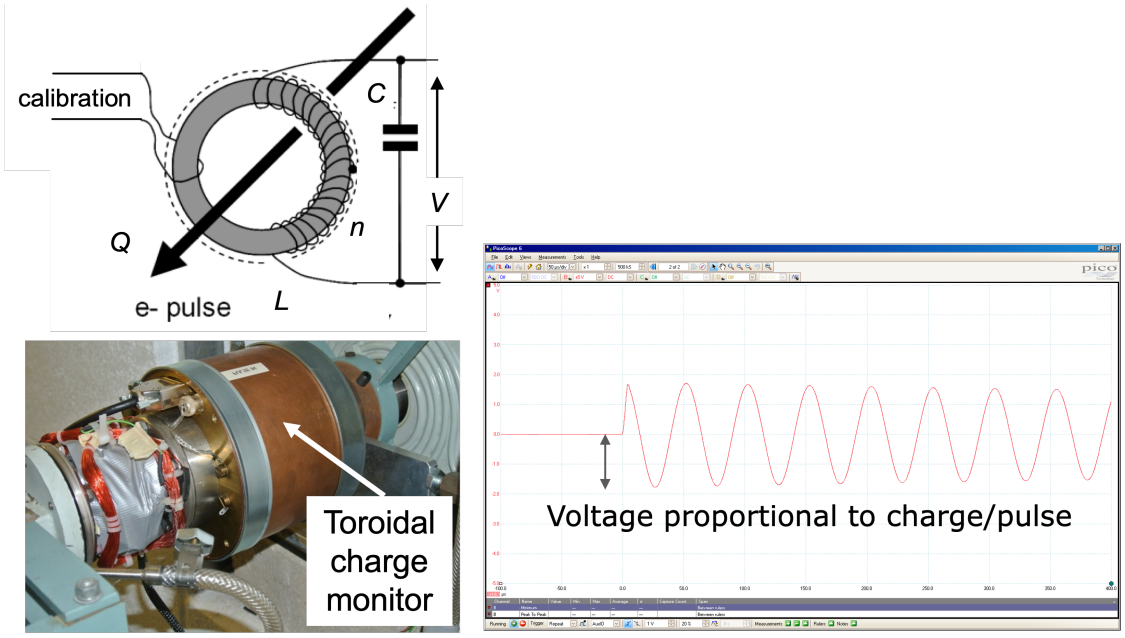

Figure 3.3: Toroidal charge monitor

within a Faraday cage, where a diode-type gun is pulsed synchronously with the radiofrequency source and that can deliver (macro)pulses with a width of 3.4 μs. A quadrupole doublet focusing systems enables the beam positioning, orientation and focus to be adjusted with the use of two quadrupole magnets; one in the horizontal and one in the vertical axes. A silica disk can be used to monitor beam properties from the collection of Čerenkov emission from each pulse with a charge-coupled device (CCD) camera. The charge leaving the accelerator can be monitored using a non-intercepting electron beam charge monitor (toroidal inductive sensor) (Figure 3.3) [529].

The monitor is composed of a 26 mm thick ferrite core, with an internal and external diameter of 65 mm, and 105 mm respectively. The monitor forms a tuned circuit which resonates when the beam passes through its centre. Monitor output can be monitored at all frequencies (25-300 Hz [530]) and can be correlated with dose measurements. It can also be used to integrate total charge delivered and can switch off triggering of the accelerator once the required charge has been delivered. The beam emerges from a thin output window (10 μm beryllium copper foil) into the experimental area. The exit window marginally influences the electron energy

spectrum and scatters electrons (as shown in Supplementary appendix Figure A.1).

Table 3.1: Linear accelerator characteristics

Linac structure	Travelling wave type
Nominal Electron Energy	6 MeV
Resonant frequency	2.998 GHz
RF peak input power	2 MW
Pulse length	3.4 μs
Pulse Repetition rate	25-300 Hz
Peak Pulse Current	∼100 mA
Average Pulse Current	∼0.1 mA
Maximum Beam Power	∼700 W

3.1.2 Positioning

A "working distance" can be set by measuring the displacement of each component with a string potentiometer type sensor (Strainsense, Milton Keynes, UK, type CD80-2000-R01K-L15-L4) within the experimental area. Components can be placed on rails, enabling variable positioning up to 100 cm from the output window (Figure 3.4).

3.1.3 Energy monitoring

A Ti scattering foil (30 μm thick, positioned 8.5 mm downstream from the output window) can be used to spread out the beam to obtain a flat profile across the central portion. To monitor beam energy from pulse to pulse, two independent annular discs (collector plates) are used to collect peripheral electron fringes. Meanwhile, the centremost subsubsection of the beam (within the central 50 mm energy monitor aperture) can impact irradiation samples without interference [530]. A transient digitiser, can be used (PicoScope 6403, 200 MHz Bandwidth, 1 GS/s, 512 MS memory; Pico Technology, St Neots, Cambs., United Kingdom) to obtain and display signals from energy monitor output connectors attached to collector plates. Values of charges deposited on each collector plate can be mapped to beam energy through an energy monitor ratio (Equation (3.1))

$$E_{monitor\ ratio} = \frac{Q_{rear}}{Q_{front} + Q_{rear}} \tag{3.1}$$

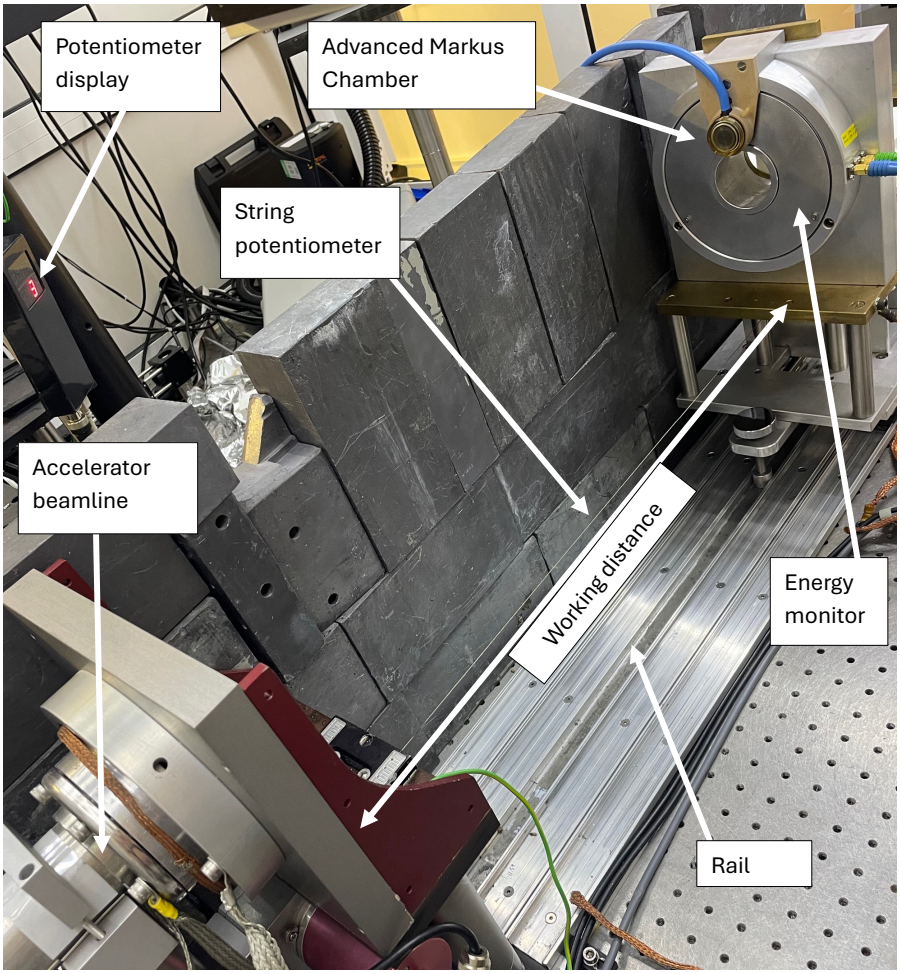

Figure 3.4: Experimental area

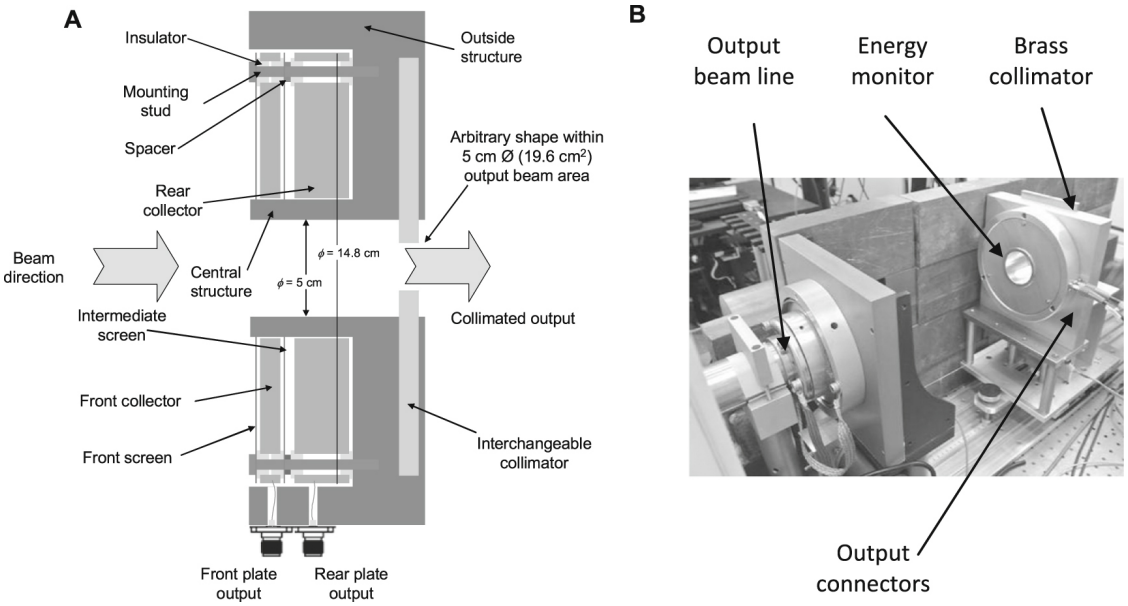

Figure 3.5: (A) Sketch of energy monitor with collimation (B) Image of energy monitor mounted on movable rail system, from [530]

For working distances > 50 cm an energy monitor ratio of ∼0.7 had been seen to produce a 6 MeV electron output [530]. Because our linac is a travelling wave type, beam output energy can be varied by detuning the magnetron matching network. The beam energy output can thereby be maintained at a constant value irrespective of electron pulse amplitude [529].

3.1.4 Collimation systems

Immediately downstream of the energy monitor apparatus (see Figures 3.5 and 3.7), 6 mm brass collimator plates (with outer dimensions of width and height of 150 mm × 100 mm respectively) could be installed with apertures of variable shape and size (Figure 6.1, panels A and B).

3.1.5 Current measurement

A beam collection device was used to measure the approximate electron beam current (without a bremsstrahlung target in place) (Figure 3.6). This consisted of an insulated 46 mm diameter, 50 mm thick aluminium disc, placed inside a grounded aluminium cup placed ∼36 mm downstream of the exit window and connected (using RG58 coaxial cable) to a 50 Ω terminated at the input of a transient digitizer (Picoscope 4603, Pico Technology, St Neots, Cambridgeshire, UK). This beam collection device acted as an unbiased Faraday cup and since the collecting electrode was thick enough to stop all incoming electrons, provided an output directly proportional to the accelerator output current. Here, secondary electron production and backscatter [531] inevitably affect the collected current. Calibrated attenuators could be inserted in series when the peak voltage generated exceeded the capabilities of the digitizer input stage. Gun heater current was adjusted from 6 to 8 A, in increments of 0.04 A, where settings were repeatable to within ±0.02 A. This current is an indicator of electron emission from the gun, but no physical meaning can be attributed to it. With the bremsstrahlung target assembly in place, photon charge output was measured with the AMC (positioned at 10 cm depth in RW3 solid water) by delivering 30 pulses for each gun heater current setting.

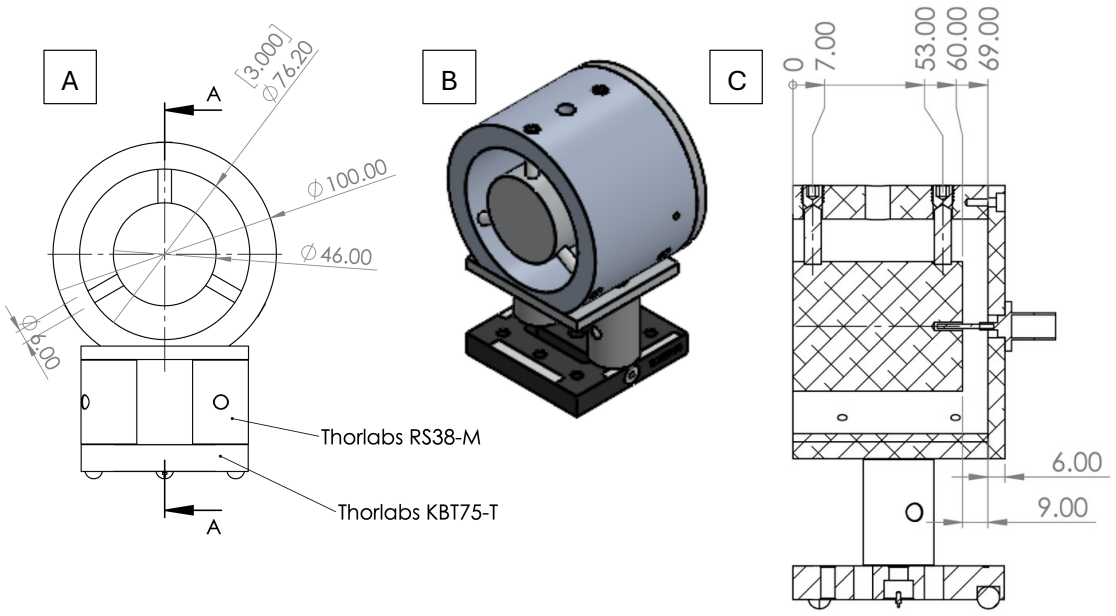

Figure 3.6: (A) Sketched front view of beam collection device (B) SolidWorks CAD, (C) side view

3.1.6 Mouse cradle

A mouse cradle, based on previously described designs [532], was used, either to perform dosimetric measurements with films taped to the upstream surface of a Perspex mouse phantom (see Figure 3.8, and appendices Figure A.14) in place, or to fix the position of anaesthetised mice throughout irradiations (Figure 3.7).

3.1.7 Dosimetry

Advanced Markus® Ionisation Chamber

A plane-parallel Advanced Markus® ionisation chamber (AMC) (model 34045, PTW-Freiburg, Freiburg, Germany) (Table 3.2) was connected to an electrometer (UNIDOS Webline, PTW-Freiburg, Freiburg, Germany), operated in an appropriate measurement range (Table 3.3) and operated at a bias voltage of +300 V.

Two chambers had previously been calibrated in ^{60}Co beams under standard conditions with absorbed dose to water calibrations of (a) 0.6501 nC/Gy and (b) 0.6716 nC/Gy. These chambers could be used in tandem throughout a given set of irradiations to measure average dose rate over an entire exposure, with one

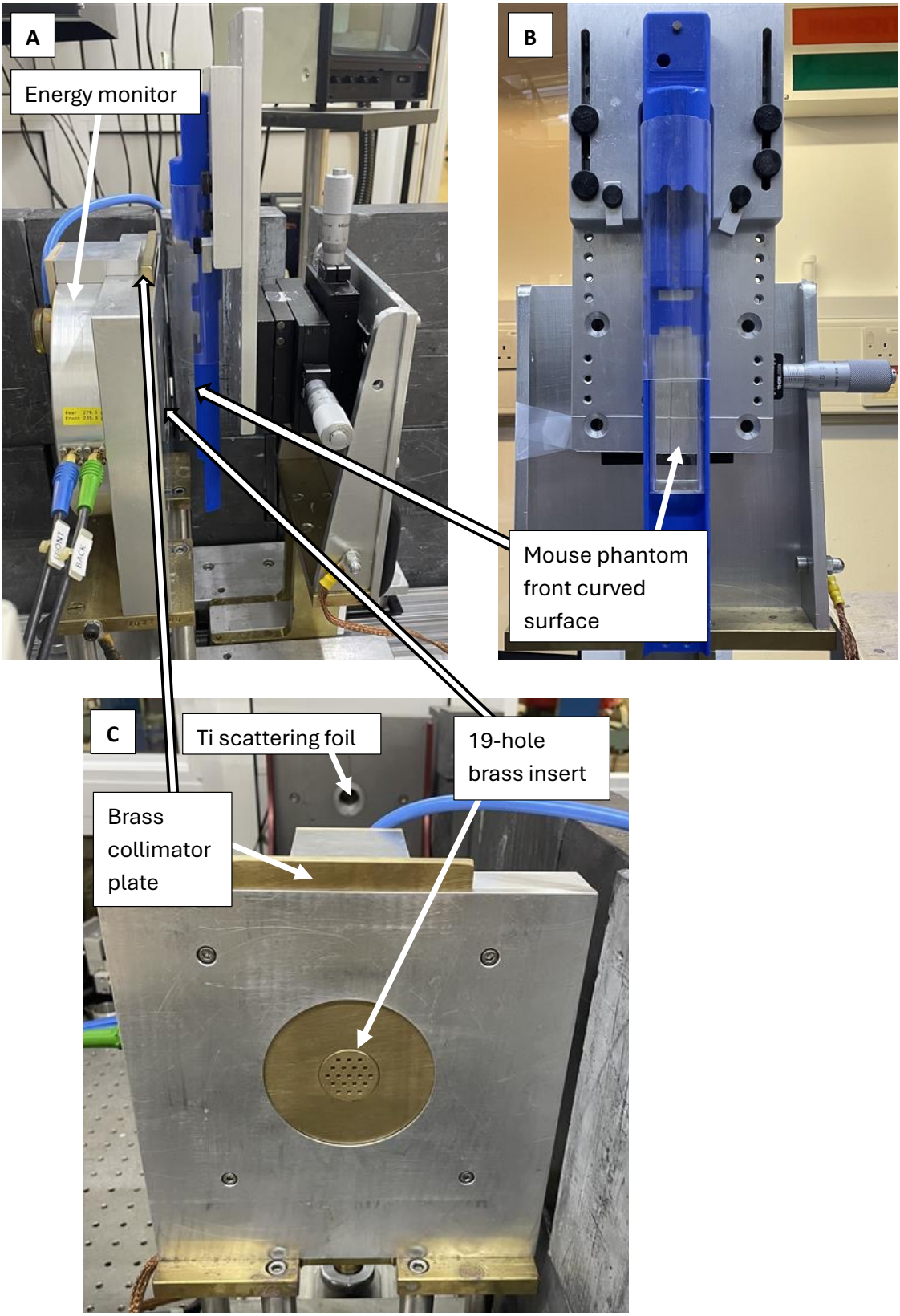

Figure 3.7: (A) Side view of preclinical mouse irradiation platform beamline setup (B) Downstream view of mouse phantom within the mouse cradle (C) Upstream view of brass collimator plate and 19-hole insert

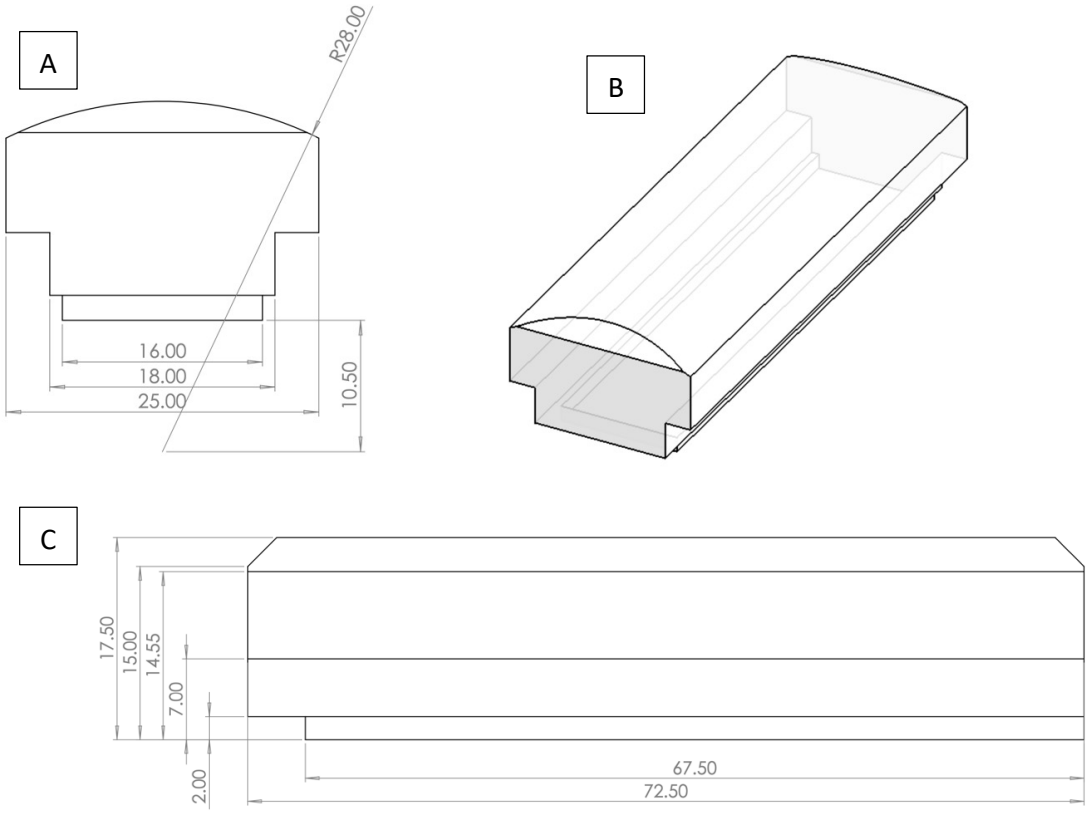

Figure 3.8: Perspex mouse phantom used for dose delivery prescription and validation using GafChromic EBT-XD film at the front curved surface of the phantom, facing the beam when placed in the mouse cradle. All dimensions are displayed in mm: A) Top view B) Isometric view C) Side view

Table 3.2: Advanced Markus® ionisation chamber features [533]

Sensitive volume	0.02 cm^3
Sensitive volume radius	2.5 mm
Sensitive volume depth	1 mm
Ion collection time	22 μs
Maximum dose-per-pulse for $\geq$ 99 % saturation	5.56 mGy
Nominal dose response	0.67 nC/Gy

positioned upstream of the energy monitor, radially offset from the central aperture (a) and connected to the UNIDOS Webline electrometer, and one positioned at any given depth in solid water (b) connected to a UNIDOS Romeo electrometer (PTW-Freiburg, Freiburg, Germany). Throughout mouse irradiations only the off axis chamber was used (a). For electron irradiations at high dose-per-pulse (DPP), the chamber could be used by indirectly accounting for ion recombination

Table 3.3: UNIDOS webline electrometer measuring ranges

Setting	Min. Dose	Max. Dose	Min. Dose rate	Max. Dose rate
LOW	3 mGy	1.3 MGy	0.3 mGy/s	0.3$\dot{6}$ Gy/s
MEDIUM	150 mGy	130 MGy	15 mGy/s	36.$\dot{6}$ Gy/s
HIGH	15 Gy	13 GGy	1.5 Gy/s	366.$\dot{6}$ Gy/s

through matching known on-axis film doses to off-axis readings from chamber (a) acquired during the same experimental setup [534].

microDiamond

A synthetic single crystal microDiamond detector (model 60019, PTW, Freidberg, Germany) (Table 3.4) was used for dose measurements at a bias voltage of 0 V because of its high spatial resolution and output consistency for small field sizes [535]. Here prior calibration indicated a response of 1.29 nC/Gy.

Table 3.4: microDiamond features [536, 537]

Sensitive volume	0.004 cm^3
Sensitive volume radius	1.1 mm
Sensitive volume depth	1 μm
Ion collection time	<1 μs [538]
Maximum dose-per-pulse for $\geq$ 99 % saturation	<0.5 mGy [539]
Nominal dose response	1 nC/Gy

Gafchromic EBT-XD film

Gafchromic EBT-XD film ((Ashland Inc., Covington, KY, USA)) is an energy independent method of analysing dose deposition. The film is comprised of a 25 μm thick active layer sandwiched between two 125 μm matte polyester substrates. When the active layer is exposed to radiation, a blue coloured polymer forms (with a maxima at 633 nm). The dynamic dose range of the film spans from 0.1 Gy to 60 Gy. Meanwhile, the recommended optimal dose range is 0.1 Gy to 40 Gy [540]. The atomic composition and density of each layer is given in 3.5 from Palmer et al., and the effective atomic number of the active layer is 7.37 compared to 7.3 for water [458]. Gafchromic EBT-XD films were used for measurements of average dose rates, beam profiles and for generation of percentage depth-dose (PDD). Films were used

Table 3.5: EBT-XD Film Composition from [458, 541]

EBT-XD layer	Thickness μm	Density gcm^{-3}	Composition (atomic %)
Polyester base	125	1.35	H: 36.4, C: 45.5, O: 18.2
Active layer	25	1.35	H: 57.0, Li: 0.6, C: 28.5, N: 0.4, O: 11.7, S: 0.1, Na: 0.1, Cl: 0.1, Al: 1.4

from their dose rate and energy independence, their tissue equivalence and high achievable spatial resolution (resolving features down to 25 μm or less [542]) [543], as well as their prior usage for electron and photon measurements [214, 540]. These were cut from a 8' × 10' sheet into dimensions appropriate for each experiment, whilst maintaining identical orientation throughout irradiation and handling. The readout of irradiated films was conducted 24 hours after exposure using a film scanner (Epson Perfection v850 Pro, Seiko Epson Corporation, Nagano, Japan) to obtain 48-bit colour images (16 bits per colour channel, RGB). Prior to each scan, 5 warm up scans were taken without a film present to reduce warm-up effects. In addition, the scanner base was wiped with a cloth to eliminate dust and artifacts on the glass surface. Calibration of films from a given batch was performed with 6 MV photon and 6 MeV electron clinical beams from a Varian TrueBeam (Varian Medical Systems Inc., Palo Alto, CA, USA) linac at the Churchill Hospital in Oxford, United Kingdom. Delivered doses were varied from 0.5-40 Gy and scanned at 96 dpi over a field of view (FOV) of 75 × 75 pixels. From each scanned film a 16-bit TIFF image was obtained where a pixel value (PV) was determined in the red channel within a region of interest (ROI) using ImageJ (v2.14.0/1.54f). Pixel values ranged from 0 to 65,535. Two unirradiated background films were kept consistently from the same sheet for all films to convert the optical density (OD) value to dose.

$$OD = log_{10}\left(\frac{PV_{background}}{PV_{irradiated}}\right) \tag{3.2}$$

For all 6 MeV electron measurements, and for 6 MV photon measurements above 5 Gy a Rodbard fit was applied [541, 544], of the form:

$$D = c\left(\frac{OD - a}{d - OD}\right)^{\frac{1}{b}} \tag{3.3}$$

where a, b, c, and d were fitting parameters and D is the dose (in Gy). Meanwhile, for photon doses from 0.5 - 5 Gy (OD $\sim$ 0.02-0.14), a quadratic fit was

applied of the form:

$$D = e(OD)^2 + f(OD) + g \tag{3.4}$$

where again e, f, and g were fitting parameters.

3.2 Biological materials and methods

3.2.1 Licensing

Animal research was conducted in accordance with UK Home Office Guidelines, following the ARRIVE (Animal Research: Reporting of In Vivo Experiments) guidelines, and approved by the University of Oxford Animal Welfare and Ethical Review Body (AWERB), under University of Oxford project licence P8415318.

3.2.2 Maintenance

Mice were housed in a temperature-controlled environment with a 12-hours reversed-phase light/dark cycle (lights on 07:00 h), and were provided with food and water ad libitum at the Department of Biomedical Services, Radiobiology Research Institute, University of Oxford, Oxford.

3.2.3 Anaesthetic

For the irradiation, the mice were anaesthetised using isoflurane (4% for anaesthetic induction and 2% for maintenance, with a total anaesthesia time of less than 10 minutes) supplemented with 95% oxygen (1/1 mixture with air resulting in a mixture of approximate 60% oxygen), and then placed upright in a mouse cradle in front of the horizontal beam (Figure A.12 in supplementary material)

3.2.4 Statistical analysis

GraphPad Prism 10 software (GraphPad Software Inc., La Jolla, CA, USA) was used for statistical analysis.

3.3 Material science methods

3.3.1 Target disk manufacture

Tungsten sheets of thicknesses of 0.5, 0.7, and 1 mm were utilized (Goodfellow, Cambridge, England) of 99.95% purity [420]. Electrical discharge machining (EDM) was used to produce discs of 25 mm diameter for each of the target thicknesses.

3.3.2 Transient Grating Spectrometry (TGS)

Transient grating spectrometry (TGS) was used to detect electron induced dpa damage (see theory section 2.8) in the tungsten bremsstrahlung targets from measurements of their thermal diffusivities (see Figure 3.9) [525, 526, 545]. Targets were polished following irradiation with a Struers LectroPol-5 (Stuers S.A.S, Paris, France) electrolytic polisher. Settings of 12 V at 25 $°C$, with a solution of dissolved 20 g sodium hydroxide in 1000 ml distilled water. For 20 s irradiations of targets, a significant oxidised layer was present, so electropolishing times were ∼10 minutes per side, meanwhile unirradiated targets were polished for ∼4 minutes per side. Targets were measured using the TGS setup described by Reza et al. [528] using a nominal grating period of 2.8 μm on the sample surface. Thermal diffusivity measurements were taken with scans over the upstream irradiated surface, following previously described measurement procedures [545–547].

3.3.3 Fatigue analysis

Fatigue limits and lifetime calculations often consider two dynamic loading regimes; low cycle fatigue (LCF) and high cycle fatigue (HCF). For LCF, high plastic strain occurs for typically $<10^5$ cycles, whilst high elastic strain occurs in HCF for typically $>10^5$ cycles [548]. Criteria for failure differ, with some studies using the yield strength at 0.2% strain [438, 549], crack formation [418], or complete sample separation [550]. Here, fatigue lifetime has often been found to be shortest in locations undergoing greatest temperature fluctuation [551]. For LCF analysis,

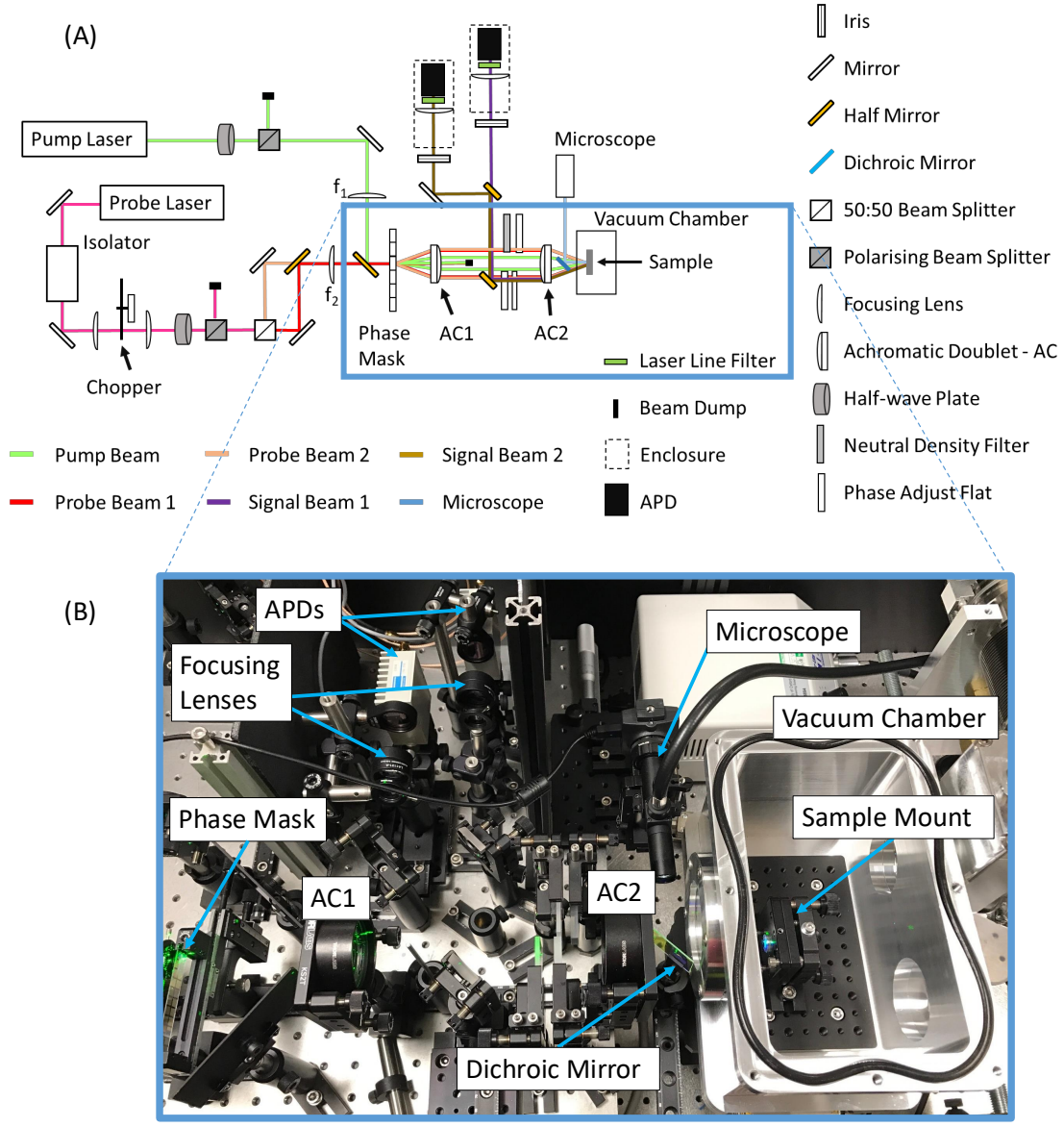

Figure 3.9: Transmission Grating Spectrometry (TGS) setup adapted from [546] (A) System level overview (B) Image of components highlighted from highlighted section in (A)

the Coffin-Manson relation has been utilised

$$\varepsilon_{pa} = \frac{\Delta\varepsilon_p}{2} = \varepsilon'_f \left(2N_f\right)^c \tag{3.5}$$

where ε_{pa} is the plastic strain amplitude, $\Delta\varepsilon_p$ is the plastic strain range, ε'_f is the fatigue ductility coefficient and is usually approximated as the true (monotonic) fracture ductility ε_f $\left(ln\left(\frac{100}{100-RA}\right)\right)$ $\approx$ 0.5 (brittle) or 1.0 (ductile) metals [552, 553]. Here $2N_f$ is the number strain reversals to failure (N_f cycles = $2N_f$ reversals) and c is the fatigue ductility exponent $\approx$ -0.5 (brittle) and -0.6 (ductile) metals [404, 416, 552, 554]. For HCF analysis, Basquin's equation has been utilised (see Figure A.31 & Table A.23)

$$\sigma_a = \frac{\Delta\sigma}{2} = \sigma'_f \left(2N_f\right)^b \tag{3.6}$$

where σ_a is the equivalent fully reversed true stress amplitude, and b is the fatigue strength exponent ($-0.12 < b < -0.05$ for metals, with average of -0.085)[548, 555]. Combining these equations has resulted in the uniaxial Coffin-Manson strain-life equation

$$\varepsilon_a = \varepsilon_{ea} + \varepsilon_{pa} = \frac{\sigma'_f}{E}\left(2N_f\right)^b + \varepsilon'_f \left(2N_f\right)^c \tag{3.7}$$

where $\varepsilon_{ea} = \frac{\Delta\varepsilon_e}{2} = \frac{\sigma_a}{E}$, and E is the elastic modulus. Here the damage per reversal can be simplified to

$$\frac{1}{2N_f} = \left[\frac{\sigma'_f}{\varepsilon'_f E}\frac{\varepsilon_{pa}}{\varepsilon_{ea}}\right]^{\frac{1}{b-c}} \tag{3.8}$$

This equation is usually applied in scenarios where yielding occurs [556]. The fatigue lifetime under repeated irradiations for irregular loading can be accumulated for every cycle in the form of Palmgren-Miner's rule [557].

$$\sum_i^{N_{tot}} U_i = \sum_i^{N_{tot}} \frac{n_i}{N_i} = \sum_i^{N_{tot}} \frac{n_i}{2N_{f_i}} = 1 \tag{3.9}$$

Where U_i is the life fraction applied for n_i cycles (i.e., one for each pulse) at a particular stress, and N_i is the number of cycles to failure, (where $N_i = 2N_{f_i}$, and N_{f_i} is the number of reversals to failure). Lifetimes of each element can thus be followed for every time increment, with the lifetime of the target determined by the

element with shortest lifetime such that the number of repetitions to failure is represented by [548],

$$B_f = \frac{1}{\sum_i^{N_{tot}} \frac{1}{N_i}} \tag{3.10}$$

However, values for parameters in Equations (3.7) and (3.8) are scarce, so approximating the shape of the fatigue curve has been performed using the simplified form of the universal slopes equation [550, 558], (see Figure A.32 & Table A.24).

$$\Delta\varepsilon = \Delta\varepsilon_e + \Delta\varepsilon_p = 3.5\frac{\sigma_u}{E}N_f^{-0.12} + \varepsilon_f^{0.6}N_f^{-0.6} \tag{3.11}$$

Where $\Delta\varepsilon$ is the strain range, and σ_u is the ultimate tensile strength. Here N_f is now the number of cycles to failure, defined by the separation of the two halves of the sample [559]. By analogy,

$$\frac{1}{N_f} = \left[3.5\frac{\sigma_u}{\varepsilon_f^{0.6}E}\frac{\Delta\varepsilon_p}{\Delta\varepsilon_e}\right]^{-\frac{1}{0.6}} \tag{3.12}$$

In addition other forms of the universal slopes equation have been proposed [558], discussed [418], and utilised in similar analysis [560], whereby

$$\varepsilon_a = \frac{\Delta\varepsilon}{2} = 0.0196\varepsilon_f^{0.155}\left(\frac{\sigma_u}{E}\right)^{-0.53}(2N_f)^{-0.56} + 0.623\left(\frac{\sigma_u}{E}\right)^{0.832}(2N_f)^{-0.09} \tag{3.13}$$

Where $2N_f$ is the number of reversals to failure. This formulation utilises data from 47 materials, includes tensile strength and ductility, and has been said to give better predictions of fatigue life [560, 561]. For our analysis the range of equivalent plastic strain was estimated from half the increment of the accumulated equivalent plastic strain [562], at the end of the simulation following the full sequence of pulsed heating for 1s and cooling for 60s.

3.4 In silico methods

3.4.1 Geant4

Geant4 is a simulation software which tracks the passage of particles as they interact through matter. It is widely used in medical physics to model sophisticated beam

geometries with using electromagnetic and hadronic physics [563]. The toolkit is written in C++ as an open source object orientated software that finds numerical solutions to macroscopic problems by simulating the interaction of components using random sampling and convergence where analytical techniques would otherwise be too complex. The simulation of particles and interactions are defined by physical processes, particle descriptions and an array of abstract and concrete base classes to support the tracking of particles through material geometries.

User specifications

The user must define region geometry, material compositions, relevant physics, action sequences for each run and for resulting events. Materials are created by defining the material's composition of elements, density, and percentage abundance of each element. For commonly used materials, a NIST database can be imported. A central constants header file was established to store all the parameters associated with the positioning, configuration, naming and geometries of all geometries and output files. Incident particles are defined by a creating a primary particle generator which defines its type, position, direction and energy distribution. Particle properties, including physical processes that they are sensitive to, are defined in a particle table which can be imported. Random number generators can be used to ascribe the initial position and momentum of each incident particle [503]. Physics lists define the physical processes that particles will undergo in simulation for specific particles in a particular energy range. Select physics lists are validated and tested regularly as part of an inventory of lists for specified common use cases. The *G4EmStandardPhysics_option3* physics list [564–567] was chosen on the recommendation of the application user guide for gamma therapy, the agreement with the gammaknife example provided with the installation, and prior benchmarking studies [566, 568–570]. Geant4 uses the Bethe-Heitler-Born approximation to sample bremsstrahlung photons, with cross sections based on the work of Berger and Seltzer [571]. Bremsstrahlung models have been experimentally

verified [572]. However, in simulation the uncertainties in photon cross section data range from 1-2% in the energy range from 5 keV - MeV [496].

Scoring

Volumes can be defined as sensitive to accumulate physical quantities such as flux, dose and charge. These volumes can be parameterised, repeated, re-orientated and re-positioned to construct a sensitive volume of interest [573]. Volumes are represented as logical and physical, where logical volumes represents an element of a certain shape which can contain other volumes, while the physical volume represents the placement of the logical volume with respect to an enclosing 'mother' volume. These volumes can be parameterised to save memory [574].

Step size

In Geant4, there are a number of parameters which affect the step size of a given particle. The *StepFunction* has two parameters *dRoverRange* and *finalRange* where the step size

$$s < max\left\{\rho_R, \alpha_R R + \rho_R\left(1-\alpha_R\right)\left(2-\frac{\rho_R}{R}\right)\right\} \tag{3.14}$$

$\alpha_R \in [0,1]$ is *dRoverRange* (default value 0.2), while ρ_R is *finalRange* (default value 1 mm), and R is the particle range at the start of the step. At high energies this means ($\alpha_R R \gg \rho_R$) so $s < \alpha_R R$, whilst at low energies step size reduces until below *finalRange* and $R < \rho_R$ and a single step occurs [575].

For electrons and positrons, the multiple scattering algorithm in Geant4 uses the Urban model. In addition, with EM Opt3, the *SafetyPlus* step limitation is used. This option ensures a sufficient number of steps occur in thin or low density layers and has been used in similar X-ray therapy contexts [576], with comparable computational efficiency and accuracy [577]. At the start of each track the step size is limited to

$$s < \frac{2d_{geom}}{f_g} \tag{3.15}$$

where f_g is the geometric parameter *GeomFactor* (default value 2.5), and d_{geom} is the distance in the direction of the particle to the next boundary. The algorithm also checks if the particle has entered a new volume and makes sure that steps

$$s < min \left\{ f_r max \left\{ r, \lambda \right\}, f_s s', \frac{d_{geom}}{f_g} \right\} \tag{3.16}$$

where λ is the inverse transport cross section, $f_r \in [0, 1]$ is the *RangeFactor* (default 0.03), f_s is the *SafetyFactor* (default 0.6), and s' is the geometrical safety distance; namely the distance to the closest boundary computed along the initial direction of the step [510, 575, 578]. If the range of an electron is less than the safety distance, the multiple scattering process does not introduce a step limitation [579]. In addition the *G4UserLimits* class can also limit the maximum step size in a volume or region [510]. It is recommended to make the step size within a material 0.3% to 1% of the CSDA range of the electrons in the material [568, 577]. However, it is more efficient to set a small fractional range reduction than to reduce the maximum step size [510].

Cuts

Cuts in Geant4 can be classified into two groups; production and tracking. Production cuts refer to the energy thresholds above which secondary particles are created. The cut is defined using the *SetCut* method, as a range in terms of distance which is converted into an energy for a given material and particle type. In photon simulations processes such as bremsstrahlung and ionisation will use these limits directly. A single cut value in range is usually applied to electrons, positrons, and gammas. The cut value for electrons is usually chosen to be $< 1/3$ of the smallest dimension of the dose scoring region [580].

Parallelisation

Geant4 supports multithreading using multi-core machines, which provides substantially reduces simulation times. The master starts the run and will spawn threads to distribute computations. Worker threads will distribute events between them whilst sharing invariant objects such as definitions of geometry, particle and physics.

Meanwhile objects which control events, tracking, stepping, fields and sensitive detectors are thread-local. After each thread is created, unique seeds will be used to create events. Each thread will have an event loop and an end of local run. Once finished, the data from the threads will be merged in the global run.

Simulations can be run on multicore central processing units (CPU)s, CPU clusters, cloud computing environments and graphical processing units (GPUs). For parallel simulations a computing cluster is widely used with a parallel processing interaface such as the Message Passing Interface (MPI) [581]. Geant4 contains a native interface with MPI libraries to enable further parallelisation via the use of multiple processors. To create a multithreaded application, a multithreaded run manager can be instantiated that controls and configures the tasks into a number of worker threads. Each thread shares core user initialization attributes, whilst owning a private copy of action classes. Events are distributed throughout the workers until the events are complete and data is pooled from all the threads [582]. To reduce the memory consumption further, a user can schedule a single MPI job for each node and use multi-threading to scale across the CPUs and cores available on the node. Each MPI is an exact clone of the master, therefore, to ensure the same seed is not used for each run, the rank of the node accessed from the run manager and can be passed as the seed for each MPI job [583]. Other cloud computing technologies issued by a third party can also be used for parallel processing, where efficiency improvement is similar to that of a CPU cluster [503, 581]. The run manager was setup in multithreaded mode, with the number of threads assigned by the number of cores found on the host machine.

3.4.2 EGSnrc

EGSnrc is a simulation software that performs Monte Carlo simulation of electrons, photons, and positrons through matter. For many circumstances EGSnrc is considered the most efficient code system. EGSnrc contains a number of user-codes that are packaged in the software to calculate specific quantities for specific use cases. The code base is written in Fortran, and applications have been developed

in MORTRAN3 (the native EGSnrc language) or C++. The EGSnrc core contains data about cross sections and materials (PEGS4 with density corrections), and enables particle transport functionality.

User specifications

MORTRAN applications must define particle sources, geometries, I/O functionality, and interactions with the EGSnrc core. Meanwhile egs++ acts as a C++ library of shared classes that can be inherited to define particle sources, geometries and I/O functionality. Standard egs++ applications require in input file containing the geometry, media, source, transport parameters, run control, variance reduction, and other program specific inputs [584]. Material information is contained within the PEGS4 material data set [585]. User codes such as 'cavity' [586] and 'egs_chamber' [587, 588] are based on the egs++ library and can be used to simulate detector response [589]. Recommended physics processes used for bremsstrahlung cross sections and angular sampling were the NRC and Koch-Motz (KM) distribution, as the NRC list is recommended for low ($\sim$ MeV) energy simulations, whilst the KM option is recommended for linac simulations [590].

Scoring

The HOWFAR and HOWNEAR subroutines within the egs++ core are used to determine the nearest distance to a boundary along the particle's trajectory and in any direction respectively. Meanwhile, the AUSGAB subroutine provides the toolset to score quantities when a particle is discarded, or deposits energy locally within a sensitive region or group of regions. For each volume or each medium, a mass is required to enable dose calculation in regions formed from Boolean operations of simple shapes [503], with each volume ascribed a region number and each medium an index. Absorbed dose or energy can be scored in a voxelized geometry and output to an ascii or 3D dose file (.3ddose). Fluence (planar or volumetric) can also be scored for specification energy ranges and volumetric regions over range of field sizes. To score phase spaces, particles entering or leaving a given surface, geometry, or region can be compiled into lists of data detailing each particle's energy, position,

direction and type. The resulting phase space can then be used as an input to other applications as a particle source. Here, the number of times a particle is redistributed (when there is geometric symmetry) or recycled, can be specified. The number of times the full phase space analysis will be restarted can also be specified [591].

Step size

The standard electron step algorithm in EGSnrc inputs a maximum fractional energy loss per step (ESTEPE) (default 0.25), and maximum scattering angle (ximax) (default 0.5). The transport algorithm by default subdivides the step into two sub-steps where it samples multiple elastic scattering angles. To move across boundaries an 'exact' boundary crossing algorithm (BCA) is employed, which employs single scattering near a boundary interface within a perpendicular distance from the boundary surface called the skin depth (default 3 — specified in terms of elastic mean free paths).

Cuts

Minimum thresholds can be set for the production of secondary electrons (AE), and secondary photons (AP). Above, or below these thresholds, interactions are either regarded as discrete and evaluated individually, or grouped as part of a continuous energy loss mechanism respectively. Likewise, the equivalent maximum thresholds can also limit the maximum energy of produced particles (UE & UP). In addition, transport cut-offs are defined for electrons (ECUT) and photons (PCUT), these defined the minimum energy below which the particle transport is stopped and particle energy is deposited locally. Here the rule of thumb is that ECUT must be $<1/3$ of the geometric dimension of interest [590].

Parallelisation

Parallel processing is afforded by the egs-parallel utility script which runs the job in multiple processes in parallel. Results are combined on completion of the final job.

3.4.3 Advanced Research Computing service (ARC)

The Advanced Research Computing (ARC) service provides parallelisation of computer tasks for software including python, MATLAB, Abaqus, EGSnrc and Geant4. The arc cluster provides CPU compute nodes. Per node it uses 2×Intel Platinum 8628, Cascade Lake, 2.90 GHz CPUs which overall provide 48 CPU cores and 380 GB of memory. The cluster can be logged into via an ssh connection within the University network range. Submission scripts can be developed in bash to request modules, software, partitioning, and resources for a specific application. The submission script can be submitted for allocation using the SLURM resource manager which can monitor and report the state of the system and jobs to the user. Output can be obtained by navigating to defined working directories and secure copying (scp) or remote file copying (rsync) to a local computer [592].

4

Megavoltage photon FLASH for preclinical experiments

Contents

4.1 Introduction

In this chapter, we present an approach that allows the use of a conventional linac to deliver FLASH photon beams suitable for preclinical research. Most clinical photon sources are able to deliver a flattening-filter-free (FFF) average dose rate of ∼0.2 Gy/s (12 Gy/min) at a source-to-surface distance (SSD) of ∼1 m [453]. Assuming the inverse-square law holds (despite a linac source not being a point

source), it can be estimated that an average dose rate of 80 Gy/s can be obtained at an SSD of 5 cm, allowing FLASH dose rates to be reached. However, the treatment area is also, of course, reduced. This work shows that such a reduction of SSD can be exploited for preclinical irradiations, where field sizes are usually small. Also highlighted here is a suitable tungsten target that can be used as an 'add-on' to linacs used for preclinical FLASH irradiations using electrons.

4.2 Methods

4.2.1 Target construction

A hollow cylindrical aluminium tube was placed directly downstream of the exit window and varying numbers of tungsten discs were placed as a bremsstrahlung target at the end of the tube, held in place by two retaining rings. The beam diameter at target location is ∼10 mm (FWHM) (Figure A.2). Two arrangements were investigated, as outlined in Figure 4.1.

The first arrangement uses a copper disc some distance away from the target (Figure 4.1A) and generates a cone of essentially uncollimated photons, while the second arrangement collimates the photon beam (Figure 4.1B) and uses a copper disc placed close to the tungsten discs. The photon collimator was fabricated from a 53 mm long 316 stainless-steel tube with 1060 aluminium alloy ends, allowing for a 50 mm thick layer of Wood's metal [593] to fill the remaining volume, surrounding the 14 mm diameter central aperture. The aluminium tube housing with the (in-air target) tungsten discs, the collimator, and copper disk are easily removable, which enables a fully reversible (and interchangeable) setup for preclinical photon and electron beam arrangements.

4.2.2 Target thickness

Thin tungsten discs (thickness $\approx 55\ \mu m$) were stacked to enable a range of target thicknesses. Charge output measurements were performed with an Advanced Markus® ionisation chamber (AMC, model 34045, PTW-Freiburg, Freiburg, Germany, connected to an electrometer (UNIDOS Webline, PTW-Freiburg, Freiburg,

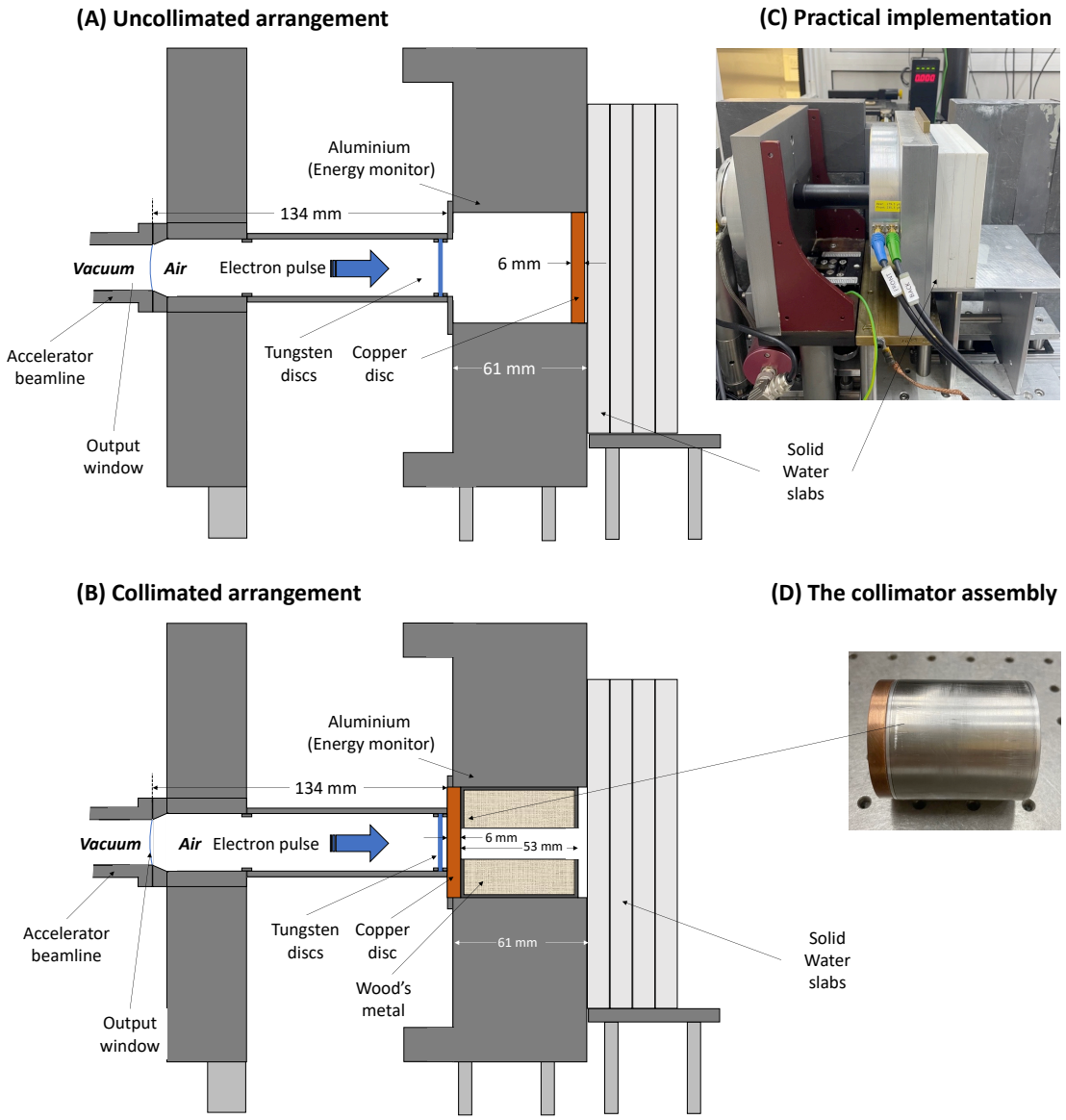

Figure 4.1: Uncollimated (A) and collimated (B) bremsstrahlung target assemblies, drawn to scale, showing the electron beam impacting a series of tungsten discs. The large aluminium structure is an electron beam energy monitor as described in [530]; it is not used when the target materials are inserted but forms a convenient support structure. Solid water slabs (150×150 mm^2) cross-section, of varying thicknesses are placed downstream (SSD $\geq$ 64 mm) and enable EBT-XD film and Advanced Markus® ionisation chamber charge output measurements to be performed at any given depth in the solid water. In the case of the collimated arrangement, a 14 mm aperture allows passage of photons. Panel (C): practical arrangement of the target assembly. Panel (D): Image of the collimator.

Germany, and operated at a bias voltage of +300 V), at the surface (SSD of 64 mm) and at various depth in solid water (150 × 150 mm^2 RW3 slabs of 1, 2, 5, and, 10 mm thicknesses from PTW-Freiburg) in the uncollimated photon setup (Figure 4.1B), to experimentally determine the photon output variation with tungsten thickness, as well as the thickness required to remove primary electrons.

4.2.3 Measurements of dose rates, beam profiles and depth-dose curves

Gafchromic EBT-XD films were used for measurements of average dose rates, beam profiles and for generation of percentage depth-dose (PDD) curves. Average dose rate measurements were performed with 35 × 35 mm^2 films placed on the surface of the solid water phantom at various SSDs, in both the photon and electron beams (Figure A.3). The average dose rates were determined within a 6.6 mm (25 pixel) diameter region of interest (ROI). For depth-dose measurements with electrons (Figure A.4) and photons (Figure 4.6), a square 5 × 5 mm^2 (19 × 19 pixels) area ROI was analysed. For each depth-dose measurement, the total thickness of solid water was such that at least 5 cm of solid water backscatter material was present (to closely link to TRS-398 [454] and TRS-483 [442] protocols). Three repeated film measurements were averaged for average dose rate and depth-dose measurements. Beam profiles were analysed using 80 × 80 mm^2 films by averaging along a 5 mm (19 pixel) line perpendicular to the profile axis, for each pixel traversed across the profile axis. For vertical and horizontal measurements, two repeated measurements were averaged. Two unirradiated background films were consistently used for all films to convert the optical density value to dose.

4.3 Results

4.3.1 Target thickness

The charge output was found to be largely independent of target thickness (Figure 4.2), within the investigated range (0.11 – 0.99 mm), with a 6 mm copper backer in place downstream to remove transmitted primary electrons (see equation

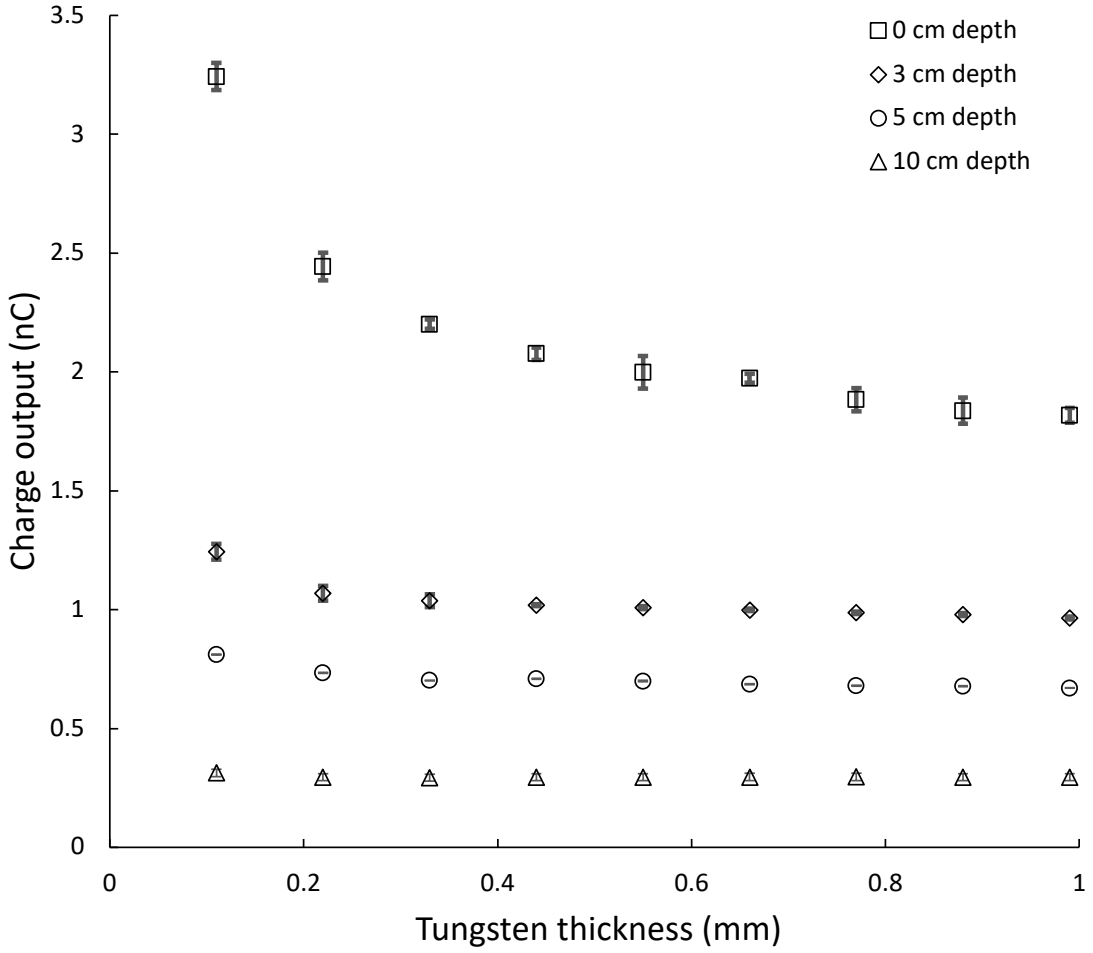

Figure 4.2: Charge output measured with the Advanced Markus® ionisation chamber positioned at various depth in solid water vs. Tungsten thickness using the uncollimated photon setup (Figure 4.1A) at an SSD of 64 mm. Markers and error bars represent the mean value and standard deviation, respectively, of five measurements.

2.24 and supplementary figure A.9). However, there was a pronounced increase at the surface of the solid water for small foil thicknesses, which was most likely due to contribution from the low energy photon fluence to the collected charge (Figure A.6). This effect became small for target thicknesses $\geq$ 0.3 mm and negligible at depths beyond the CSDA range of 6 MeV electrons in water $\sim$3 cm. The contribution of low energy photon components was reduced with thicker foils, and with collimation (see Figures A.6 to A.10). Based on these results, a tungsten target thickness of 0.55 mm was found to be a suitable compromise and was therefore used in all subsequent measurements.

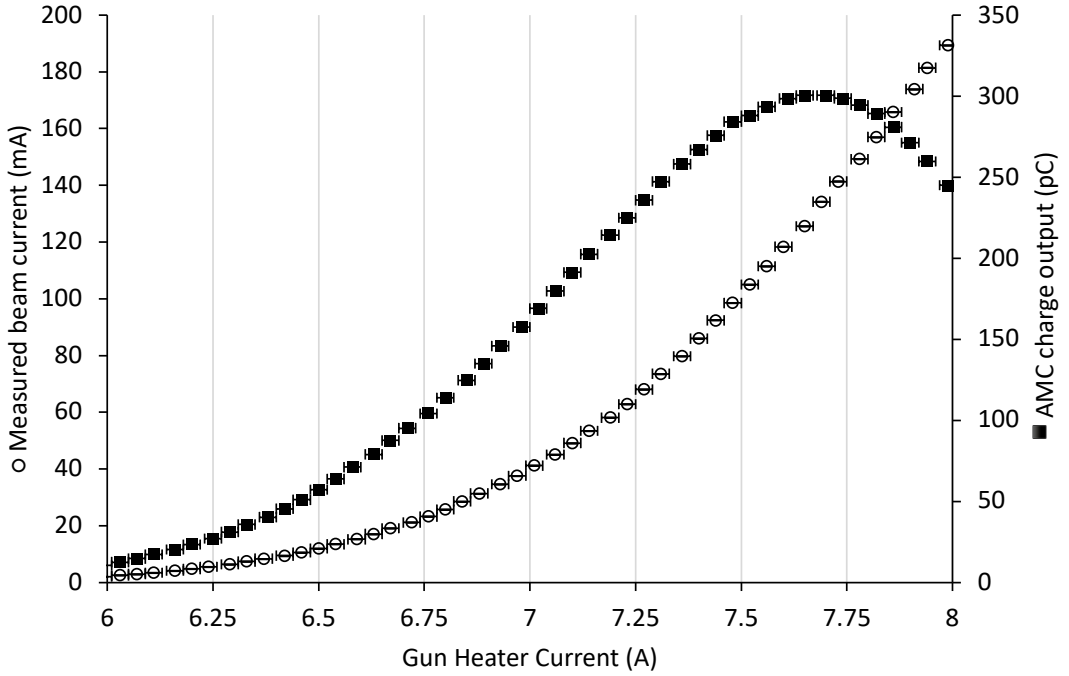

Figure 4.3: Beam currents measured with a beam collection device placed in the centre of the electron beam path (circles), and charge outputs (squares) from the bremsstrahlung target measured with the Advanced Markus® ionisation chamber (AMC) as a function of gun heater current using the uncollimated photon setup (Figure 4.1A) at an SSD of 64 mm. A 30-pulse delivery was used, with the AMC placed at 10 cm depth in solid water in the centre of the beam axis. Error bars represent the standard deviation of five measurements.

4.3.2 Photon output variation with gun heater current

Measurements with the beam collection device placed in the centre of the beam (replacing the bremsstrahlung target) showed how the beam current increased with increasing gun heater current (Figure 4.3).

However, because beam loading caused a reduced beam energy at high beam currents and associated reduction in electron penetration (see appendices Figures A.4 and A.5), photon charge output was found to be maximized at a gun heater current in the range of 7.56 - 7.78 A (within 2% of its maximum value in this range). Using the lowest gun heater current value (7.56 A) in this range, electron PDD measurements (at an SSD[1] of 72 cm) show that the produced electron beam has therapeutic (R_{80}) and practical (R_P) ranges of around 20 mm, and 30 mm, respectively (20.4 mm

[1]defined for electrons as the distance from the beam exit window to the Solid Water surface

and 29.9 mm in Figure A.4). These could be considered as typical values for a standard clinical 6 MeV electron beam, though these beams use electron applicators and PDDs are commonly measured at an SSD of 100 cm. Therefore, a gun heater current value of 7.56 A was chosen for all subsequent experiment with photons.

4.3.3 Photon Beam characteristics

A square-law dependence would be expected from point-like radiation sources. Our electron beam diameter is 10 mm at the target, but we still see a good agreement with the inverse square law with an R^2 value of 0.99 (Figure 4.4).

Beam profile measurements show that without collimation the beam profile is similar to an FFF beam (Figure 4.5A), with a fairly flat ($\geq$97% of the maximum dose) central 10 mm diameter section and 90% dose relative to the maximum of the profile within 15 mm diameter of the circular beam.

With collimation, the surface dose rate increases slightly and the flatness is similar, with 90% dose relative to the maximum of the profile within 12 mm diameter of the circular beam. At larger distances from the beam centre, the resulting beam penumbra from the collimation is evident (Figure 4.5B).
Depth-dose measurements showed an increased dose rate at the surface of the solid water phantom from scattered photons (Figure 4.6), particularly for the collimated beam, where a decrease in dose rate occurs with depth mainly due to the inverse square law (Figure 4.4), as the SSD is short (64 mm).

For a long SSD of 85 cm, the measured depth-dose curve is similar to depth-dose curves from clinical 6 MV (nominal) beams from a Varian TrueBeam [491] at 100 cm SSD, with or without flattening filter (Figure 4.7A). These depth-dose curves were further characterized using the ratio of doses at depths of 20 and 10 cm ($D_{20,10}$) in solid water, to show further agreement with published beam data (Figure 4.7B).

4.4 Discussion

Photon FLASH radiotherapy has shown potential with kilovoltage (kV) continuous (non-pulsed) beams [103, 133]. Unfortunately, such beams have large surface average

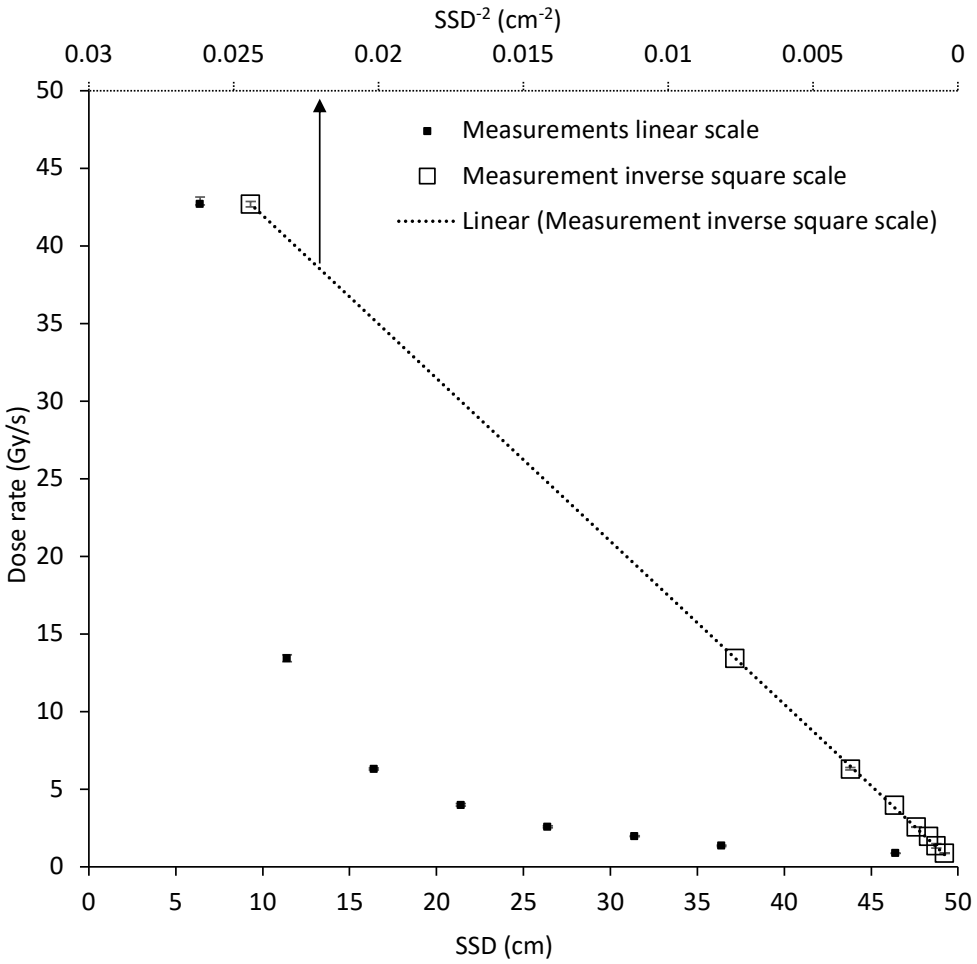

Figure 4.4: Photon surface average dose rate at different source-to-surface distances (SSDs), measured with EBT-XD film on the surface of a 150 × 150 × 150 mm^3 solid water phantom. The markers indicate the mean value of 3 repeated measurements, with error bars indicating the standard deviation. The additional horizontal axis represents the inverse square of the SSD, with a linear fit applied to the data points with an R^2 of 0.99.

dose rates which drop steeply from the surface and enable delivery of FLASH dose rates at depths of only up to a few mm. To reach ultra-high average dose rates, the SSD is short which limits beam size e.g., with a uniform beam over a ∼1 cm diameter, for an SSD of ∼3.5 cm [216]. Several preclinical studies have also indicated the potential of photon FLASH radiotherapy to spare normal tissue at MV energies [103, 119, 165, 233]. Photons at these energies can target deep seated tumours by depositing energy at larger depths, with less surface dose. The average dose rates and distributions from kV and MV photon beams could also be improved using

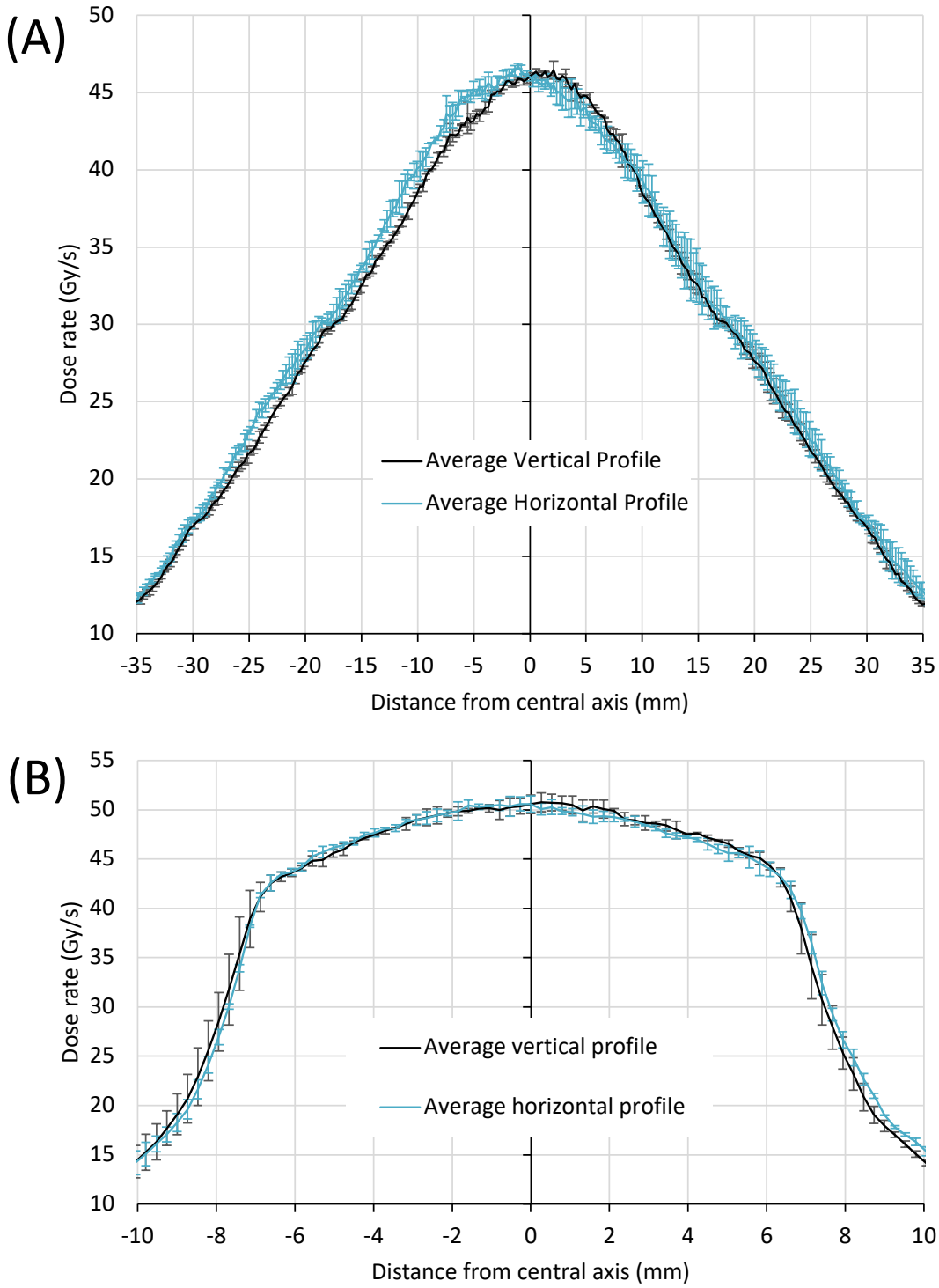

Figure 4.5: Beam profiles measured with EBT-XD film on the surface of a 150 × 150 × 150 mm^3 solid water phantom, at 0 mm depth for uncollimated beam (A) and with (B) 14 mm collimated beam. The markers indicate the mean value of 3 repeated measurements, with error bars indicating the standard deviation.

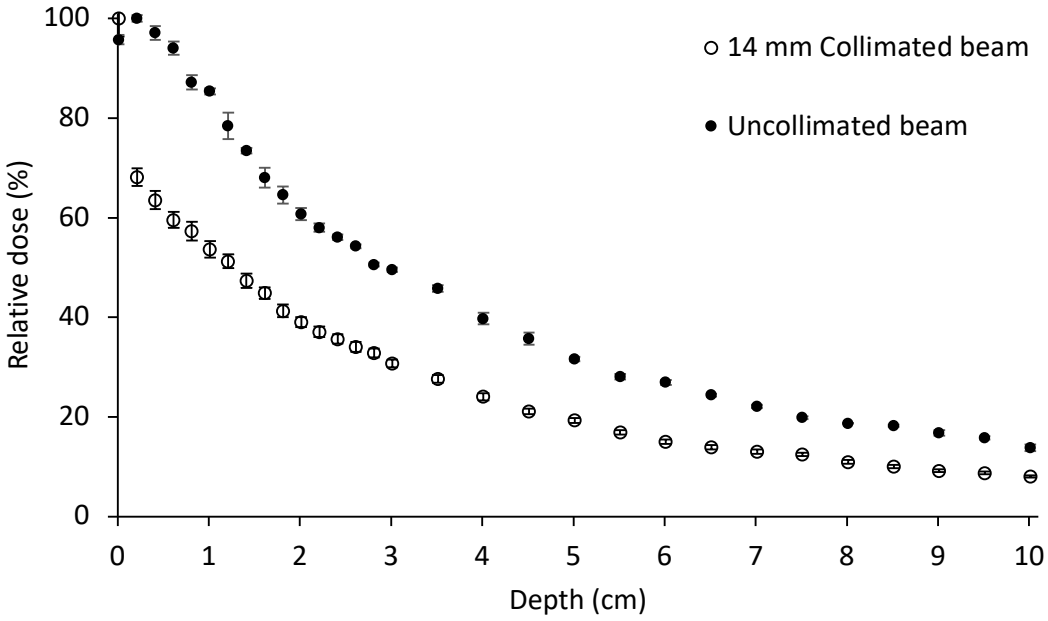

Figure 4.6: Depth-dose curves measured with EBT-XD film averaged over a square 5 $\times$ 5 mm^2 (19 $\times$ 19 pixels) area ROI at various depths in a 150 $\times$ 150 $\times$ 150 mm^3 solid water phantom, for the uncollimated beam as well as the 14 mm collimated beam at a source-to-surface distance (SSD) of 64 mm. The markers indicate the mean value of 3 repeated measurements, with error bars indicating the standard deviation.

multiple beams from different directions simultaneously [103, 225]. At the Chengdu Terahertz Free Electron Laser facility (CTFEL), a large superconducting linac has been shown to produce 6 MeV - 8 MeV electrons with average currents up to 10 mA, enabling photon average dose rates of >1000 Gy/s, albeit with a significantly different pulse structure (no macropulses) than clinical linacs. Shi et al. 2022 [111] used the CTFEL for preclinical FLASH studies with 5 ps micro pulses at 54 MHz, with instantaneous photon dose rates of $>1.8 \times 10^5$ Gy/s, and an average dose rate between 110 Gy/s - 120 Gy/s [111]. Here, FLASH normal tissue sparing effects were seen in mice following abdominal irradiation, and in intestinal crypt organoid irradiations. However, another facility with beam parameters such as total dose, pulse structure, field size and beam energy different than the CTFEL beam was used for the conventional average dose rate irradiations. This makes it difficult to draw any strong conclusions from these preclinical experiments. The work described in this chapter enables delivery of pulsed beams of varying ultra-high average dose rates that are appropriate for routine preclinical FLASH experiments with MV

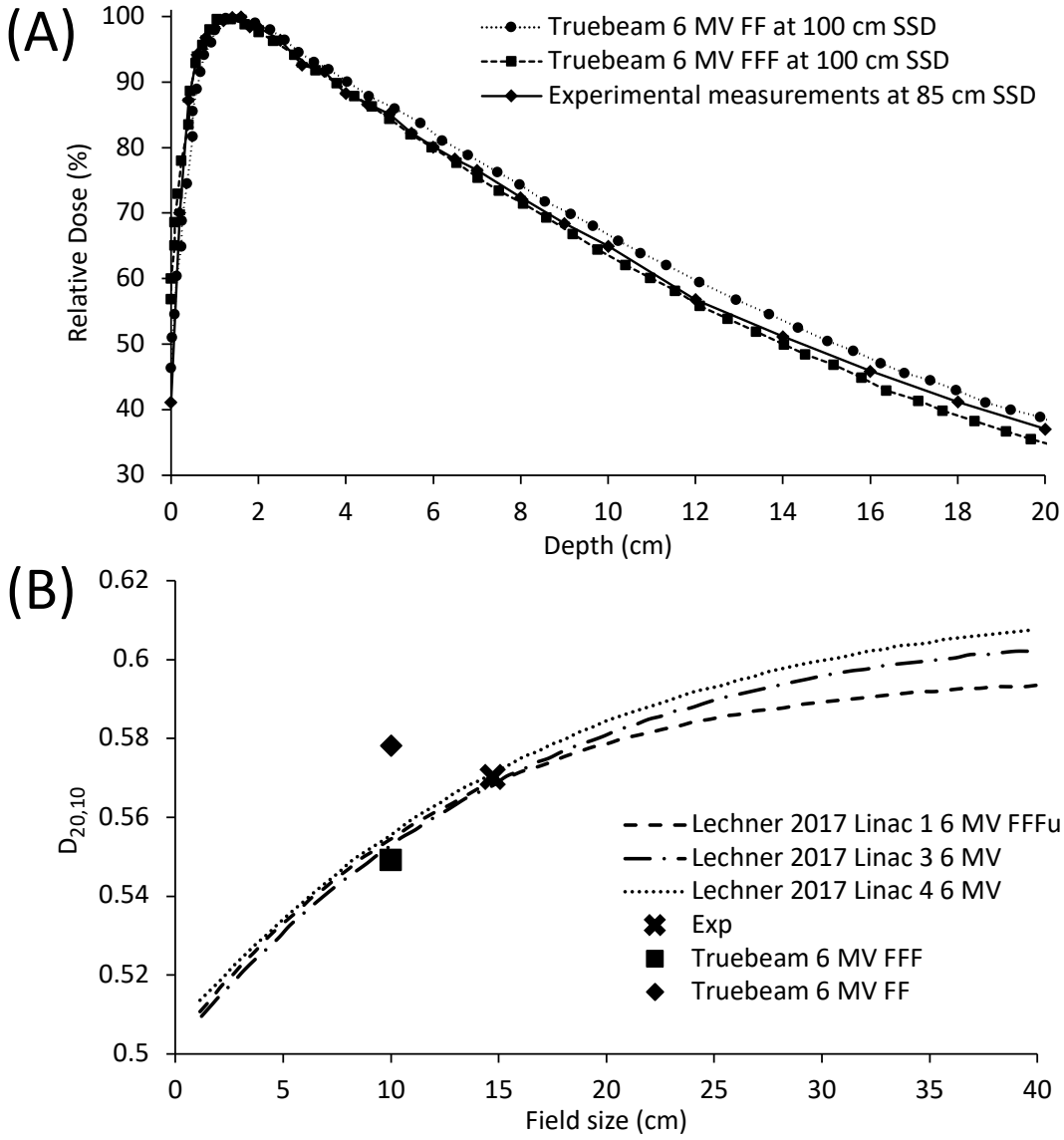

Figure 4.7: (A) Percentage depth-dose curves; measured with EBT-XD film at various depths in a 150 × 150 × 250 mm^3 solid water phantom, at a source-to-surface distance (SSD) of 85 cm, for the 14 mm collimated beam, which expands to 16.3 cm FWHM at the surface of the phantom. The markers indicate the mean value of 3 repeated measurements, with error bars indicating the standard deviation. Also included are published curves for 10×10 cm^2 fields from a 6 MV TrueBeam at an SSD of 100 cm, with (FF) and without flattening filter (FFF) [491].
(B) Published ratio of doses at depths of 20 and 10 cm ($D_{20,10}$) [486, 491] for 6 MV FFF beams with various field sizes, with points added from measured and published doses in (A). The measurement field size was multiplied by a correction factor of 0.9 to convert from a circular to a square field size to be 14.7 cm, with a $D_{20,10}$ value of 0.57.

photons. Albeit, on the low end of the average dose rates that have exhibited a FLASH effect (>40 Gy/s and >30 Gy/s from surface to ∼8 mm depth, for the uncollimated and collimated beam respectively) with similar beam parameters [59]. This system also has the advantage of being able to perform preclinical FLASH experiments with varying average dose rates from ultra-high down to conventional (∼0.1 Gy/s), by varying the pulse repetition rate and/or macropulse amplitude (by adjusting the gun heater current while slightly (de)tuning the RF to maintain the beam energy [530]), with either MV photons or MeV electron beams. With our system, a direct comparison between these modalities (with identical pulse structures) is possible, which is invaluable to understand the applicability of previous MeV electron preclinical FLASH data to clinical MV photon beams — arguably the modality of interest for clinical translation of FLASH radiotherapy. Meanwhile, the limited field size (∼12-15 mm diameter) is akin to the kV-systems described above, but still useful for a range of biological assays involving thin samples to avoid a large average dose rate falloff with depth. We have described easily reversible modifications using an in-air target system that can be applied to linacs with similar beam parameters, e.g., clinical linacs modified for electron FLASH delivery. For accuracy, repeatability and reproducibility, we followed the recommendations of dosimetric reporting standards [220, 594–596], where we obtained results using reproducible dosimetric procedures based on primary dosimetric standards with a fully defined experimental setup. Here we stated the average dose rate, distance from source, field size at surface, filtering systems, flatness, shape, and symmetry with high resolution, with low uncertainties for repeated measurements. The guidance from TG-51 [480], TRS-398 [454], and TRS-483 [442] were implemented in so far as their scope pertained in preclinical contexts; where field size and SSD are reduced relative to clinical beams. Furthermore, we highlight our beam pulse structure as it is likely to impact biological outcome in preclinical FLASH studies [190]. The dose rate efficiency of our beam is ∼0.05% (comparing average dose rates in Figures 4.5 and Figure A.3). To increase this efficiency, the photon dose rate may be increased slightly by decreasing the copper thickness, e.g., from 6 to 3 mm. However, this

would increase the magnitude of contaminant electron dose (Figure A.11). Our current linac is limited by the peak power generated by our 2 MW magnetron; other linacs, fitted with higher peak/average power radiofrequency sources or with more efficient accelerating waveguide designs, would likely allow for photon beams to be produced with even higher dose rates. Photon targets optimized through simulation by Geant4 [597], FLUKA [598], MCNP6 [439], and other techniques [599] for use with 6 MeV electron beams have been published. Such targets are intended for continuous operation rather than short operation times associated with FLASH irradiations. Nevertheless, these studies show that a combination of materials (such as tungsten and copper) are generally superior to a single-material target. It is noted that targets for continuous work in electron linear accelerators are subjected to high-frequency and intense thermal shocks. Elevated temperatures in the target may lead to target re-crystallization, fatigue cracking, creep and vaporization [600]. Tungsten target thicknesses for optimal photon production have often been found to be $\sim$0.3 R_{CSDA} [427, 486, 597, 598, 601, 602]. In this work we used an experimental approach and found it straightforward to reach an average dose rate appropriate for preclinical FLASH work. Further target optimization is the subject of ongoing work.

5

Quantifying the FLASH effect and its dependence on average dose rate *in vivo* for 6 MeV electron and 6 MV photon beams

Contents

5.1 Introduction

Most preclinical FLASH studies have used electron or proton beams [61]. However, the vast majority of all radiotherapy treatments utilise MV photon beams [103]. Therefore, for the future clinical translation of FLASH radiotherapy, it is important

to also investigate the FLASH effect for MV photon beams. However, it is challenging to reach the ultra-high dose rates needed for FLASH with MV photon beams because of the relatively poor efficiency of production of bremsstrahlung photons [103]. Using our previous work, with a thin in-air tungsten bremsstrahlung target at a reduced SSD in the preclinical 6 MeV electron FLASH beamline [530], we can investigate the utility of 6 MV photon beams in preclinical FLASH studies. In this chapter, we investigate how the FLASH effect varies with average dose rate for radiation-induced skin toxicity in mice, following irradiation from 6 MeV electron and 6 MV photon beams.

5.2 Methods

5.2.1 Collimation

To obtain an electron field for hemi-thorax irradiation, a 6 mm thick brass collimator plate with a central square 20×20 mm^2 aperture was placed in the collimator assembly. Meanwhile, for photon beam irradiations, beam collimation was achieved using a 50 mm thick Wood's metal layer, with a 17×17, or 20×20 mm^2 central aperture (Figure A.13 in supplementary material). The outer diameter of the collimator enabled it to be housed within the central (50 mm diameter) aperture of the energy monitor.

5.2.2 Dose prescription

Mice were positioned such that the collimator shielding only enabled exposure of the right half of the thorax. A single dose of 20, 25 or 30 Gy was prescribed and verified with Gafchromic EBT-XD film measurements before and after mice irradiation, at the surface of the mouse phantom (Figure A.14 in supplementary material). For photon deliveries, a 20 × 20 mm^2 Wood's metal collimator was used for the 20 Gy irradiations, whereas the 17 × 17 mm^2 collimator was used for 25 Gy and 30 Gy irradiations.

Additional online dosimetry was performed with an Advanced Markus® ionisation chamber at 1 mm depth in solid water (150×150×21 mm^3 RW3 slabs, PTW-Freiburg

GmbH, Freiburg, Germany). The beam energy was maintained for all dose rates by slight detuning of the radiofrequency source and online monitoring of the resulting beam energy [530]. Variations in dose rate were achieved by changing the pulse amplitude (by adjusting gun heater current) and the repetition rate of the 3.4 μs wide (macro-) pulses delivered (Tables A.3 to A.6).

5.2.3 Skin toxicity

Female C57BL/6 mice (aged 8-10 weeks at time of irradiation) were purchased from Charles Rivers UK Ltd. An ordinal scale was used to score skin toxicity (Figure 5.3A): a score of 0 = normal; 1 = depigmentation; 2 = alopecia (± depigmentation); 3 = erythema (± alopecia and depigmentation); 4 = dry desquamation; 5 = moist desquamation-ulceration. All mice were monitored every other day for 8 weeks post irradiation for development of skin toxicity within the radiation field. Mice noted to develop cutaneous lesions were monitored daily. Mice whose cutaneous lesions progressed and met skin toxicity euthanasia criteria (moist desquamation-ulceration or most desquamation that did not improve after 10 days) were euthanised via cardiac exsanguination at any point the criteria were met during the study. All other mice were euthanised at the 8-week timepoint.

5.2.4 Statistical analysis

For skin radiotoxicity emergence, one-way ANOVA with Šídák's multiple comparisons test was used to analyse the data, with results presented as mean ± standard error of the mean. Mann-Whitney test was used to compare the distribution of skin toxicity scoring. The Kaplan-Meier method was performed to compare the median survival using Log-Rank test.

5.3 Results

5.3.1 Dosimetric measurements with collimators

Measurements of the full width at half maxima (FWHM) were consistent at FLASH and CONV dose rates (Figure 5.1). For photon irradiations with the 17 × 17 mm^2 and 20 × 20 mm^2 collimators, a greater broadening with depth was observed compared to electron irradiations with the 20 × 20 mm^2 collimator. For these electron irradiations, the FWHM remained nearly constant up to ∼10 mm depth, gradually increasing toward the end of its range (∼30 mm). Meanwhile, depth-dose measurements showed consistency for all dose rates, with similar photon curves using both collimator sizes (Figure 5.2).

5.3.2 Preclinical Experiments

For 20 Gy photon beam hemi-thorax irradiations, a delay in onset of radiation-induced skin toxicity with increasing average dose rates was seen from 0.7 Gy/s, with a significant delay seen from 2 Gy/s, with a further delay at higher dose rates (Figure 5.3B). Similar results with delay in onset of toxicity were seen for 25 and 30 Gy irradiations (significant for 30 Gy/s and ≥3 Gy/s, for 25 and 30 Gy, respectively), albeit with a shorter delay with increased doses (Figure 5.3C-D). While mice irradiated with 20 Gy could be kept alive until the 8-week time point post irradiation, this was not the case for those that received 25 and 30 Gy. At this time, the severity of the skin toxicity showed a trend to be reduced with increasing dose rate (Figure 5.3E-G). Significant sparing was seen for ≥3 Gy/s and ≥1 Gy/s for 25 and 30 Gy irradiation, respectively.

For 30 Gy electron beam hemi-thorax irradiations, a trend towards a delay in onset of skin toxicity was seen for increased average dose rates, and a significant delay seen from 10 Gy/s (Figure 5.4A).

The majority of mice in this cohort required euthanasia due to the severity of their skin toxicity prior to the 8-week time point post irradiation. Increasing average

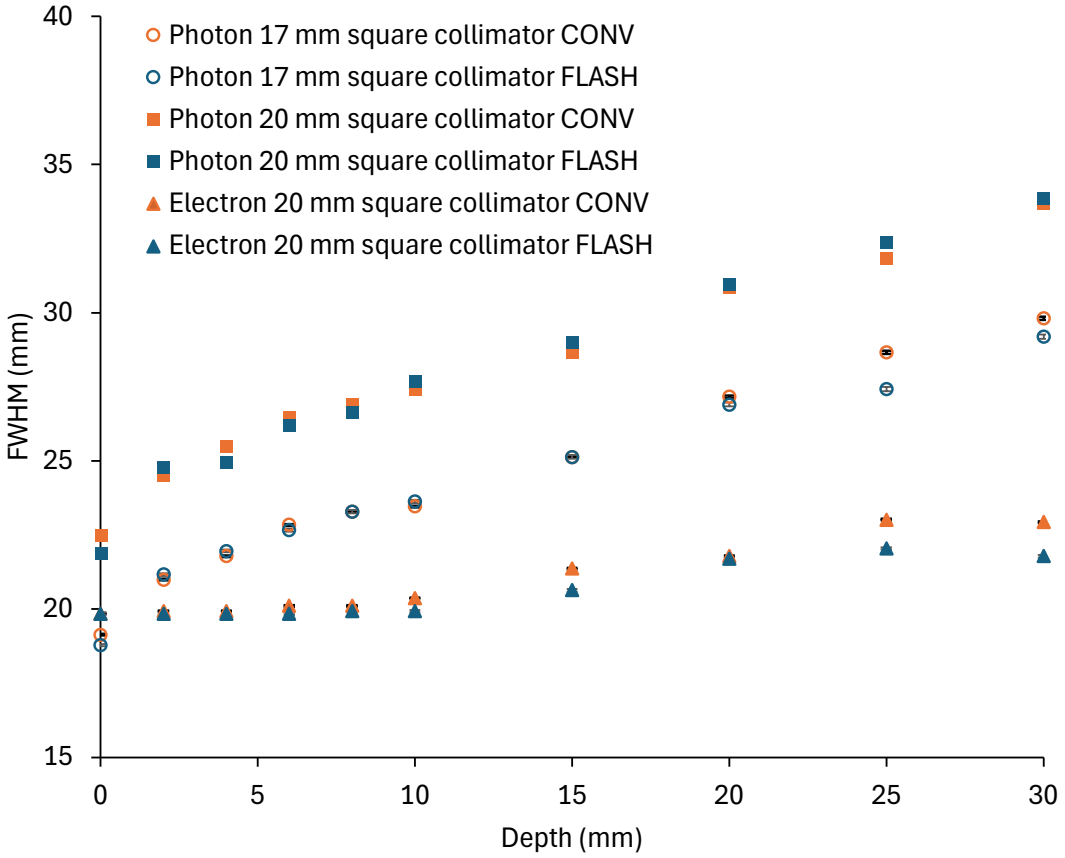

Figure 5.1: Full width at half maximum (FWHM) measurements with EBT-XD film at various depths in a 150×150×150 mm^3 solid water phantom (RW3), positioned immediately downstream of the collimator (Figure A.12). Irradiations were performed for electrons, using a 6 mm thick brass collimator with a 20×20 mm^2 square aperture (triangles), and with photons (Figure A.13), using a 6 mm thick copper disk, and 50 mm thick Wood's metal layer with a 17×17 mm^2 square aperture (circles) or a 20×20 mm^2 square aperture (squares). A 1×45 mm^2 (4×170 pixels) profile on the films analysed. For FLASH (blue markers) irradiations, 6 and 200 pulses, at a pulse repetition rate of 300 Hz, were used for electron and photon measurements, respectively. For CONV (orange markers), ∼2500 pulses were used at a pulse repetition rate of 25 Hz for both electron and photon measurements. The markers indicate the mean value of 3 repeated measurements, with error bars (often within markers) indicating the standard deviation.

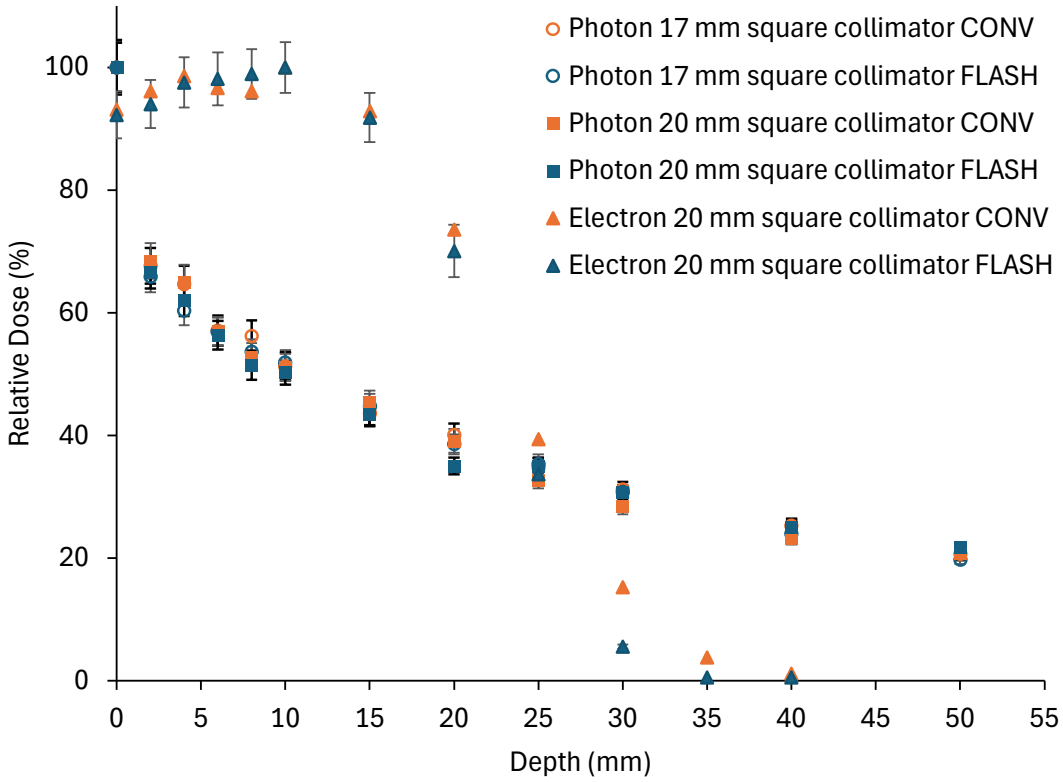

Figure 5.2: Depth-dose curves measurements with EBT-XD film at various depths in a 150×150×150 mm^3 solid water phantom positioned immediately downstream of the collimator (Figure A.12). Irradiations were performed for electrons, using a 6 mm thick brass collimator with a 20×20 mm^2 square aperture (triangles), and with photons (Figure A.13), using a 6 mm thick copper disk, and 50 mm thick Wood's metal layer with a 17×17 mm^2 square aperture (circles) or a 20×20 mm^2 square aperture (squares). For FLASH (blue markers) irradiations, 6 and 200 pulses, at a pulse repetition rate of 300 Hz, were used for electron and photon measurements, respectively. For CONV (orange markers), ∼2500 pulses were used at a pulse repetition rate of 25 Hz for both electron and photon measurements. A 5×5 mm^2 (19×19 pixels) square in the centre of the films was analysed. The markers indicate the mean value of 3 repeated measurements, with error bars indicating the standard deviation.

dose rates resulted in significantly ($p<0.01$) better survival (Figure 5.4B), with all mice irradiated at the highest average dose rate of 1,800 Gy/s surviving until the 8-week time point. The severity of the skin toxicity was reduced with increased average dose rate, with significant sparing seen at 1,800 Gy/s (Figure 5.4C). By matching the lowest and highest photon dose rates with our electron dose rates, while also evaluating a much higher electron dose rate, we were able to assess what the effect of an increased dose rate beyond the current capabilities of our photon

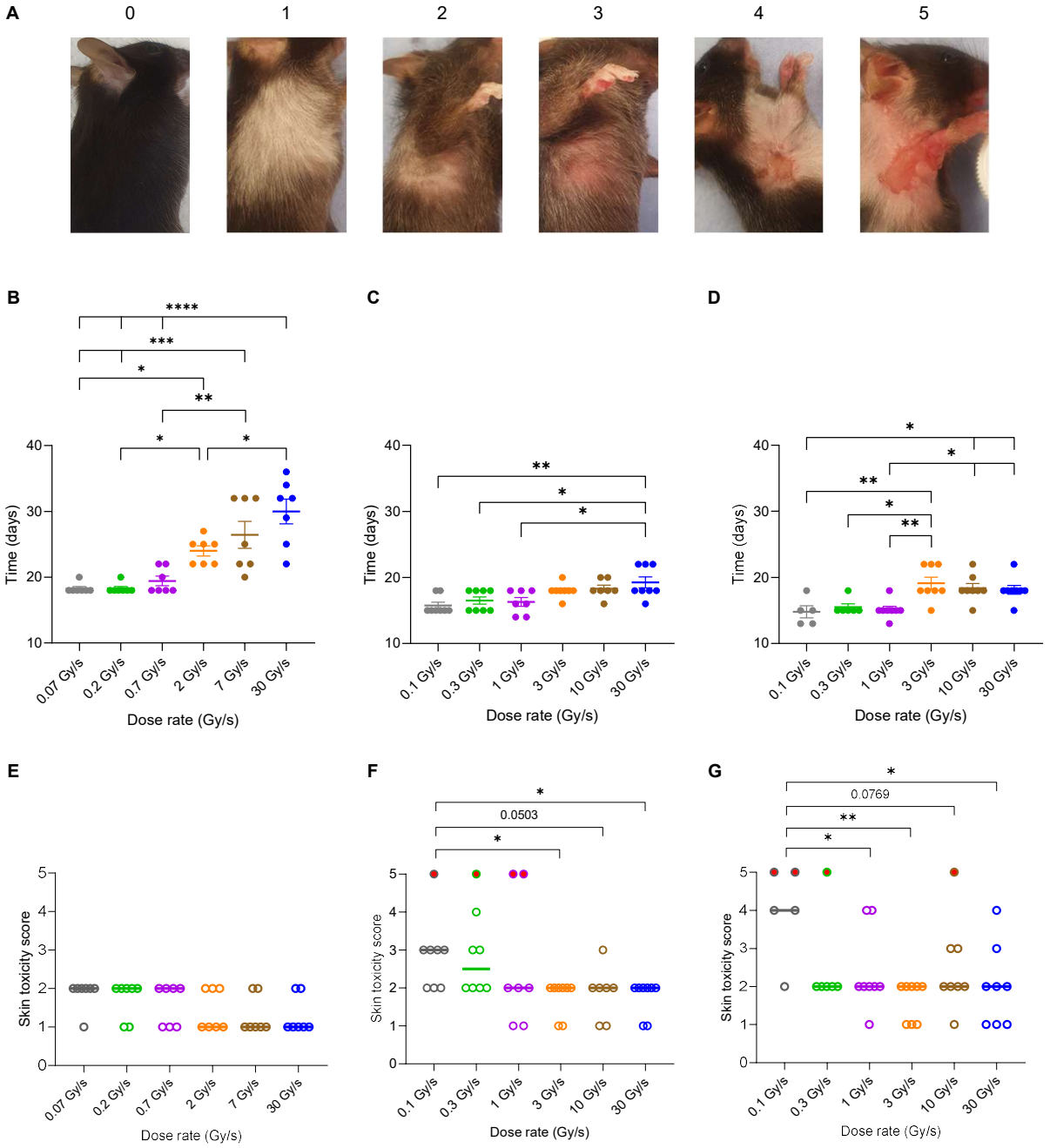

Figure 5.3: Increasing the average dose rate of photon beam irradiations delays the radiotoxicity emergence and reduces skin toxicity. (A) Skin toxicity scoring scale with representative pictures. (B-D) Skin radiotoxicity emergence. Right lung of mice was irradiated to a single dose of 20 Gy (B), 25 Gy (C) or 30 Gy (D) at different dose rates and mice were monitored every other day to determine the time of skin toxicity onset. Mean values are shown with error bars representing ± SEM. (E-G) Macroscopic skin lesions scoring at 8 weeks post irradiation, based on the skin toxicity scoring scale, after 20 Gy (E), 25 Gy (F) or 30 Gy (G) photon beam irradiation. Bars represent the median and red dots indicate animals that had to be euthanised for meeting skin toxicity euthanasia criteria (moist desquamation-ulceration). * $p<0.05$; ** $p<0.01$; *** $p<0.001$; **** $p<0.0001$.

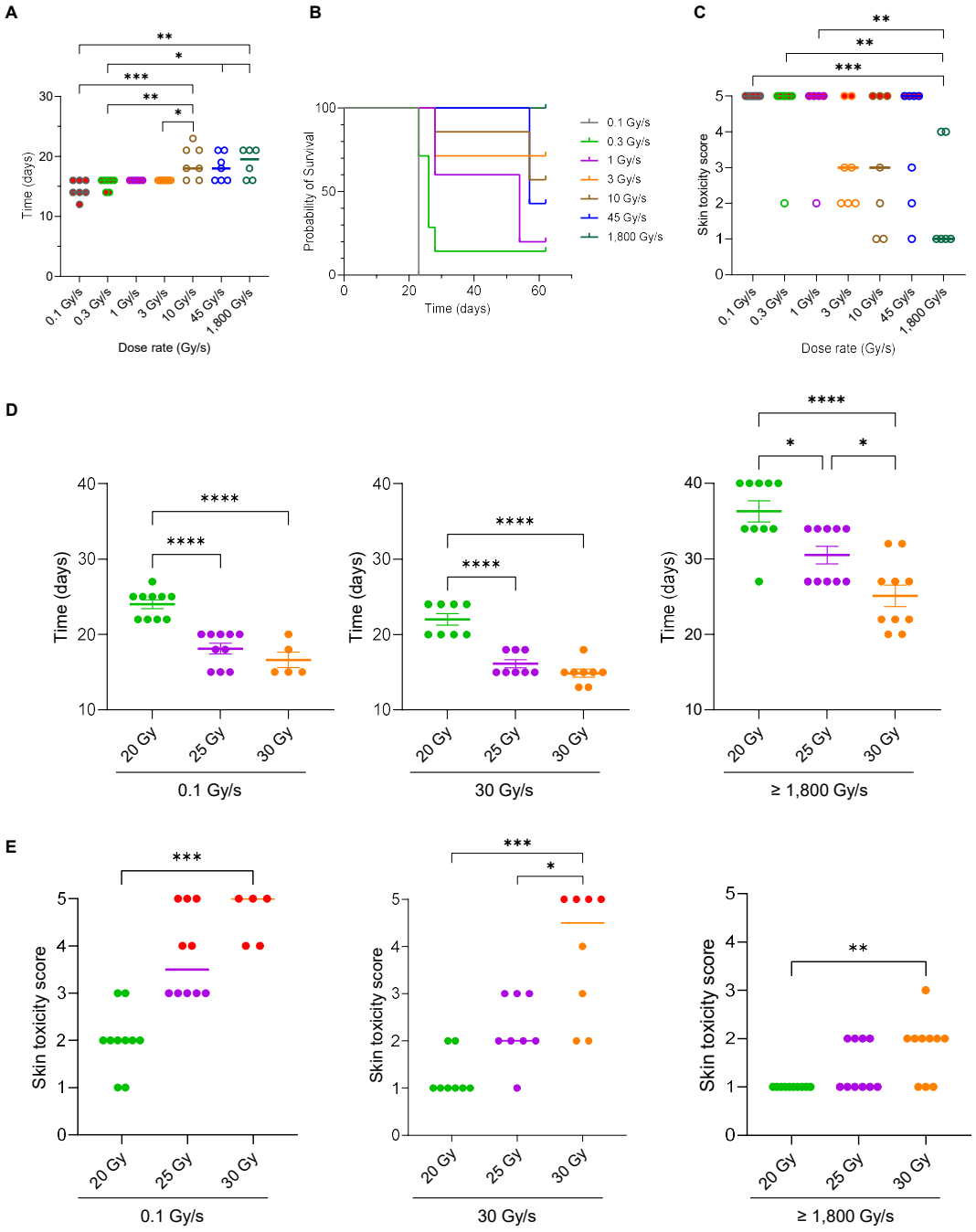

Figure 5.4: Increasing the average dose rate of electron beam irradiations delays the radiotoxicity emergence and reduces skin toxicity. (A) Skin radiotoxicity emergence. Right lung of mice was irradiated with electrons to a single dose of 30 Gy at different dose rates and mice were monitored every other day to determine the time of skin toxicity onset. Mean values are shown with error bars representing ± SEM. (B) Kaplan-Meier survival curves for 30 Gy irradiation at different dose rates. (C) Macroscopic skin lesions scoring at 8 weeks post irradiation, based on the skin toxicity scoring scale, for 30 Gy irradiation at different dose rates. A separate experiment evaluating skin radiotoxicity emergence (D) and macroscopic skin lesions scoring (E) at 8 weeks post irradiation, for mice irradiated with electron beams in the dose range of 20 to 30 Gy in a single fraction at 0.1 Gy/s (left panel), 30 Gy/s (middle panel) or ≥ 1,800 Gy/s (right panel). Bars represent the median and red dots indicate animals that had to be euthanised for meeting skin toxicity euthanasia criteria (moist desquamation-ulceration or most desquamation that did not improve after 10 days). * $p<0.05$; ** $p<0.01$; *** $p<0.001$; **** $p<0.0001$.

setup would mean for the FLASH effect. Significant differences between 20, 25 and 30 Gy could be seen in delay in onset and severity of toxicity at the 8-week timepoint (Figure 5.4D-E). A dose-modifying factor (DMF) (defined as the dose required for a given effect in the higher dose rate group divided by the dose resulting in the same effect in the 0.1 Gy/s group [603]) for FLASH of ≈1.5 could be seen for the highest vs. lowest electron dose rate (as 30 Gy at 1,800 Gy/s showed a similar delay and severity of toxicity to 20 Gy at 0.1 Gy/s), while this DMF was reduced to ≈1.2-1.25 for 30 Gy/s (where 25 Gy at 30 Gy/s was slightly more toxic than 20 Gy at 0.1 Gy/s, while 30 Gy at 30 Gy/s showed a similar toxicity to 25 Gy at 0.1 Gy/s, Figure 5.3D-E). Similarly, for the photon irradiation our results indicated a FLASH DMF for 30 Gy/s of ≈1.2-1.25 (where 25 Gy at 30 Gy/s showed a similar toxicity to 20 Gy at 0.2 Gy/s, while 30 Gy at 30 Gy/s showed slightly less toxicity than 25 Gy at 0.1 Gy/s, Figure 5.4).

5.4 Discussion

Whilst preclinical FLASH studies have mainly been performed with electron and proton beams, the vast majority of all radiotherapy treatments are delivered with MV photon beams [103]. The photon beam studies published so far have mostly used kilovoltage (kV) photon beams, e.g., with beams from large synchrotron facilities [133, 134] or beams form x-ray tubes [217, 604]. A limitation with such beams is their penetration ability in tissue, and for x-ray tubes in FLASH studies there is also the issue with photoelectric effect, which has a significant role in the biological response for the soft energy spectra produced [605]. FLASH studies published so far using MV photon beams have utilised large facilities [606], with the majority coming from the PARTER platform at the superconducting linac at the Chengdu THz Free Electron Laser (CTFEL) facility [607]. Though capable of higher dose rates, these large facilities share comparable limitations to our setup; with a short SSD and limited field size. By using the same linac for ultra-high as conventional dose rates, with the same mouse setup and pulse structure for electron and photon irradiations, our setup enables a direct comparison of the FLASH effect between

these modalities. The short SSD results in a divergent beam (Figure 5.1) and a large effect on dose with any variation in SSD. This sensitivity to variation in SSD was reflected by the larger spread of toxicity scores within the photon irradiated groups, meaning that even a small setup variation could result in a large variation in toxicity as exemplified by the outlier mouse with a skin toxicity score of 5 in the 10 Gy/s irradiation group in Figure 5.4G. The beam divergence and wide penumbra required the use of a collimator with a smaller aperture for the 25 and 30 Gy photon beam deliveries, to limit the dose to the gastrointestinal tract, and to better match the area of irradiated skin on the mouse for electron beam irradiations (Figure A.13 in supplementary material). Dosimetry is challenging at ultra-high dose rates. However, for the dose rates used in this study, the dose-per-pulse only reaches 100-150 mGy, except for the highest electron dose rate (5 Gy/pulse). So, for all but the highest electron dose rate, the ion recombination correction needed for the Advanced Markus® is limited (a few %) [534], making it useful for relative online dosimetry. In this study, we show that the time to onset of radiation-induced skin toxicity in mice following hemi-thorax irradiation is delayed, and the severity of toxicity reduced with increasing dose rate (Figures 5.3 and 5.4). We see similar skin toxicity profiles following 6 MV photon, and 6 MeV electron irradiations, though the differences in dose distributions (beam divergence, penumbra and depth-dose Figures 5.1 and 5.2) prevents a perfect correlation between prescribed doses and observed toxicity between the modalities. For example, the full width at half maximum (FWHM) of the electron beam is consistently ≈20 mm from surface to 10 mm depth in solid water, while the FWHM of the diverging photon beam increases with distance from the surface, from ≈19 and ≈22 mm at surface to ≈23.5 and ≈27.5 mm at 10 mm depth for the 17×17 mm^2 and 20×20 mm^2 collimators, respectively. Furthermore, the penumbra (if defined as the distance of 75 % to 25 % of maximum dose) at the surface of the mouse phantom was substantially different between the electron (<1 mm) and the photon beam (≈9 mm). As demonstrated previously for skin toxicity following proton beam irradiation [192], an increase in average dose rate from conventional values (0.1 Gy/s) to a few Gy/s is enough for

significant sparing. Further increase to 30 Gy/s (the highest achievable dose rate with our photon setup) shows a DMF of ≈1.2-1.25, for both photon and electron irradiation. This DMF was increased to ≈1.5 for our highest used electron dose rates (≥1,800 Gy/s), similar to FLASH DMF published values for skin toxicity following electron (1.45-1.54) and proton (1.44-1.58) beam irradiation [128, 608]. These studies reached a DMF value of ∼1.5 while using substantially lower average dose rates than our maximum here, of around 80 Gy/s for protons and 230 Gy/s for electrons. This indicates that the DMF for skin toxicity increases with average dose rate, becomes significant at a few (1–10) Gy/s, and continues to increase with dose rate to the 80–230 Gy/s range [192, 609], where it seems to saturate with limited additional benefits of using even higher average dose rates.

6

A preclinical setup for spatially fractionated radiotherapy

Contents

6.1 Introduction

Despite early successes with SFRT, clinical adoption remains slow because because key aspects, including dose prescription, are not yet well understood. Most protocols prescribe only the vertex (peak) dose, ignoring potentially influential parameters such as valley dose, PVDR, fractionation scheme, sequencing, or vertex geometry [254, 285, 372, 373]. Similarly, links between treatment efficacy and a given parameter

have been complicated by inconsistent primary endpoints, prior or post conventional irradiation or fractionation [302], or combining treatments with chemotherapy or immunotherapy [258, 263, 287, 298, 610]. For LRT, optimal vertex number, size, and spacing, and how these should be adjusted to tumour composition or proximity to organs at risk (OARs) are unknown [240, 265]. Without consistent standards, comparisons across studies are difficult and mechanistic insights remain elusive [611]. Therefore, extended numbers of radiobiological experiments are required to explore the parameter spaces, and discern the most sensitive and relevant delivery parameters. Progress here would benefit from reproducible pre-clinical platforms that can isolate dosimetric variables and correlate them with biological endpoints in vivo. Electron beams at MeV energies are well-suited to this task. They can deliver high dose rates through simple scanning or collimation, and their radiobiological effectiveness is comparable to that of MV photons for the small field sizes and doses typical of SFRT [277, 612]. Moreover, electrons lend themselves naturally to ultra-high dose rate delivery, which has been shown to spare normal tissue while preserving tumour control in conventional field geometries. Combining FLASH with SFRT could further mitigate motion-induced blurring of steep dose gradients and enhance normal-tissue protection.

In this chapter we present a preclinical SFRT platform based on an electron linac that can deliver 6 MeV electron beams with dose rates ranging from conventional to ultra-high, combined with a flexible collimator system designed to generate customizable spatial dose patterns suitable for small animal models.

6.2 Methods

6.2.1 Collimation

Cylindrical 6.5 mm thick brass inserts were manufactured in 7-hole, and a 19-hole hexagonally packed arrangements (Figure 6.1). The coin shaped inserts were designed to fit tightly within the 6.5 mm, 100 mm $\times$ 150 mm, brass collimator plate positioned adjacent and downstream of the energy monitor. The insert used for our pilot mice experiment was manufactured with 2 mm holes, and a

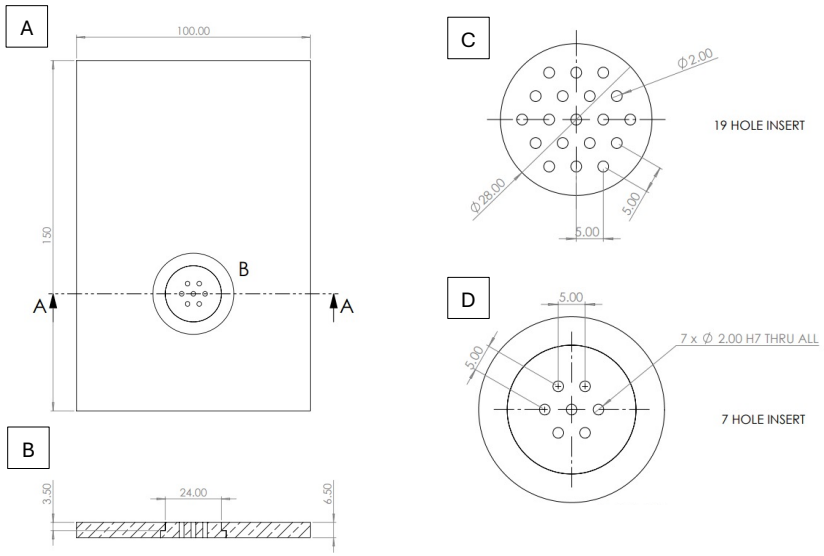

Figure 6.1: Electron SFRT brass inserts with 7 and 19 holes, with hole diameters of 2 mm, and centre-to-centre distances of 5 mm, hexagonally packed and placed within a brass collimator plate (all dimensions are displayed in mm): A) Beam's eye view of 7-hole insert within brass backer plate B) Top view of 7-hole insert within brass backer plate C) 19-hole brass insert dimensions D) 7-hole brass insert dimensions

centre-to-centre distance of 5 mm (Figure 6.1, panel D). Other 7-hole inserts were also manufactured with smaller hole diameters and centre-to-centre distances (supplementary Figure A.15).

6.2.2 Dose prescription

Prescribed surface peak doses were verified with EBT-XD film measurements before and after mice irradiation, at the surface of a mouse phantom (Figure 3.8), positioned as the mice in the mouse cradle in the beam (Figure 3.7). Average doses were analysed over a 6.6 × 6.6 mm^2 central area of exposed film (for consistency with measurements for homogeneous irradiations). For the SFRT, the average dose in this area (corresponded to 1/3 of the peak dose) as well as the peak doses were analysed. Additional online dosimetry was performed with an Advanced Markus® ionisation chamber at 1 mm depth in solid water (150×150×21 mm^3 RW3 slabs, PTW-Freiburg GmbH) [534]. The beam energy was maintained for all dose rates by slight detuning of the radiofrequency source and online monitoring of the resulting beam energy [530].

6.2.3 Macro development

To obtain dose, dose rate, and PVDR measurements, 34 × 34 mm^2 EBT-XD films were used with macro scripts developed in ImageJ (v2.14.0/1.54f) to obtain dose values in every pixel on the scanned films. Three single-pixel lines separated rotationally by 60° were analysed; with each line connecting the centres of adjacent beam spots along the principal axes of symmetry that intersected the central axis (CAX) (Figure 6.2). From dose profiles along these lines, average values of FWHM, dose maxima and minima were obtained, where the ratio of these was used to extract an average PVDR value.

6.2.4 Cell Culture

UPPL1541 bladder carcinoma cells were sourced from Applied Biological Materials (ABM), used within 5 passages after purchase, and confirmed to be free of mycoplasma contamination. Cells were maintained in high-glucose DMEM (Gibco, 11995065) supplemented with 10% fetal bovine serum (FBS) and 1% penicillin-streptomycin (100 U/mL). Cultures were maintained at 37°C in a humidified atmosphere containing 5% CO_2. For in vivo injections, cells were mixed 1:1 with high-concentration Matrigel (Corning, 354262).

6.2.5 Subcutaneous tumour model

A total of 31 (male & female) C57BL/6J mice (mean weight 26.04 ± 1.03 g) were injected subcutaneously in the right flank with 5×10^6 UPPL1541 cells (see methods section 6.2.4). Tumours developed over 10–13 days, reaching an average volume of 90.83 ± 21.78 mm^3 (average volume ± SD, CI 82.84-98.83 mm^3) before mice were randomly assigned to treatment groups (Table 6.1). For the radiotherapy, the mice were anaesthetized using isoflurane (4% for anaesthetic induction and 2% for maintenance, with total anaesthesia time of less than 10 minutes), supplemented with 95% oxygen (1/1 mixture with air resulting in a mixture of approximate 60% oxygen), and then placed upright in a mouse cradle in front of the horizontal beam [105]. The mice were positioned such that collimators shielded everything other

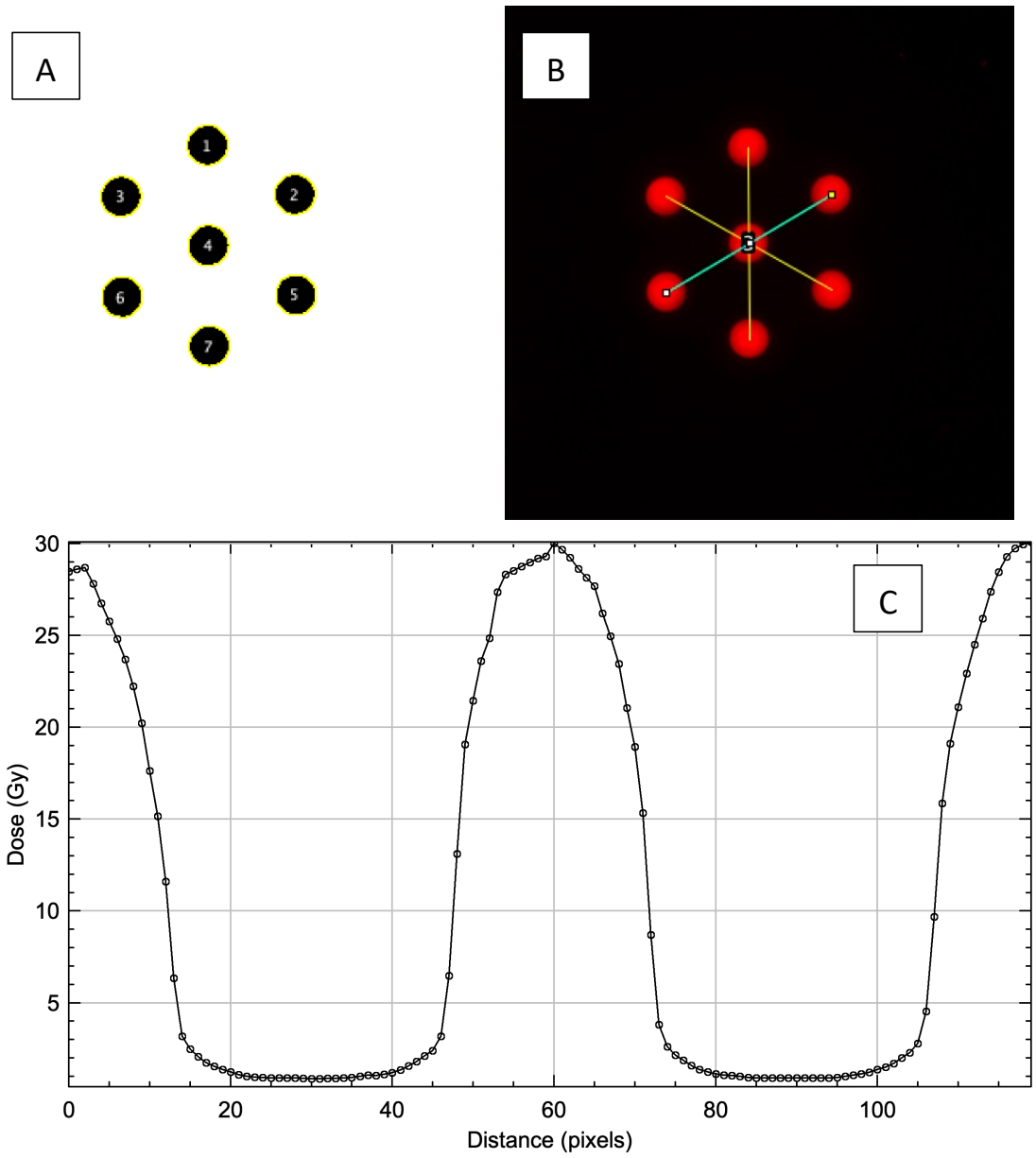

Figure 6.2: (A) Electron beam spots detected (in black) algorithmically using ImageJ (v2.14.0/1.54f) from an example EBT-XD film dose measurements using the 7-hole electron collimator (Figure 6.1D). (B) Three single-pixel lines separated rotationally by 60° were analysed (with profiles in yellow and blue, and beam spots in red); with each line connecting the centres of adjacent beam spots along the principal axes of symmetry that intersected the centre axis (CAX). (C) Dose across the blue single-pixel line profile shown in (B).

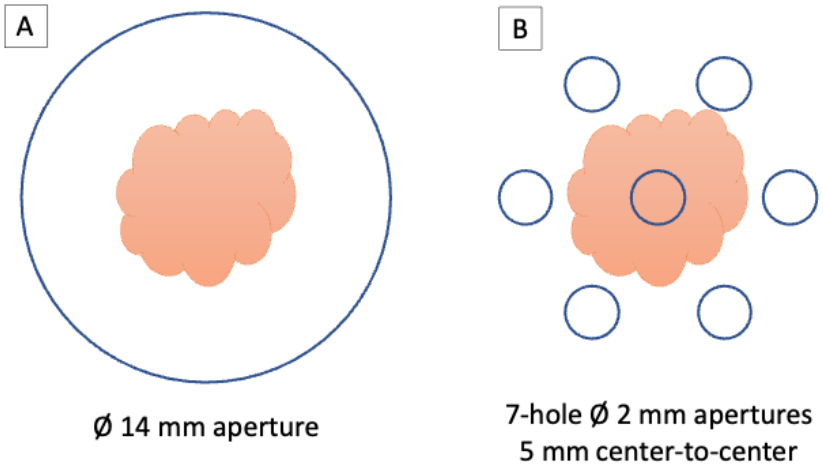

Figure 6.3: Illustration of how the tumour (schematic representation of a tumour at ~100 mm^3 volume, ~7-mm diameter) was aligned with A) the centre of the 14-mm diameter aperture collimator for homogenous RT, or B) with the central aperture of the 7-hole 2 mm diameter apertures (5 mm centre-to-centre distance) collimator for SFRT.

than the subcutaneous tumour which was aligned with the centre hole of the SFRT collimator, or to the centre of the 14 mm aperture (Figure 6.3).

Table 6.1: Electron mice irradiation regimens

Regimen label	Brass collimation / hexagonally packed spatial fractionation	Dose prescription at mouse surface	Single dose delivered (Gy)	Peak dose rate (Gy/s)	Mice in cohort (n)
eFLASH 10 Gy	ϕ14 mm aperture	Homogeneous	10	3,000	7
eSFRT-CONV 20 Gy	7-hole insert, ϕ2 mm, 5 mm ctc	Peak, Valley, Average	20, 1.4, 6.7	<0.1	7
eSFRT-FLASH 20 Gy	7-hole insert, ϕ2 mm, 5 mm ctc	Peak, Valley, Average	20, 1.4, 6.7	860	6
eSFRT-FLASH 30 Gy	7-hole insert, ϕ2 mm, 5 mm ctc	Peak, Valley, Average	30, 2.1, 10	820	7

Tumour size was monitored using callipers, and animals were euthanised once tumour size exceeded 700 mm^3. Tumour volume was calculated using the formula:

$$Volume = Length \times Width \times Height \times \frac{\pi}{6} \tag{6.1}$$

6.2.6 Statistical analysis

For subcutaneous tumours, survival curves were constructed based on the endpoint of tumour volume reaching three times its initial size and analysed using the Log-Rank test. Pairwise multiple comparisons were performed with Holm correction for 10 tests. Two-way repeated measures ANOVA followed by Tukey's HSD test was applied for analyses involving multiple groups. Statistical significance was set at $p < 0.05$.

6.3 Results

6.3.1 Electron SFRT (eSFRT)

PVDR values with the 7 and 19-hole inserts (Figure 6.1) were similar at 35 ± 2, and 31 ± 4 (Figure 6.4, panel A).

The slightly lesser average PVDR value from the 19-hole insert was due to lateral off-axis falloff causing less pronounced peaks in the outer ring of 12 holes. However, differences diminished at increasing depths. The FWHM (Figure 6.4, panel B) increased with depth for both insert arrangements. The 19-hole insert showed more FWHM variation, especially at depths >6 mm, where some peaks began to merge. This was most noticeable for the outer ring of 12 holes with wider FWHMs than those close to the central axis. Maximal peak doses in the beam spots were consistent for both inserts with similar variability (Figure 6.4, panel C). At surface, peak dose rates in beam spots were found to be >1.8 $kGy\ s^{-1}$. Equivalent simulation and experiments with other collimator designs are highlighted in supplementary materials (Figures 3.7, A.15 and A.16).

As the solid water phantom was displaced farther from the collimator exit, the PVDR measured at the front surface decreased from 32 at the surface to 16 at ∼10 mm distance, and to 6 at ∼20 mm distance (Figure 6.5, panel A). Meanwhile, the beam spot size increased (Figure 6.5, panel B), with the average maximum dose in the beam spot reducing exponentially (R^2>0.99) from 29 Gy at the surface to 17 Gy at ∼10 mm distance, and to 10 Gy at ∼20 mm distance (Figure 6.5, panel C).

Film measurements at the surface of the mouse phantom (Figure 3.8) showed that ultra-high (FLASH) dose rates >850 $Gy\,s^{-1}$ were achievable (Figure 6.6). Here, the PVDR was also >14, with maximal surface peak dose rates within 3% of one another, and FLASH dose rates in surface valley regions between peaks of ∼60 Gys^{-1} (identical film measurements with other collimators are indicated in Figure A.15).

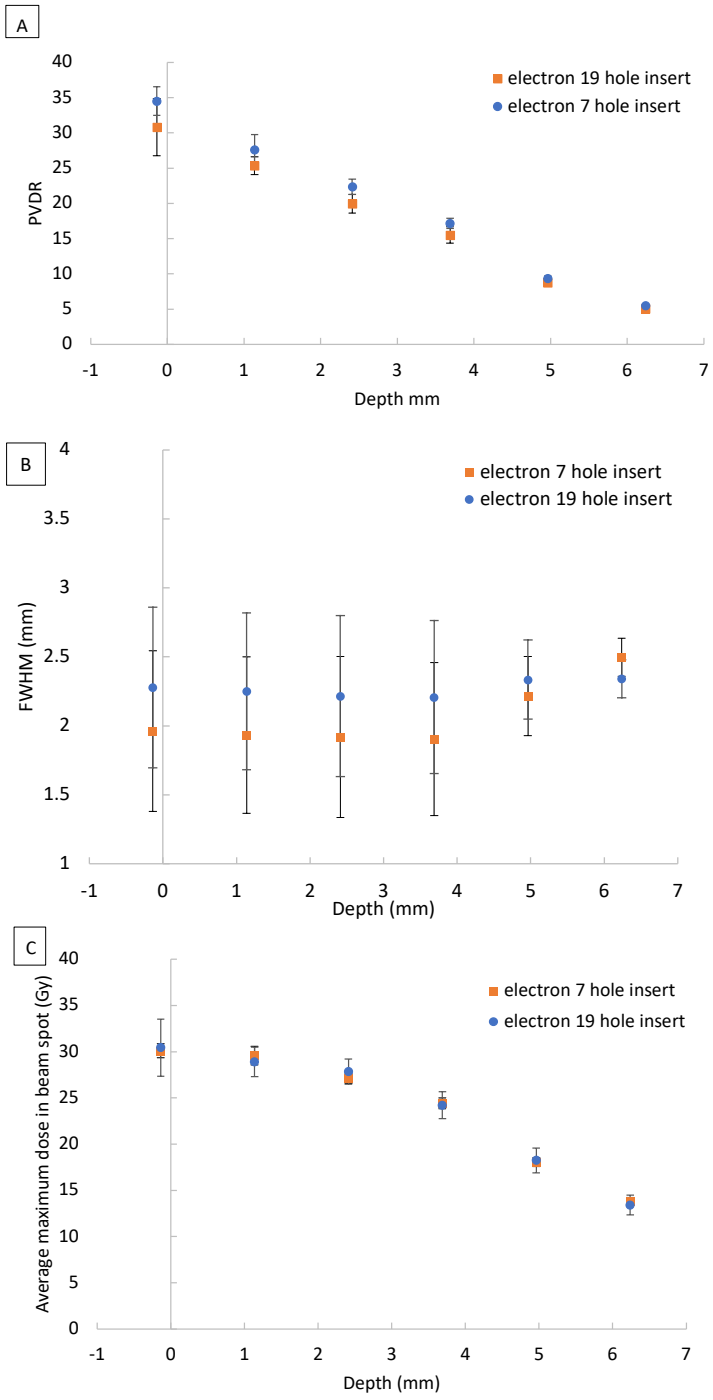

Figure 6.4: Electron 7-hole and 19-hole insert EBT-XD film irradiations at various depth in solid water where 0 mm indicates the surface. A 5-pulse delivery at 300 Hz was used for both arrangements, here: A) Average peak-to-valley dose ratio (PVDR) with depth B) Average full width at half maximum (FWHM) of beam spots C) Average dose maxima in beam spots. Markers and error bars represent the mean value and standard deviation respectively of values obtained from the films via three symmetric single-pixel line dosimetric profiles obtained with a 60° offset from one another whilst intercepting the centre of adjacent beam spots, and the central axis.

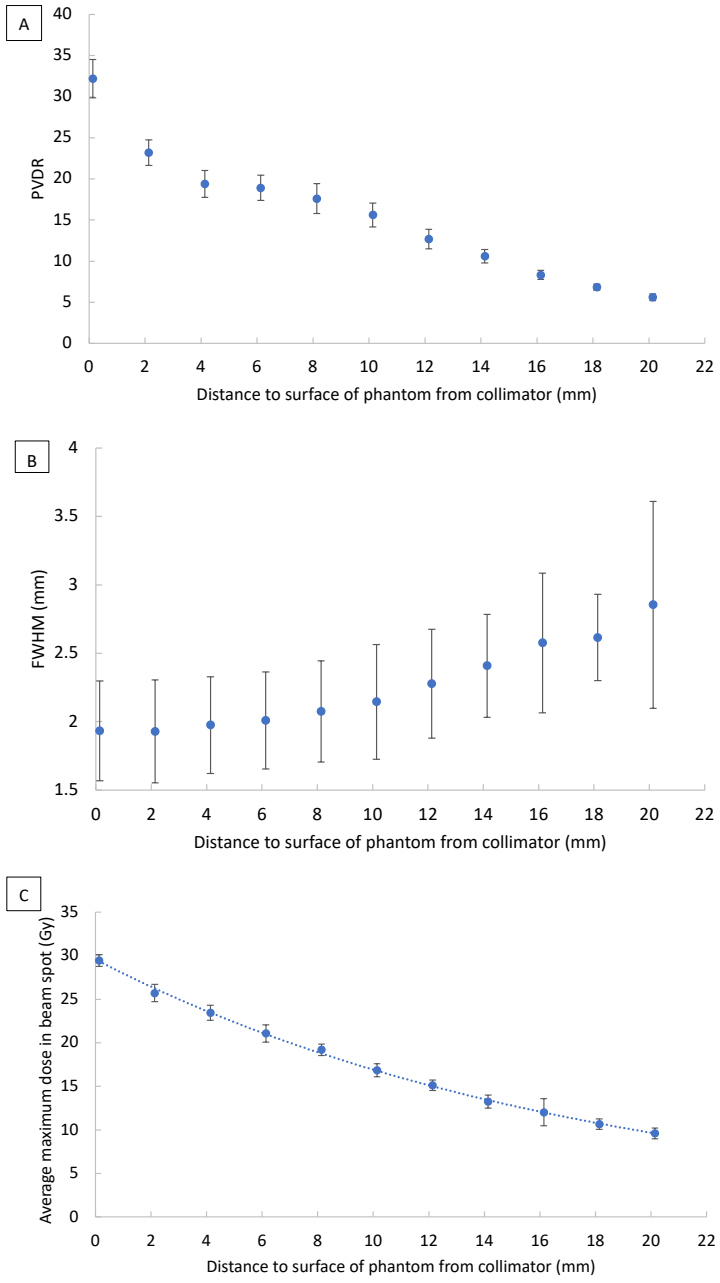

Figure 6.5: Electron 7-hole insert EBT-XD film irradiations, with film placed on the surface of 50 mm thick slab of solid water ($150\times150\times50$ mm^3). Air separation between the downstream surface of the collimator and the solid water phantom (with upstream surface-mounted films) was varied. A 5-pulse delivery was used. A) Average peak-to-valley dose ratio (PVDR) with distance B) Average full width at half maximum (FWHM) of beam spots C) Average dose maxima in beam spots. Markers and error bars represent the mean value and standard deviation respectively of values obtained from the films via three symmetric single-pixel line dosimetric profiles obtained with a 60° offset from one another whilst intercepting the centre of adjacent beam spots, and the central axis.

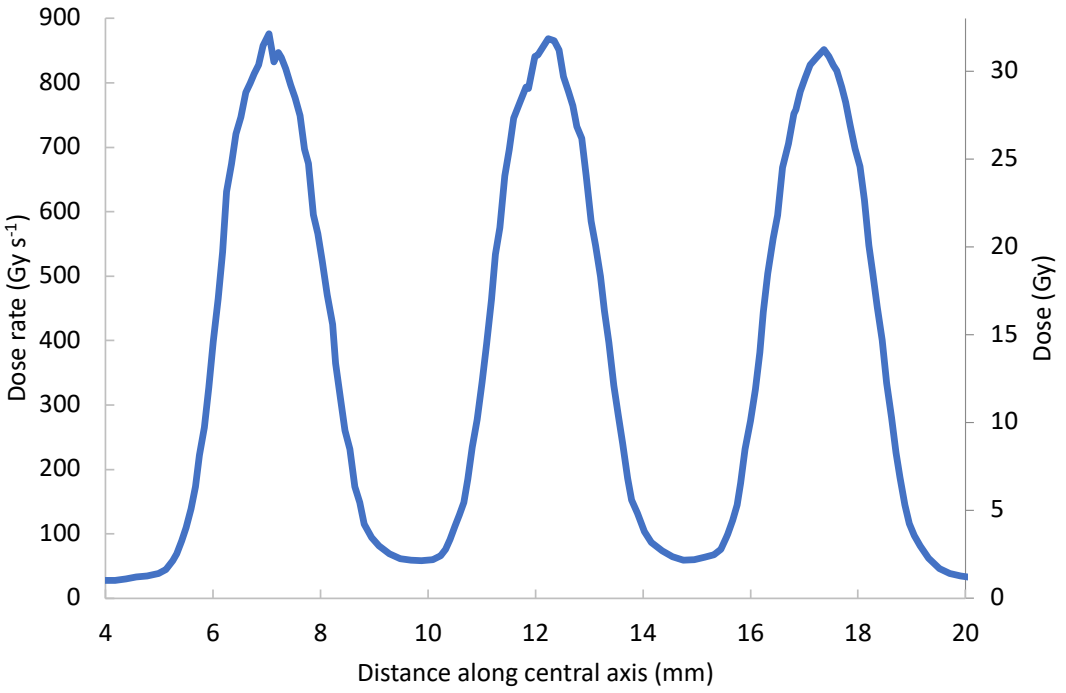

Figure 6.6: EBT-XD film beam profile measurement of doses and dose rates at the surface of the mouse phantom (Figure 3.8) for an 11-pulse irradiation using the 7-hole electron insert (Figure 6.1, panel D)

6.3.2 Preclinical experiments

Tumour growth varied significantly across treatment groups (Table 6.1), with a significant interaction between treatment type and time in tumour growth (Figure 6.7, panel A, and Figure A.18). The control group showed continuous tumour progression, whilst irradiation with electron SFRT, with peak dose of 20 Gy and a valley dose of 1.4 Gy, at a conventional (<0.1 Gy/s) dose rate (eSFRT-CONV 20 Gy) resulted in modest growth inhibition. In contrast, both eSFRT-FLASH groups demonstrated improved tumour control relative to the eSFRT-CONV 20 Gy group, with the eSFRT-FLASH 30 Gy group (peak & valley doses of 30 Gy & 2.1 Gy, delivered at ultra-high dose rates of 820 Gy/s & 60 Gy/s respectively) exhibiting a more pronounced and sustained effect. No significant differences in tumour volume were observed at day 0 or day 14. By day 21, the eSFRT-FLASH 30 Gy group ($p = 0.027$) had significantly smaller tumours than the control and eSFRT-CONV 20 Gy groups ($p = 0.019$). At day 30, the significant difference

persisted only between the eSFRT-CONV 20 Gy and the eSFRT-FLASH 30 Gy groups ($p = 0.021$), while the difference between control and eSFRT-FLASH 30 Gy was no longer statistically significant ($p = 0.1$). The tumour growth in the eSFRT-FLASH 30 Gy group was comparable to that in the homogeneous eFLASH 10 Gy group, indicating similar therapeutic benefit from spatial dose fractionation. The time to triple tumour volume (TTTV) was evaluated. TTTV varied substantially between treatment groups, reflecting differences in therapeutic efficacy (Figure 6.7, panel B). In the control group, the median survival was 12.5 days, indicating rapid tumour progression and early endpoint attainment. Treatment with eSFRT-CONV 20 Gy modestly extended survival to 17 days. A greater benefit was observed in the eSFRT-FLASH 20 Gy group, with a median survival of 19 days. The eSFRT-FLASH 30 Gy group showed a similar improvement, with a median survival of 25 days. Notably, the homogeneously treated tumours in the FLASH 10 Gy group also achieved a median survival of 25 days, with some mice surviving beyond 60 days, suggesting a more sustained suppression of tumour growth. Analysis of TTTV revealed that tumours in the FLASH 10 Gy group ($p = 0.011$), eSFRT-FLASH 20 Gy group ($p = 0.029$), and eSFRT-FLASH 30 Gy group ($p = 0.036$) reached triple their initial volume significantly later than those in the control group, with the largest delays observed for eSFRT-FLASH 30 Gy. Additionally, TTTV was significantly prolonged in the eSFRT-FLASH 30 Gy group compared with the eSFRT-CONV 20 Gy group ($p = 0.032$).

Our findings suggest that eSFRT-FLASH 30 Gy is effective at delaying tumour progression and providing prolonged tumour control comparable to homogeneous irradiation protocols. In addition, no significant differences in body weight as well as no skin damage were observed, indicating acceptable treatment tolerability (Figure 6.7, panel C).

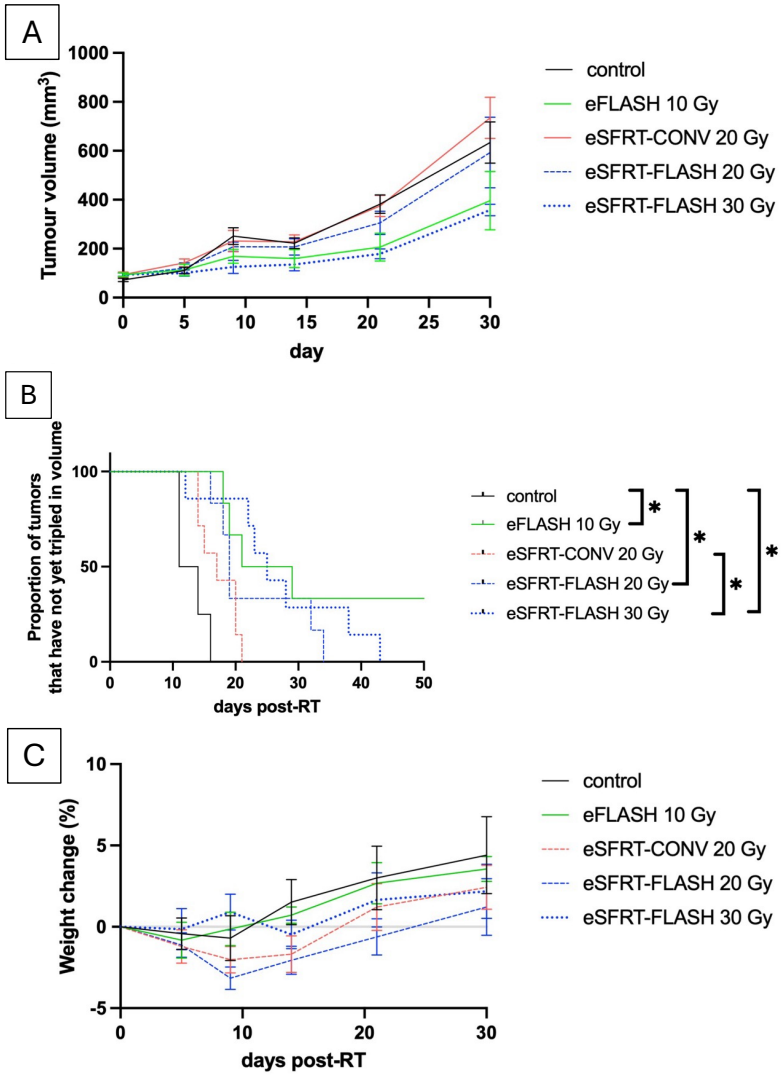

Figure 6.7: SFRT-FLASH delays tumour growth without causing significant weight loss. (A) Tumour sizes across different treatment groups. Data showed mean with standard error of the mean. (B) Kaplan–Meier curves showing the proportion of tumours in each group that have not yet tripled in volume.*$p < 0.05$. (C) Relative change in body weight compared to baseline (pre-radiotherapy) measurements. Data showed mean with standard error of the mean.

6.4 Discussion

Our electron inserts enable a straightforward and flexible modulation of spatial fractionation parameters in the beamline. Reducing the centre-to-centre distances between collimator holes can help mitigate the off-axis falloff of the incident Gaussian beam profile, thereby reducing disparities in PVDR between the 7- and 19-hole inserts. However, when the centre-to-centre distances $\leq$ hole diameters, the dose

peaks begin to merge and the resulting biological effects are expected to resemble the those from a homogeneous irradiation. Decreasing hole diameter along with reducing centre-to-centre distances allow for more beam spots to cover the tumour. However, this approach would also reduce the dose rate and PVDR with depth. Additionally, prolonged treatment times associated with this configuration may introduce motion-induced blurring effects. It is also evident that increasing the distance between the irradiated sample and the collimator offers a practical approach for fine-tuning spatial modulation parameters (e.g., PVDR, FWHM, dose rate), without the need to manufacture multiple collimators. Our measurements of PVDR are similar to other static GRID collimation systems [252, 613, 614], with higher dose rates, but present a challenge for non-superficial spatial modulation, as heterogeneity of dose quickly diminishes with depth [277, 612]. While Small Animal Radiation Research Platforms (SARRP) can improve accessibility and reduced the cost of MBRT with kV beams compared to synchrotrons, (with shortened delivery times and source-target distances [331, 615]), their peak doses and PVDRs also reduce quickly with depth and high power input may risk anode overheating without additional modifications to spot size, heat capacity, rotation rate, or employing scanned beams or parallel-opposed configurations [219]. Instead, MV photon SFRT at FLASH dose rates may better maintain spatial modulation in deep-seated tumours and reduce delivery times with flattening-filter-free (FFF) beams [242, 616], despite the greater divergence and lateral scattering which make spatial modulation more challenging [617]. Crucially, the compatibility in results between electron and photon modalities preclinically provides opportunity to establish a platform to inform future clinical treatments.

Results from the subcutaneous tumour model indicate that eSFRT-FLASH may have the potential to enhance tumour control and delay progression compared to SFRT delivered at conventional dose rates. While spatial modulation at a 20 Gy peak dose under conventional dose rates showed only modest improvement in tumour control relative to untreated controls, delivering the same peak dose at FLASH dose rates prolonged TTTV. Moreover, increasing peak dose to 30 Gy under FLASH

dose rate resulted in more sustained and substantial tumour growth inhibition than the 20 Gy regimen, suggesting a dose-dependent therapeutic benefit. Interestingly, the 30 Gy eSFRT-FLASH regimen, despite delivering only a low ($\sim$ 2 Gy) valley dose to most of the tumour, was nearly as effective in delaying tumour growth as the 10 Gy homogeneous eFLASH treatment (Figure 6.7). Our previous data demonstrated that higher homogenous irradiation doses further delay tumour growth with comparable tumour response between conventional and FLASH dose rates in the same animal model (Figure A.19 and Table A.8). However, homogeneous doses $>$ 20 Gy often cause intolerable skin toxicity [99, 612]. Spatial modulation offers a method to overcome these toxicity constraints while achieving improved tumour control. Notably in all treatment groups in this study, including those with high SFRT peak dose, doses were well-tolerated, with no significant weight loss or skin damage observed, highlighting the feasibility of dose escalation in SFRT. Together, our results suggest that the combined effects of spatial modulation, higher peak doses, and (potentially) FLASH dose rates contribute to an improved therapeutic response.

Several limitations in our current study should be acknowledged. First, our electron-based platform is constrained to superficial tumours at depths up to 5 mm. Investigations beyond this depth will require the use of higher energy electron or photon beams. Second, in our SFRT setting, only a limited number of beam spots cover the tumours, whereas the homogeneous regimens irradiated the entire tumour and surrounding normal tissue. These differences may influence both treatment efficacy and normal tissue response. Additionally, some beam spots partially overlapped with normal tissues adjacent to the tumour. The biological impact of this peripheral exposure likely depends on spot size, spacing, and the dose rate delivered in both peak and valley regions. Another limitation lies in the challenges of comparing homogenous and spatially modulated dose regimes [618]. While we use average dose (defined here as the total dose delivered over a consistent enclosing area) as a comparative metric, this metric may not adequately reflect the biological response across modalities. More representative or biologically weighted

measures are needed to accurately compare treatment outcomes and guide future SFRT treatment planning.

Future work will focus on expanding our platform to accommodate deeper tumour targets by developing photon-based collimation systems. In particular, the use of thick Cerrobend or tungsten blocks can provide sufficient photon attenuation for effective spatial modulation, allowing direct comparisons with our current electron SFRT inserts. Further optimization of SFRT beam geometry and placement are also required. Reducing centre-to-centre distances and hole diameters may enable more extensive tumour coverage but must be balanced against the risk of peak merging and compromised spatial modulation. In parallel, the biological impact of dose delivered to surrounding normal tissues, especially in peripheral beam spots, warrants detailed evaluation, including its potential contribution to local or systemic immune responses.

Lastly, the therapeutic potential of SFRT may be enhanced when used as a priming strategy in combination with immunotherapy and/or chemotherapy [619, 620].

7

Managing Bremsstrahlung target heating in megavoltage photon FLASH radiotherapy

Contents

7.1 Introduction

In photon FLASH radiotherapy, targets will be exposed to high repetition rates and peak currents for up to 1s per irradiation. As the target deteriorates, dose output will likely reduce with abnormalities [600] and beam hardening [224]. In conventional irradiations, the target is usually placed within the accelerator's vacuum system to eliminate the possibility of target oxidation. However, short irradiation timescales with FLASH (typically <1s), should limit oxidation and the need for water-cooling. Without removable sealed vacuum units, beamline flexibility is also limited and complicates the switching of electron/photon & FLASH/CONV operational modes [621]. Therefore, mounting the target in air offers a straightforward and accessible setup. Though this risks oxide formation, the approach allows flexible beamline positioning to adjust beam spot size, reducing incident power density while maintaining photon FLASH dose rates and enabling rapid switching between operational modes [378].

In this chapter we show a simple method to enable FLASH photon dose rates using thin in-air (0.5, 0.7, and 1.0 mm) tungsten targets whilst circumventing large temperature rises, displacement damage, oxidation, and fatigue by increasing target separation from the beam exit window.

7.2 Methods

7.2.1 Incident electron beam profile measurement

Gafchromic EBT-XD films were used for measurements of beam profiles and average dose rates. These were read out 24 h post-irradiation using a film scanner at 96 dpi and were analyzed (red channel) using ImageJ (v2.14.0/1.54f).

7.2.2 Incident electron beam energy deposition simulation in bremsstrahlung target

To estimate the distribution and magnitude of energy deposition throughout a bremsstrahlung target from each pulse from the linac, Geant4 (v11.2.2, CERN,

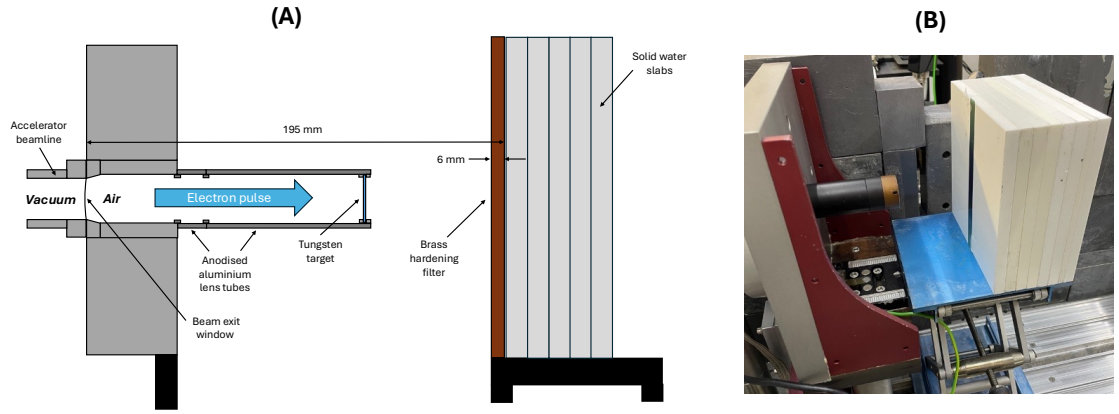

Figure 7.1: Bremsstrahlung target assembly for photon dose rate and beam profile measurements. (A) A sketch of the beamline assembly (not to scale) (B) Practical beamline setup with brass hardening filter removed to show EBT-XD film position. A lab jack stand was used to position the solid water phantom at 195 mm downstream of the beam exit. A brass hardening filter $150 \times 100 \times 6\ mm^3$ was positioned at 189 mm. Solid water slabs ($150 \times 150\ mm^2$) of varying thicknesses enabled EBT-XD surface dose measurements.

Geneva, Switzerland) simulation software was used to obtain a volumetric heating power density input [396, 574, 622]. Beam shape, pulse current, and energy inputs were taken from measurements (Figures A.23 to A.25), and prior beam energy evaluations [530]. The G4EmStandardPhysics_option3 physics list was chosen because of its stricter step limitation, benchmarked agreement with experiment, and higher accuracy of electron tracking [623].

7.2.3 Photon dose rate output measurement from bremsstrahlung target

With a 0.5 mm tungsten target and 6 mm brass hardening filter in place, beam profile measurements were performed at varying distances from the beam exit window (Figure 7.1). Average dose rate measurements were performed with $150 \times 12\ mm^2$ EBT-XD films placed centrally on the surface of the solid water phantom at various beam exit window-to-target separations in air, with three repeats for each position. A Gaussian fit was applied to each profile to calculate the FWHM, and average dose rates were determined from averaging peak doses in the centre of the profile.

7.2.4 Thermocouple apparatus

Three Nickel Aluminium, Nickel Chrome (K-type) thermocouples (RS Components Ltd., Corby, UK) were setup within a thermocouple measurement jig (Figure 7.2). Thermocouples consisted of a two-wire junction wound tightly together with a bead of 0.3 mm diameter connecting the ends of the wires [624]. The jig was constructed by modifying an anodised SML05 aluminium lens tube (Thorlabs LTD. Ely, UK). Within the lens tube, interposed between retaining rings were the tungsten target, thermocouples, and a transparent 1" diameter, 1 mm thick silica glass UVFS Broadband Precision Window (Thorlabs LTD. Ely, UK). Transparent silica glass was used to ensure secure thermal contact of thermocouples on the target surface, while enabling the position of each thermocouple bead to be measured with a microscope (IM-6225, Keyence, Milton Keynes, UK). Silica glass is an insulator, with a very low thermal conductivity [625], so was deemed to contribute insignificantly to measurements of temperature rises compared with the tungsten. Thermocouples were placed at various radial displacements from the beam centre by up to ∼9 mm. An AD8497 series evaluation board (Analog Devices, Inc., Wilmington, USA) was connected to each thermocouple [626]. The board was used in a linear mode of operation throughout, with voltage output correlated to temperature at the measurement junction,

$$T_{MJ} = f_{NIST}\left(\frac{V_{OUT} - V_{REF} - V_{OFF}}{G}\right) \tag{7.1}$$

where T_{MJ} is the measurement junction temperature, V_{REF} is the reference voltage for an ambient temperature of $25°C$, V_{OFF} is the offset voltage at $0°C$ to obtain 125 mV at $25°C$ (-0.98 mV), G is the amplifier gain (122.4), and V_{OUT} is the output voltage. Here, f_{NIST} is the millivolt-to-temperature function based on thermocouple data from the NIST Temperature Scale Database (SRD 60, v3) [627, 628]. A transient digitizer (Picoscope 4603 from Pico Technology, St Neots, Cambridgeshire, UK) was used to measure V_{OUT} at the measurement junction. Three input channels connected to the thermocouples were used in parallel with a sampling rate of 100 kS/s. The response of the beam current integrated transformer

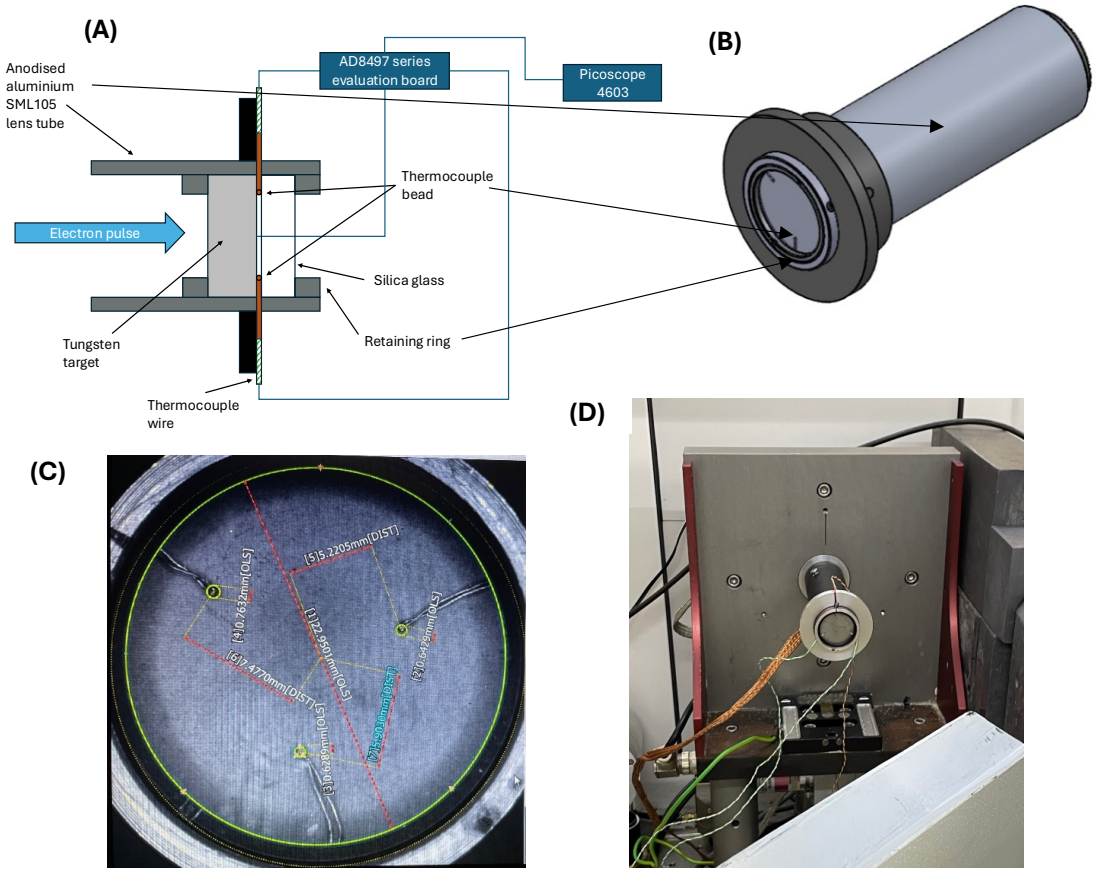

Figure 7.2: Thermocouple apparatus for temperature experiments. A) Side view sketch (not to scale) of the SML105 lens tube containing the tungsten target and silica glass interposed by retaining rings to secure thermocouple beads to the target surface B) 3D CAD model of A) with three thermocouples in place (C) IM-6225 (Keyence, Milton Keynes, UK) microscope measurements of thermocouple bead position on tungsten target surface (D) Upstream view of practical arrangement of thermocouple apparatus in the beamline.

(BCIT) was used with an edge trigger condition (a 10% voltage rise) to trigger temperature measurements when linac output began.

7.2.5 Finite Element Model

An axisymmetric finite element model was developed using the commercially available finite element code, Abaqus (2022, SIMULIA, Dassault Systèmes, Paris, France) (Figure 7.3). A volumetric pulsed heat load was applied to the tungsten target. Axial symmetry was used to reduce simulation time [420]. The off-axis ends of the tungsten were constrained with boundary conditions [629] (kinematic and

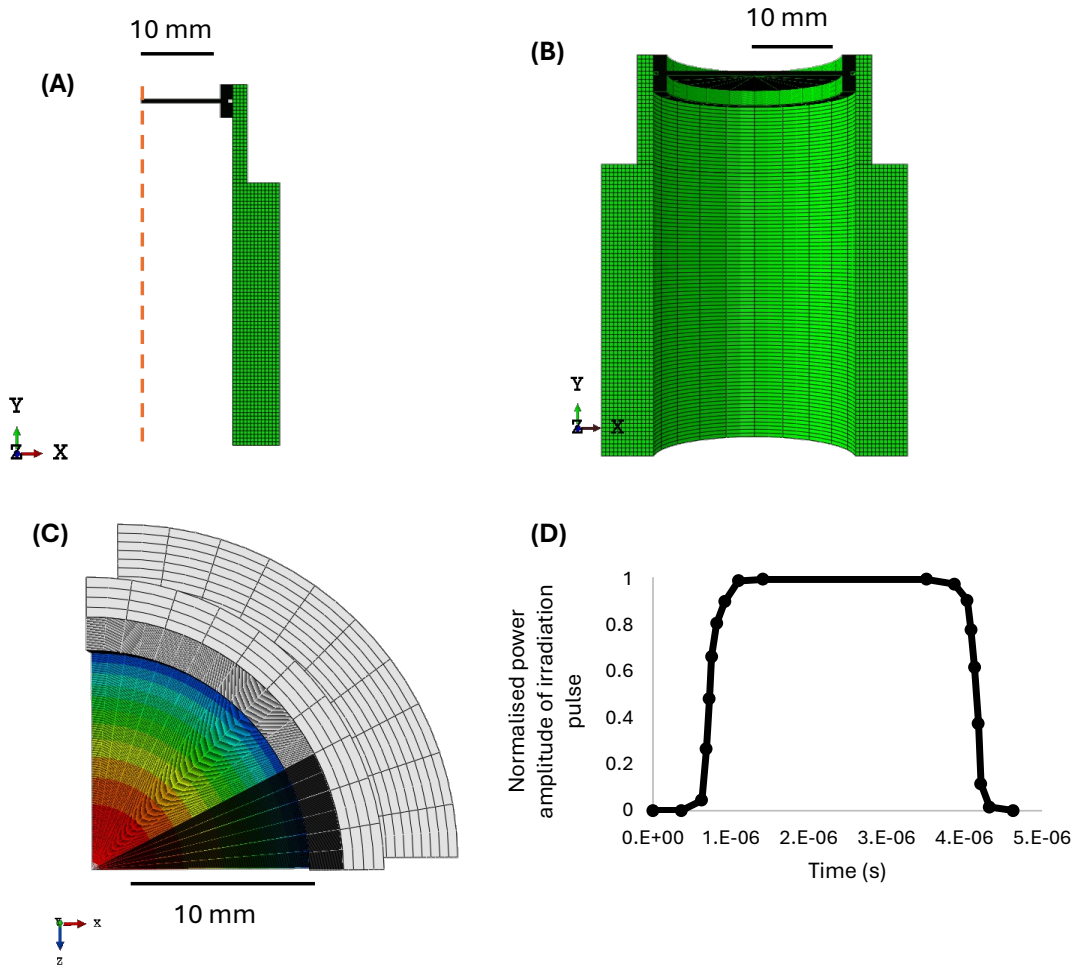

Figure 7.3: Abaqus axisymmetric FEM model for 0.5 mm target within a SML05 lens tube held between two retaining rings. A) Full axisymmetric model mesh (dashed line indicates the axis of symmetry) B) Side profile of extruded mesh C) Top view of section of full model after an irradiation D) Normalised power amplitude of irradiation pulse with time.

thermal), and the furthest upstream surface of the aluminium housing was fixed at 25 $°C$. The heat transfer coefficient between tungsten and aluminium surfaces was set to 1000 W/m^2K to better mimic the thermal resistance in the experiment [420]. Convective heat transfer was neglected [429]. Friction was also neglected and contact surfaces were assumed to be tied [630]. Outer Aluminium surfaces were constrained in all axes to provide conservative values for stress and strain. Temperature-dependent material properties such as density, thermal expansion coefficient [631], thermal conductivity [632], specific heat capacity (at constant pressure) [633], were added in tabular form whilst tungsten emissivity was fixed to

a value of 0.5 [634]. Temperature-dependent elastic properties were also added [635, 636], assuming isotropic elasticity. Meanwhile plastic response was integrated using the Johnson-Cook model with strain-rate dependence [637–640], and kinematic hardening was not included (see supplementary Tables A.10 to A.20). Radiative properties were defined on the upper and lower surfaces of the tungsten target with open cavity radiation properties. The target and retaining ring parts were meshed with element sizes of <0.02 mm such that the number of elements was 15,650, 21,910, and 31,300 for 0.5, 0.7, and 1.0 mm targets, and 8,600 in each retaining ring for all simulations to utilise similar element numbers to those used previously (1e4-1e6) [234, 396, 409, 552, 562, 629, 641] with mesh size <1/20 of the incident beam FWHM [429]. Mesh size and shape was kept consistent in the tungsten target because of the comparable size of the irradiated volume. For the coupled thermal-mechanical model, 8-node quadratic (CAX8RT) elements were chosen with reduced integration. Prior to irradiation, the initial temperature of the model was set to 25 $^{\circ}C$ and began in a stress-free state [419]. Secondary effects such as oxidation, melting, cracking and resolidification were not included. The model was coupled thermally and mechanically in time. Here sequential beam-on, and beam-off coupled-heat transfer steps were applied with pulsed heat loads in beam-on steps with temporal amplitude structure identical to the FWHM of our electron pulses (Figure 3, panel D) [642]. The energy deposition per unit volume (per incident history) was obtained from a Geant4 simulation of an incident monoenergetic, 6 MeV electron beam, of variable FWHM applied to the surface of the 25 mm diameter, 0.5, 0.7, or 1.0 mm thick tungsten targets. Energy deposition was scored within (50 × 50) 2500 annular bins, with a 2-D Gaussian fit applied which propagated radially and axially.

$$\left[\frac{E_{dep\,sim}}{V}\right] = E_{norm} e^{\frac{-(r-r_{mean})^2}{2\sigma_r^2}} e^{\frac{-(z-z_{mean})^2}{2\sigma_z^2}} \tag{7.2}$$

Here, r_{mean}, and z_{mean} refer to the radial and axial displacement of the point of maximum deposition along these axes respectively. Similarly, σ_r and σ_z are the standard deviations of the Gaussian distributions along these axes. The value E_{norm} was taken as the normalised energy density amplitude with which all other

energy density values were scaled (see supplementary Tables A.21 and A.22 for calculated inputs). Because the simulation physics included processes that alter the nominal power input e.g., backscatter, secondary electron absorption [643], and photon production, the energy density in each bin was equivalent to scaling a nominal incident power density by an absorption power density coefficient α_W (typically 0.46-0.55 [396, 420, 643, 644], and 0.55 for tungsten [645–647]. Scored energy densities were scaled such that,

$$n_{exp} = \frac{I_{peak\,pulse} t_{pulse}}{Q_{e^-}} \tag{7.3}$$

$$\frac{E_{dep\,per\,pulse}}{V} = \frac{n_{exp}}{n_{sim}} \left[\frac{E_{dep\,sim}}{V} \right] \tag{7.4}$$

where $I_{peak\,pulse} = 110\,mA$ (see Figure A.25)[3], $Q_{e^-} \sim 1.6 \times 10^{-19} C$, $t_{pulse} = 3.4\,\mu s$ [530], $n_{sim} = 10^8$, $n_{exp} = 2.3375 \times 10^{12}$. Maximal power density values had a <2% error about their mean, evaluated with the history-by-history method [515]. Two types of convergence parameters were required for each increment in the finite element model. The first was the maximum temperature step permissible which acted as a proxy setting for the maximum time step whilst the second was the mesh size. Time steps were calculated adaptively with small upper bounds and initial steps, to ensure convergence of scored quantities for a given beam-on or beam-off step. A maximum temperature step per increment of 1 degree and target global element size of 0.02 mm was seen to sufficiently resolve temperature fluctuations within pulses. Time increments for convergence for each beam on and beam off step were initially set to ∼0.25% of the step duration with adaptive increment time alteration to aid convergence of thermal and mechanical calculations. These converged such that each beam-on step required 75 increments with increments of up to ∼2.2% of the total step time. Likewise for beam off steps, 36 increments were required with increments up to ∼6.6% of the total step time.

The mechanical model assumed isotropic von Mises plasticity with yield function, $f(\sigma) = \sigma_{eq} - \sigma_y \leq 0$, i.e., yielding occurs where f=0, where σ_y is the yield stress, and σ_{eq} is the von Mises stress and is given by

$$\sigma_{eq} = \frac{1}{\sqrt{2}} \left[(\sigma_{xx} - \sigma_{yy})^2 + (\sigma_{yy} - \sigma_{zz})^2 + (\sigma_{zz} - \sigma_{xx})^2\, 6 \left(\tau_{xy}^2 + \tau_{yz}^2 + \tau_{zx}^2 \right) \right]^{\frac{1}{2}} \tag{7.5}$$

In addition, the equivalent plastic strain ε_{eq}^{pl} (PEEQ) is output as

$$\varepsilon_{eq}^{pl} = \sqrt{\frac{2}{3}\varepsilon_{ij}^{pl}\varepsilon_{ij}^{pl}} \tag{7.6}$$

where ε_{eq}^{pl} is the plastic strain component. Here the accumulated plastic strain is given by $\bar{\varepsilon}_{eq}^{pl}|_0 + \int_0^t \dot{\bar{\varepsilon}}_{eq}^{pl} dt$, with the initial equivalent plastic strain $\bar{\varepsilon}_{eq}^{pl}|_0$ and equivalent plastic strain rate $\dot{\bar{\varepsilon}}_{eq}^{pl} dt = \sqrt{\frac{2}{3}\dot{\varepsilon^{\mathbf{pl}}} : \dot{\varepsilon^{\mathbf{pl}}}}$, and t is time [648].

7.3 Results

7.3.1 Photon dose rate as a function of target separation from beam exit window

Photon dose rate at surface was seen to increase in a quadratic way when increasing the separation of the target from the exit window, mainly because of the reduced target-to-measurement point this resulted in (Figure 7.4). Similarly, the FWHM of the photon profile was seen to reduce with the inverse square of distance for increased target separations from the beam exit window. Based on applied quadratic fits ($R^2 \geq 0.99$), photon dose rates above the commonly recognised FLASH threshold (>40 Gy/s) were predicted with extrapolation to a separation of ∼136 mm, which would correspond to a photon beam with a FWHM of ∼44 mm. These findings agreed with our prior work in chapter 4 which obtained >40 Gy/s at 134 mm. No dose rate differences were seen between the 0.5, 0.7, and 1.0 mm target thicknesses, at 10 cm depth in solid water (Figure A.26).

7.3.2 Thermocouple temperature measurements and Abaqus simulations

Temperature history

The temperature history of each element was obtained (Figure 7.5), and was seen to fall off rapidly with time. Here at ∼5-10s after irradiation, the temperature returned to its starting value of $25°C$. Deviation in the rate of cooling after irradiations accounted for a large difference between simulation and experiment, likely from the effect of boundary conditions.

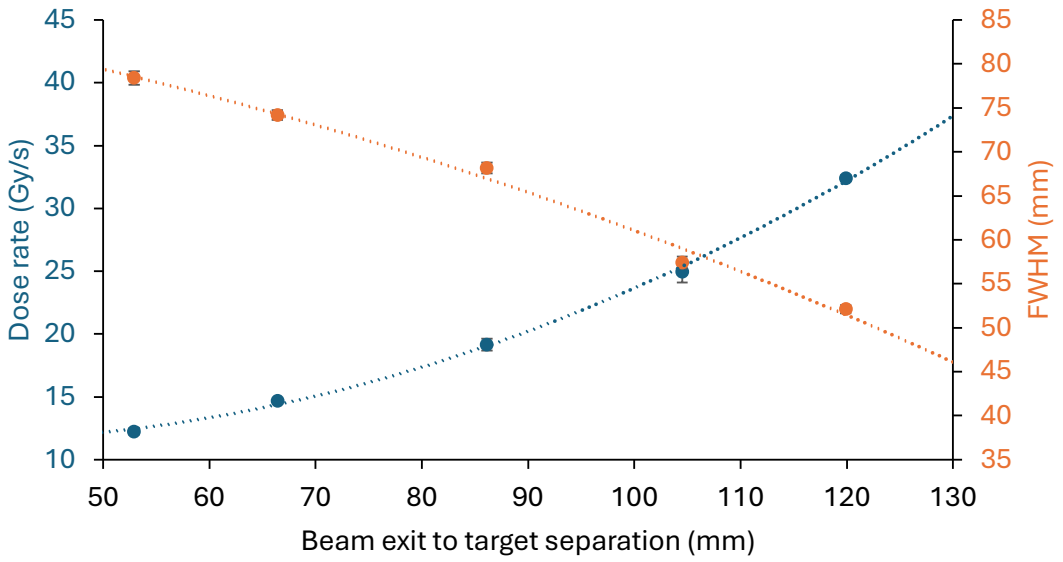

Figure 7.4: EBT-XD film dose rate and vertical full width at half maximum (FWHM) measurements from 300 pulses incident at 300 Hz of the photon beam from a 0.5 mm thick tungsten disc with 6 mm brass hardening filter at different distances from the beam exit window. Films were fixed to the surface of a 5 cm solid water block 195 mm downstream of the beam exit window. Error bars indicate the standard deviation of 3 repeated measurements. Quadratic fits are indicated with dotted lines ($R^2 \geq 0.99$)

Temperature rise with beam exit to target distance

All maximum temperatures for targets decayed exponentially for increased separations from the beam exit window following 1s irradiations (Figure 7.6). Variability was seen in temperature measurements from the variable; position of the beam with respect to the mechanical centre, placement of thermocouple beads on target surfaces (supplementary Figure A.27), and quality of thermal contact between thermocouple beads and the target surface. To aid comparison, similar downstream radial element positions were evaluated to measured thermocouple positions. Greater variability was seen for targets at shorter separations from the exit window from a narrower radial electron beam profile causing faster radial temperature falloff. The maximum temperatures reached within the target were, according to simulations, similar for each target thickness, with the 0.7 mm target consistently reaching the highest temperature (supplementary Figure A.28).

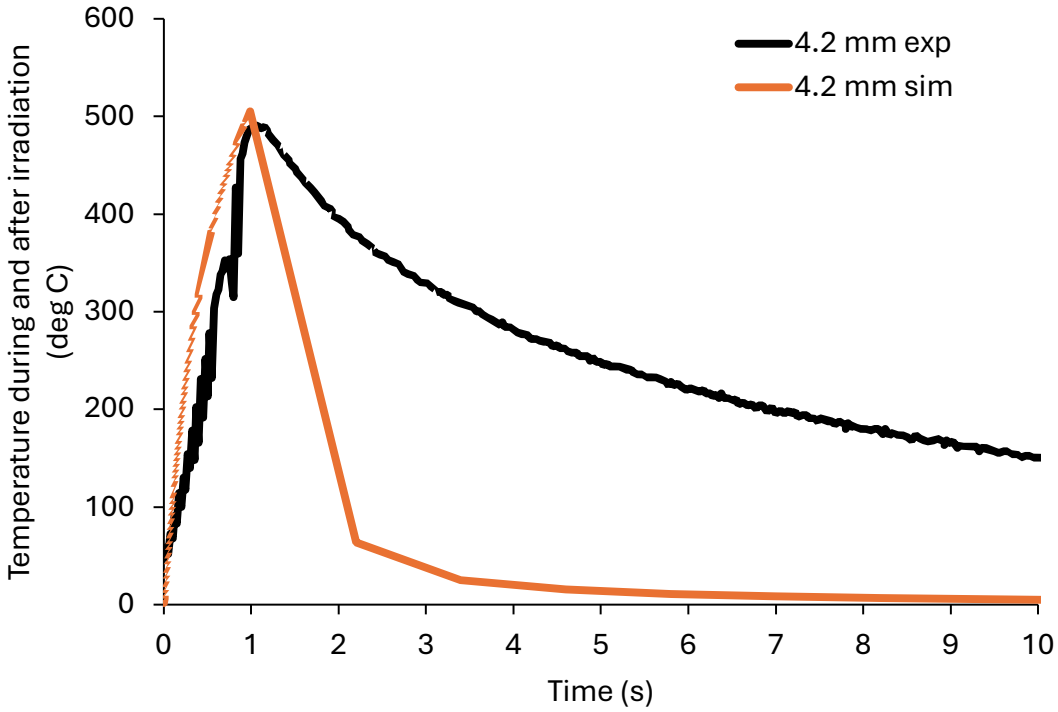

Figure 7.5: Temperature history of a 0.7 mm tungsten target at 53.9 mm separation from the exit window for simulation and experiment, measured at a radial position of 4.2 mm from the beam centre following a 1s irradiation of 300 pulses beginning at 0s

7.3.3 Transient grating spectrometry (TGS) measurements

TGS measurements indicated a similar thermal diffusivity of 6×10^{-5} to 7×10^{-5} $m^2s^{-1}$for unirradiated and irradiated targets (Figure 7.7). For irradiated 0.7 mm targets, persistent and severe surface roughening and pitting prevented signal acquisition, even after the surface oxide layer was removed with polishing. Significant difference ($p < 0.001$) was seen between irradiated and unirradiated 0.5 mm targets. However, their values ($\sim6.4\times10^{-5}$ and $\sim6.8\times10^{-5}$ m^2s^{-1}, respectively) and distribution were within expected margins for pristine targets and matched expectations of prior simulations (supplementary Figure A.29).

7.3.4 Simulated plastic equivalent Strain and Von Mises stress

A sudden increase of compressive stress was seen from irradiation induced heating, which had similar increases for all sample thicknesses. As the target temperature

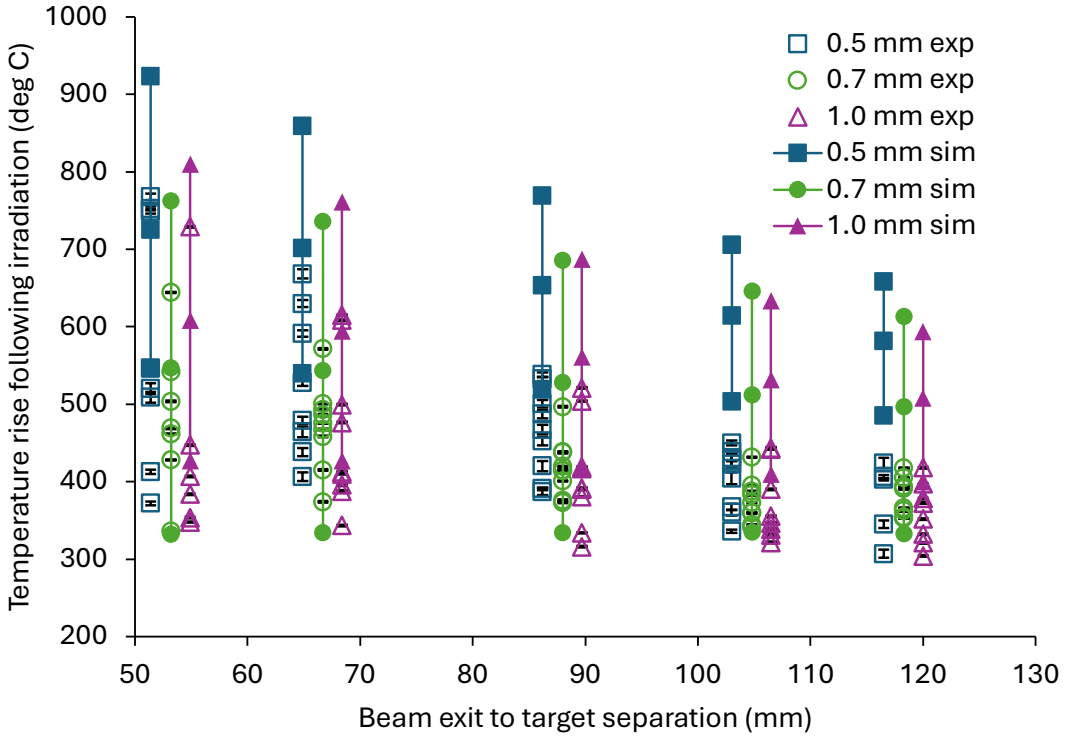

Figure 7.6: Temperature rise on downstream target surface from thermocouple measurements and simulations after a 1s irradiation of 300 pulses at 300 Hz. Tungsten disc thicknesses of 0.5, 0.7, and 1 mm are represented by blue squares, green circles, and purple triangles, respectively. Filled markers indicate simulated temperature rises at radial positions of: 2.9±1.1 mm, 4.5±1.6 mm, 3.2±1.4 mm for 0.5, 0.7, and 1.0 mm thicknesses, respectively, to match the spread of radial position in experiment. Unfilled markers indicate experimental values from thermocouples. Error bars indicate the standard deviation of 3 repeated measurements. Points are adjusted by -2, 0, and +2 mm in x-axis for clarity of presentation.

and stress increased, plastic yielding eventually occurred (Figure 7.8), with yielding causing the accumulation of plastic strain (supplementary Figure A.30). With increasing numbers of incident pulses, elastic shakedown behaviour was seen which reduced material stress, where thinner samples accumulated greater plastic strain. Following irradiation, during cooling, minimal plastic strain accumulated except for the thinnest sample, caused by a large tensile stress buildup from constrained thermal contraction. This indicated that greater damage, and shorter material lifetimes would occur for the thinnest samples from their higher accumulated plastic strain. Here, most of the plastic strain accumulation occurred during pulsed irradiation.

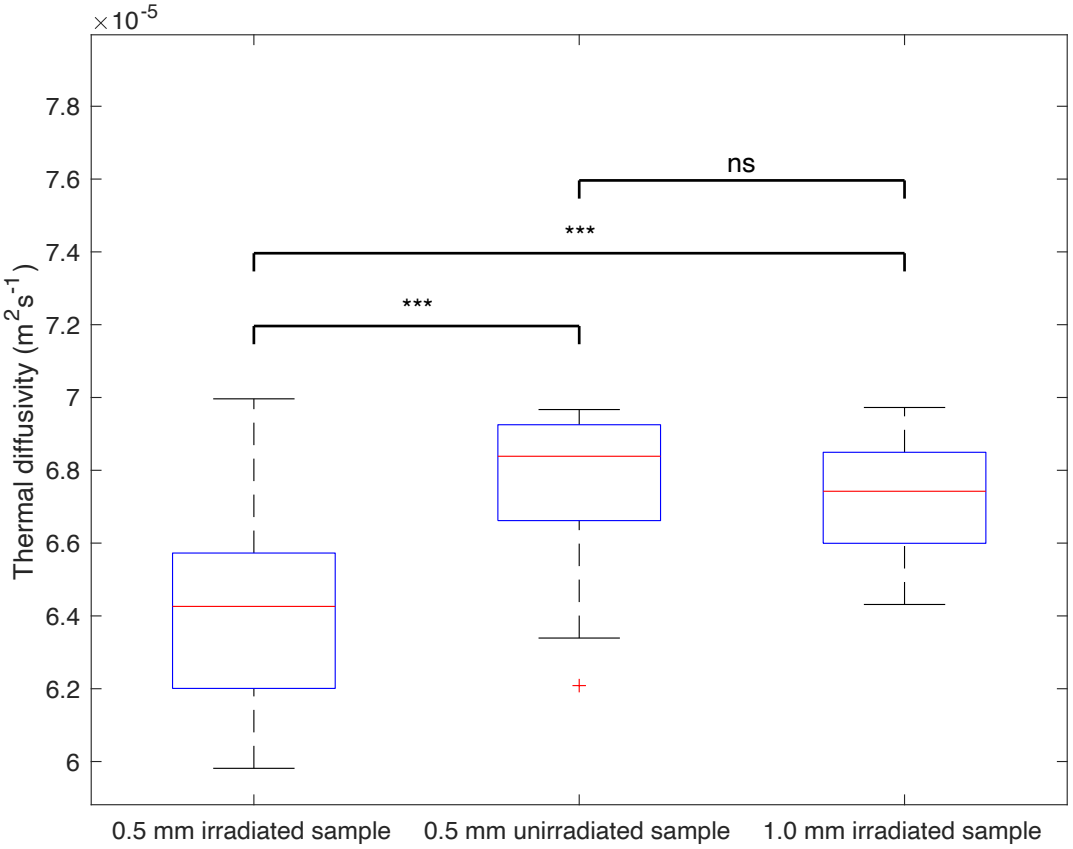

Figure 7.7: Transient grating spectrometry thermal diffusivity measurements on polished tungsten targets irradiated for 20s at 300 Hz or unirradiated. Scanning over the surface was performed in 0.1 mm steps over a 0.8 × 0.6 mm^2 (0.5 mm irradiated), 0.9 x 0.8 mm^2 (0.5 mm unirradiated), or 0.5 × 1.0 mm^2 (1.0 mm irradiated) area in horizontal and vertical directions respectively. Differences of mean values were compared using the Tukey-Kramer 'multicompare' statistical test tool in MATLAB, values are displayed as ns p>0.05; * p<0.05; ** p<0.01; *** p<0.001

7.3.5 Simulated total plastic equivalent strain

The maximum equivalent plastic strain (PEEQ) % within the irradiated region of each target was taken at the final time increment of each simulation for simulations of different separations from the beam exit window (Figure 7.9). The 0.5 mm target accumulated the greatest strain, with the strains for all targets decaying exponentially for increased separations (with each $R^2 > 0.99$). Here, the rate of falloff for the thickest sample was largest, whilst the rate of falloff with target separation was smallest for the thinnest sample.

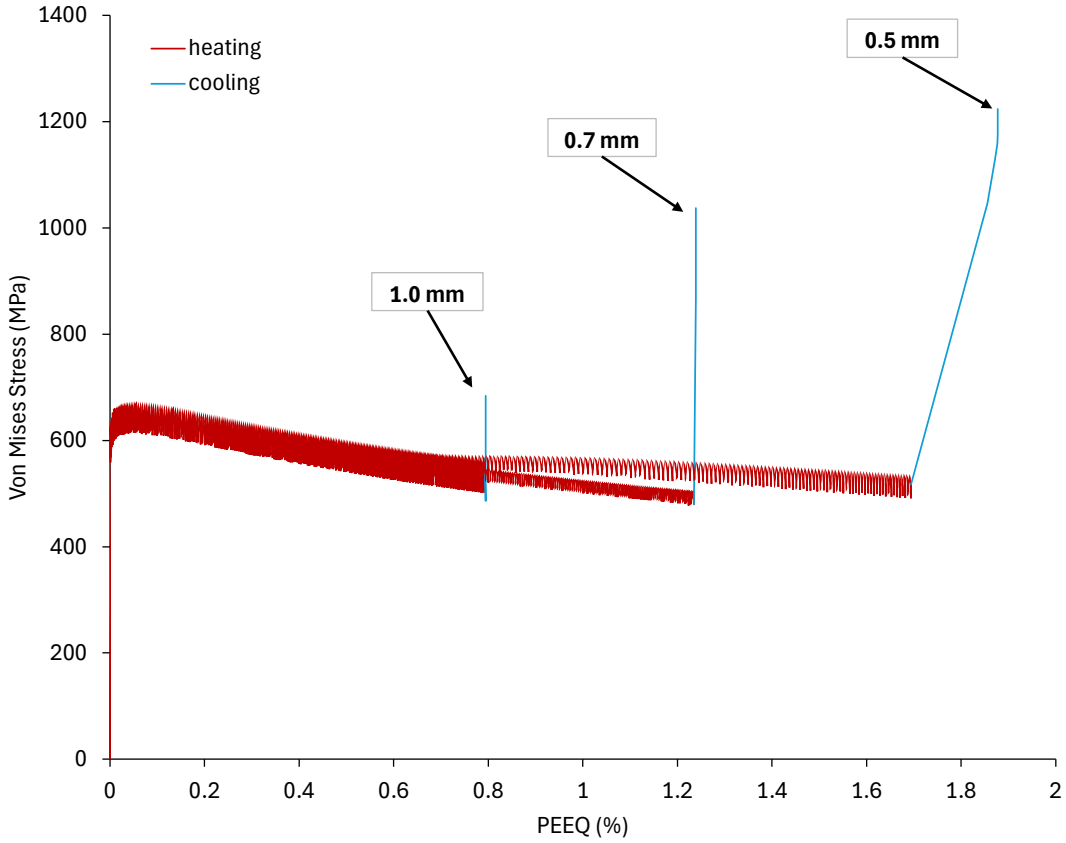

Figure 7.8: Plastic equivalent strain (PEEQ) vs Von Mises stress for 0.5, 0.7 and 1.0 mm targets with values taken at the element in the irradiated region which accumulated highest PEEQ, for a simulation at 53.9 mm separation from the exit window following a 1s irradiation of 300 pulses.

7.3.6 Fatigue lifetime estimate

By taking the plastic equivalent strain values, utilising equation 3.13, and by setting the values of $\varepsilon_f = 0.108$, $\sigma_u = 981\ MPa$, and $E = 409\ GPa$ from a fit to the data of Cho et al. 2002 [560] (see Figures A.31 and A.32 and Tables A.23 and A.24 in appendices), an estimate for the fatigue life of each simulated sample could be obtained (Figure 7.10). The lifetime of thicker targets was seen to be considerably larger, with the 1.0 mm displaying the highest lifetime at every separation from the beam exit window.

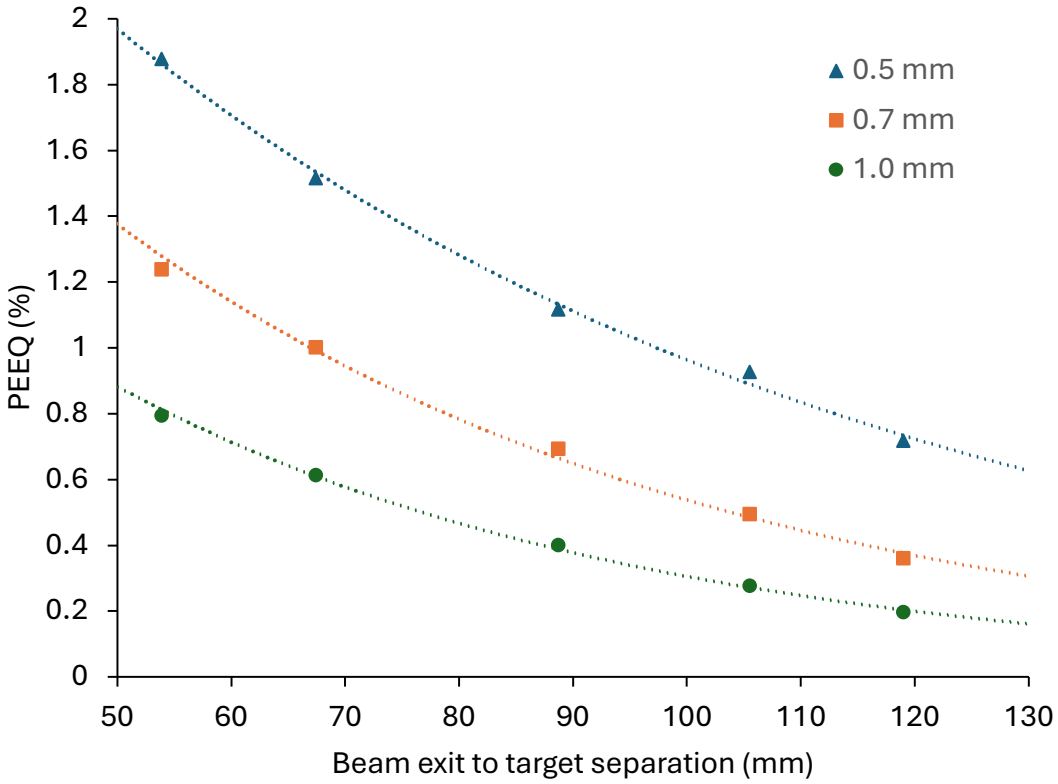

Figure 7.9: Element from simulation with highest percentage plastic equivalent strain (PEEQ) developed after a 300 pulse, 1s irradiation and 60s cooling period for 0.5, 0.7, and 1.0 mm tungsten targets placed at different separations from the beam exit window. Exponential fits (dotted lines) were applied for every target thickness with each $R^2 > 0.99$

7.4 Discussion

Here we try to describe, through simulations and measurements, the material effects of delivering pulsed 6 MeV electron beams on tungsten targets to achieve FLASH dose rates in MV photon beams. Our study shows the temperature reductions possible when increasing electron beam size (FWHM) on thin targets, in our case by increasing target separations beyond 136 mm from the beam exit window.

Analytical models of electron beam heating effects have been developed [649–651] but often neglect radiative cooling [224, 652], property changes with temperature, scattering of electrons, and mechanical effects. Analytical thermal models of X-ray tube targets indicate that focal spot temperatures are limited by the heat capacity. Where temperature increases are proportional to power and pulse duration and

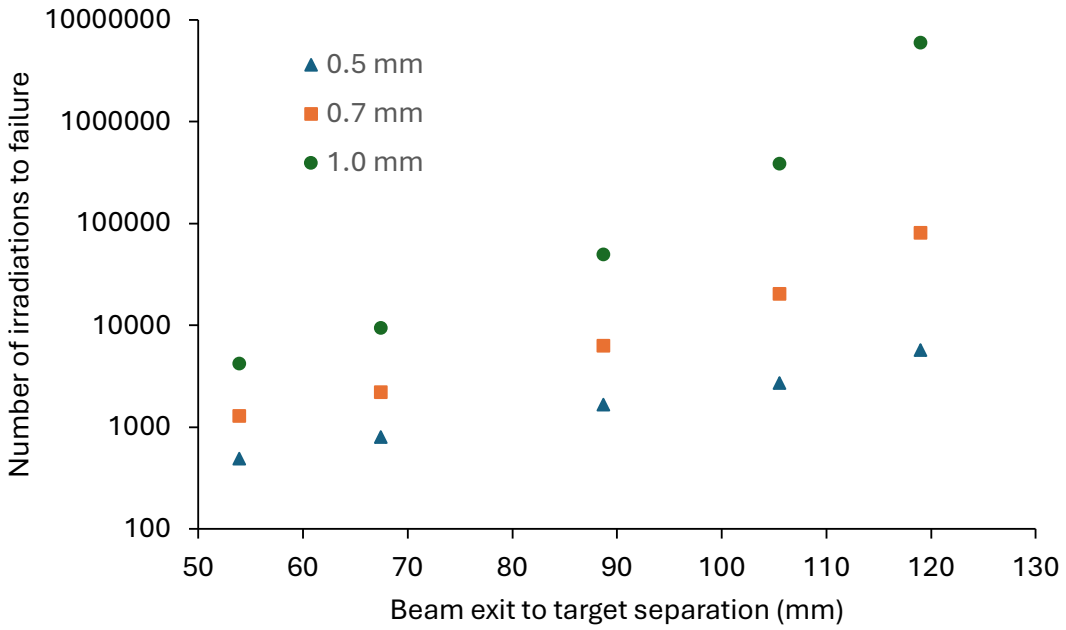

Figure 7.10: Fatigue lifetime estimates for 0.5 mm, 0.7 mm, and 1.0 mm targets undergoing 300 pulse, 1s irradiations with 60s cooling afterward.

inversely proportional to element mass and heat capacity [393, 438, 440]. These models are also limited in our case with; radiative effects, lateral heat redistribution, greatest energy absorption at appreciable depths (i.e., a volumetric instead of surface heat source), and pulsed irradiations (not continuous). However, they do indicate that peak temperature reductions can occur by increasing focal spot size without sacrificing photon dose rate.

Mechanical responses following irradiation have been modelled using finite element analysis in ANSYS, COMSOL, and ABAQUS [403, 409, 419, 420, 422, 552, 562, 653, 654]. These models assume equivalence to multiaxial mechanical loading to integrate mechanical properties. Models for X-ray tubes have also shown that higher power density input increased temperature, stress, and size of plastic zone [396, 653]. Whilst experimental high-heat-flux fatigue tests of tungsten as a plasma facing material [395, 644, 645], monoblock [551, 655], and spallation target [408], with pulsed electron beams have revealed yielding, plastic deformation, fatigue damage, and crack formation [551].

Similar reductions in peak target temperatures have been obtained for 10 MeV

electron beam models when increasing beam full width at half-maxima (FWHM) [429]. Temperature fluctuations also reduced with increasing pulse repetition rates, with current correlating linearly with peak temperature. Thinner targets were seen to reduce average temperature build up, provide similar depth-dose profiles (for 0.2-1 mm), and shift the depth of dose maxima toward the phantom surface [429]. However, in this study, thermo-mechanical effects were not considered.

Though experimental temperature measurements showed considerable variability on the target surface from a radial offset of the thermocouple bead relative to the beam centre, as well as variability in thermal contact, their overall trend follows that of the simulated exponential peak temperature decay. The observation that a temperature rise of <500 degrees was seen for targets beyond ∼100 mm from the beam exit window, is also within common design criteria for previous high heat flux tests in normal target operation in oxidising atmospheres [408]. This shows that although oxidative buildup could accelerate damage mechanisms and reduce yield strength [656], oxides may not form substantially in air throughout our FLASH irradiations for targets beyond ∼100 mm from the beam exit window independent of sample thickness. The temperature falloff for thin targets will reduce the time for which oxidation can occur but is indicative of a greater susceptibility to yielding from a faster transition through the DBTT [407, 551, 657].

By contrast, it is likely our simulated temperature results are conservative as they overestimate the maximum input power density from an assumption of a purely monoenergetic incident beam. The finding that the 0.7 mm target reaches a higher temperature peak than the 0.5 or 1.0 mm targets may be a result of a lower surface area to volume ratio (i.e. less radiative cooling) or lower thermal mass (i.e., faster temperature rise) than the 0.5 and 1.0 mm targets, respectively.

Although our depths of maximal energy deposition were similar to literature (∼0.35 mm [429]), a more realistic energy spectrum may shift the depth of energy density maxima toward the upstream target surface. Likewise, the relatively high thermal conductance and specification of consistent contact between surfaces may have provided conservative estimates of the temperature gradients and therefore values

of stress and strains. The shakedown behaviour seen, mirrors those highlighted in plasma facing components with tungsten [658]. In addition, the strains accumulated from tie constraint surrounding the targets are likely to be mitigated by loosening the contact with the retaining rings to balance surface heat transfer whilst allowing spaces for thermal expansion to relieve stress (and therefore strain).

Despite these limitations alongside the lack of substantive material literature (see appendices Figures A.31 and A.32, & Tables A.23 and A.24) with the assumptions of fully reversed loading in isothermal conditions [551], the fatigue lifetime estimates indicate all targets tested could survive an appreciable lifetime for separations beyond ∼100 mm from the beam exit window. The fatigue life estimation and our FEM simulation, however, may not fully account for the increased UTS of thinner targets [399], the reduced yield strength with temperature, as well as the non-linear accumulation of damage toward the end of the material lifetime. Our lifetime estimates however, indicate the long-term feasibility of using our setup at target separations from the exit window which enable photon dose rates in the FLASH range.

Our separation of the target and backer materials also exploits favourable radiative cooling properties of unpolished targets without the additional constraints imposed by the fatigue life of backing materials [234, 429, 431]. However, our analysis did indicate material yielding and residual tensile plastic deformation which could risk crack development [395, 653]. Though crack development is a major contributor to other use cases, the function of a target with non-critical cracks to produce FLASH dose rates is the subject of ongoing work. Here, stacking thin targets may also enhance the rigidity of targets from utilising the enhanced ductility and strength of thinner targets but may enhance oxidation due to increased surface area. Our transient grating spectrometry and simulation results also indicate negligible displacement damage, likely from a combination of very short irradiation timescales, a low displacement cross section, and annealing effects at higher temperatures. These results followed were consistent with those from 8 MeV irradiations with extremely high applied doses where damage barely reached 1e-4 dpa [659]. Though

our analysis did not include considerations of pulse repetition rate, for an equal stress range, higher frequencies have been seen to reduce peak to trough amplitudes of temperature spikes [429], and to increase component lifetimes [660]. Transitioning from FLASH to CONV irradiations with repetition rate will most likely alter damage accumulation from low cycle (high strain) to high cycle (low strain) domains. However, it is anticipated that the cumulative fatigue of targets in the latter case will endure pulses of lesser amplitude and thus undergo more gradual, observable degradation over timescales longer than our required fatigue lifetime. Our lifetime calculations are also well above previously assumed values for FLASH irradiations with $\sim$50 $\times$ 1s irradiations per week, for a lifetime of 5 years ($\sim$3000 cycles) at separations $\geq$100 mm [234, 405]. With further equipment optimisation, our thermocouple system could behave as a calorimetry system for real time non-destructive irradiation monitoring [661]. Higher energy incident electron beams may also produce higher FLASH dose rates, and more favourable depth-dose profiles with lower peak temperatures and temperature gradients to increase target longevity [234]. Here, the thickness of each optimal target is likely to increase with beam energy (see Figures A.20 and A.21, and Table A.9), and higher dose rate output may enable dose rate flexibility to produce broader field sizes for larger animal experiments more akin to clinical treatment volumes.

8
Conclusion

This thesis aimed to establish preclinical platforms to deliver MV photons at FLASH dose rates while ensuring bremsstrahlung target longevity, and to provide electron SFRT with flexible collimation systems. Such research is extremely relevant to highlight the critical issues that must be overcome to enable their clinical translation and to inform how future beamline systems and technologies could be developed. An approach is presented in chapter 4 that can be used to perform preclinical FLASH irradiation studies with 6 MV Photons with thin in-air tungsten bremsstrahlung targets. Using transmission grating spectrometry, thermocouple and dosimetric film measurements, together with finite element and Monte Carlo simulations, chapter 7 demonstrates that broadening the incident electron beam and increasing the separation between the exit window and the target can produce FLASH dose rates from thin tungsten targets (12–32 Gy/s) — albeit lower than studies showing a fullest effect at ~ 100 Gy/s — while reducing peak temperatures and accumulated strains. These simple modifications enable robust targets to be used for MV photon FLASH investigations with minimal displacement damage and oxidation. The resulting photon beam characteristics show that output dose rates (average and instantaneous) are high at surface but reduce quickly with depth because of the SSD used, which also limits field size and flatness. Currently, the resulting beam is only suitable for irradiation of small, thin in vitro samples and for superficial in vivo (mice)

irradiations, e.g., investigating the FLASH effect for skin toxicity or subcutaneous tumours, where there are no stringent requirements for high conformality, and the relatively large beam penumbra will not markedly affect outcomes. Nevertheless, it remains important in these applications to minimise surface dose.

By using this setup for hemi-thorax mice irradiations in chapter 5, a delay was observed in the onset of radiation-induced skin toxicity, along with a reduction in severity with increasing dose rate. Here, a similar FLASH sparing effect for irradiations using 6 MV photon, and 6 MeV electron beams, indicated that electron preclinical FLASH data can inform MV photon delivery. However, the differences in dose distributions (beam divergence, penumbra and depth-dose) prevents a perfect correlation between prescribed doses and observed toxicity between the modalities. Through the integration of brass collimators into the preclinical electron beamline shown in chapter 6, it is demonstrated that SFRT electron FLASH treatments with high peak doses provide effective tumour growth delay and prolonged tumour control akin to homogeneous irradiations. Here, it is demonstrated that combining spatial modulation, higher peak doses, and FLASH dose rates can produce favourable tumour response even with only partial tumour coverage. This platform establishes a flexible experimental framework to assess how parameters such as peak dose, valley dose, PVDR, and fractionation define the therapeutic benefit of SFRT. Ultimately, insights gained with this platform will inform rational, standardised treatment protocols for future clinical translation. In addition, electron SFRT arrangements also enable the combination of ultra-high dose rate FLASH and SFRT to be explored. Overall, this thesis has generated preclinical platforms that can be used to investigate the biological mechanisms underpinning FLASH and SFRT. These investigations are crucial to explain previous findings, to test novel hypotheses, and to pave the way for their clinical translations both individually, and in combination with other therapeutic approaches.

9
Future work

To increase FLASH dose rates with photons, above those used in chapter 4, future work may focus on reducing the backer thicknesses (<6 mm), with sequential measurements using different target thicknesses to obtain a combination which maximises photon dose rate, and minimises electron contamination. To increase current and power input for our preclinical linac, ongoing work in the FLASH group is aimed at replacing the electron gun from a diode to a triode device, and replacing the 2 MW magnetron with a 3 MW version respectively. These modifications will likely enable higher photon dose rate output (by a factor of ~ 2)[1] without as great a need to optimise target geometry, positioning, and SSD. As a result, the beam energy for highest output would likely be altered. Therefore, to understand how the target setup for photon FLASH should be adjusted, beam energy from our current setup may be changed by altering gun heater current / RF (de) tuning to optimise target thickness at energies from 5-8 MeV. In doing so, this would predict the beam currents required for photon FLASH dose rates and preclinically relevant field sizes, at existing and future preclinical beamlines.

Likewise, the beam energy input for the Geant4 and subsequent finite element model highlighted in chapter 7 could be altered to predict the fatigue properties of potential

[1] as photon dose rate, X and the r-f peak power, P are related by $X \propto P^{\frac{n+1}{2}}$ (where $n \approx 3$ at 4 MeV, & $n \approx 2.7$ at 10 MeV) [662, 663]

targets. In addition, analysis could be extended to test other target materials such as tantalum, or tungsten alloys which may be less brittle at room temperature, and may have a larger body of literature of fatigue properties. For tungsten, other Johnson-Cook parameter, and low cycle fatigue model inputs may also highlight the potential range of feasible fatigue lifetimes. Meanwhile, mechanical loading tests could be performed on material samples to accurately determine their low-cycle fatigue properties. To better match temperature falloff between these models and simulations, the finite element model could be extended to introduce more detailed thermocouple geometry, alongside the silica glass window. Here, thin tungsten foils can be readily stacked to form layered target arrangements, enabling investigations which would highlight whether their superior mechanical properties individually would result in an improved operational lifetime collectively relative to a solid target. Adaptations to the thermocouple jig should aim a) to obtain the electron beam offset from the radial centre for each pulse non-destructively b) to address the offset by varying inputting these into the finite element model c) to intentionally place thermocouple beads at a radial distance instead of relying on retrospective measurement. Meanwhile, TGS measurements could also be performed with a compact TGS setup capable of assessing instantaneous damage in real time.

Alongside other preclinical work exploring tumour growth, the assay in chapter 5 may be extended to lower doses (10-20 Gy) to reduce the likelihood of early death from induced toxicity and to extend the period over which toxicity progression can be monitored. Similarly, prior to the collimator, for electron irradiations, a ~ 10 mm bolus could be used to obtain a PDD and scatter with depth more akin to the photon collimator setup. This may also reduce the subsurface electron dose deposited, which may have caused a greater number of mice to be euthanised from higher levels of toxicity. Collimator size could also be slightly reduced to ensure greater flatness and to better spare peripheral sensitive organs. Likewise, for photon irradiations, a diverging collimator may reduce the divergence seen with depth. For electron FLASH irradiations, a large increase of sparing was seen for electron dose rates of 1800 Gy/s compared to 30 Gy/s. Exploring dose rates above 30 Gy/s may

help identify the onset of maximal sparing and enable comparison with prior work which indicates this effect at ∼100 Gy/s [136].

Doses could also be increased for all irradiation groups in the setups highlighted in chapter 6 as doses were well tolerated. In the homogeneous group, higher doses may yield more complete responses, forming a basis for delivering identical peak doses with progressively increased spatial modulation (i.e., larger ctc distances). This would enable the transition from homogeneous to SFRT domains to be explored. Similarly, follow on investigations could investigate the effect of homogeneous and SFRT irradiations to abscopal tumour response by subcutaneous tumour implantation into the left hind limb, as well as to an irradiated right hind limb. While, for normal tissue response in skin, a number of SFRT patterns and studies could be performed with the SARRP system to determine maximum dose thresholds for a given SFRT pattern [219, 276, 327, 358, 664, 665]. Here, careful alignment of the focal spot with the collimator apertures, together with positioning the irradiated region close to the downstream collimator exit, would enable increased dose rates and consistent lateral dose profiles [666–668]. In a similar way to spatial modulation, dose rate could also be escalated by altering SSD or repetition rate to unpack the contributions of FLASH and SFRT. In doing so, this is likely to indicate the effect of dose rate in peak, or peak & valley regions as the dose rate is escalated. These investigations would indicate the extent to which normal tissue toxicity constrains the parameter space available for tumour irradiations in a given SFRT setup, while also highlighting similarities and differences in the mechanisms underlying outcomes from FLASH and SFRT irradiations.

For tumour irradiations an analytical model may highlight the doses received in irradiated volumes, taking into account electron spread with depth [669, 670]. These analytical models may be better suited for scenarios involving greater spatial modulation, which would otherwise require computationally expensive Monte Carlo simulations with small scoring volumes [671]. In doing so, matched volume-based doses could be prescribed for both homogeneous and SFRT setups, and for differing SFRT configurations, to assess the usability of this method for dose prescription and

to highlight differences from partial-volume irradiations reported by Kanagavelu et al. [286] and Tubin et al. [264, 672]. To provide a more accurate prescribed dose, matched in experiments and MC simulations with electron collimators, a more realistic mouse phantom may be beneficial to extend dose measurements to subsurface depths. In addition, altering beam parameter inputs to MC simulations such energy, beam size, direction radial offset, and tilt, as well as matching the voxel size to the resolution of scanned films could reduce observed differences. Preliminary work in our group with photon collimation systems has also highlighted their potential to preserve spatial modulation up to clinically relevant depths. Therefore, future work would adapt collimator design to mirror electron SFRT to better uncover the biological effect of subsurface spatial modulation.

Appendices

A
Appendices

Contents

A.1 Tabata, Ito and Okabe [386] practical range fitting constants

Table A.1: Expressions for a_i and c_i coefficients.

$a_1 = b_1 A/Z^{b_2}$	$c_1 = d_1/Z$
$a_2 = b_3 Z$	$c_2 = d_2 Z^{d_3}/A$
$a_3 = b_4 - b_5 Z$	$c_3 = d_4 - d_5 Z$
$a_4 = b_6 - b_7 Z$	$c_4 = d_6/Z^{d_7}$
$a_5 = b_8/Z^{b_9}$	$c_5 = d_8/Z^{d_9}$

where Z is the proton number, and A is the atomic mass

Table A.2: Values of the constants b_i and d_i

i	b_i	d_i
1	0.2335 ± 0.0091	$(2.98 \pm 0.30) \times 10^3$
2	1.209 ± 0.015	6.14 ± 0.29
3	$(1.78 \pm 0.36) \times 10^{-4}$	1.026 ± 0.020
4	0.9891 ± 0.0010	$(2.57 \pm 0.12) \times 10^2$
5	$(3.01 \pm 0.35) \times 10^{-4}$	0.34 ± 0.19
6	1.468 ± 0.090	$(1.47 \pm 0.19) \times 10^3$
7	$(1.180 \pm 0.097) \times 10^{-2}$	0.692 ± 0.039
8	1.232 ± 0.067	0.905 ± 0.031
9	0.109 ± 0.017	0.1874 ± 0.0086

A.2 Radiation length

The characteristic amount of matter traversed for high energy electrons in interactions is called the radiation length X_0 ($g\ cm^{-2}$), it is the average distance over which the electron loses e^{-1} of its energy via bremsstrahlung

$$X_0 = \left[4\alpha r_e^2 \frac{N_A}{A}\left\{Z^2\left[L_{rad} - f(Z)\right] + ZL'_{rad}\right\}\right]^{-1} \tag{A.1}$$

with

$$f(Z) = a^2\left[(1+a^2)^{-1} + 0.20206 - 0.0369a^2 + 0.0083a^4 - 0.002a^6\right] \tag{A.2}$$

with $a = \alpha Z$, $L_{rad} = ln(184.15\ Z^{-\frac{1}{3}})$ and $L'_{rad} = ln(1194\ Z^{-\frac{2}{3}})$. Here A is the atomic mass of the absorber ($g\ mol^{-1}$), Z is the atomic number, α is the fine structure constant $\frac{e^2}{4\pi\epsilon_0\hbar c} = \frac{1}{137.03599913931}$, N_A is Avogadro's number $6.02214076 \times 10^{23}$, and r_e is the classical electron radius 2.817940322719 fm.

A.3 Relevant Statistical quantities

A.3.1 Gafchromic film error propagation

$$OD_{specific} = log_{10}\left(\frac{I_0}{I}\right) \tag{A.3}$$

$$\sigma_{OD_{specific}} = \sqrt{\left(\frac{1}{ln\,(10)}\frac{\sigma_{I_0}}{I_0}\right)^2 + \left(\frac{1}{ln\,(10)}\frac{\sigma_I}{I}\right)^2} \tag{A.4}$$

A.3.2 Statistics

Error

Error has been acknowledged to have two components; random and systematic. The error is defined as the difference between the true value and the measurand value. Errors have both a value and a sign [388].

Accuracy

Accuracy is characterised by how close a single value is to the true value.

Uncertainty

Uncertainty is characterised by a distribution of values that could reasonably be attributed to the measurand. This parameter is usually an estimated standard deviation usually assumed to be symmetric. This estimate is an evaluation of the lack of knowledge of the measurand once systematic effects have been accounted for [388]. Uncertainty includes type A (random or a posteriori), and type B (systematic or a priori) uncertainties. The former is estimated from repeated independent measurements of a quantity, where the standard deviation can be calculated. The latter can only be assigned and is often not readily quantifiable. An estimated standard deviation (ESD) can be created with limits such that the correct value is likely to be found in 70 % of the measurements. These uncertainties can be combined in quadrature to provide an overall uncertainty [673].

Type A Standard Uncertainty

A number of estimated quantities can be used to defined type A uncertainties, including: [388, 674, 675]:

Sample Mean

$$\bar{x} = \frac{\sum_{i=1}^{N} x_i}{N} \tag{A.5}$$

Sample Variance

$$s^2 = \frac{\sum_{i=1}^{N} (x_i - \bar{x})^2}{N-1} \tag{A.6}$$

Sample Standard Deviation

$$s = \sqrt{\frac{\sum_{i=1}^{N} (x_i - \bar{x})^2}{N-1}} \tag{A.7}$$

Standard Deviation of the mean value

$$s(\bar{x}) = \frac{s}{\sqrt{N}} \tag{A.8}$$

Weighted mean

A weighted average of a quantity x_{wav} is given by:

$$x_{wav} = \frac{\sum w_i x_i}{\sum w_i} \tag{A.9}$$

Weighted measurement uncertainty

The uncertainty on each weighted measurement σ_i is:

$$\sigma_i = \frac{1}{\sqrt{w_i}} \tag{A.10}$$

Standard deviation of the weighted mean

The uncertainty on the weighted mean is:

$$\sigma_{wav} = \frac{1}{\sqrt{\sum w_i}} \tag{A.11}$$

Fractional uncertainty of the standard deviation (of a normally distributed quantity)

$$\frac{\sigma\left(s\left(\bar{x}\right)\right)}{\sigma(\bar{x})} = \frac{1}{\sqrt{2\left(N-1\right)}} \tag{A.12}$$

where $\sigma\left(s\left(\bar{x}\right)\right)$ is the uncertainty of $s\left(\bar{x}\right)$

Sample m^{th} Centralised Moment

$$\mu_m = \frac{\sum\limits_{i=1}^{N}\left(x_i - \bar{x}\right)^m}{N} \tag{A.13}$$

Sample Skewness

$$\beta_1 = \frac{\mu_3}{s^3} \tag{A.14}$$

Sample Kurtosis

$$\beta_2 = \frac{\mu_4}{s^4} \tag{A.15}$$

Type B Uncertainty

These uncertainties are those for which repeated measurements will not yield an estimate. These uncertainties are estimated to correspond with standard deviations. It is assumed that these uncertainties stem from probability distributions with known shapes. The distribution is often described by a rectangular probability density, such that the true value has an equal probability of being found between a symmetric upper and lower limit $\pm L$. Therefore the uncertainty is given as:

$$u_B = \frac{L}{\sqrt{3}} \tag{A.16}$$

With an assumed triangular distribution this becomes:

$$u_B = \frac{L}{\sqrt{6}} \tag{A.17}$$

If instead the distribution is assumed to be Gaussian, a confidence limit, k can be chosen corresponding to 68% confidence for k = 1, 95% for k = 2, and 99.7% for k = 3.

$$u_B = \frac{L}{k} \tag{A.18}$$

A.3.3 Statistical tests

Chi-Square Test

$$\chi^2_{N-1} = \sum_{i=1}^{N} \frac{(A_i - E_i)^2}{E_i} \tag{A.19}$$

Where A_i are observations and E_i are expected measurements and the statistic has $N - 1$ degrees of freedom

Reduced Chi-Squared / Chi-Squared per degree of freedom

$$\tilde{\chi}^2 = \frac{\chi^2}{d} \tag{A.20}$$

Where d is the number of degrees of freedom

A.3.4 Population Statistics from [512]

Population Standard Deviation

$$\sigma = \sqrt{\frac{\sum_{i=1}^{N} (x_i - \bar{x})^2}{N}} \tag{A.21}$$

Population Variance

$$\sigma^2 = \frac{\sum_{i=1}^{N} (x_i - \bar{x})^2}{N} \tag{A.22}$$

A.3.5 Normal distribution

Full Width at Half Maximum

$$FWHM = 2\sqrt{2ln2}\,\sigma \approx 2.355\sigma \tag{A.23}$$

Half Width at Half Maximum

$$HWHM = \sqrt{2ln2}\,\sigma \approx 1.177\sigma \tag{A.24}$$

A.3.6 Covariance

The covariance σ_{xy} of N pairs $(x_1, y_1), ..., (x_N, y_N)$ is

$$\sigma_{xy} = \frac{1}{N} \sum_{i=1}^{N} (x_i - \bar{x})(y_i - \bar{y}) \tag{A.25}$$

A.3.7 Average absolute deviation

$$AAD = \frac{1}{N} \sum_{i=1}^{N} (|x_i - \bar{x}|) \tag{A.26}$$

Where $\bar{x}$ is the mean of the data

A.3.8 Median absolute deviation

$$MAD = median\,(|x_i - \tilde{x}|) \tag{A.27}$$

Where $\tilde{x}$ is the median of the data

A.3.9 Propagation of Uncertainties from [675]

If $q = x + z + u + ...$ then

$$\delta q = \sqrt{(\delta x)^2 + (\delta z)^2 + (\delta u)^2 + ...} \tag{A.28}$$

If $q = Bx$ then:

$$\delta q = |B|\,\delta x \tag{A.29}$$

If q is a function of with one variable, $q(x)$ then:

$$\delta q = \left|\frac{dq}{dt}\right| \delta x \tag{A.30}$$

If q is a power, $q = x^n$, then:

$$\frac{\delta q}{|q|} = |n| \frac{\delta x}{|x|} \tag{A.31}$$

If q is a function of variables x,...,z, then (for independent random errors):

$$\delta q = \sqrt{\left(\frac{\delta q}{\delta x}\delta x\right)^2 + ... + \left(\frac{\delta q}{\delta z}\delta z\right)^2} \tag{A.32}$$

A.4 Preclinical experimental setup for megavoltage photons

A.4.1 Primary electron beam properties

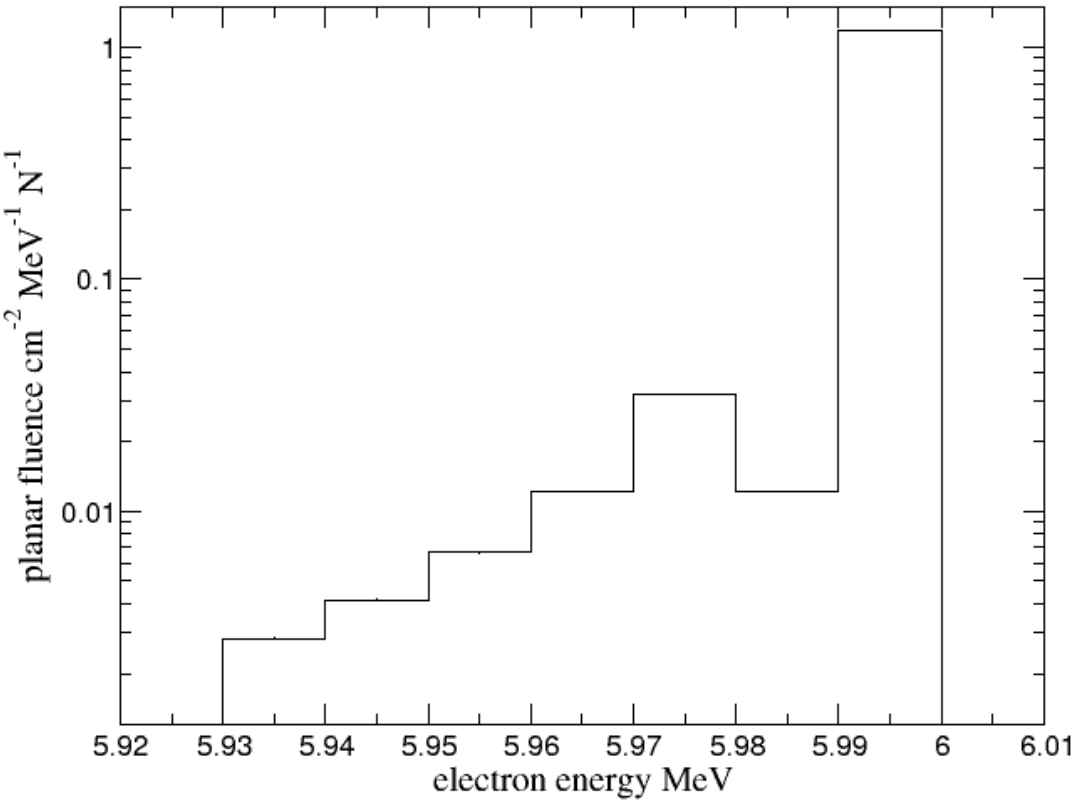

Figure A.1: EGSnrc simulation of the planar fluence energy distribution of electron beam incident on the upstream surface of the tungsten disc. A monoenergetic 6 MeV beam of 1e7 particles was modelled passing through the beryllium copper exit window and air separation before reaching the upstream tungsten surface.

A.4.2 Secondary photon beam properties

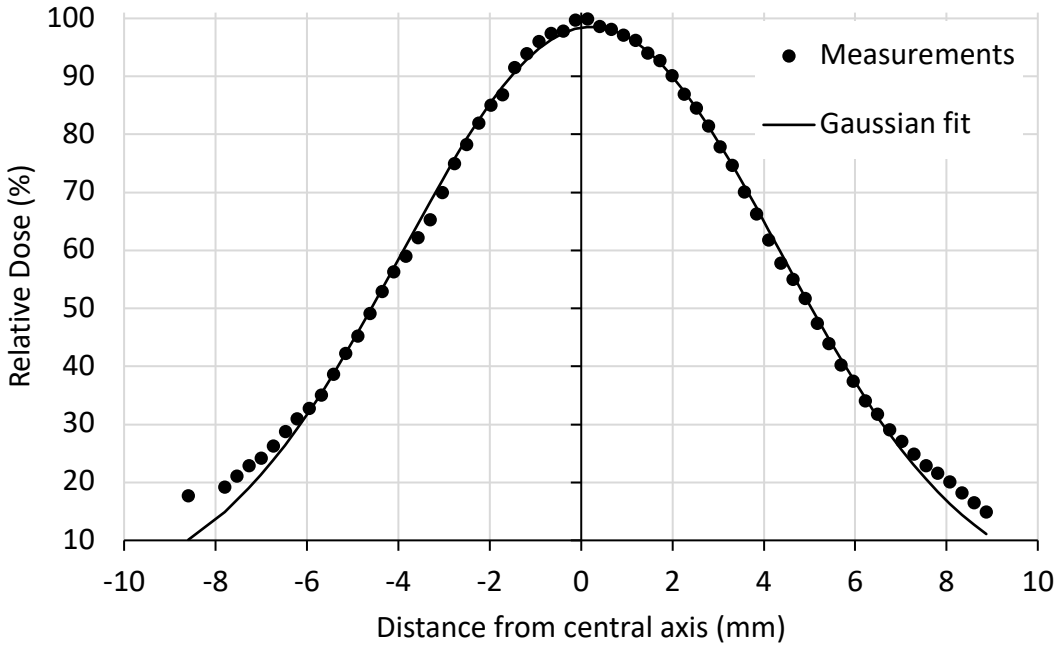

Figure A.2: Electron beam profile measurement with a 25 mm diameter EBT-XD film placed on the upstream surface of the tungsten discs, within the bremsstrahlung target assembly.

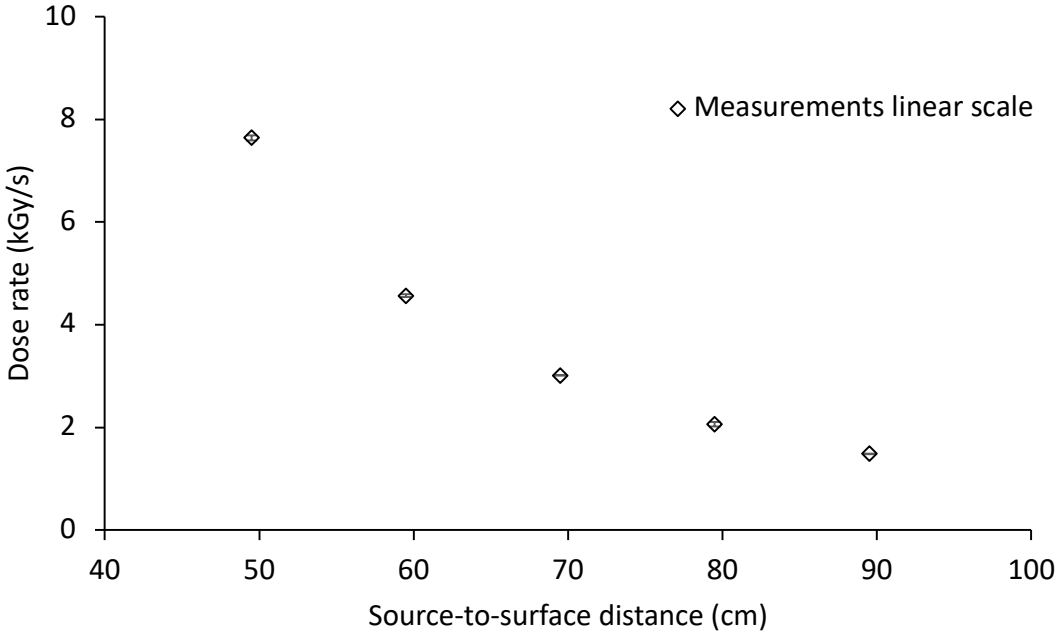

Figure A.3: Electron surface dose rate in kGy/s at different source-to-surface distances, measured with EBT-XD film on the surface of a 150 × 150 × 150 mm^3 solid water phantom. The markers indicate the mean value of 3 repeated measurements, with (small and within the marker) error bars indicating the standard deviation.

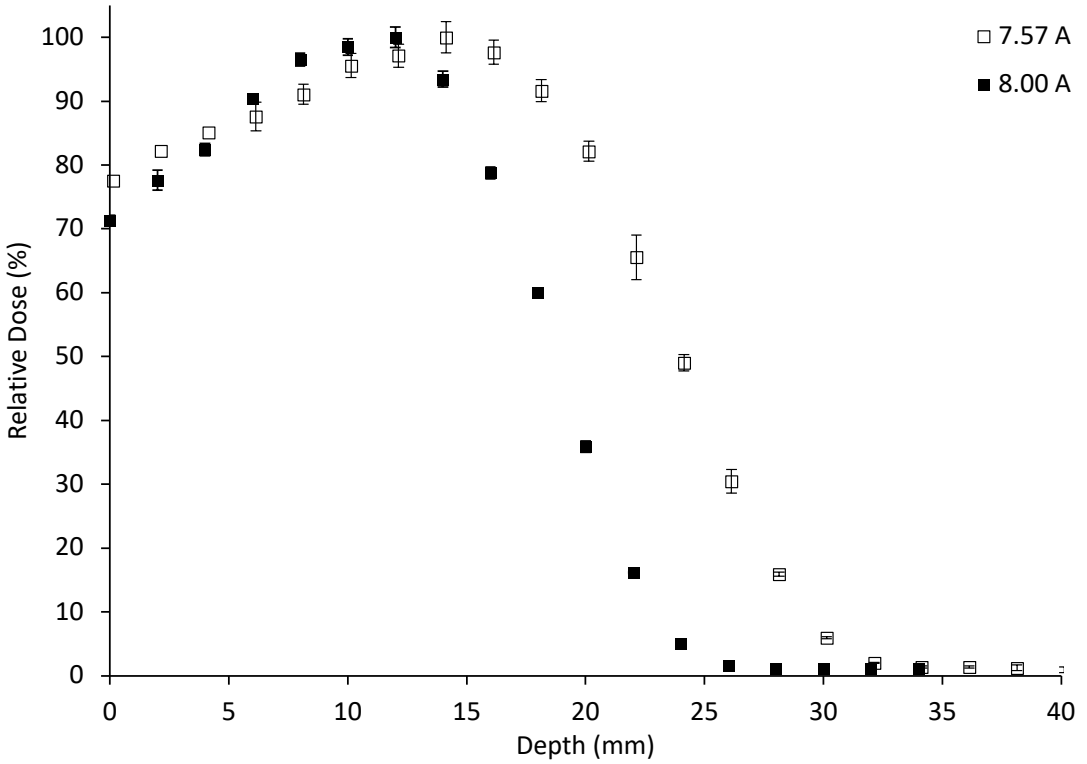

Figure A.4: Percentage depth-dose curves for our 6 MeV (nominal) electron beam, measured with EBT-XD film at various depth in a 150 × 150 × 150 mm^3 solid water phantom at a source-to-surface distance of 72 cm, for a gun heater current of 7.57 A (unfilled square markers) and 8 A (filled square markers). The markers indicate the mean value of 3 repeated measurements, with error bars indicating the standard deviation.

A.5 Preclinical comparison of megavoltage electron and photon irradiations

A.5.1 Dosimetry

Film dosimetry: Film pieces (23×34 mm^2, positioned at the surface of the mouse phantom (Figure A.14), which was placed in the mouse cradle as the mice in the beam path) were used to verify the delivered doses prior to or after mouse irradiations, for each dose rate in this study. Films were scanned 24 h after the irradiations (Epson Perfection v850 Pro, Seiko Epson Corporation, Nagano, Japan), and the red channel was analysed with ImageJ (version 1.52a, Wayne Rasband, National Institutes of Health). Dose was averaged over a 12×7 mm^2 area of the most exposed part of the film. Film calibration had previously been performed in a 6 MeV electron and a 6 MV photon beam from a clinical Varian TrueBeam (Varian Medical Systems Inc,

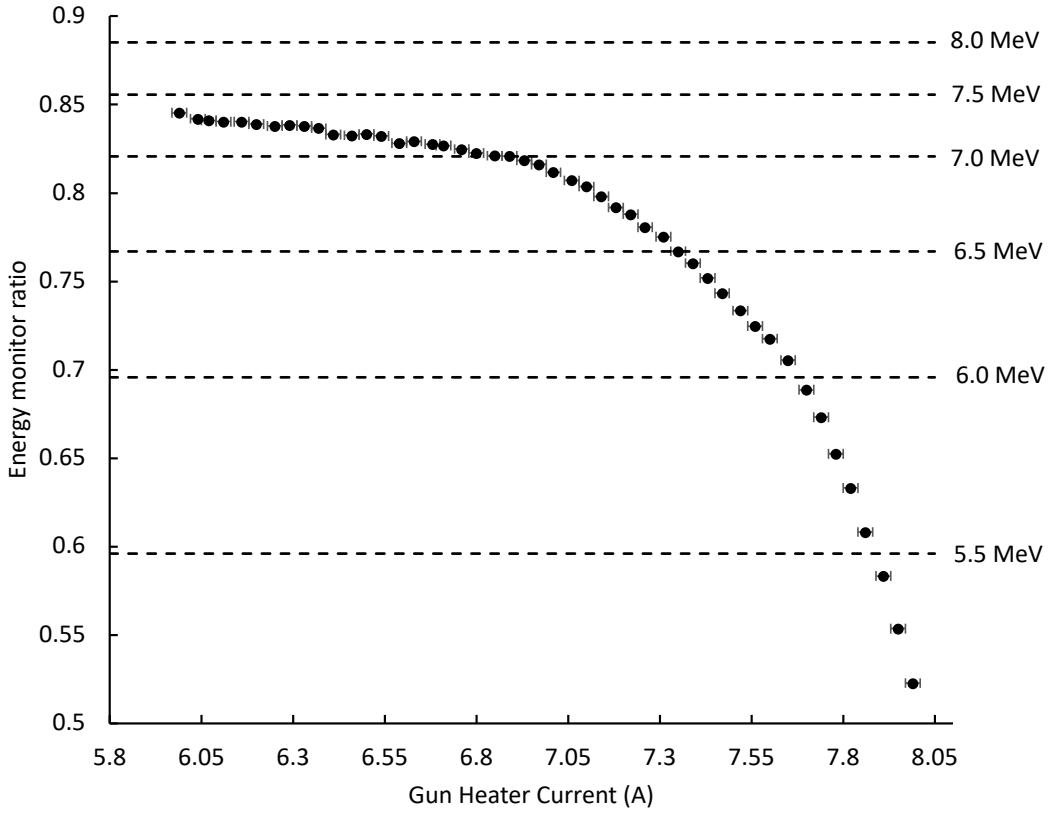

Figure A.5: Energy monitor ratios obtained at a source-to-surface distance of 72 cm, for a range of gun heater currents of 6 to 8 A in increments of 0.04 A. The markers indicate the mean value of 3 repeated measurements from single pulse irradiations, with error bars on the x and y axis indicating the repeatability of gun heater current settings (± 0.02 A), and standard deviation of the measured ratio respectively. Each dashed horizontal line represents an energy monitor ratio obtained from a simulation of a monoenergetic electron beam of a given energy, as reported in Berne et al. [530].

Palo Alto, CA) linear accelerator, at the Churchill Hospital site in Oxford, UK.

A.5.2 Experimental setup

A.5.3 Irradiation parameters

Table A.3: Beam parameters used for single dose 20 Gy hemi-thorax irradiations using a 6 MV photon beam.

Dose rate (Gy/s)	Delivery time (s)	Pulse repetition rate (Hz)	Number of pulses (n)	Dose-per-pulse (mGy)
0.07	300	25	≈7500	≈3
0.2	100	25	≈2500	≈8
0.7	30	25	≈750	≈27
2.0	10	25	≈250	≈80
7	3	100	≈300	≈67
30	0.67	300	≈200	≈100

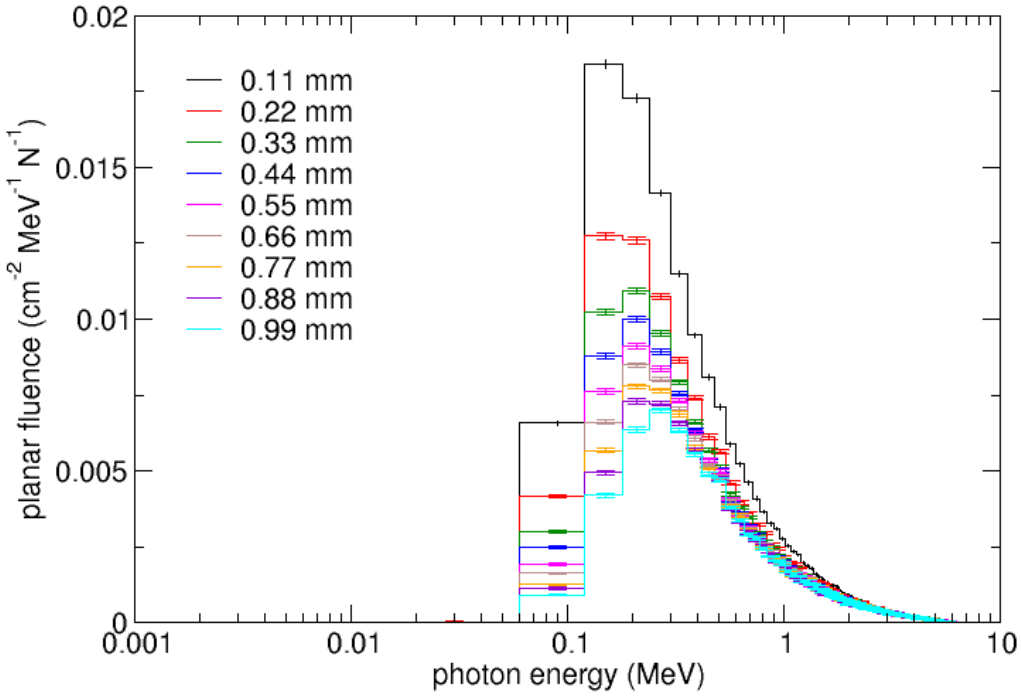

Figure A.6: EGSnrc simulation of the planar fluence energy distribution of photons reaching the surface of the solid water slabs. A monoenergetic 6 MeV beam of 1e6 particles was incident on varying tungsten discs of thicknesses 0.11-0.99 mm with a 6 mm copper hardening filter in the uncollimated arrangement in Figure 4.1A

Table A.4: Beam parameters used for single dose 25 Gy hemi-thorax irradiations using a 6 MV photon beam.

Dose rate (Gy/s)	Delivery time (s)	Pulse repetition rate (Hz)	Number of pulses (n)	Dose-per-pulse (mGy)
0.1	250	25	≈6250	≈4
0.3	83	25	≈2080	≈12
1.0	25	25	≈625	≈40
3.0	8.3	50	≈416	≈60
10	2.5	100	≈250	≈100
30	0.83	300	≈250	≈100

Table A.5: Beam parameters used for single dose 30 Gy hemi-thorax irradiations using a 6 MV photon beam.

Dose rate (Gy/s)	Delivery time (s)	Pulse repetition rate (Hz)	Number of pulses (n)	Dose-per-pulse (mGy)
0.1	300	25	≈7500	≈4
0.3	100	25	≈2500	≈12
1.0	30	25	≈750	≈40
3.0	10	50	≈500	≈60
10	3	100	≈300	≈100
30	1	300	≈300	≈100

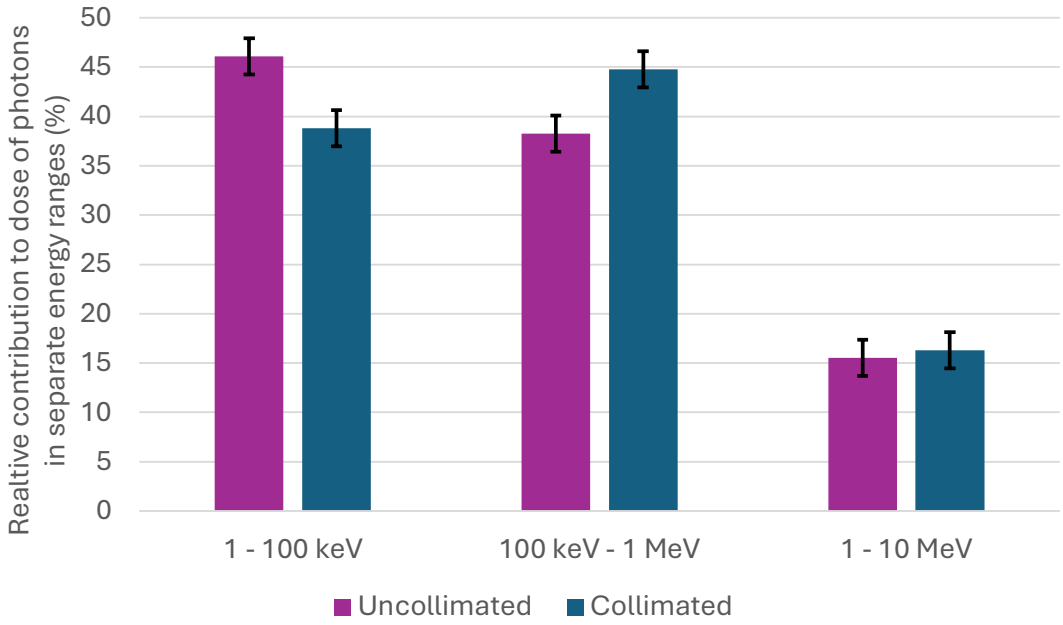

Figure A.7: Geant4 simulation of the energy distribution of particles contributing to dose at 1 mm depth in water. A 5.0 mm diameter, 1 mm thick cylindrical water scoring volume was used for uncollimated and 14 mm collimated arrangements with a 0.55 mm tungsten disc and 6 mm copper hardening filter.

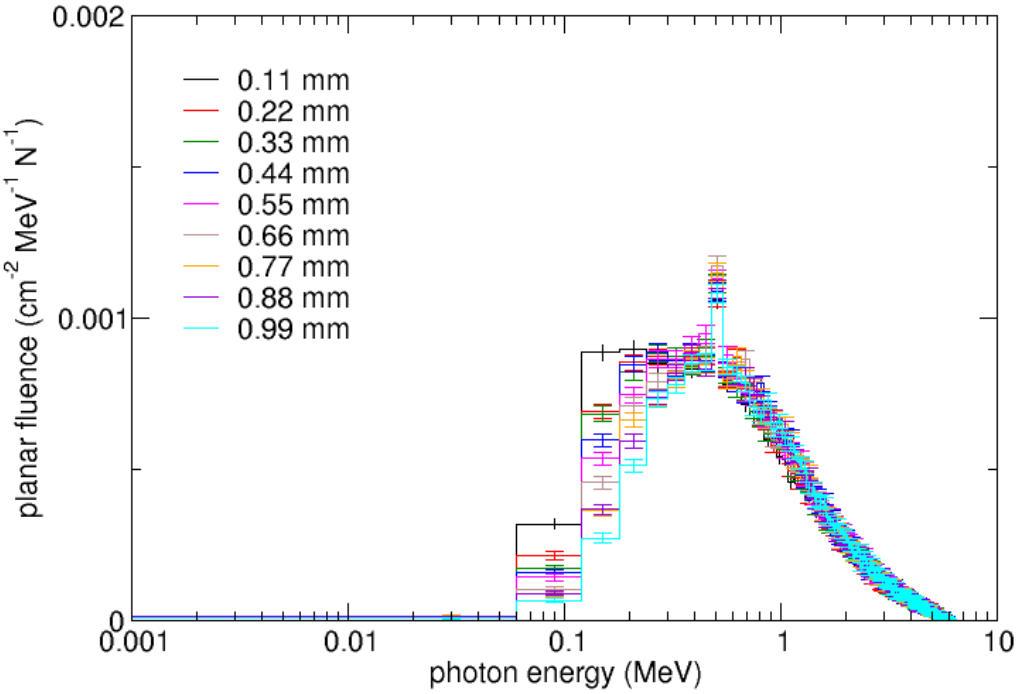

Figure A.8: EGSnrc simulation of the planar fluence energy distribution of photons reaching the surface of the solid water slabs. A monoenergetic 6 MeV beam of 1e6 particles was incident on varying tungsten discs of thicknesses 0.11-0.99 mm with a 6 mm copper hardening filter in the collimated arrangement in Figure 4.1B.

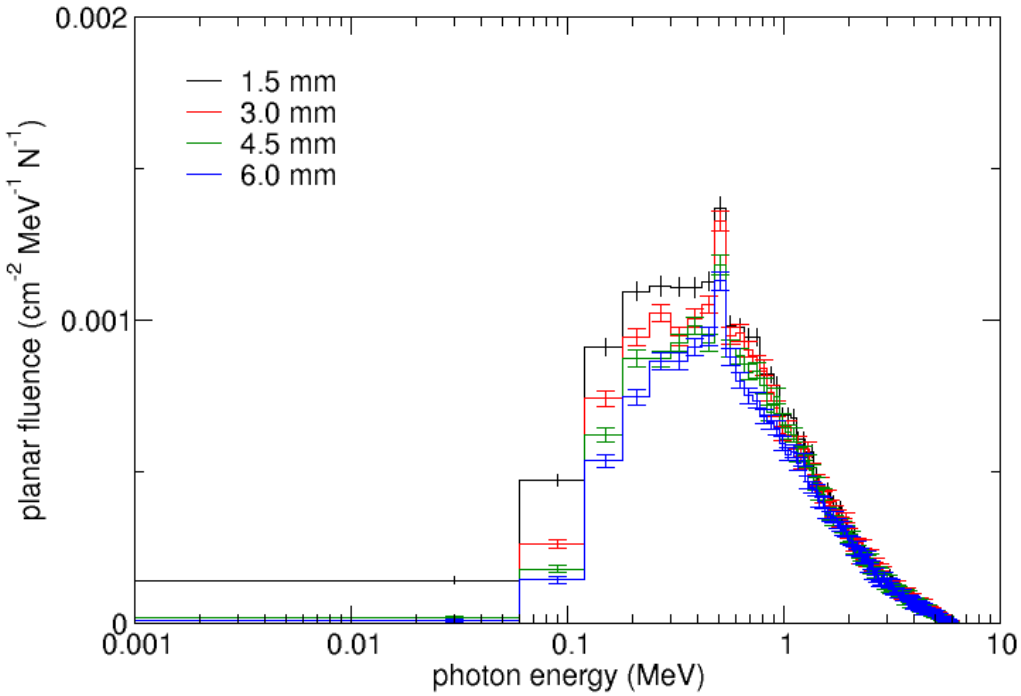

Figure A.9: EGSnrc simulation of the planar fluence energy distribution of photons reaching the surface of the solid water slabs. A monoenergetic 6 MeV beam of 1e6 particles was incident on 0.55 mm tungsten disc with varying copper hardening filter of thicknesses 1.5-6.0 mm in the collimated arrangement in Figure 4.1B.

Table A.6: Beam parameters used for single dose 30 Gy hemi-thorax irradiations using a 6 MeV electron beam.

Dose rate (Gy/s)	Delivery time (s)	Pulse repetition rate (Hz)	Number of pulses (n)	Dose-per-pulse (mGy)
0.1	300	25	≈7500	≈4
0.3	100	25	≈2500	≈12
1.0	30	25	≈750	≈40
3.0	10	25	≈250	≈120
10	3	100	≈300	≈100
45	0.67	300	≈200	≈150
1,800	0.017	300	6	5,000

A.6 Preclinical setup for spatially fractionated radiotherapy

A.6.1 Brass insert design

Item name	**Description**	**References**
Code, version/release date	EGSnrc v4 2025-1-15	[676]
Validation	Faddegon et al. 2009 Shiekh-Bagheri et al. 2000 Failing et al. 2022	[521, 677, 678]
Timing	Intel Platinum 8628, Cascade Lake, 2.90GHz CPU with 48CPU cores, and 380GB RAM	[592]
Source description	egs_chamber: Monoenergetic 6 MeV electrons Gaussian with sigma=0.0951 cm dosxyznrc: phase space from egs_chamber output	
Cross-sections	Photon cross sections = xcom Pair angular sampling = Simple Brems cross section = NRC Brems angular sampling = KM	
Transport parameters	AE=ECUT=0.521 MeV AP=PCUT=0.01MeV ESTEPE=0.25 SMAX=1e10 XIMAX=0.5 Boundary crossing=exact Skin depth for BCA=3 Electron-step algorithm=EGSnrc	
VRT and/or AEIT	Not used	[587]
Histories/Statistical uncertainty	1e9/Shown as error bars on figures	
Statistical methods	History-by-history	[515]
Postprocessing	Performed in python: a) PVDR = Average peak/Average valley [those between peaks] b) FWHM = Average width between 50% points in graph normalised to maximum c) Maximum dose in spot = Normalised to value at 0.5 mm depth	

Table A.7: Monte Carlo methods used in simulations following recommendations from TG 268 [679]

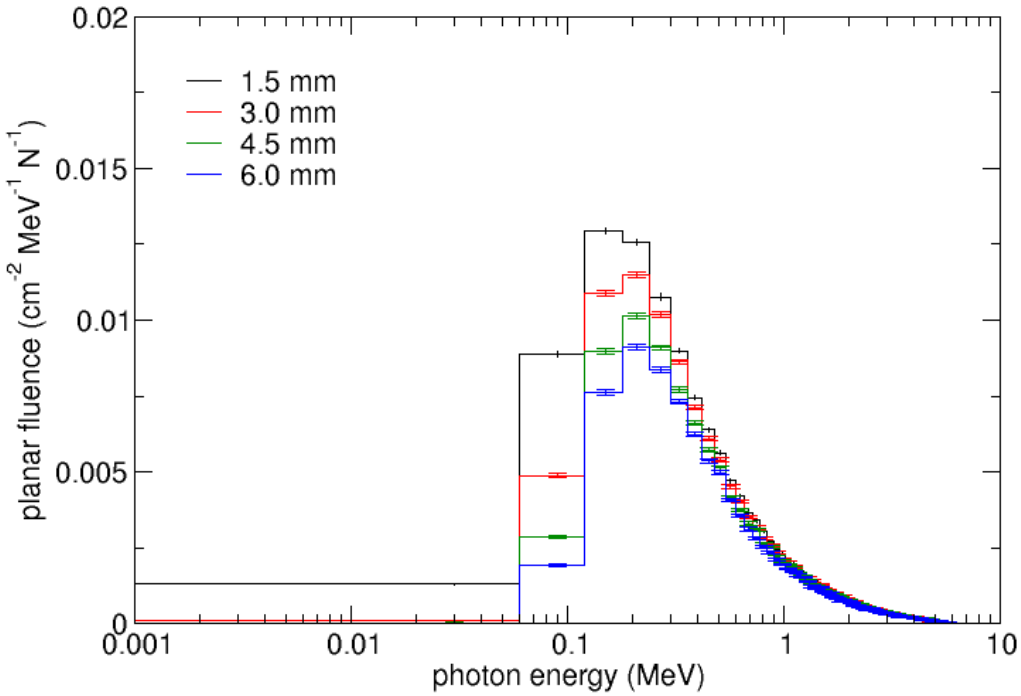

Figure A.10: EGSnrc simulation of the planar fluence energy distribution of photons reaching the surface of the solid water slabs. A monoenergetic 6 MeV beam of 1e6 particles was incident on a 0.55 mm tungsten disc with varying copper hardening filter of thicknesses 1.5-6.0 mm in the uncollimated arrangement in Figure 4.1A.

	Control	eCONV 10 Gy	eCONV 15 Gy	eCONV 20 Gy	eFLASH 10 Gy	eFLASH 15 Gy	eFLASH 20 Gy
Control	-	****	****	****	****	****	****
eCONV 10 Gy		-	ns	****	ns	ns	****
eCONV 15 Gy			-	ns	ns	ns	ns
eCONV 20 Gy				-	***	*	ns
eFLASH 10 Gy					-	ns	***
eFLASH 15 Gy						-	*
eFLASH 20 Gy							-

Table A.8: Šidák's multiple comparisons p value tests of irradiated groups shown in Figure A.19. Here markers indicate levels with: ns $p \geq 0.05$, * $p < 0.05$, *** $p < 0.001$, **** $p < 0.0001$

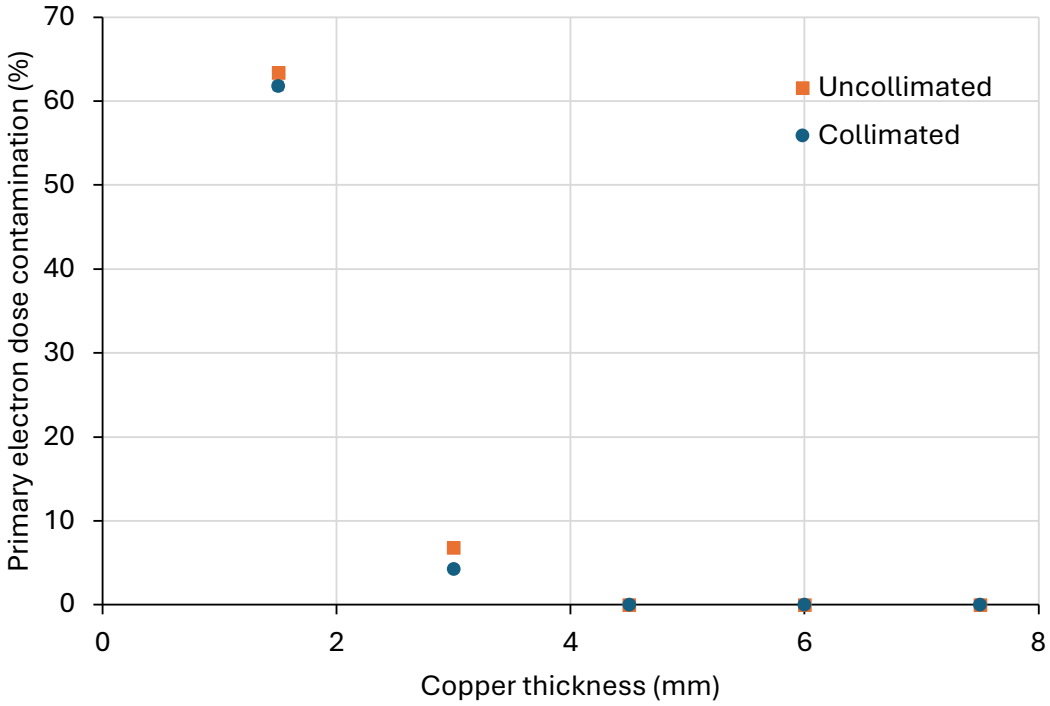

Figure A.11: Geant4 simulation of the primary electron dose contamination percentage at 1 mm depth in a 150×150×150 mm^3 water block, for a 5 mm diameter, 1 mm thick sensitive water volume. A monoenergetic 6 MeV beam of 1e7 particles was incident on a 0.55 mm tungsten disc with varying copper hardening filter of thicknesses 1.5-7.5 mm in the uncollimated and collimated arrangements in Figure 4.1A and Figure 4.1B.

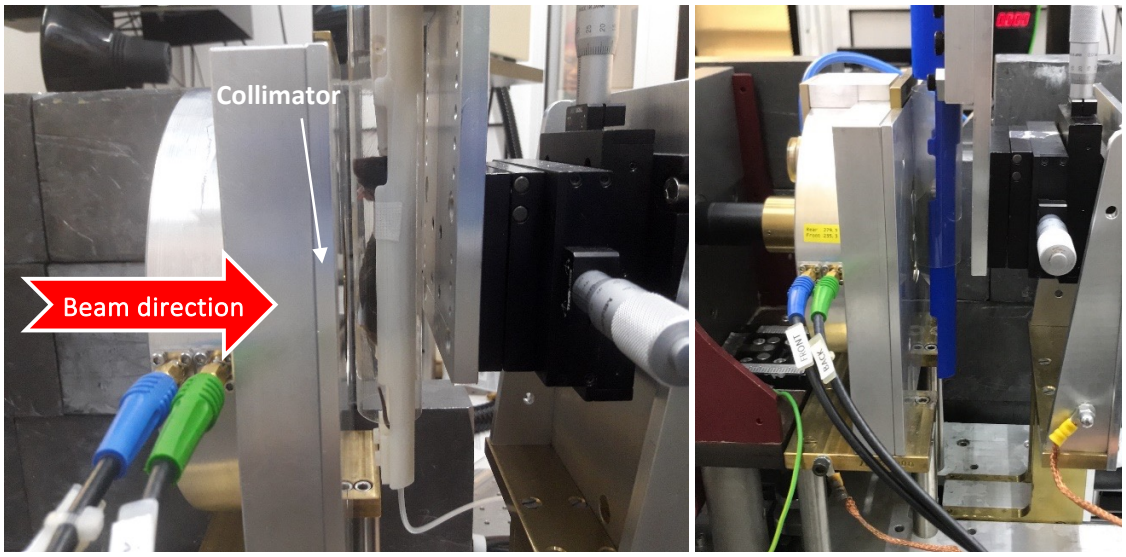

Figure A.12: The mice setup in the beam for electron beam irradiation (left, with mouse) and photon beam irradiation (right, with mouse phantom). For both modalities the same mice setup is used but with a different source-to-surface distance and collimator material/thickness.

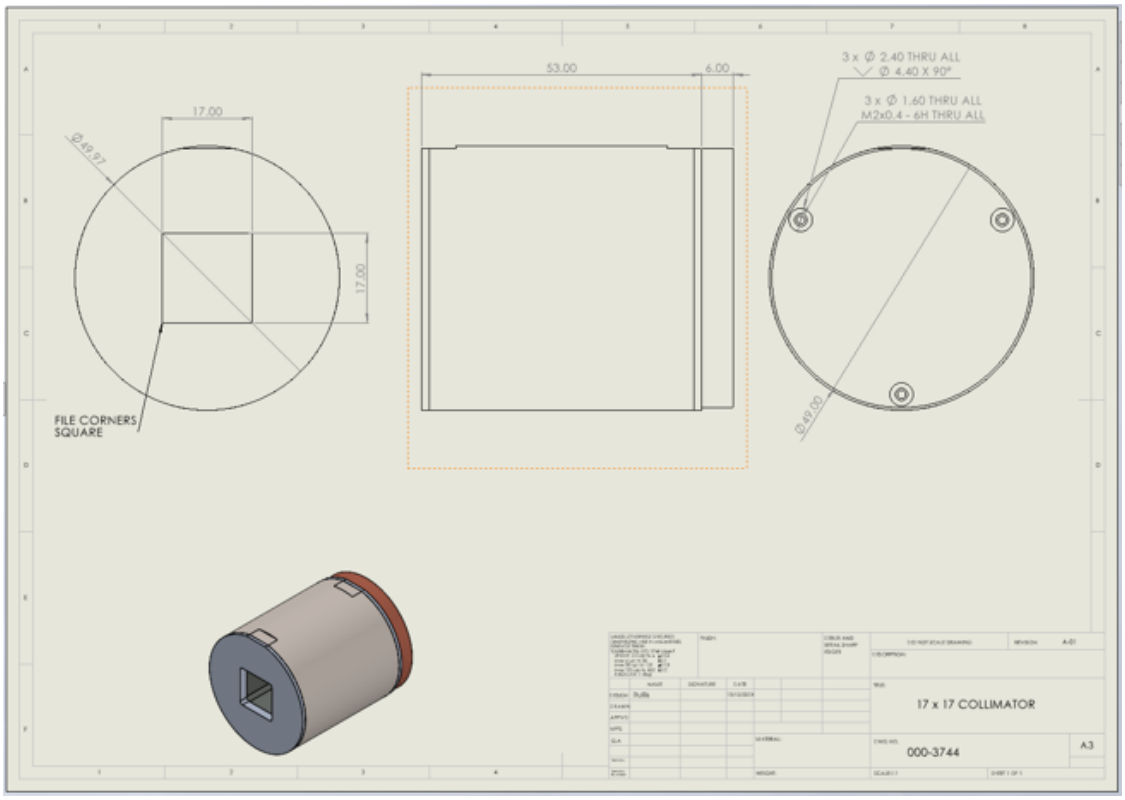

Figure A.13: The collimator was comprised of a 6 mm thick copper disc placed close to the bremsstrahlung target, a 316 stainless-steel tube with 1060 aluminium alloy ends, and a 50 mm thick layer of Wood's metal, with a square central aperture, was used to attenuate the 6 MV photon beam. The aperture in the Wood's metal was 17×17 mm^2 for 25 and 30 Gy irradiations and 20×20 mm^2 for 20 Gy irradiations.

Foil thickness mm	Gamma energy conversion %	Energy deposition %	Energy of electrons transmitted %
0.5	9.87	38.81	41.45
0.7	11.53	56.32	20.88
1.0	12.01	70.17	5.85

Table A.9: Geant4 gamma energy conversion, energy deposition, and electron energy transmission through a semi-infinite converter of a given thickness

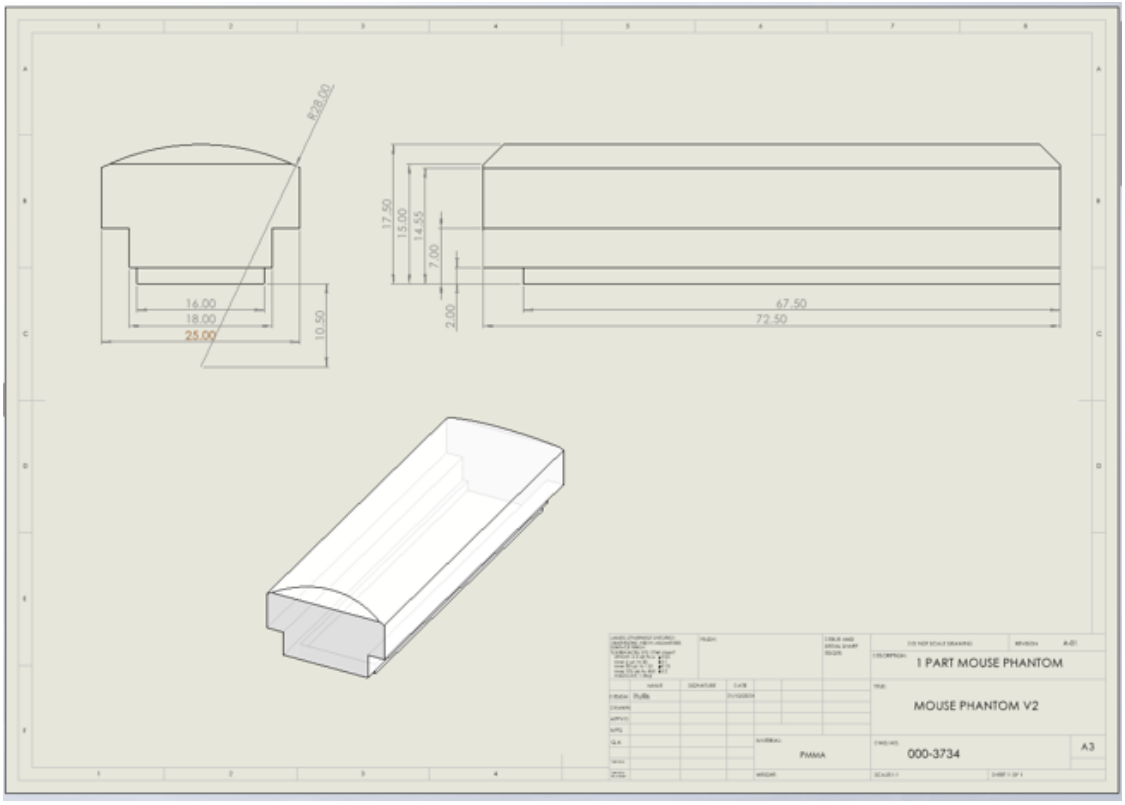

Figure A.14: The mouse phantom which was positioned in the mouse cradle and used together with film measurements, at the surface of the phantom, to verify dose deliveries before and after mice irradiations.

A.7 Managing Bremsstrahlung target heating in megavoltage photon FLASH radiotherapy

A.7.1 Electron energy deposition, transmission and photon energy conversion efficiency

A.7.2 Tungsten yield and ultimate tensile strength

A.7.3 Incident electron beam profiles

For incident electron beam radius measurements, the beam was detuned to a gun heater current of 5.6 A to lower output and prevent film dose saturation. EBT-XD films were positioned at separations ranging from 9 – 130 mm from the beam exit window. One pulse was used, with three repeated film irradiations taken for each distance. The beam radius was determined from three profiles of 50 pixels × 1 pixel at three angles intersecting the centre of the irradiated spot in the film.

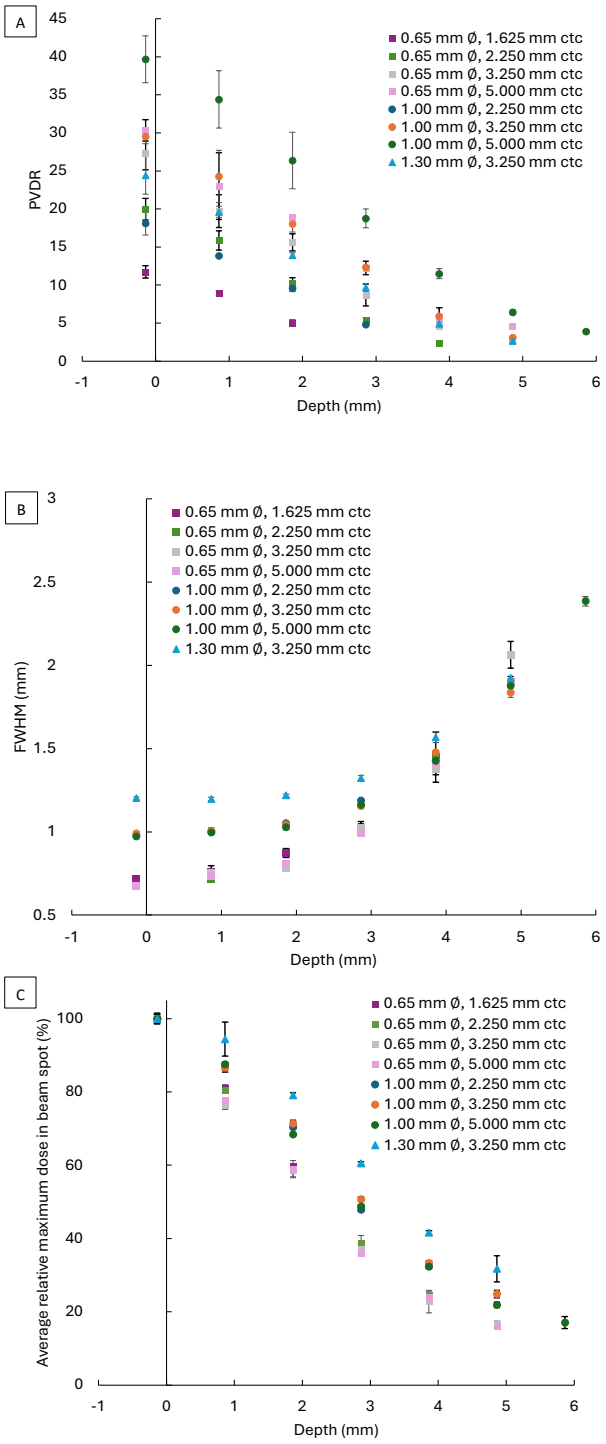

Figure A.15: Electron 7-hole insert EBT-XD film irradiations at various depth in solid water where 0 mm indicates the surface. A 5-pulse delivery was used for all inserts with different hole diameters (ϕ) [0.65-1.3 mm], and centre-to-centre distances (ctc) [1.625-5 mm]. A gun current of 7.34 A was used for 0.65 mm ϕ irradiations, whilst 7.3 A was used for 1.00 mm ϕ and 1.30 mm ϕ irradiations. An enhanced dpi of 600 was used to analyse films, here: A) Average peak-to-valley dose ratio (PVDR) with depth B) Average full width at half maximum (FWHM) of beam spots C) Average relative dose maxima in beam spots. Markers and error bars represent the mean value and standard deviation respectively of values obtained from the films via three symmetric single-pixel line dosimetric profiles obtained with a 60° offset from one another whilst intercepting the centre of adjacent beam spots, and the central axis.

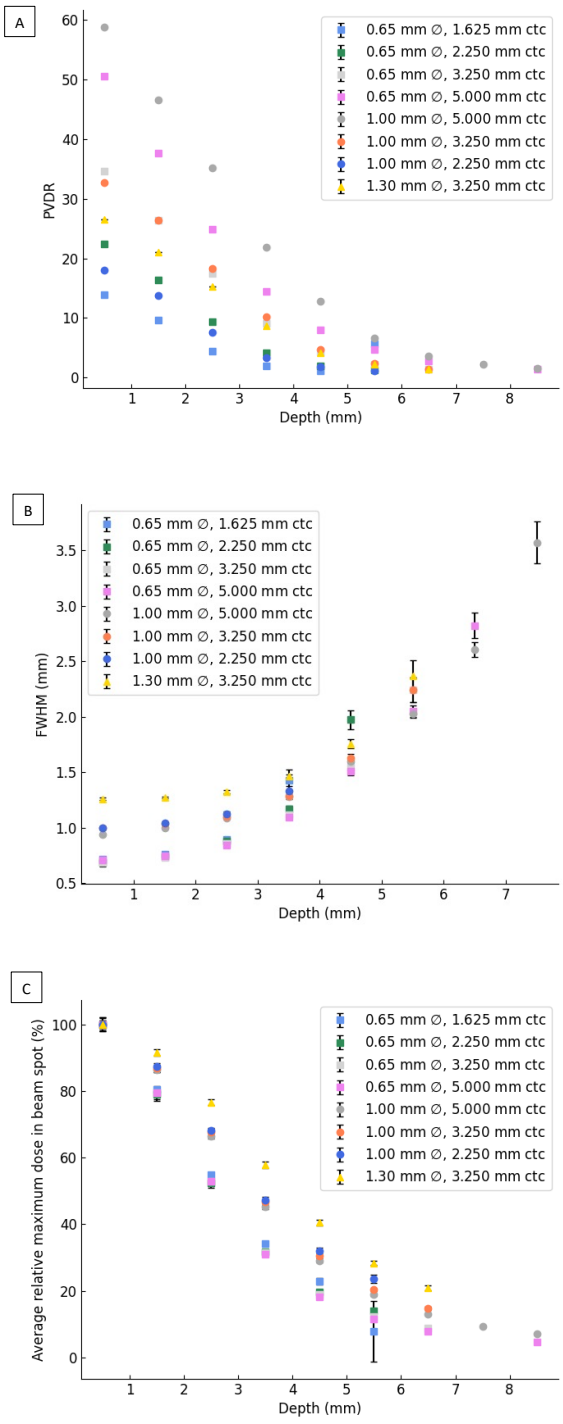

Figure A.16: Electron 7-hole insert EGSnrc simulations (see Table A.7) at various depth in solid water where 0 mm indicates the surface. A 5-pulse delivery was used for all inserts with different hole diameters (ϕ) [0.65-1.3 mm], and centre-to-centre distances (ctc) [1.625-5 mm], here: A) Average peak-to-valley dose ratio (PVDR) with depth B) Average full width at half maximum (FWHM) of beam spots C) Average relative dose maxima in beam spots. Markers and error bars represent the mean value and standard deviation respectively of values obtained from the films via one symmetric single-pixel line dosimetric profile intercepting the centre of adjacent beam spots, and the central axis.

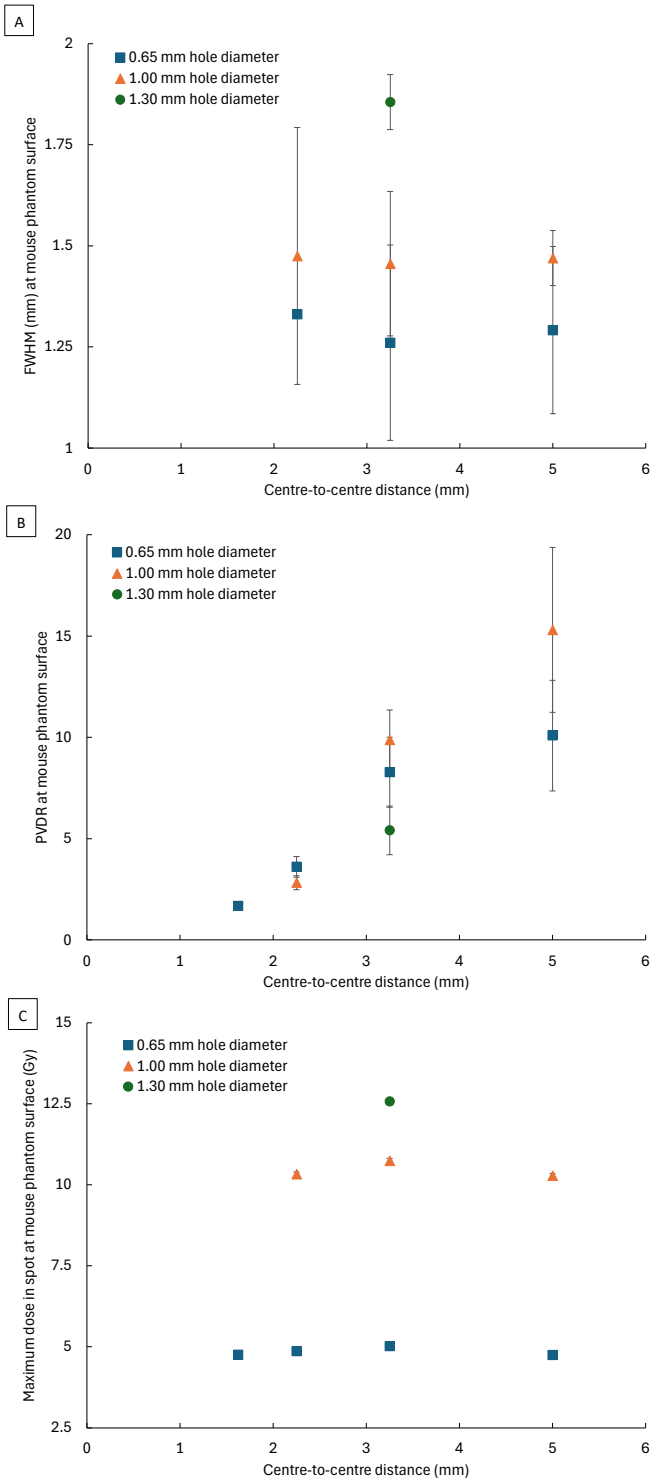

Figure A.17: Electron 7-hole insert EBT-XD film irradiations at the surface of the mouse phantom (Figure 3.8). An 8-pulse delivery was used for all inserts with different hole diameters (ϕ) [0.65-1.3 mm], and centre-to-centre distances (ctc) [1.625-5 mm]. A gun current of 7.3 A was used for all irradiations. An enhanced dpi of 600 was used to analyse films, here: A) Average peak-to-valley dose ratio (PVDR) with depth B) Average full width at half maximum (FWHM) of beam spots C) Dose maxima in beam spots. Markers and error bars represent the mean value and standard deviation respectively of values obtained from the films via three symmetric single-pixel line dosimetric profiles obtained with a 60° offset from one another whilst intercepting the centre of adjacent beam spots, and the central axis.

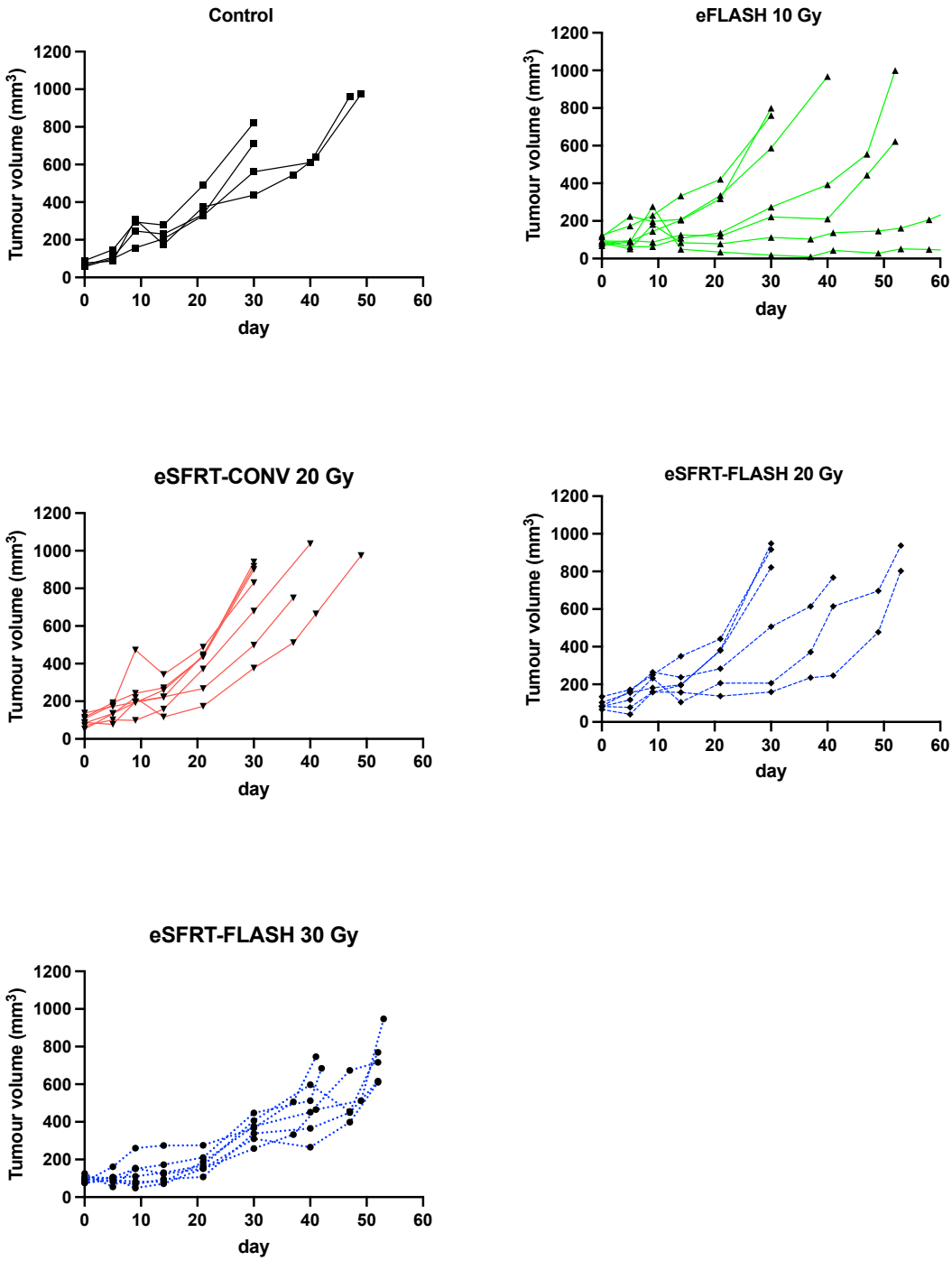

Figure A.18: Tumour growth curves for individual mice in each treatment group. Each line represents a single mouse, illustrating the variation in tumour growth trajectories over time. Mice were irradiated at day 0.

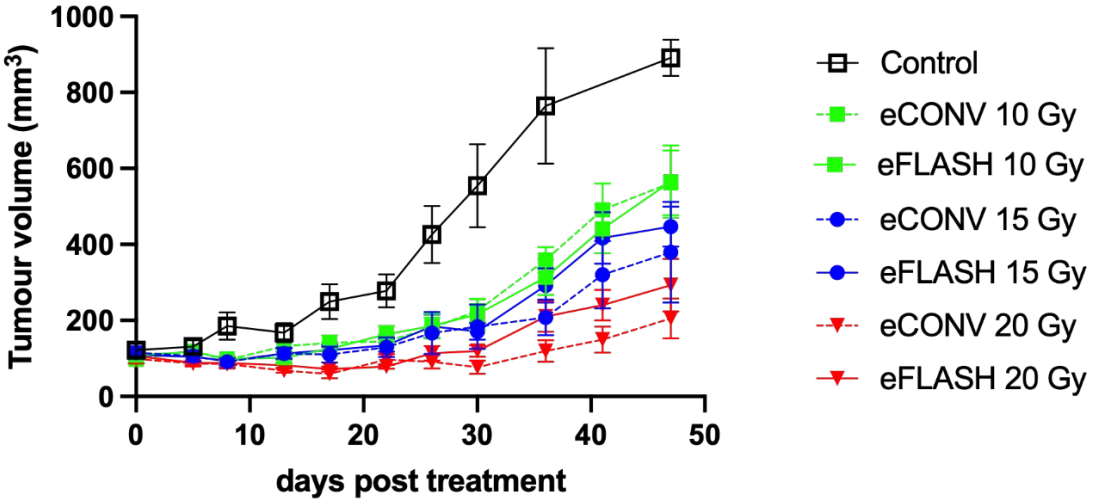

Figure A.19: Tumour growth curve from homogenous electron irradiations for mice with subcutaneous UPPL1541 tumours. Initial tumour volume at day 0 was 108 ± 28.93 mm^3 (mean ± SD). Sample sizes were n = 5 for the control group and n = 6 for all other treatment groups.

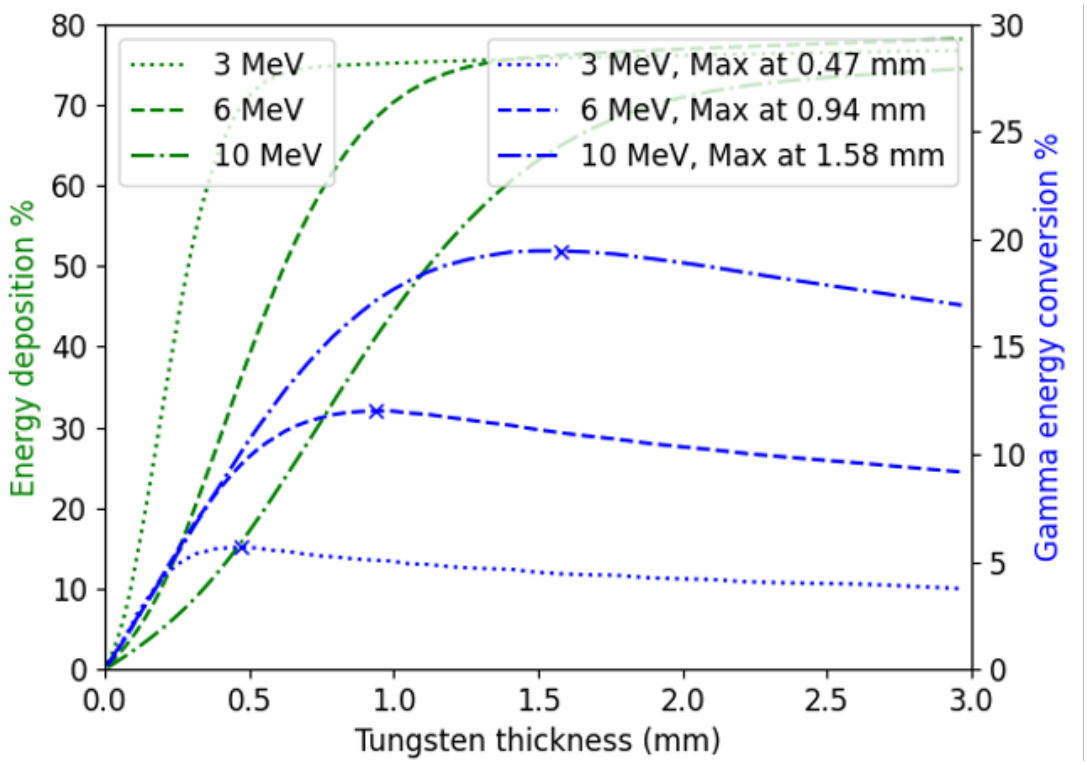

Figure A.20: Energy deposition in tungsten, and photon energy exiting the tungsten converter. From a Geant4 simulation of electron point source through a semi-infinite tungsten sheet of a given thickness. Crosses mark the points of the maxima, thickness values at these points are shown in the legend.

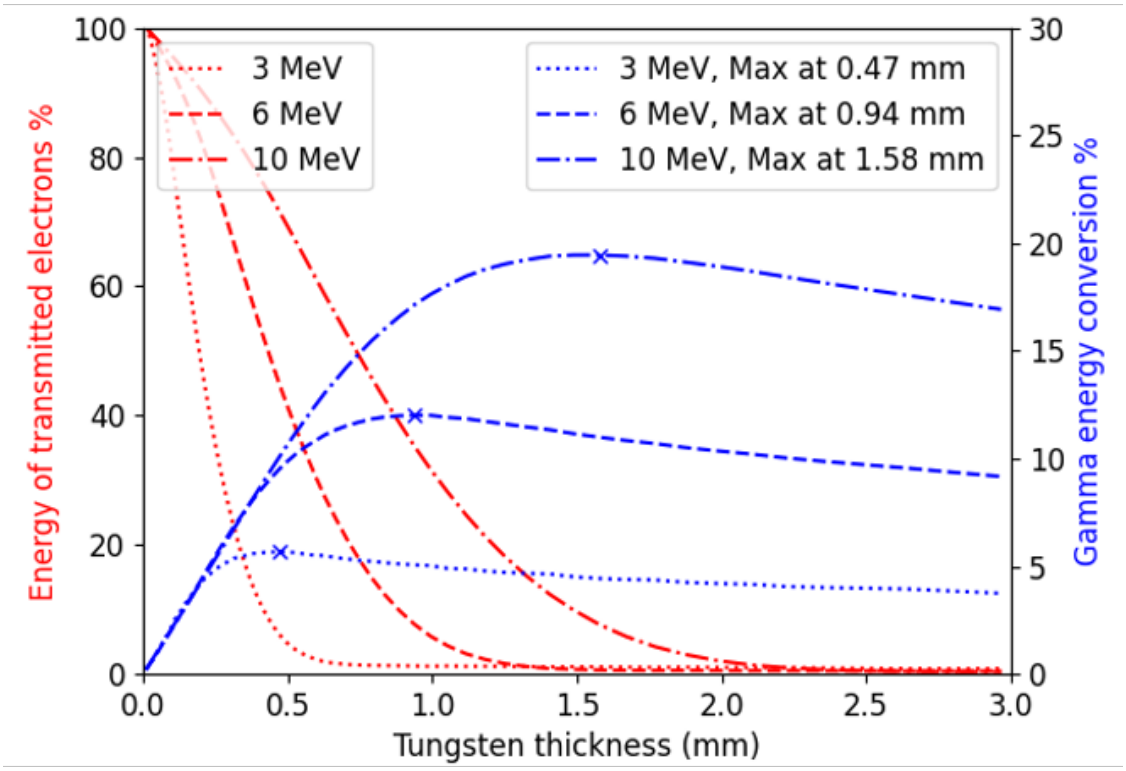

Figure A.21: Transmitted energy of electrons, and photon energy exiting the tungsten converter. From a Geant4 simulation of electron point source through a semi-infinite tungsten sheet of a given thickness. Crosses mark the points of the maxima, thickness values at these points are shown in the legend.

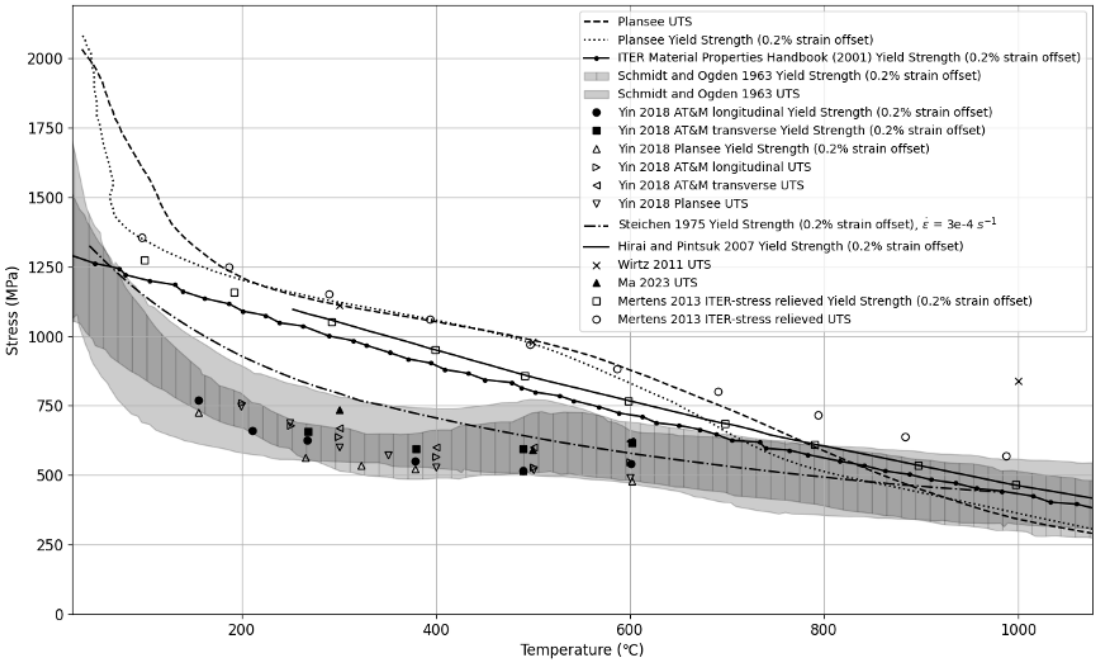

Figure A.22: Yield strength and ultimate tensile strength of Tungsten from literature

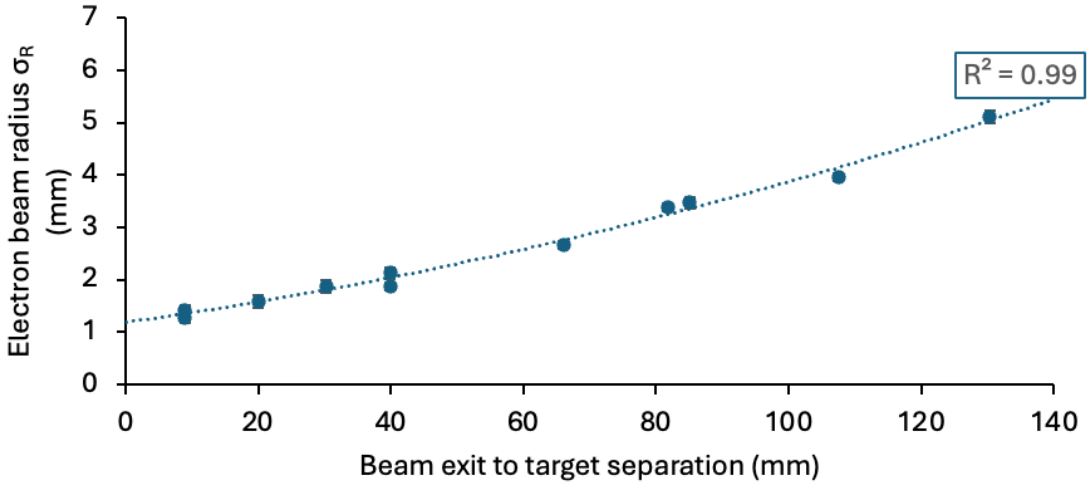

Figure A.23: Beam radius incident on upstream tungsten surface at different distances from the beam exit window. Measurements were obtained from a Gaussian fit to EBT-XD film dose measurements. Error bars represent the standard deviation of 3 repeated measurements

From profile doses, a Gaussian fit was made, and an average radius was calculated. Average dose rates were determined by taking an average of the maxima from each profile (Figure S3). Here a quadratic fit resulted in an $R^2 = 0.99$. An estimated beam radius of ≈1 mm could be obtained emerging from the beam exit window by extrapolation to the vertical intercept.

A.7.4 Incident electron current output

A beam collection device was used to measure the approximate electron beam current (without a target in place). An insulated 46 mm diameter, 50 mm thick aluminium disc, within a grounded aluminium cup was placed ∼36 mm downstream of the exit window and connected (using RG58 coaxial cable) to a 50 Ω terminated at the input of a transient digitizer (Picoscope 4603, Pico Technology, St Neots, Cambridgeshire, UK). The collection device acted as an unbiased Faraday cup as the collecting electrode was thick enough to stop all incident electrons, thereby providing an output proportional to the accelerator output current. Calibrated attenuators could be inserted in series when the peak voltage generated exceeded the ranges of the digitizer input stage. Gun heater current was adjusted from 6 to 8 A, in increments of 0.04 A, with settings repeatable within ± 0.02 A. This

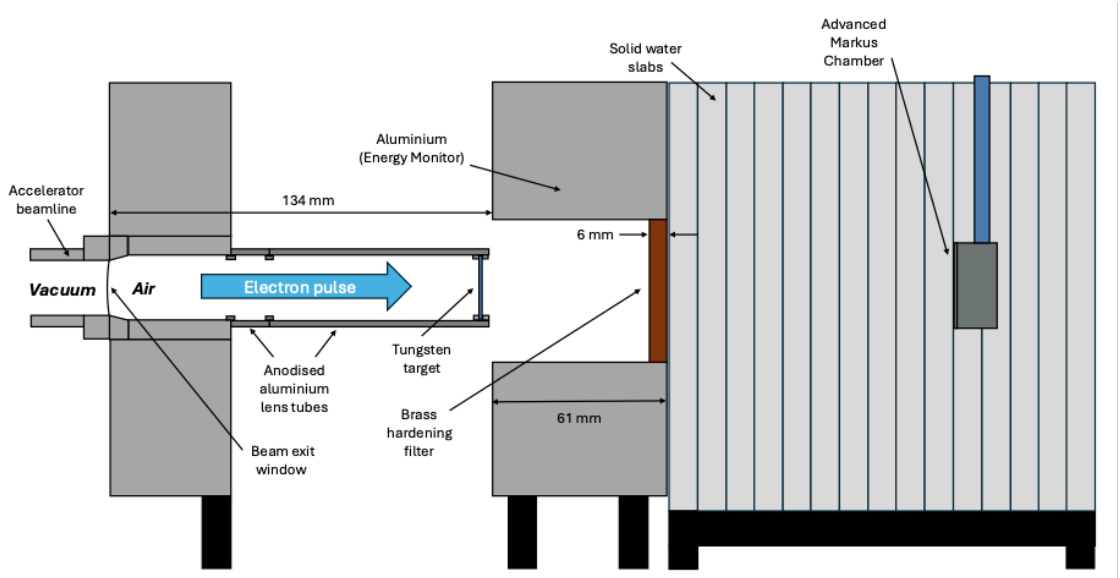

Figure A.24: Bremsstrahlung target assembly for photon charge measurements (not to scale). The aluminium structure is a beam energy monitor described in Berne et al. [530] Solid water slabs ($150 \times 150\ mm^2$) of varying thicknesses are placed downstream of the energy monitor enabling Advanced Markus® ionisation chamber charge measurements at 10 cm depth.

current is indicative of electron gun emission, with no physical meaning attributed to it. With the bremsstrahlung target assembly in place, photon charge output was measured with the AMC (positioned at 10 cm depth in RW3 solid water) by delivering 30 pulses for each gun heater current setting (Figure S4). By altering gun heater current values, the charge output to an Advanced Markus® ionisation chamber (AMC) at 10 cm depth could be maximised for a given peak pulse current. A maximum peak pulse current of between 110-130 mA was found to provide highest charge output of photons. We therefore used a gun heater current setting that provided a 110 mA current output (Figure S5).

A.7.5 Aluminium material properties

$$C_p = A + Bt + \frac{Ct^2}{2} + \frac{Dt^3}{3} + \frac{E}{t^2}\ [J/mol\ K] \tag{A.33}$$

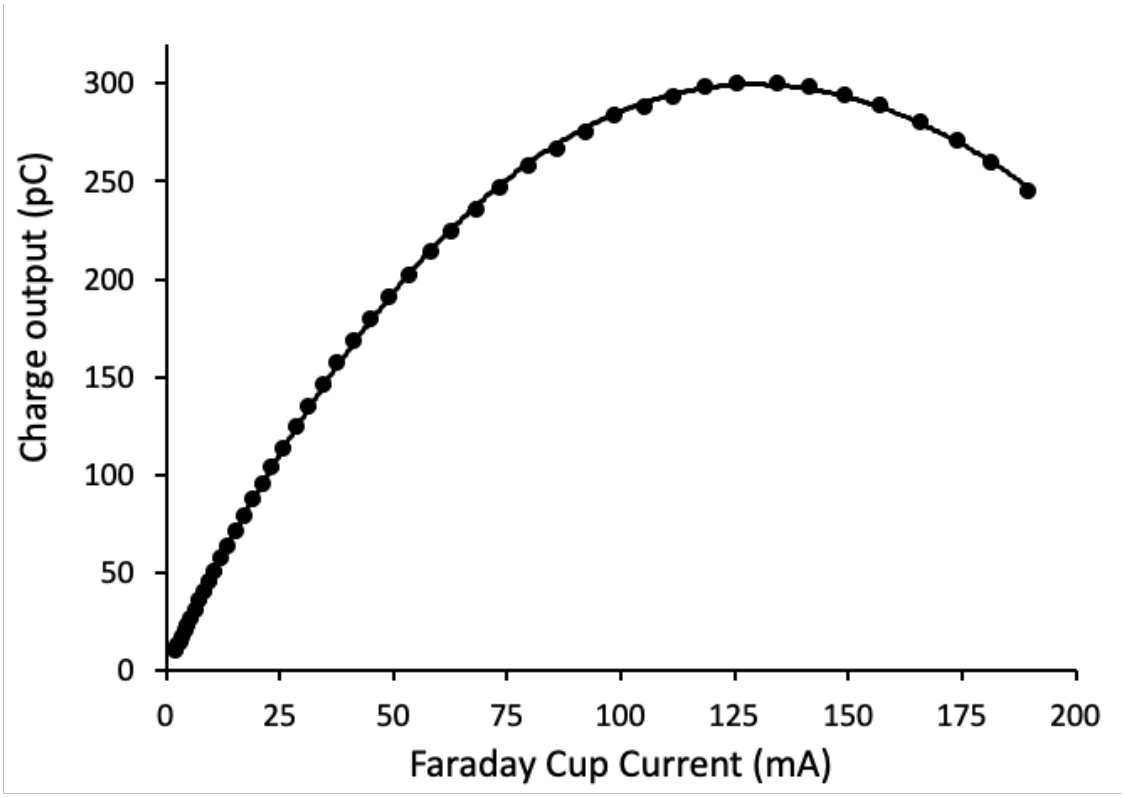

Figure A.25: Advanced Markus® ionisation chamber (AMC) photon charge output at 10 cm depth in solid water for different incident electron beam currents. Incident beam current was adjusted by altering gun heater current setting

Temperature (K)	Thermal Conductivity (W/mK)
250	235
300	237
350	240
400	240
500	237
600	232
700	226
800	220
900	213

Table A.10: Aluminium thermal conductivity from [632]

Temperature (K)	Thermal expansion coefficient
293.15	2.287E-05
300	2.299E-05
350	2.387E-05
400	2.479E-05
450	2.574E-05
500	2.671E-05
550	2.771E-05
600	2.874E-05
650	2.978E-05
700	3.083E-05
750	3.190E-05
800	3.297E-05
850	3.404E-05
900	3.511E-05

Table A.11: Aluminium thermal expansion coefficient from [631]

Temperature (K)	298-933
A	28.08920
B	-5.414849
C	8.560423
D	3.427370
E	-0.277375

Table A.12: Aluminium specific heat capacity coefficients for equation A.33, at constant pressure [633]

Temperature (K)	Density (kg/m^3)
293.15	2699.2
300	2697.9
350	2688.5
400	2678.7
450	2668.5
500	2658.1
550	2647.2
600	2636.1
650	2624.5
700	2612.6
750	2600.4
800	2587.7
850	2574.8
900	2561.4
933.473	2552.3

Table A.13: Aluminium density from [631]

Temperature (K)	Thermal Conductivity (W/mK)
250	186
273	182
300	178
350	170
400	162
500	149
600	139
700	133
800	128
900	124
1000	121
1100	118
1200	115
1300	113
1400	111
1500	109
1600	107
1700	105
1800	103
1900	102
2000	100
2200	98
2400	96
2600	94
2800	92.5
3000	91.5
3200	90.5
3400	90.0
3600	89.5

Table A.14: Tungsten thermal conductivity from [632]

A.7.6 Tungsten material properties

Johnson Cook model

$$\hat{\theta} = \begin{cases} 0 & \theta < \theta_{\text{transition}} \\ (\theta - \theta_{\text{transition}}) \,/\, (\theta_{\text{melt}} - \theta_{\text{transition}}) & \theta_{\text{transition}} \leq \theta \leq \theta_{\text{melt}} \\ \theta > \theta_{\text{melt}} & \end{cases} \tag{A.34}$$

$$\bar{\sigma} = \left[A + B\left(\bar{\varepsilon}_{pl}\right)^{n}\right]\left[1 + C\left(\frac{\dot{\bar{\varepsilon}}^{pl}}{\dot{\varepsilon}_0}\right)\right]\left(1 - \hat{\theta}^{m}\right) \tag{A.35}$$

Temperature (K)	Thermal expansion coefficient
293.15	4.42E-06
300	4.43E-06
400	4.55E-06
500	4.66E-06
600	4.75E-06
700	4.84E-06
800	4.91E-06
900	4.99E-06
1000	5.06E-06
1100	5.13E-06
1200	5.20E-06
1300	5.28E-06
1400	5.36E-06
1500	5.45E-06
1600	5.56E-06
1700	5.67E-06
1800	5.80E-06
1900	5.94E-06
2000	6.11E-06
2100	6.29E-06
2200	6.49E-06
2300	6.72E-06
2400	6.97E-06
2500	7.24E-06
2600	7.55E-06
2700	7.88E-06
2800	8.24E-06
2900	8.63E-06
3000	9.05E-06
3100	9.51E-06
3200	1.00E-05
3300	1.05E-05
3400	1.11E-05
3500	1.17E-05
3600	1.23E-05
3687	1.29E-05

Table A.15: Tungsten thermal expansion coefficient from [631]

Temperature (K)	Density (kg/m^3)
293.15	19254
300	19252
400	19226
500	19200
600	19172
700	19145
800	19117
900	19089
1000	19060
1100	19031
1200	19001
1300	18971
1400	18941
1500	18910
1600	18879
1700	18847
1800	18815
1900	18782
2000	18748
2100	18712
2200	18677
2300	18640
2400	18602
2500	18563
2600	18521
2700	18479
2800	18434
2900	18388
3000	18339
3100	18288
3200	18234
3300	18178
3400	18120
3500	18058
3600	17993

Table A.16: Tungsten density from [631]

Temperature (K)	Young's modulus (GPa)
295	388
471	382
672	376
873	369
1077	363
1273	357
1483	349
1676	342
1879	333
2080	309
2278	284
2482	257

Table A.17: Tungsten Young's modulus from [635]

Temperature (K)	Poisson ratio
305	0.279
499	0.282
699	0.287
896	0.292
997	0.296
1107	0.300
1193	0.303

Table A.18: Tungsten Poisson ratio from [636]

Temperature (K)	298-1900	1900-3680
A	23.95930	-22.57640
B	2.639680	90.27980
C	1.257750	-44.27150
D	-0.254642	7.176630
E	-0.048407	-24.09740

Table A.19: Tungsten specific heat capacity coefficients for equation A.33, at constant pressure [633]

Symbol	Parameter	Value
θ	temperature	-
$\hat{\theta}$	non dimensional temperature	-
$\theta_{transition}$	the temperature threshold below which the yield stress is independent of temperature	298.15 K
θ_{melt}	melting temperature	3683 K
$\bar{\sigma}$	yield stress at nonzero strain rate	-
$\bar{\varepsilon}_{pl}$	equivalent plastic strain rate	-
$\dot{\varepsilon}_0$	reference strain rate	1s-1
$\dot{\bar{\varepsilon}}^{pl}$	plastic strain rate	-
A	-	330.17 MPa
B	-	1027.4 MPa
n	-	0.018752
C	-	0.034454
m	-	0.40552

Table A.20: Johnson-Cook plasticity model for tungsten from [638] for Equations (A.34) and (A.35)

A.7.7 Simulated electron beam shape and incident power density

Geant4 simulations were performed with different air separations from the exit window to the tungsten surface using a series of aluminium lens tube combinations. The electron FWHM used for simulation (using measurements in Figure S1) and power density is detailed in Tables S11 & S12 respectively. Here the 2D gaussian fit to the energy deposited in the voxelized tungsten target gave depths of maximum energy deposition of ∼0.22, ∼0.27, ∼0.33 mm for 0.5, 0.7, and 1 mm targets, respectively. These values were used as input parameters to the Abaqus FEM simulations for each lens tube arrangement and tungsten thickness.

A.7.8 Photon charge output

Charge output measurements were performed using an Advanced Markus® ionisation chamber (AMC, model 34045, PTW-Freiburg, Freiburg, Germany, connected to an electrometer (UNIDOS Webline, PTW-Freiburg, Freiburg, Germany, with a bias voltage of +300 V), at 10 mm depth in solid water (150 × 150 mm^2 RW3 slabs from PTW-Freiburg) to determine photon output variation for each tungsten

		Full width at half maximum incident on tungsten target (FWHM)		
Arrangement of lens tubes	Beam exit to target separation (mm)	0.5 mm tungsten	0.7 mm tungsten	1.0 mm tungsten
SM1L[05]	53.9	3.92	3.92	3.90
SM1L[05, 05]	67.4	4.55	4.54	4.52
SM1L[03, 10, 05]	88.7	5.52	5.52	5.50
SM1L[20, 05]	105.5	6.30	6.29	6.27
SM1L[20, 05, 05]	119	6.91	6.91	6.89

Table A.21: Incident electron beam full width at half maximum values for positions of tungsten in thermocouple holder for each thickness and lens tube arrangement

		Incident maximum power density on tungsten target (TWm^{-3})		
Arrangement of lens tubes	Beam exit to target separation (mm)	0.5 mm tungsten	0.7 mm tungsten	1.0 mm tungsten
SM1L[05]	53.9	33.7	36.9	37.7
SM1L[05, 05]	67.4	25.4	27.8	28.3
SM1L[03, 10, 05]	88.7	17.5	19.2	19.4
SM1L[20, 05]	105.5	13.4	14.8	15.1
SM1L[20, 05, 05]	119	11.2	12.3	12.5

Table A.22: Incident electron maximum power density deposition values for positions of tungsten in thermocouple holder for each thickness and lens tube arrangement

thickness (0.5 mm, 0.7 mm, 1.0 mm) (Figure S6). Measured sample thicknesses for nominal thicknesses of 0.5, 0.7, and 1.0 mm were: 0.536±0.009 mm, 0.752pm0.008 mm, and 1.039±0.005 mm respectively. For photon charge measurements, greater variability was seen pulse to pulse for a given sample or for different targets of the same thickness, than between sample thicknesses. It was concluded that the photon output for different tungsten thicknesses, at a depth where electron contamination could not be present, was indistinguishable.

A.7.9 Radial temperature profiles following irradiation

Simulated temperatures following a 300-pulse irradiation at a time of 1s, and after 60s of cooling were recorded along radial paths at three axial positions in targets

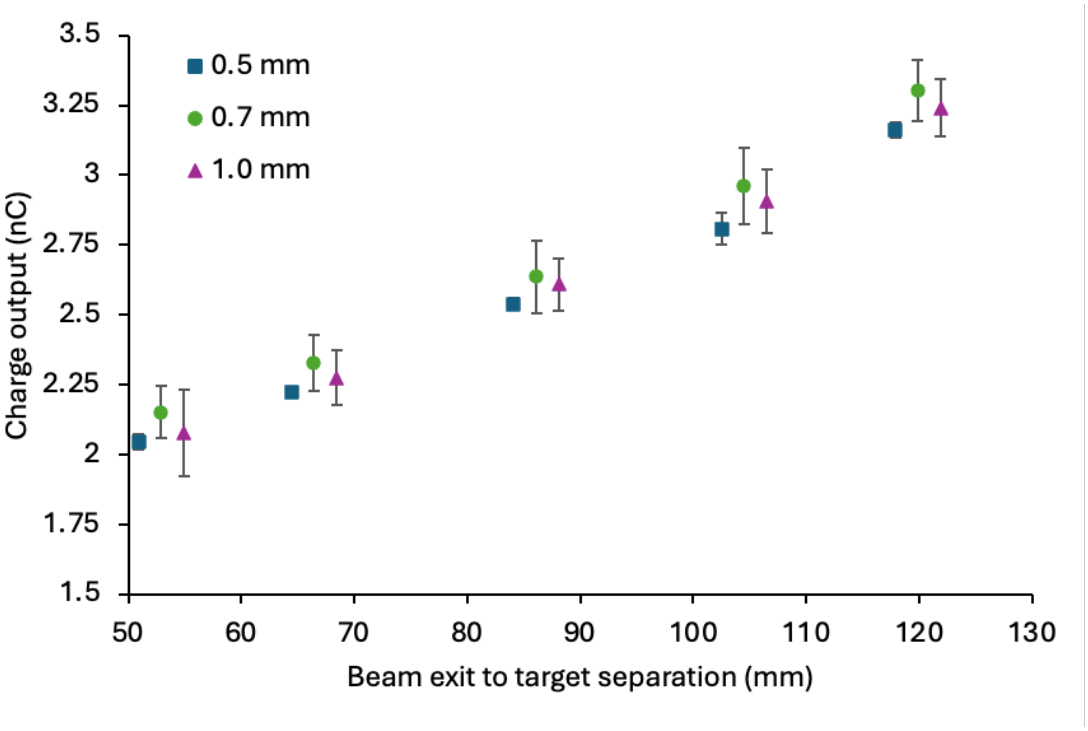

Figure A.26: Advanced Markus® ionisation chamber (AMC) charge output at 10 cm depth in RW3 solid water (SW), with 5 cm SW backing. Here the SW block was positioned 195 mm downstream of the beam exit window, with the tungsten target displaced at variable distances from the beam exit window. Three samples were measured for each target thickness of 0.5, 0.7, and 1.0 mm. Squares denote the 0.5 mm targets, circles the 0.7 mm targets, and triangles the 1.0 mm targets. Error bars denote the average of 3 targets of each thickness, with 3 repeated measurements per sample.

(the upstream, midpoint, and downstream positions. After cooling all targets at all positions, and in all elements were seen to return to a starting temperature of 25 degrees (Figure S7). For all foil positions, the 0.7 mm target temperature following irradiation was slightly higher than the 0.5 and 1.0 mm targets at each separation from the beam exit window. The similarity between temperatures reached along each radial path indicated consistency with depth within the targets.

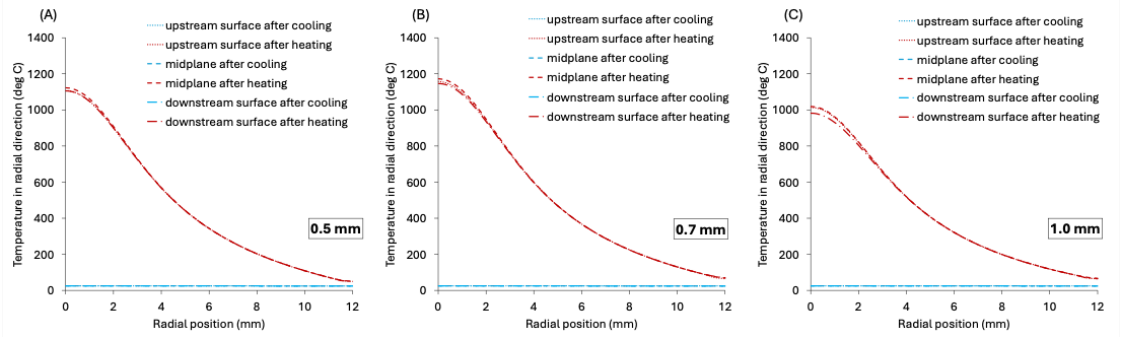

Figure A.27: Radial temperature profiles of (A) 0.5 mm, (B) 0.7 mm, and (C) 1.0 mm foil simulations immediately following a 300 pulse, 1s irradiation (red), or following a 60s cooling period after the 1s irradiation (blue) at 53.9 mm separation from the exit window

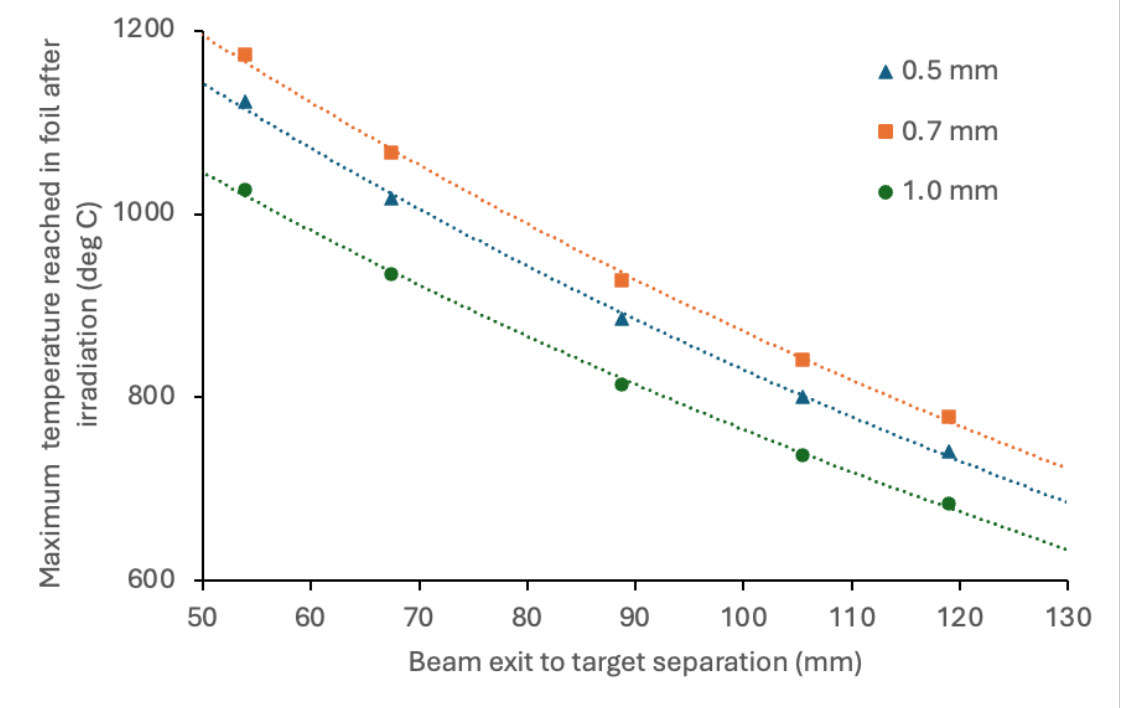

Figure A.28: Simulated maximum temperature reached within a 0.5 mm (blue triangle), 0.7 mm (orange square), and 1.0 mm (green circle) targets after a 300 pulse, 1s irradiation. Exponential fits (dotted lines) were applied for every target thickness with each $R^2 > 0.99$

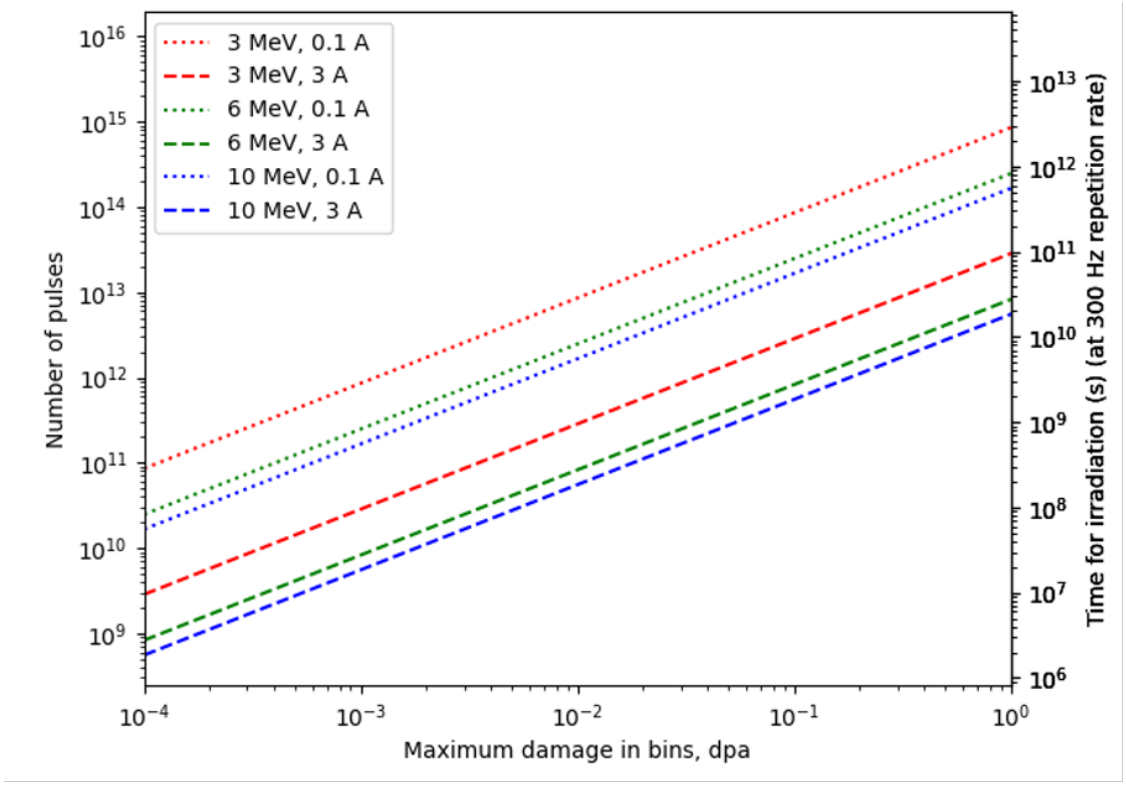

Figure A.29: FLUKA dpa damage simulation in FLAIR (v3.3) with 1e7 incident electrons. Here a combined setup as seen in figure 2 with a contiguous SML[05,30] tube housed a 0.5 mm thick, 25 mm diameter tungsten foil which was subdivided into 92 radial, 1 azimuthal, and 10 axial bins. The DPA-NRT scorer (in dpa/cm^3/primary)) was used to measure the maximum dpa damage in all bins for each simulation (with an error not shown of <0.05%), and scaled with incident beam current. Three different energies were simulated 3,6, and 10 MeV (red, green, and blue), with a scaling to 100 mA [fluence ~1e15 cm^{-2}](dashed) and 3 A (dotted).

A.7.10 Maximum simulated foil temperature following irradiation

A.7.11 Displacement damage simulation

A.7.12 Plastic equivalent strain history

The maximum equivalent plastic strain (PEEQ) of the element in the irradiated region was found and its buildup monitored over the course of the 300-pulse irradiation (<1s) and the cooling time (1-60s) (Figure S10). The PEEQ was seen to develop rapidly and linearly throughout the irradiation, with a smaller and much more gradual buildup throughout the cooling time.

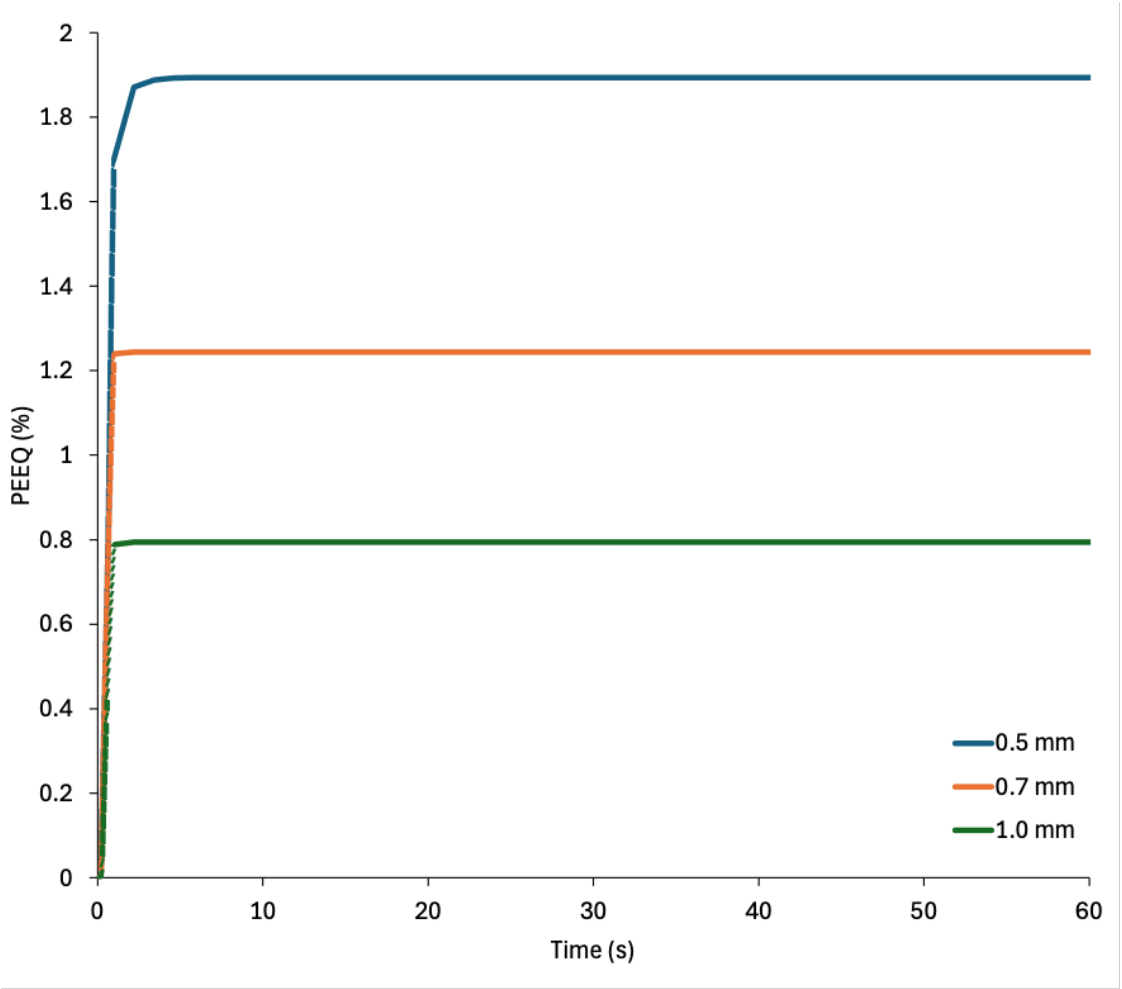

Figure A.30: Plastic equivalent strain (PEEQ) history of element with highest strain build-up for 0.5, 0.7, and 1 mm simulations at 53.9 mm separation from exit window following a 1s irradiation of 300 pulses incident at 0s

A.7.13 High cycle fatigue literature

Sample type	σ'_f(MPa)	b	Source
Sintered and HIPed (SH)	376.94	-0.0501	Habainy 2018 [680]
Thick forged tungsten plate	536.98	-0.0367	Tipton 2022 [629]
Rolled tungsten 0.02" sheet	2173.8	-0.0602	Tipton 2022 [629, 656]

Table A.23: Fatigue strength coefficient and components

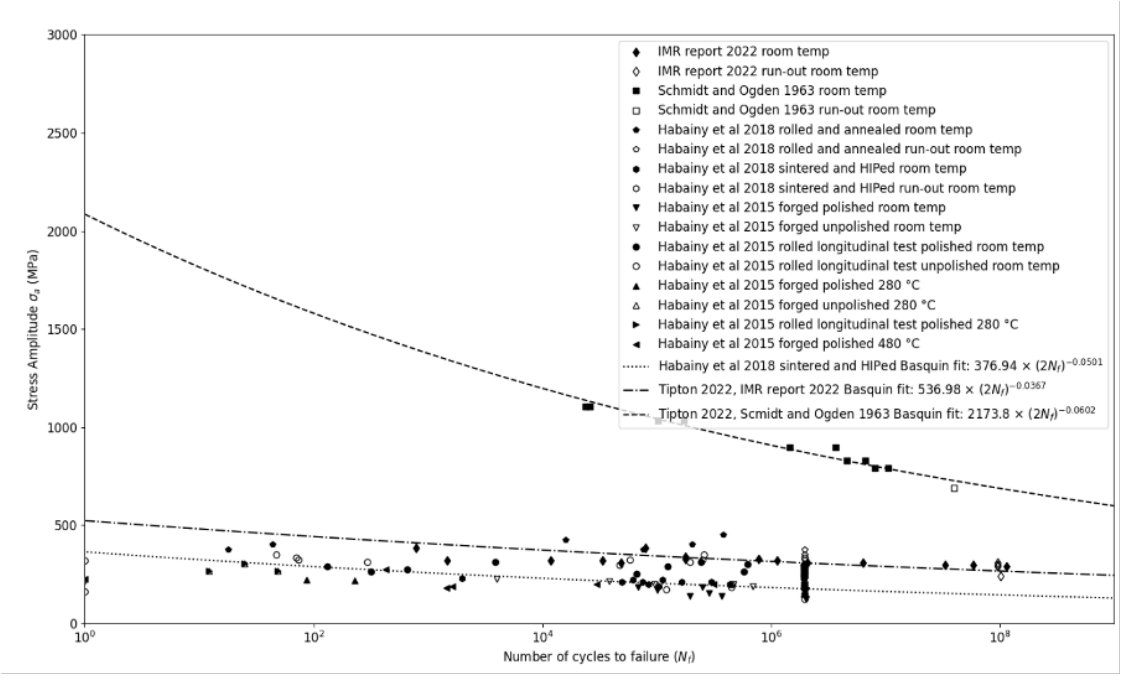

Figure A.31: Literature with fits of high-cycle fatigue results [404, 656, 680]

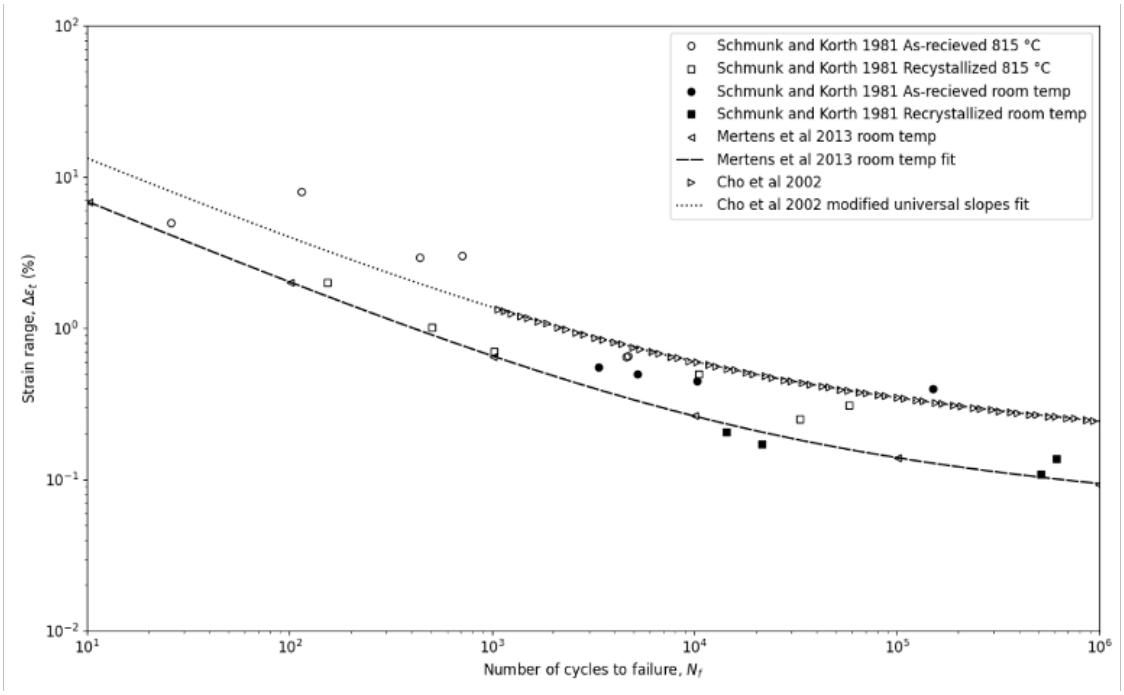

Figure A.32: Literature with fits for low-cycle fatigue using the universal slopes equation and modified form [556, 560, 681, 682]

Sample type	σ'_f(MPa)	ε'_f	b	c	Source
Room temperature	553	17.8	-0.0813	-0.558	Mertens et al. 2013 [681]

Table A.24: Parameter values for strain life equation from literature and fits with interpolated elastic modulus from [683]

A.7.14 Low cycle fatigue literature

A.7.15 Radial profiles of plastic strain components

The radial plastic strain profiles were taken immediately following a 300-pulse irradiation at a time of 1s, and after 60s of cooling following this irradiation for three axial positions; the upstream, midpoint, and downstream radial paths within the tungsten targets (Figure S13). The 0.5 mm profile demonstrated the highest radial compressive plastic strain, and for each sample the upstream surface accumulated a higher radial plastic strain than both the path through along the midpoint and downstream surfaces. A greater difference in values between paths was seen with thinner targets, with the radial distribution of radial plastic strain slightly broader for the thinnest targets. All targets in all positions other than the 0.5 mm at the upstream surface maintained an identical radial plastic strain sustained from irradiations to the end of cooling. The circumferential plastic strain followed identical trends to the radial plastic strain. Here less sporadic plastic strain values were seen at boundary positions away from the central axis. The largest component of plastic strain at the end of each simulation was the axial strain. Of all the targets the thinnest target developed the largest axial strain. No strain recovery occurred for the 0.7 and 1.0 mm targets, with only the 0.5 mm sample showing a slight reduction in axial strain between the end of irradiation and the end of cooling.

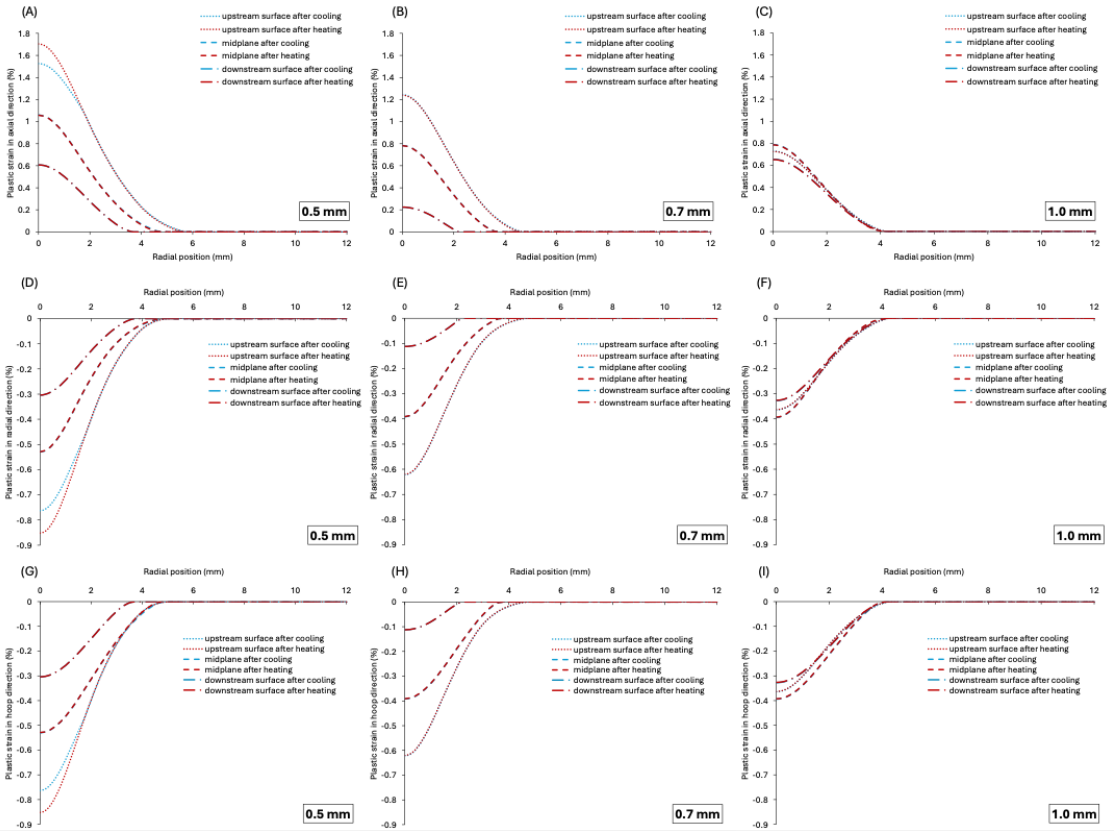

Figure A.33: Radial (panels A,B,C), axial (panels D,E,F) and circumferential (panels G,H,I) plastic strain for a simulation of 0.5 mm (panels A,D,G), 0.7 mm (panels B,E,H), and 1.0 mm (panels C,F,I) targets positioned at 53.9 mm separation from the exit window following a 1s, 300 pulse irradiation

References

[1] Cancer Research UK. *Cancer in the UK: Overview 2025*. Report. Policy, Information and Communications directorate, Cancer Research UK, June 2025. URL: https://www.cancerresearchuk.org/sites/default/files/cancer_in_the_uk_overview_2025.pdf?_gl=1*1er8cwl*_gcl_au*MTAwMzA2NjExLjE3NTgyNzM4MDE.*_ga*MTY4ODU4MjM4Mi4xNzU4MjczODAx*_ga_58736Z2GNN*czE3NTgyNzM4MDEkbzEkZzEkdDE3NTgyNzM4MzQkajI3JGwwJGgw.

[2] Macmillan. *Throwing light on the consequences of cancer and its treatment*. Report. 2013. URL: https://www.macmillan.org.uk/dfsmedia/1a6f23537f7f4519bb0cf14c45b2a629/14615-10061/throwing-light-on-the-consequences-of-cancer-and-its-treatment-july-2013.

[3] R. Baskar et al. "Cancer and radiation therapy: current advances and future directions". In: *Int J Med Sci* 9.3 (2012). 1449-1907 Baskar, Rajamanickam Lee, Kuo Ann Yeo, Richard Yeoh, Kheng-Wei Journal Article Research Support, Non-U.S. Gov't Review Australia 2012/03/13 Int J Med Sci. 2012;9(3):193-9. doi: 10.7150/ijms.3635. Epub 2012 Feb 27., pp. 193–9.

[4] Eduardo Rosenblatt et al. "Radiotherapy capacity in European countries: an analysis of the Directory of Radiotherapy Centres (DIRAC) database". In: *The Lancet Oncology* 14.2 (2013), e79–e86. URL: https://www.sciencedirect.com/science/article/pii/S1470204512705569.

[5] IAEA. *The IAEA Directory of Radiotherapy Centres (DIRAC)*. Accessed: 2022–18-07. URL: https://dirac.iaea.org.

[6] R F Mould. "Röntgen and the discovery of X-rays". In: *British Journal of Radiology* 68.815 (2014), pp. 1145–1176. URL: https://doi.org/10.1259/0007-1285-68-815-1145.

[7] Philip C Goodman. "The new light: discovery and introduction of the X-ray". In: *AJR. American journal of roentgenology* 165.5 (1995), pp. 1041–1045.

[8] RJ Berry. "Therapeutic uses of X-rays". In: *International Journal of Radiation Biology and Related Studies in Physics, Chemistry and Medicine* 51.5 (1987), pp. 873–895.

[9] Eleanor D Montague. "Radiation therapy and breast cancer: past, present, and future". In: *American journal of clinical oncology* 8.6 (1985), pp. 455–462.

[10] H. Dieter Kogelnik. "Inauguration of radiotherapy as a new scientific speciality by Leopold Freund 100 years ago". In: *Radiotherapy and Oncology* 42.3 (1997). doi: 10.1016/S0167-8140(96)01887-7, pp. 203–211. URL: https://doi.org/10.1016/S0167-8140(96)01887-7.

[11] "THE THERAPEUTICS OF RADIUM". In: *Br Med J* 1.3353 (1925). Journal Article England 1925/04/04 Br Med J. 1925 Apr 4;1(3353):670-2., pp. 670–2.

[12] William R. Hendee, Geoffrey S.Ibbott, and Eric G.Hendee. *Radiation Therapy Physics*. Vol. 3. 111 River Street, Hoboken, NJ 07030, (201) 748-6011: John Wiley & Sons, 2005.

[13] Rolf Behling. "X-ray tubes development-IOMP history of medical physics". In: *Medical Physics International* 6 (2018), pp. 8–55.

[14] J. G. Trump, C. R. Moster, and R. W. Cloud. "Efficient deep tumor irradiation with Roentgen rays of several million volts". In: *Am J Roentgenol Radium Ther* 57.6 (1947). Trump, j g Moster, c r Cloud, r w Journal Article United States 1947/06/01 Am J Roentgenol Radium Ther. 1947 Jun;57(6):703-10., pp. 703–10.

[15] David I. Thwaites and John B. Tuohy. "Back to the future: the history and development of the clinical linear accelerator". In: *Physics in Medicine & Biology* 51.13 (2006), R343. URL: https://dx.doi.org/10.1088/0031-9155/51/13/R20.

[16] Peter Hoskin. *External Beam Therapy*. Oxford University Press, 2019. URL: https://doi.org/10.1093/med/9780198786757.001.0001.

[17] D. W. Kerst. "The Betatron". In: *Radiology* 40.2 (1943), pp. 115–119. URL: https://pubs.rsna.org/doi/abs/10.1148/40.2.115.

[18] Robert R. Wilson. "Radiological Use of Fast Protons". In: *Radiology* 47.5 (1946), pp. 487–491. URL: https://pubs.rsna.org/doi/abs/10.1148/47.5.487.

[19] E. A. Knapp, B. C. Knapp, and J. M. Potter. "Standing Wave High Energy Linear Accelerator Structures". In: *Review of Scientific Instruments* 39.7 (1968), pp. 979–991. URL: https://doi.org/10.1063/1.1683583.

[20] J. Daniel Bourland. "Chapter 6 - Radiation Oncology Physics". In: *Clinical Radiation Oncology (Fourth Edition)*. Ed. by Leonard L. Gunderson and Joel E. Tepper. Philadelphia: Elsevier, 2016, 93–147.e3. URL: https://www.sciencedirect.com/science/article/pii/B978032324098700006X.

[21] H. Svensson et al. "A 22 MeV microtron for radiation therapy". In: *Acta Radiol Ther Phys Biol* 16.2 (1977). Svensson, H Jonsson, L Larsson, L G Brahme, A Lindberg, B Reistad, D Journal Article Sweden 1977/04/01 Acta Radiol Ther Phys Biol. 1977 Apr;16(2):145-56. doi: 10.3109/02841867709134308., pp. 145–56.

[22] Radhe Mohan. "A review of proton therapy – Current status and future directions". In: *Precision Radiation Oncology* 6.2 (2022), pp. 164–176. URL: https://onlinelibrary.wiley.com/doi/abs/10.1002/pro6.1149.

[23] E. B. Podgorsak. *Radiation physics for medical physicists*. 2016. URL: http://rave.ohiolink.edu/ebooks/ebc/9783319253824.

[24] Robin J. Wilks. *Principles of radiological physics*. Edinburgh ; New York: Churchill Livingstone, 1981, x, 542 p.

[25] B. Vojnovic. "THE NOVICE'S GUIDE TO ELECTRON LINEAR ACCELERATORS". Unpublished Work. 1995.

[26] T. Greener, E. Jones, and C. Thomas. "External Beam Radiotherapy". In: 1st ed. CRC Press, 2022. URL: https://doi-org.ezproxy-prd.bodleian.ox.ac.uk/10.1201/9780429155758-9.

[27] Philip Mayles, Alan E. Nahum, and Jean-Claude Rosenwald. *Handbook of radiotherapy physics : theory and practice*. Second edition. 2021051826 W.P.M. Mayles, formerly at The Clatterbridge Cancer Centre NHS Foundation Trust, UK Mayles, A. E. Nahum, formerly at The Clatterbridge Cancer Centre NHS Foundation Trust, UK, J.-C. Rosenwald, formerly at Institut Curie, Paris, France. Includes bibliographical references and index. Boca Raton: CRC Press/Taylor and Francis Group, 2022, volumes cm.

[28] Murshed Hossain. "Output trends, characteristics, and measurements of three megavoltage radiotherapy linear accelerators". In: *Journal of Applied Clinical Medical Physics* 15.4 (2014), pp. 137–151. URL: https://doi.org/10.1120/jacmp.v15i4.4783.

[29] Pam Cherry and Angela Duxbury. *Practical radiotherapy physics and equipment*. Greenwich medical media, 1998.

[30] C. J. Karzmark, Craig S. Nunan, and Eiji Tanabe. *Medical electron accelerators*. 92049307 C.J. Karzmark, Craig S. Nunan, and Eiji Tanabe. ill. ; 29 cm. Includes bibliographical references and index. New York: McGraw-Hill, Inc., Health Professions Division, 1993, xiv, 316 p.

[31] Maurizio Vretenar. *Linear accelerators*. en. 2013. URL: http://cds.cern.ch/record/1536738.

[32] M. Weiss. "Introduction to Rf Linear Accelerators". In: *Cern Accelerator School Fifth General Accelerator Physics Course: Proceedings, Vol Ii* 94.1 (1994), pp. 913–953. URL: %3CGo%20to%20ISI%3E://WOS:A1994BA72J00019.

[33] A. Sidorin. "Linear accelerators". In: *4th International Summer School on Nuclear Physics Methods and Accelerators in Biology and Medicine*. Vol. 958. Aip Conference Proceedings. 2007, pp. 46–52. URL: %3CGo%20to%20ISI%3E://WOS:000252138700008.

[34] P. G. Maxim, P. Keall, and J. Cai. "FLASH radiotherapy: Newsflash or flash in the pan?" In: *Medical Physics* 46.10 (2019). Je9wk Times Cited:16 Cited References Count:25, pp. 4287–4290. URL: %3CGo%20to%20ISI%3E://WOS:000484107500001%20https://aapm.onlinelibrary.wiley.com/doi/pdfdirect/10.1002/mp.13685?download=true.

[35] Thomas P. Wangler. *Introduction*. John Wiley & Sons, Ltd, 2008. Chap. 1, pp. 1–31. eprint: https://onlinelibrary.wiley.com/doi/pdf/10.1002/9783527623426.ch1. URL: https://onlinelibrary.wiley.com/doi/abs/10.1002/9783527623426.ch1.

[36] David Alesini. *Linear Accelerators*. https://cas.web.cern.ch/sites/default/files/Alesini_LINEAR_ACCELERATORS_2019.pdf. Accessed: 2022–31-06. 2019.

[37] Eric J. Hall and Amato J. Giaccia. *Radiobiology for the radiologist*. 8th. Radiobiology for the radiologist. Includes bibliographical references and index. Philadelphia: Wolters Kluwer, 2019.

[38] Roger G. Dale and Bleddyn Jones. *Radiobiological modelling in radiation oncology*. Includes bibliographical references and index. London: British Institute of Radiology, 2007.

[39] Pam Duxbury Angela Cherry. *Practical Radiotherapy Physics and Equipment.* 2nd ed. 2009.

[40] H. Rodney Withers. "The Four R's of Radiotherapy". In: *Advances in Radiation Biology.* Ed. by John T. Lett and Howard Adler. Vol. 5. Elsevier, 1975, pp. 241–271. URL: https://www.sciencedirect.com/science/article/pii/B9780120354054500128%20https://www.sciencedirect.com/science/article/abs/pii/B9780120354054500128?via%3Dihub.

[41] G. G. Steel, T. J. McMillan, and J. H. Peacock. "The 5Rs of radiobiology". In: *Int J Radiat Biol* 56.6 (1989). Steel, G G McMillan, T J Peacock, J H Journal Article England 1989/12/01 Int J Radiat Biol. 1989 Dec;56(6):1045-8. doi: 10.1080/09553008914552491., pp. 1045–8. URL: https://www.tandfonline.com/doi/pdf/10.1080/09553008914552491.

[42] Sarah Baatout. *Radiobiology Textbook.* 1st 2023. Radiobiology Textbook. Cham: Springer International Publishing, 2023.

[43] Farzad Taghizadeh-Hesary et al. *From Radiobiology to Radiation Oncology.* 1st 2025. From Radiobiology to Radiation Oncology. Cham: Springer Nature Switzerland, 2025.

[44] B. M. Sutherland et al. "Clustered DNA damages induced by high and low LET radiation, including heavy ions". In: *Phys Med* 17 Suppl 1 (2001). Sutherland, B M Bennett, P V Schenk, H Sidorkina, O Laval, J Trunk, J Monteleone, D Sutherland, J Journal Article Research Support, Non-U.S. Gov't Research Support, U.S. Gov't, Non-P.H.S. Italy 2002/01/05 Phys Med. 2001;17 Suppl 1:202-4., pp. 202–4.

[45] Bleddyn Jones and Mark A. Hill. "The physical separation between the LET associated with the ultimate relative biological effect (RBE) and the maximum LET in a proton or ion beam". In: *Biomedical Physics Engineering Express* 6.5 (2020), p. 055001. URL: https://doi.org/10.1088/2057-1976/ab9e13.

[46] Beth Wilkinson, Mark A. Hill, and Jason L. Parsons. *The Cellular Response to Complex DNA Damage Induced by Ionising Radiation.* Electronic Article. 2023.

[47] Rositsa Dueva and George Iliakis. "Alternative pathways of non-homologous end joining (NHEJ) in genomic instability and cancer". In: *Translational Cancer Research* 2.3 (2013), pp. 163–177. URL: https://tcr.amegroups.org/article/view/1152.

[48] Joonyoung Her and Samuel F. Bunting. "How cells ensure correct repair of DNA double-strand breaks". In: *Journal of Biological Chemistry* 293.27 (2018), pp. 10502–10511. URL: https://www.sciencedirect.com/science/article/pii/S0021925820338084.

[49] Kai Yang, Rong Guo, and Dongyi Xu. "Non-homologous end joining: advances and frontiers". In: *Acta Biochimica et Biophysica Sinica* 48.7 (2016), pp. 632–640. URL: https://doi.org/10.1093/abbs/gmw046.

[50] A. Kakarougkas and P. A. Jeggo. "DNA DSB repair pathway choice: an orchestrated handover mechanism". In: *Br J Radiol* 87.1035 (2014), p. 20130685.

[51] M. A. Hill. “Radiation Track Structure: How the Spatial Distribution of Energy Deposition Drives Biological Response”. In: *Clinical Oncology* 32.2 (2020). doi: 10.1016/j.clon.2019.08.006, pp. 75–83. URL: https://doi.org/10.1016/j.clon.2019.08.006.

[52] Stephen Joseph McMahon. “The linear quadratic model: usage, interpretation and challenges”. In: *Physics in Medicine Biology* 64.1 (2019), 01TR01. URL: https://dx.doi.org/10.1088/1361-6560/aaf26a.

[53] C. M. van Leeuwen et al. “The alfa and beta of tumours: a review of parameters of the linear-quadratic model, derived from clinical radiotherapy studies”. In: *Radiat Oncol* 13.1 (2018), p. 96.

[54] J. Z. Wang et al. “A generalized linear-quadratic model for radiosurgery, stereotactic body radiation therapy, and high-dose rate brachytherapy”. In: *Sci Transl Med* 2.39 (2010), 39ra48.

[55] H. Li. “Invalidity of, and alternative to, the linear quadratic model as a predictive model for postirradiation cell survival”. In: *Cancer Sci* 114.7 (2023), pp. 2931–2938.

[56] H. Rodney Withers, Jr. Thames Howard D., and Lester J. Peters. “A new isoeffect curve for change in dose per fraction”. In: *Radiotherapy and Oncology* 1.2 (1983). doi: 10.1016/S0167-8140(83)80021-8, pp. 187–191. URL: https://doi.org/10.1016/S0167-8140(83)80021-8.

[57] G. W. Barendsen. “Dose fractionation, dose rate and iso-effect relationships for normal tissue responses”. In: *Int J Radiat Oncol Biol Phys* 8.11 (1982). Barendsen, G W Journal Article Review United States 1982/11/01 Int J Radiat Oncol Biol Phys. 1982 Nov;8(11):1981-97. doi: 10.1016/0360-3016(82)90459-x., pp. 1981–97.

[58] J. F. Fowler. “The linear-quadratic formula and progress in fractionated radiotherapy”. In: *Br J Radiol* 62.740 (1989). Fowler, J F Journal Article Research Support, Non-U.S. Gov’t Review England 1989/08/01 Br J Radiol. 1989 Aug;62(740):679-94. doi: 10.1259/0007-1285-62-740-679., pp. 679–94.

[59] Pierre Montay-Gruel et al. “Irradiation in a flash: Unique sparing of memory in mice after whole brain irradiation with dose rates above 100 Gy/s”. In: *Radiotherapy and Oncology* 124.3 (2017). doi: 10.1016/j.radonc.2017.05.003, pp. 365–369. URL: https://doi.org/10.1016/j.radonc.2017.05.003.

[60] Vincent Favaudon et al. “Ultrahigh dose-rate FLASH irradiation increases the differential response between normal and tumor tissue in mice”. In: *Science Translational Medicine* 6.245 (2014). doi: 10.1126/scitranslmed.3008973, 245ra93–245ra93. URL: https://doi.org/10.1126/scitranslmed.3008973.

[61] J. D. Wilson et al. “Ultra-High Dose Rate (FLASH) Radiotherapy: Silver Bullet or Fool’s Gold?” In: *Front Oncol* 9 (2019), p. 1563. URL: https://www.ncbi.nlm.nih.gov/pubmed/32010633%20https://www.ncbi.nlm.nih.gov/pmc/articles/PMC6979639/pdf/fonc-09-01563.pdf.

[62] D. L. Dewey and J. W. Boag. “Modification of the oxygen effect when bacteria are given large pulses of radiation”. In: *Nature* 183.4673 (1959). DEWEY, D L BOAG, J W eng England Nature. 1959 May 23;183(4673):1450-1. doi: 10.1038/1831450a0., pp. 1450–1. URL: https://www.ncbi.nlm.nih.gov/pubmed/13657161.

[63] Edward R. Epp, Herbert Weiss, and Ann Santomasso. In: *Radiat. Res.* 34.2 (May 1968), pp. 320–325. URL: https://www.jstor.org/stable/3572557.

[64] Theodore L. Phillips and B. Ralph Worsnop. "Ultra-high Dose-rate Effects in Radiosensitive Bacteria". In: *International Journal of Radiation Biology and Related Studies in Physics, Chemistry and Medicine* 14.6 (1969). doi: 10.1080/09553006914551761, pp. 573–575. URL: https://doi.org/10.1080/09553006914551761%20https://www.tandfonline.com/doi/pdf/10.1080/09553006914551761?needAccess=true.

[65] H. Weiss et al. "Oxygen Depletion in Cells Irradiated at Ultra-high Dose-rates and at Conventional Dose-rates". In: *International Journal of Radiation Biology and Related Studies in Physics, Chemistry and Medicine* 26.1 (1974), pp. 17–29. URL: https://doi.org/10.1080/09553007414550901.

[66] E. R. Epp et al. "Oxygen Diffusion Times in Bacterial Cells Irradiated with High-Intensity Pulsed Electrons: New Upper Limit to the Lifetime of Oxygen-Sensitive Species Suspected to Be Induced at Critical Sites in Bacterial Cells". In: *Radiation Research* 54.2 (1973), pp. 171–180. URL: http://www.jstor.org/stable/3573695.

[67] H. Weiss et al. "Irradiation of Serratia marcescens by Single and Double Pulses of High-Intensity Electrons: Oxygen Diffusion Kinetics and Lifetime of Oxygen-Sensitive Species". In: *Radiation Research* 61.3 (1975), pp. 355–365. URL: http://www.jstor.org/stable/3574111.

[68] C. D. Town. "Radiobiology. Effect of high dose rates on survival of mammalian cells". In: *Nature* 215.5103 (1967). Town, C D eng England Nature. 1967 Aug 19;215(5103):847-8. doi: 10.1038/215847a0., pp. 847–8. URL: https://www.ncbi.nlm.nih.gov/pubmed/6049731%20https://www.nature.com/articles/215847a0.

[69] H. B. Michaels et al. "Oxygen sensitization of CHO cells at ultrahigh dose rates: prelude to oxygen diffusion studies". In: *Radiat Res* 76.3 (1978). Michaels, H B Epp, E R Ling, C C Peterson, E C Journal Article Research Support, U.S. Gov't, P.H.S. United States 1978/12/01 Radiat Res. 1978 Dec;76(3):510-21., pp. 510–21.

[70] E. R. Epp et al. "Studies on Mammalian Cells Exposed to Electrons at Ultrahigh Dose Rates from a 600 KV Field Emission Pulsed Source". In: *IEEE Transactions on Nuclear Science* 26.1 (1979), pp. 1750–1757.

[71] E. R. Epp et al. "RADIOSENSITIVITY OF CULTURED MAMMALIAN-CELLS EXPOSED TO SINGLE HIGH-INTENSITY PULSES OF ELECTRONS IN VARIOUS CONCENTRATIONS OF OXYGEN". In: *Radiation Research* 52.2 (1972), pp. 324–+. URL: %3CGo%20to%20ISI%3E://WOS:A19720206100009.

[72] P.W.Todd et al. "Abstracts of the Fifteenth Annual Meeting of the Radiation Research Society, San Juan, Puerto Rico May 7-11, 1967". In: *Radiation Research* 31.3 (1967), pp. 644–645. URL: http://www.jstor.org/stable/3572370.

[73] Paul Todd et al. "Pulsed High-Intensity Roentgen Rays: Inactivation of human cells cultured in vitro and limitations on usefulness in radiotherapy". In: *Acta Radiologica: Therapy, Physics, Biology* 7.1 (1968). doi: 10.3109/02841866809133174, pp. 22–26. URL: https://doi.org/10.3109/02841866809133174.

[74] R. J. Berry. "Effects of radiation dose-rate from protracted, continuous irradiation to ultra-high dose-rates from pulsed accelerators". In: *Br Med Bull* 29.1 (1973), pp. 44–7.

[75] A. H. W. Nias et al. "Effects of pulses of radiation on the survival of mammalian cells". In: *The British Journal of Radiology* 42.499 (1969), pp. 553–553. URL: https://www.birpublications.org/doi/abs/10.1259/0007-1285-42-499-553-b.

[76] R. J. Berry et al. "Survival of mammalian cells exposed to x rays at ultra-high dose-rates". In: *Br J Radiol* 42.494 (1969). Berry, R J Hall, E J Forster, D W Storr, T H Goodman, M J eng England Br J Radiol. 1969 Feb;42(494):102-7. doi: 10.1259/0007-1285-42-494-102., pp. 102–7. URL: https://www.ncbi.nlm.nih.gov/pubmed/4975207.

[77] A. H. W. Nias et al. "Survival of Hela Cells from 10 Nanosecond Pulses of Electrons". In: *International Journal of Radiation Biology and Related Studies in Physics Chemistry and Medicine* 17.6 (1970), p. 595. URL: %3CGo%20to%20ISI%3E://WOS:A1970G810400012%20https://www.tandfonline.com/doi/pdf/10.1080/09553007014550751?needAccess=true.

[78] R. J. Berry and J. B. H. Stedeford. "Reproductive survival of mammalian cells after irradiation at ultra-high dose-rates: further observations and their importance for radiotherapy". In: *The British Journal of Radiology* 45.531 (1972). doi: 10.1259/0007-1285-45-531-171, pp. 171–177. URL: https://doi.org/10.1259/0007-1285-45-531-171.

[79] J. W. Purdie, E. R. Inhaber, and N. V. Klassen. "Increased sensitivity of anoxic mammalian cells irradiated with single pulses at very high dose rates". In: *Symposium on microdosimetry*.

[80] P. Lindop and J. Rotblat. *Cellular Basis and Aetiology of Late Somatic Effects of Ionizing Radiation*. Vol. null. null. 1963, p. 313.

[81] E. J. Ainsworth et al. "Pulsed Irradiation Studies in Mice, Rats and Dogs". In: *Biological effects of neutron and proton irradiations*. IAEA, 1964, pp. 15–30. URL: https://inis.iaea.org/records/2wg4x-68p86.

[82] Shirley Hornsey and Tikvah Alper. "Unexpected Dose-rate Effect in the Killing of Mice by Radiation". In: *Nature* 210.5032 (1966), pp. 212–213. URL: https://doi.org/10.1038/210212a0.

[83] Shirley Hornsey and D. K. Bewley. "Hypoxia in Mouse Intestine Induced by Electron Irradiation at High Dose-rates". In: *International Journal of Radiation Biology and Related Studies in Physics, Chemistry and Medicine* 19.5 (1971). doi: 10.1080/09553007114550611, pp. 479–483. URL: https://doi.org/10.1080/09553007114550611.

[84] S. B. Field and D. K. Bewley. "Effects of dose-rate on the radiation response of rat skin". In: *Int J Radiat Biol Relat Stud Phys Chem Med* 26.3 (1974), pp. 259–67.

[85] Tetsuo Inada et al. "High Dose-rate Dependence of Early Skin Reaction in Mouse". In: *International Journal of Radiation Biology and Related Studies in Physics, Chemistry and Medicine* 38.2 (1980). doi: 10.1080/09553008014551031, pp. 139–145. URL: https://doi.org/10.1080/09553008014551031%20https://www.tandfonline.com/doi/pdf/10.1080/09553008014551031?needAccess=true.

[86] J. H. Hendry et al. "The Constant Low Oxygen Concentration in All the Target Cells for Mouse Tail Radionecrosis". In: *Radiation Research* 92.1 (1982), pp. 172–181. URL: http://www.jstor.org/stable/3575852.

[87] Billy W. Loo et al. "(P003) Delivery of Ultra-Rapid Flash Radiation Therapy and Demonstration of Normal Tissue Sparing After Abdominal Irradiation of Mice". In: *International Journal of Radiation Oncology*Biology*Physics* 98.2, Supplement (2017), E16. URL: https://www.sciencedirect.com/science/article/pii/S0360301617305047.

[88] M. C. Vozenin et al. "The Advantage of FLASH Radiotherapy Confirmed in Mini-pig and Cat-cancer Patients". In: *Clin Cancer Res* 25.1 (2019), pp. 35–42.

[89] E. Abel et al. "Characterization of Radiation-Induced Lung Fibrosis and Mode of Cell Death Using Single and Multi-Pulsed Proton Flash Irradiation". In: *International Journal of Radiation Oncology, Biology, Physics* 105.1 (2019). doi: 10.1016/j.ijrobp.2019.06.1033, E652–E653. URL: https://doi.org/10.1016/j.ijrobp.2019.06.1033.

[90] Swati Girdhani et al. "Abstract LB-280: FLASH: A novel paradigm changing tumor irradiation platform that enhances therapeutic ratio by reducing normal tissue toxicity and activating immune pathways". In: *Cancer Research* $79.13_{Supplement}$ (2019), LB-280-LB–280. URL: https://doi.org/10.1158/1538-7445.AM2019-LB-280.

[91] N. Rama et al. "Improved Tumor Control Through T-cell Infiltration Modulated by Ultra-High Dose Rate Proton FLASH Using a Clinical Pencil Beam Scanning Proton System". In: *International Journal of Radiation Oncology*Biology*Physics* 105.1, Supplement (2019), S164–S165. URL: https://www.sciencedirect.com/science/article/pii/S0360301619310223.

[92] D. A. Simmons et al. "Reduced cognitive deficits after FLASH irradiation of whole mouse brain are associated with less hippocampal dendritic spine loss and neuroinflammation". In: *Radiother Oncol* 139 (2019), pp. 4–10.

[93] Bhanu Prasad Venkatesulu et al. "Ultra high dose rate (35 Gy/sec) radiation does not spare the normal tissue in cardiac and splenic models of lymphopenia and gastrointestinal syndrome". In: *Scientific Reports* 9.1 (2019), p. 17180. URL: https://doi.org/10.1038/s41598-019-53562-y.

[94] Y. Alaghband et al. "Neuroprotection of Radiosensitive Juvenile Mice by Ultra-High Dose Rate FLASH Irradiation". In: *Cancers (Basel)* 12.6 (2020).

[95] B. D. Allen et al. "Maintenance of Tight Junction Integrity in the Absence of Vascular Dilation in the Brain of Mice Exposed to Ultra-High-Dose-Rate FLASH Irradiation". In: *Radiat Res* 194.6 (2020), pp. 625–635.

[96] Eric S. Diffenderfer et al. “Design, Implementation, and in Vivo Validation of a Novel Proton FLASH Radiation Therapy System”. In: *International Journal of Radiation Oncology*Biology*Physics* 106.2 (2020), pp. 440–448. URL: https://www.sciencedirect.com/science/article/pii/S0360301619340556.

[97] C. Fouillade et al. “FLASH Irradiation Spares Lung Progenitor Cells and Limits the Incidence of Radio-induced Senescence”. In: *Clin Cancer Res* 26.6 (2020), pp. 1497–1506.

[98] K. Levy et al. “Abdominal FLASH irradiation reduces radiation-induced gastrointestinal toxicity for the treatment of ovarian cancer in mice”. In: *Sci Rep* 10.1 (2020), p. 21600.

[99] L. A. Soto et al. “FLASH Irradiation Results in Reduced Severe Skin Toxicity Compared to Conventional-Dose-Rate Irradiation”. In: *Radiat Res* 194.6 (2020), pp. 618–624.

[100] Xu Cao et al. “Quantification of Oxygen Depletion During FLASH Irradiation In Vitro and In Vivo”. In: *International Journal of Radiation Oncology*Biology*Physics* 111.1 (2021), pp. 240–248. URL: https://www.sciencedirect.com/science/article/pii/S0360301621003588.

[101] S. Chabi et al. “Ultra-high-dose-rate FLASH and Conventional-Dose-Rate Irradiation Differentially Affect Human Acute Lymphoblastic Leukemia and Normal Hematopoiesis”. In: *Int J Radiat Oncol Biol Phys* 109.3 (2021), pp. 819–829.

[102] S. Cunningham et al. “FLASH Proton Pencil Beam Scanning Irradiation Minimizes Radiation-Induced Leg Contracture and Skin Toxicity in Mice”. In: *Cancers (Basel)* 13.5 (2021). URL: https://www.ncbi.nlm.nih.gov/pubmed/33804336%20https://mdpi-res.com/d_attachment/cancers/cancers-13-01012/article_deploy/cancers-13-01012.pdf?version=1614587134.

[103] P. Montay-Gruel et al. “FLASH radiotherapy with photon beams”. In: *Medical Physics* (2021), p. 13. URL: %3CGo%20to%20ISI%3E://WOS:000715051700001%20https://aapm.onlinelibrary.wiley.com/doi/pdfdirect/10.1002/mp.15222?download=true.

[104] Pierre Montay-Gruel et al. “Hypofractionated FLASH-RT as an Effective Treatment against Glioblastoma that Reduces Neurocognitive Side Effects in Mice”. In: *Clinical Cancer Research* 27.3 (2021), pp. 775–784. URL: https://doi.org/10.1158/1078-0432.CCR-20-0894.

[105] Jia-Ling Ruan et al. “Irradiation at Ultra-High (FLASH) Dose Rates Reduces Acute Normal Tissue Toxicity in the Mouse Gastrointestinal System”. In: *International Journal of Radiation Oncology*Biology*Physics* 111.5 (2021), pp. 1250–1261. URL: https://www.sciencedirect.com/science/article/pii/S0360301621026432%20https://www.ncbi.nlm.nih.gov/pmc/articles/PMC7612009/pdf/EMS138176.pdf.

[106] B. S. Sorensen et al. “In vivo validation and tissue sparing factor for acute damage of pencil beam scanning proton FLASH”. In: *Radiotherapy and Oncology* 161 (2021), S447–S448. URL: %3CGo%20to%20ISI%3E://WOS:000709667201129.

[107] Anastasia Velalopoulou et al. “FLASH Proton Radiotherapy Spares Normal Epithelial and Mesenchymal Tissues While Preserving Sarcoma Response”. In: *Cancer Research* 81.18 (2021), pp. 4808–4821. URL: https://doi.org/10.1158/0008-5472.CAN-21-1500.

[108] Barrett D Allen et al. “Elucidating the neurological mechanism of the FLASH effect in juvenile mice exposed to hypofractionated radiotherapy”. In: *Neuro-Oncology* 25.5 (2022), pp. 927–939. URL: https://doi.org/10.1093/neuonc/noac248.

[109] Feng Gao et al. “First demonstration of the FLASH effect with ultrahigh dose rate high-energy X-rays”. In: *Radiotherapy and Oncology* 166 (2022), pp. 44–50. URL: https://www.sciencedirect.com/science/article/pii/S016781402108796X.

[110] D. Miles et al. “FLASH Effects Induced by kV X-Rays in a Murine Skin Model”. In: *International Journal of Radiation Oncology, Biology, Physics* 114.3 (2022). doi: 10.1016/j.ijrobp.2022.07.2077, e508. URL: https://doi.org/10.1016/j.ijrobp.2022.07.2077.

[111] Xiaolin Shi et al. “FLASH X-ray spares intestinal crypts from pyroptosis initiated by cGAS-STING activation upon radioimmunotherapy”. In: *Proceedings of the National Academy of Sciences* 119.43 (2022), e2208506119. URL: https://www.pnas.org/doi/abs/10.1073/pnas.2208506119.

[112] Walter Tinganelli et al. “FLASH with carbon ions: Tumor control, normal tissue sparing, and distal metastasis in a mouse osteosarcoma model”. In: *Radiotherapy and Oncology* 175 (2022), pp. 185–190. URL: https://www.sciencedirect.com/science/article/pii/S0167814022002389.

[113] H. Zhu et al. “Radioprotective effect of X-ray abdominal FLASH irradiation: Adaptation to oxidative damage and inflammatory response may be benefiting factors”. In: *Med Phys* (2022). URL: https://www.ncbi.nlm.nih.gov/pubmed/35451077.

[114] Yasaman Alaghband et al. “Uncovering the Protective Neurologic Mechanisms of Hypofractionated FLASH Radiotherapy”. In: *Cancer Research Communications* 3.4 (2023), pp. 725–737. URL: https://doi.org/10.1158/2767-9764.CRC-23-0117.

[115] S. Melemenidis et al. “Comparison of Tumor Control between FLASH and CONV in an Orthotopic Breast Cancer Model”. In: *International Journal of Radiation Oncology*Biology*Physics* 117.2, Supplement (2023), e251–e252. URL: https://www.sciencedirect.com/science/article/pii/S0360301623056286.

[116] D. Miles et al. “FLASH Effects Induced by Orthovoltage X-Rays”. In: *Int J Radiat Oncol Biol Phys* 117.4 (2023), pp. 1018–1027. URL: https://pmc.ncbi.nlm.nih.gov/articles/PMC11189000/.

[117] S. Shukla et al. “Ultra-high dose-rate proton FLASH improves tumor control”. In: *Radiother Oncol* 186 (2023), p. 109741.

[118] Qixian Zhang et al. *Absence of Tissue-Sparing Effects in Partial Proton FLASH Irradiation in Murine Intestine*. Electronic Article. 2023.

[119] Hongyu Zhu et al. "Comparison of intratumor and local immune response between MV X-ray FLASH and conventional radiotherapies". In: *Clinical and Translational Radiation Oncology* 38 (2023). doi: 10.1016/j.ctro.2022.11.005, pp. 138–146. URL: https://doi.org/10.1016/j.ctro.2022.11.005.

[120] Olivia G. G. Drayson et al. "A multi-institutional study to investigate the sparing effect after whole brain electron FLASH in mice: Reproducibility and temporal evolution of functional, electrophysiological, and neurogenic endpoints". In: *Radiotherapy and Oncology* 201 (2024). doi: 10.1016/j.radonc.2024.110534. URL: https://doi.org/10.1016/j.radonc.2024.110534.

[121] J. Fu et al. "Exploring Deep Learning for Estimating the Isoeffective Dose of FLASH Irradiation From Mouse Intestinal Histological Images". In: *Int J Radiat Oncol Biol Phys* 119.3 (2024), pp. 1001–1010.

[122] R. J. Leavitt et al. "Acute Hypoxia Does Not Alter Tumor Sensitivity to FLASH Radiation Therapy". In: *Int J Radiat Oncol Biol Phys* 119.5 (2024), pp. 1493–1505.

[123] Oscar Padilla et al. "Immune Response following FLASH and Conventional Radiation in Diffuse Midline Glioma". In: *International Journal of Radiation Oncology*Biology*Physics* 119.4 (2024), pp. 1248–1260. URL: https://www.sciencedirect.com/science/article/pii/S0360301624003006.

[124] Sarah Rudigkeit et al. "Proton-FLASH: effects of ultra-high dose rate irradiation on an in-vivo mouse ear model". In: *Scientific Reports* 14.1 (2024), p. 1418. URL: https://doi.org/10.1038/s41598-024-51951-6.

[125] K. H. Brown et al. "Dose, dose rate and split dose impacts murine skin responses following photon FLASH irradiation". In: *Radiother Oncol* (2025), p. 111125. URL: https://www.thegreenjournal.com/article/S0167-8140(25)04629-8/pdf.

[126] F. Gao et al. "Electron-beam FLASH whole brain irradiation induced a unique changes of intestinal flora". In: *Mol Med* 31.1 (2025), p. 165.

[127] V. Grilj et al. "Average Dose Rate is the Major Temporal Beam Structure Parameter for Preserving Murine Intestines with Pulsed Electron FLASH-RT". In: *Int J Radiat Oncol Biol Phys* (2025).

[128] L. Kristensen et al. "Electron vs proton FLASH radiation on murine skin toxicity". In: *Radiother Oncol* 206 (2025). 1879-0887 Kristensen, Line Rohrer, Sky Hoffmann, Lone Præstegaard, Lars H Ankjærgaard, Christina Andersen, Claus E Kanouta, Eleni Johansen, Jacob Graversen Sahlertz, Morten Nijkamp, Jasper Poulsen, Per Rugaard Sørensen, Brita Singers Comparative Study Journal Article Ireland 2025/02/22 Radiother Oncol. 2025 May;206:110796. doi: 10.1016/j.radonc.2025.110796. Epub 2025 Feb 19., p. 110796.

[129] O. Zlobinskaya et al. "The Effects of Ultra-High Dose Rate Proton Irradiation on Growth Delay in the Treatment of Human Tumor Xenografts in Nude Mice". In: *Radiation Research* 181.2 (2014), pp. 177–183. URL: https://doi.org/10.1667/RR13464.1.

[130] K. Liu et al. "Redefining FLASH Radiation Therapy: The Impact of Mean Dose Rate and Dose Per Pulse in the Gastrointestinal Tract". In: *Int J Radiat Oncol Biol Phys* 121.4 (2025), pp. 1063–1076.

[131] S. Melemenidis et al. “Effectiveness of FLASH vs. Conventional Dose Rate Radiotherapy in a Model of Orthotopic, Murine Breast Cancer”. In: *Cancers (Basel)* 17.7 (2025).

[132] Armin D. Tavakkoli et al. “Anesthesia is a potent determinant of ultra-high dose rate sparing in the murine total abdominal irradiation model”. In: *Frontiers in Oncology* Volume 15 - 2025 (2025). URL: https://www.frontiersin.org/journals/oncology/articles/10.3389/fonc.2025.1666489.

[133] Pierre Montay-Gruel et al. “X-rays can trigger the FLASH effect: Ultra-high dose-rate synchrotron light source prevents normal brain injury after whole brain irradiation in mice”. In: *Radiotherapy and Oncology* 129.3 (2018). doi: 10.1016/j.radonc.2018.08.016, pp. 582–588. URL: https://doi.org/10.1016/j.radonc.2018.08.016.

[134] Lloyd M. L. Smyth et al. “Comparative toxicity of synchrotron and conventional radiation therapy based on total and partial body irradiation in a murine model”. In: *Scientific Reports* 8.1 (2018), p. 12044. URL: https://doi.org/10.1038/s41598-018-30543-1.

[135] E. Beyreuther et al. “Feasibility of proton FLASH effect tested by zebrafish embryo irradiation”. In: *Radiother Oncol* 139 (2019), pp. 46–50.

[136] Pierre Montay-Gruel et al. “Long-term neurocognitive benefits of FLASH radiotherapy driven by reduced reactive oxygen species”. In: *Proceedings of the National Academy of Sciences* 116.22 (2019). doi: 10.1073/pnas.1901777116, pp. 10943–10951. URL: https://doi.org/10.1073/pnas.1901777116.

[137] Jörg Pawelke et al. “Electron dose rate and oxygen depletion protect zebrafish embryos from radiation damage”. In: *Radiotherapy and Oncology* 158 (2021). doi: 10.1016/j.radonc.2021.02.003, pp. 7–12. URL: https://doi.org/10.1016/j.radonc.2021.02.003.

[138] H. Kacem et al. “Comparing radiolytic production of H(2)O(2) and development of Zebrafish embryos after ultra high dose rate exposure with electron and transmission proton beams”. In: *Radiother Oncol* 175 (2022), pp. 197–202. URL: https://www.ncbi.nlm.nih.gov/pubmed/35868604.

[139] L. Karsch et al. “Beam pulse structure and dose rate as determinants for the flash effect observed in zebrafish embryo”. In: *Radiother Oncol* 173 (2022), pp. 49–54.

[140] F. Horst et al. “Dose and dose rate dependence of the tissue sparing effect at ultra-high dose rate studied for proton and electron beams using the zebrafish embryo model”. In: *Radiother Oncol* 194 (2024), p. 110197. URL: https://www.ncbi.nlm.nih.gov/pubmed/38447870.

[141] A. Faggian et al. “Investigating the Influence of Conventional vs. Ultra-High Dose Rate Proton Irradiation Under Normoxic or Hypoxic Conditions on Multiple Developmental Endpoints in Zebrafish Embryos”. In: *Cancers (Basel)* 17.15 (2025). URL: https://www.ncbi.nlm.nih.gov/pubmed/40805259.

[142] S. B. Field and D. K. Bewley. “Effects of Dose-rate on the Radiation Response of Rat Skin”. In: *International Journal of Radiation Biology and Related Studies in Physics, Chemistry and Medicine* 26.3 (1974). doi: 10.1080/09553007414551221, pp. 259–267. URL: https://doi.org/10.1080/09553007414551221.

[143] D N Slatkin et al. “Subacute neuropathological effects of microplanar beams of x-rays from a synchrotron wiggler”. In: *Proceedings of the National Academy of Sciences* 92.19 (1995), pp. 8783–8787. URL: https://www.pnas.org/doi/abs/10.1073/pnas.92.19.8783.

[144] Elise Konradsson et al. “Comparable Long-Term Tumor Control for Hypofractionated FLASH Versus Conventional Radiation Therapy in an Immunocompetent Rat Glioma Model”. In: *Advances in Radiation Oncology* 7.6 (2022). doi: 10.1016/j.adro.2022.101011. URL: https://doi.org/10.1016/j.adro.2022.101011.

[145] Emma Liljedahl et al. “Long-term anti-tumor effects following both conventional radiotherapy and FLASH in fully immunocompetent animals with glioblastoma”. In: *Scientific Reports* 12.1 (2022), p. 12285. URL: https://doi.org/10.1038/s41598-022-16612-6.

[146] Emma Liljedahl et al. “Comparable survival in rats with intracranial glioblastoma irradiated with single-fraction conventional radiotherapy or FLASH radiotherapy”. In: *Frontiers in Oncology* Volume 13 - 2023 (2024). URL: https://www.frontiersin.org/journals/oncology/articles/10.3389/fonc.2023.1309174.

[147] M. T. Williams et al. “Effects of whole brain proton irradiation at conventional or ultra-high dose rate (FLASH), in adult male Sprague Dawley rats”. In: *Sci Rep* 15.1 (2025), p. 10602.

[148] E. Konradsson et al. “Establishment and Initial Experience of Clinical FLASH Radiotherapy in Canine Cancer Patients”. In: *Front Oncol* 11 (2021), p. 658004.

[149] E. Konradsson et al. “Intracavitary Electron FLASH Radiotherapy in a Canine Cancer Patient With Oral Malignant Melanoma”. In: *International Journal of Radiation Oncology, Biology, Physics* 111.3 (2021). doi: 10.1016/j.ijrobp.2021.07.097, S31. URL: https://doi.org/10.1016/j.ijrobp.2021.07.097.

[150] B. Børresen et al. “Evaluation of single-fraction high dose FLASH radiotherapy in a cohort of canine oral cancer patients”. In: *Front Oncol* 13 (2023), p. 1256760.

[151] B. W. Gjaldbæk et al. “Long-term toxicity and efficacy of FLASH radiotherapy in dogs with superficial malignant tumors”. In: *Front Oncol* 14 (2024), p. 1425240.

[152] C. Rohrer Bley et al. “Dose- and Volume-Limiting Late Toxicity of FLASH Radiotherapy in Cats with Squamous Cell Carcinoma of the Nasal Planum and in Mini Pigs”. In: *Clin Cancer Res* 28.17 (2022), pp. 3814–3823.

[153] C. O. Abana et al. “Feasibility and Clinical Implementation of Electron FLASH Radiation Therapy in the Yorkshire Swine Model”. In: *International Journal of Radiation Oncology*Biology*Physics* 117.2, Supplement (2023), e637–e638. URL: https://www.sciencedirect.com/science/article/pii/S0360301623064763.

[154] L. Schoenauen et al. “C. elegans: A potent model for high-throughput screening experiments investigating the FLASH effect”. In: *Clin Transl Radiat Oncol* 45 (2024), p. 100712.

[155] C. L. Limoli et al. “The sparing effect of FLASH-RT on synaptic plasticity is maintained in mice with standard fractionation”. In: *Radiother Oncol* 186 (2023), p. 109767.

[156] Aymeric Almeida et al. “Antitumor Effect by Either FLASH or Conventional Dose Rate Irradiation Involves Equivalent Immune Responses”. In: *International Journal of Radiation Oncology, Biology, Physics* 118.4 (2024). doi: 10.1016/j.ijrobp.2023.10.031, pp. 1110–1122. URL: https://doi.org/10.1016/j.ijrobp.2023.10.031.

[157] F. Gao et al. “Effects of ultra-high dose rate radiotherapy with different fractions and dose rate on acute and chronic lung injury in mice”. In: *Heliyon* 10.22 (2024), e40298.

[158] Y. E. Kim et al. “Effects of Ultra-high doserate FLASH Irradiation on the Tumor Microenvironment in Lewis Lung Carcinoma: Role of Myosin Light Chain”. In: *Int J Radiat Oncol Biol Phys* 109.5 (2021), pp. 1440–1453.

[159] J. T. Eggold et al. “Abdominopelvic FLASH Irradiation Improves PD-1 Immune Checkpoint Inhibition in Preclinical Models of Ovarian Cancer”. In: *Mol Cancer Ther* 21.2 (2022), pp. 371–381.

[160] M. C. Cuitiño et al. “Comparison of Gonadal Toxicity of Single-Fraction Ultra-High Dose Rate and Conventional Radiation in Mice”. In: *Adv Radiat Oncol* 8.4 (2023), p. 101201.

[161] Till Tobias Böhlen et al. “Effect of Conventional and Ultrahigh Dose Rate FLASH Irradiations on Preclinical Tumor Models: A Systematic Analysis”. In: *International Journal of Radiation Oncology*Biology*Physics* 117.4 (2023), pp. 1007–1017. URL: https://www.sciencedirect.com/science/article/pii/S0360301623005357.

[162] E. Schüler et al. “Ultra-high dose rate electron beams and the FLASH effect: from preclinical evidence to a new radiotherapy paradigm”. In: *Med Phys* (2022). 2473-4209 Schüler, Emil Acharya, Munjal Montay-Gruel, Pierre Loo, Billy W Jr Vozenin, Marie-Catherine Maxim, Peter G Journal Article United States 2022/01/09 Med Phys. 2022 Jan 8. doi: 10.1002/mp.15442. URL: https://aapm.onlinelibrary.wiley.com/doi/pdfdirect/10.1002/mp.15442?download=true.

[163] Till Tobias Böhlen et al. “Normal Tissue Sparing by FLASH as a Function of Single-Fraction Dose: A Quantitative Analysis”. In: *International Journal of Radiation Oncology, Biology, Physics* 114.5 (2022). doi: 10.1016/j.ijrobp.2022.05.038, pp. 1032–1044. URL: https://doi.org/10.1016/j.ijrobp.2022.05.038.

[164] Marie-Catherine Vozenin et al. “FLASH: New intersection of physics, chemistry, biology, and cancer medicine”. In: *Reviews of Modern Physics* 96.3 (2024). RMP, p. 035002. URL: https://link.aps.org/doi/10.1103/RevModPhys.96.035002.

[165] N. Esplen, M. S. Mendonca, and M. Bazalova-Carter. “Physics and biology of ultrahigh dose-rate (FLASH) radiotherapy: a topical review”. In: *Physics in Medicine and Biology* 65.23 (2020), p. 37. URL: %3CGo%20to%20ISI%3E://WOS:000595999100001%20https://iopscience.iop.org/article/10.1088/1361-6560/abaa28/pdf.

[166] M. C. Vozenin, J. Bourhis, and M. Durante. "Towards clinical translation of FLASH radiotherapy". In: *Nat Rev Clin Oncol* 19.12 (2022). 1759-4782 Vozenin, Marie-Catherine Bourhis, Jean Durante, Marco Orcid: 0000-0002-4615-553x Journal Article Review England 2022/10/28 Nat Rev Clin Oncol. 2022 Dec;19(12):791-803. doi: 10.1038/s41571-022-00697-z. Epub 2022 Oct 27., pp. 791–803.

[167] Qixian Zhang et al. "FLASH Investigations Using Protons: Design of Delivery System, Preclinical Setup and Confirmation of FLASH Effect with Protons in Animal Systems". In: *Radiation Research* 194.6 (2020), pp. 656–664. URL: https://doi.org/10.1667/RADE-20-00068.1.

[168] O. Gaide et al. "Comparison of ultra-high versus conventional dose rate radiotherapy in a patient with cutaneous lymphoma". In: *Radiother Oncol* 174 (2022), pp. 87–91. URL: https://www.thegreenjournal.com/article/S0167-8140(21)09093-9/pdf.

[169] J. Doyen et al. "Early Toxicities After High Dose Rate Proton Therapy in Cancer Treatments". In: *Front Oncol* 10 (2020), p. 613089.

[170] A. E. Mascia et al. "Proton FLASH Radiotherapy for the Treatment of Symptomatic Bone Metastases: The FAST-01 Nonrandomized Trial". In: *JAMA Oncol* 9.1 (2023), pp. 62–69. URL: https://watermark02.silverchair.com/jamaoncology_mascia_2022_oi_220075_1677706677.72324.pdf?token=AQECAHi208BE49Ooan9kkhW_Ercy7Dm3ZL_9Cf3qfKAc485ysgAAAzgwggM0BgkqhkiG9w0BBwagggMlMIIDIQIBADCCAxoGCSqGSIb3DQEHATAeBglghkVry-3yDWrRQlSM8mxQZc4TJKkM0UC7PFbifrfYJl1uQP9s-Z3f_y3qkbhw8HZSq-OeWSryBYdmekdbAaDobQ9n1f-XEq6FBpMqoVbaCwy9uhjEJtREim0n0e3WiORemA14UNBE24P0LxFhjSUSskZa7J1xPJ7yHLje0SWcbKwcTvCFx7J3V2b22IgHiTnQqV9G9RHSkxvLTeCz-2Q4sKq70Pw7ls9fVRTAFk0BBo7Navy8ai4ZgKGDEhyHB254BLVlLrWfmtyqYlVQRa_kCH5wp--SPy9-rfwZYNs5Qg7YrCICYUFKdqWWAmY3bwHy7qVXcoz0n-gVBeWYaSrdAUHnBNNInmZav7DdghW_ASa0UXiUBpaHAsCpe9ZaUwHU6fhGTPmdzUBhZn5YHan6pHbek6r_CCE2tU06TzYGRID6qw_NhegOJXslabrE7FehZGoSMfIOpzjYYkfisY4iINlZKdvKN_zXDgaRxFTccr_lRolYs0g3GCwwcFLW_j3lEOwAjSLHF7aLd2Ha8TPoK3Qb4fOqeAxFXIks2kvxEBqd3_csqGFXx_ksGGai_XBYRYMDt-aAqeZX1chdsRCEA6JmZUHCKVOEVgzQFDHrKuAvPi_q1JUgjBcZ01QODLOqSwrGnNE8eMRa4kQ8ODIqkKP7Cdi25vxHP9cnLekkFD3EIZ5qxW0FElMbDu_iBkWqbwqm3Mm-lhicyvhPRP17zydBJMpWdqEBPwFavOjUCQEOOWb7xiQENQ00wM39XB1kGMdH6WIRwpL7tklZ7RFxzMdn5oDft_63qxnfPbxs7EWHtGjCOzE0SeV99fh_8TheP1ZVgRkGehBFrufY3wJ2iAMpbuGpiE6U_ePgau7_AaeuE5keVvvFC6xL_COnkoXr_MRk7TPUwlxQ.

[171] R. Kinj et al. "Phase 1 dose escalation trial of FLASH radiotherapy in patients with skin metastases from melanoma". In: *EJC Skin Cancer* 3 (2025). doi: 10.1016/j.ejcskn.2025.100507. URL: https://doi.org/10.1016/j.ejcskn.2025.100507.

[172] E. C. Daugherty et al. "FLASH Radiotherapy for the Treatment of Symptomatic Bone Metastases (FAST-01): Protocol for the First Prospective Feasibility Study". In: *JMIR Res Protoc* (2022).

[173] Rémy Kinj et al. "Randomized phase II selection trial of FLASH and conventional radiotherapy for patients with localized cutaneous squamous cell carcinoma or basal cell carcinoma: A study protocol". In: *Clinical and Translational Radiation Oncology* 45 (2024). doi: 10.1016/j.ctro.2024.100743. URL: https://doi.org/10.1016/j.ctro.2024.100743.

[174] Subir Nag et al. "Feasibility of intraoperative high-dose rate brachytherapy to boost low dose external beam radiation therapy to treat pediatric soft tissue sarcomas". In: *Medical and Pediatric Oncology* 31.2 (1998), pp. 79–85. URL: https://onlinelibrary.wiley.com/doi/abs/10.1002/%28SICI%291096-911X%28199808%2931%3A2%3C79%3A%3AAID-MPO6%3E3.0.CO%3B2-W.

[175] National Cancer Institute. *External Beam Radiation Therapy for Cancer*. Web Page. 2025. URL: https://www.cancer.gov/about-cancer/treatment/types/radiation-therapy/external-beam.

[176] Craig Elith et al. "An Introduction to the Intensity-modulated Radiation Therapy (IMRT) Techniques, Tomotherapy, and VMAT". In: *Journal of Medical Imaging and Radiation Sciences* 42.1 (2011), pp. 37–43. URL: https://www.sciencedirect.com/science/article/pii/S1939865410000822.

[177] S. Karaca and M. Kırlı Bölükbaş. "Time Matters: A Review of Current Radiotherapy Practices and Efficiency Strategies". In: *Technol Cancer Res Treat* 24 (2025), p. 15330338251345376.

[178] Ranald MacKay et al. "FLASH radiotherapy: Considerations for multibeam and hypofractionation dose delivery". In: *Radiotherapy and Oncology* 164 (2021). doi: 10.1016/j.radonc.2021.09.011, pp. 122–127. URL: https://doi.org/10.1016/j.radonc.2021.09.011.

[179] J. Bourhis et al. "Treatment of a first patient with FLASH-radiotherapy". In: *Radiother Oncol* 139 (2019). Bourhis, Jean Sozzi, Wendy Jeanneret Jorge, Patrik Goncalves Gaide, Olivier Bailat, Claude Duclos, Frederic Patin, David Ozsahin, Mahmut Bochud, Francois Germond, Jean-Francois Moeckli, Raphael Vozenin, Marie-Catherine eng Case Reports Research Support, Non-U.S. Gov't Ireland Radiother Oncol. 2019 Oct;139:18-22. doi: 10.1016/j.radonc.2019.06.019. Epub 2019 Jul 11., pp. 18–22. URL: https://www.ncbi.nlm.nih.gov/pubmed/31303340%20https://www.thegreenjournal.com/article/S0167-8140(19)32959-7/fulltext.

[180] Marco Schwarz et al. "Treatment planning for Flash radiotherapy: General aspects and applications to proton beams". In: *Medical Physics* 49.4 (2022), pp. 2861–2874. URL: https://aapm.onlinelibrary.wiley.com/doi/abs/10.1002/mp.15579.

[181] P. Symonds and G. D. D. Jones. "FLASH Radiotherapy: The Next Technological Advance in Radiation Therapy?" In: *Clinical Oncology* 31.7 (2019). doi: 10.1016/j.clon.2019.05.011, pp. 405–406. URL: https://doi.org/10.1016/j.clon.2019.05.011.

[182] Michael M. Folkerts et al. "A framework for defining FLASH dose rate for pencil beam scanning". In: *Medical Physics* 47.12 (2020), pp. 6396–6404. URL: https://doi.org/10.1002/mp.14456.

[183] Jiayun Chen et al. “Influence of maximum MLC leaf speed on the quality of volumetric modulated arc therapy plans”. In: *Journal of Applied Clinical Medical Physics* 21.11 (2020), pp. 37–47. URL: https://doi.org/10.1002/acm2.13020.

[184] G Joyet and K Hohl. “Die biologische hautreaktion in der tiefentherapie als funktion der feldgro Èûe: ein gesetz der strahlentherapie”. In: *Fortschr. Ro Èntgenstr.* (1955).

[185] J. W. Hopewell and C. M. Young. “The effect of field size on the reaction of pig skin to single doses of X rays”. In: *Br J Radiol* 55.653 (1982). Hopewell, J W Young, C M Comparative Study Journal Article England 1982/05/01 Br J Radiol. 1982 May;55(653):356-61. doi: 10.1259/0007-1285-55-653-356., pp. 356–61. URL: https://academic.oup.com/bjr/article-abstract/55/653/356/7314471?redirectedFrom=fulltext.

[186] J. W. Hopewell et al. “The acute effects of different energy beta-emitters on pig and mouse skin”. In: *Br J Radiol Suppl* 19 (1986), pp. 47–51. URL: https://www.ncbi.nlm.nih.gov/pubmed/3480026.

[187] J. W. Hopewell et al. “Dose- and source-size-related changes in the late response of pig skin to irradiation with single doses of beta radiation from sources of differing energy”. In: *Radiat Res* 133.3 (1993). Hopewell, J W Sieber, V K Heryet, J C Wells, J Charles, M W Journal Article Research Support, Non-U.S. Gov’t United States 1993/03/01 Radiat Res. 1993 Mar;133(3):303-11., pp. 303–11.

[188] J. D. Wilson et al. “Ultra-High Dose Rate (FLASH) Radiotherapy: Silver Bullet or Fool’s Gold?” In: *Front Oncol* 9 (2019), p. 1563. URL: https://www.ncbi.nlm.nih.gov/pubmed/32010633%20https://www.ncbi.nlm.nih.gov/pmc/articles/PMC6979639/pdf/fonc-09-01563.pdf.

[189] M. M. Kim et al. “Development of Ultra-High Dose-Rate (FLASH) Particle Therapy”. In: *Ieee Transactions on Radiation and Plasma Medical Sciences* 6.3 (2022), pp. 252–262. URL: %3CGo%20to%20ISI%3E://WOS:000766267000006.

[190] M. C. Vozenin et al. “All Irradiations that are Ultra-High Dose Rate may not be FLASH: The Critical Importance of Beam Parameter Characterization and In Vivo Validation of the FLASH Effect”. In: *Radiat Res* 194.6 (2020). Vozenin, Marie-Catherine Montay-Gruel, Pierre Limoli, Charles Germond, Jean-Francois eng Validation Study 2020/08/28 Radiat Res. 2020 Dec 1;194(6):571-572. doi: 10.1667/RADE-20-00141.1., pp. 571–572. URL: https://www.ncbi.nlm.nih.gov/pubmed/32853355.

[191] K. Liu et al. “Discordance in acute gastrointestinal toxicity between synchrotron-based proton and linac-based electron ultra-high dose rate irradiation”. In: *bioRxiv* (2024).

[192] B. S. Sorensen et al. “Proton FLASH: Impact of Dose Rate and Split Dose on Acute Skin Toxicity in a Murine Model”. In: *Int J Radiat Oncol Biol Phys* 120.1 (2024), pp. 265–275. URL: https://www.ncbi.nlm.nih.gov/pubmed/38750904.

[193] P. Howard-Flanders and D. Moore. "The Time Interval after Pulsed Irradiation within Which Injury to Bacteria Can Be Modified by Dissolved Oxygen: I. A Search for an Effect of Oxygen 0.02 Second after Pulsed Irradiation". In: *Radiation Research* 9.4 (1958), pp. 422–437. URL: http://www.jstor.org/stable/3570768.

[194] M. A. Shenoy et al. "Time-Resolved Oxygen Effects in Irradiated Bacteria and Mammalian Cells: A Rapid-Mix Study". In: *Radiation Research* 62.3 (1975), pp. 498–512. URL: http://www.jstor.org/stable/3574143.

[195] Peter Wardman. "Time as a Variable in Radiation Biology: The Oxygen Effect". In: *Radiation Research* 185.1 (2015), pp. 1–3, 3. URL: https://doi.org/10.1667/RR14323.1.

[196] Marco Durante, Elke Bräuer-Krisch, and Mark Hill. "Faster and safer? FLASH ultra-high dose rate in radiotherapy". In: *British Journal of Radiology* 91.1082 (2018), p. 20170628. URL: https://doi.org/10.1259/bjr.20170628.

[197] D. R. Spitz et al. "An integrated physico-chemical approach for explaining the differential impact of FLASH versus conventional dose rate irradiation on cancer and normal tissue responses". In: *Radiother Oncol* 139 (2019), pp. 23–27. URL: https://www.ncbi.nlm.nih.gov/pubmed/31010709%20https://www.ncbi.nlm.nih.gov/pmc/articles/PMC6761031/pdf/nihms-1527496.pdf.

[198] Vincent Favaudon, Rudi Labarbe, and Charles L. Limoli. "Model studies of the role of oxygen in the FLASH effect". In: *Medical Physics* 49.3 (2022), pp. 2068–2081. URL: https://aapm.onlinelibrary.wiley.com/doi/abs/10.1002/mp.15129.

[199] James F. Mead. "The Irradiation-Induced Autoxidation of Linoleic Acid". In: *Science* 115.2991 (1952), pp. 470–472. URL: https://www.science.org/doi/abs/10.1126/science.115.2991.470.

[200] Veljko Grilj et al. "Average dose rate is the primary determinant of lipid peroxidation in liposome membranes exposed to pulsed electron FLASH beam". In: *Radiation Physics and Chemistry* 222 (2024), p. 111887. URL: https://www.sciencedirect.com/science/article/pii/S0969806X24003797.

[201] Pascal Froidevaux et al. "FLASH irradiation does not induce lipid peroxidation in lipids micelles and liposomes". In: *Radiation Physics and Chemistry* 205 (2023), p. 110733. URL: https://www.sciencedirect.com/science/article/pii/S0969806X22007964.

[202] L. Jiang et al. "Ferroptosis as a p53-mediated activity during tumour suppression". In: *Nature* 520.7545 (2015), pp. 57–62.

[203] N. Vilaplana-Lopera et al. "Tissue-specific iron levels modulate lipid peroxidation and the FLASH radiotherapy effect". In: *Cell Death Dis* 16.1 (2025), p. 668.

[204] Rudi Labarbe et al. "A physicochemical model of reaction kinetics supports peroxyl radical recombination as the main determinant of the FLASH effect". In: *Radiotherapy and Oncology* 153 (2020), pp. 303–310. URL: https://www.sciencedirect.com/science/article/pii/S016781402030308X.

[205] R. Roots and S. Okada. "Estimation of life times and diffusion distances of radicals involved in x-ray-induced DNA strand breaks of killing of mammalian cells". In: *Radiat Res* 64.2 (1975), pp. 306–20.

[206] E. Schuler et al. "Experimental Platform for Ultra-high Dose Rate FLASH Irradiation of Small Animals Using a Clinical Linear Accelerator". In: *Int J Radiat Oncol Biol Phys* 97.1 (2017), pp. 195–203. URL: https://www.ncbi.nlm.nih.gov/pubmed/27816362.

[207] M. Lempart et al. "Modifying a clinical linear accelerator for delivery of ultra-high dose rate irradiation". In: *Radiother Oncol* 139 (2019), pp. 40–45. URL: https://www.ncbi.nlm.nih.gov/pubmed/30755324.

[208] Giuseppe Felici et al. "Transforming an IORT Linac Into a FLASH Research Machine: Procedure and Dosimetric Characterization". In: *Frontiers in Physics* Volume 8 - 2020 (2020). URL: https://www.frontiersin.org/journals/physics/articles/10.3389/fphy.2020.00374.

[209] M. Rahman et al. "Electron FLASH Delivery at Treatment Room Isocenter for Efficient Reversible Conversion of a Clinical LINAC". In: *International Journal of Radiation Oncology Biology Physics* 110.3 (2021), pp. 872–882. URL: %3CGo%20to%20ISI%3E://WOS:000657308400036.

[210] Stanislaw Szpala et al. "Dosimetry with a clinical linac adapted to FLASH electron beams". In: *Journal of Applied Clinical Medical Physics* 22.6 (2021), pp. 50–59. URL: https://aapm.onlinelibrary.wiley.com/doi/abs/10.1002/acm2.13270.

[211] Kyuhak Oh et al. "Initial experience with an electron FLASH research extension (FLEX) for the Clinac system". In: *Journal of Applied Clinical Medical Physics* 25.2 (2024). (James), e14159. URL: https://aapm.onlinelibrary.wiley.com/doi/abs/10.1002/acm2.14159.

[212] Laurence J. Newell et al. "In Regard to Rahman et al". In: *International Journal of Radiation Oncology*Biology*Physics* 110.3 (2021), pp. 908–909. URL: https://www.sciencedirect.com/science/article/pii/S0360301621003084.

[213] Maud Jaccard et al. "High dose-per-pulse electron beam dosimetry: Commissioning of the Oriatron eRT6 prototype linear accelerator for preclinical use". In: *Medical Physics* 45.2 (2018), pp. 863–874. URL: https://aapm.onlinelibrary.wiley.com/doi/abs/10.1002/mp.12713.

[214] Pierre Lansonneur et al. "Simulation and experimental validation of a prototype electron beam linear accelerator for preclinical studies". In: *Physica Medica* 60 (2019), pp. 50–57. URL: https://www.sciencedirect.com/science/article/pii/S1120179719300560.

[215] H. Lim et al. "Implementation of ultra-high dose-rate electron beam from 6-MeV C-band linear accelerator for preclinical study". In: *Journal of Instrumentation* 15.9 (2020). Export Date: 09 July 2025; Cited By: 6. URL: https://www.scopus.com/inward/record.uri?eid=2-s2.0-85091699012&doi=10.1088%2f1748-0221%2f15%2f09%2fP09013&partnerID=40&md5=5a086cb3b9319c5ec51706bab4ecd132.

[216] M. Bazalova-Carter and N. Esplen. "On the capabilities of conventional x-ray tubes to deliver ultra-high (FLASH) dose rates". In: *Medical Physics* 46.12 (2019), pp. 5690–5695. URL: %3CGo%20to%20ISI%3E://WOS:000491531500001%20https://aapm.onlinelibrary.wiley.com/doi/pdfdirect/10.1002/mp.13858?download=true.

[217] Mohammad Rezaee, Iulian Iordachita, and John W. Wong. "Ultrahigh dose-rate (FLASH) x-ray irradiator for pre-clinical laboratory research". In: *Physics in Medicine & Biology* 66.9 (2021), p. 095006. URL: https://dx.doi.org/10.1088/1361-6560/abf2fa%20https://iopscience.iop.org/article/10.1088/1361-6560/abf2fa.

[218] D. Sforza et al. "Preclinical FLASH-SARRP System: Initial Experience on Small Animal Setup and Workflow". In: *International Journal of Radiation Oncology, Biology, Physics* 120.2 (2024). doi: 10.1016/j.ijrobp.2024.07.428, e191–e192. URL: https://doi.org/10.1016/j.ijrobp.2024.07.428.

[219] Mohammad-Ali Tajik Mansoury et al. "Dosimetric commissioning of small animal FLASH radiation research platform". In: *Physics in Medicine & Biology* 70.11 (2025), p. 115015. URL: https://dx.doi.org/10.1088/1361-6560/add641.

[220] F. Verhaegen, P. Granton, and E. Tryggestad. "Small animal radiotherapy research platforms". In: *Phys Med Biol* 56.12 (2011). Verhaegen, Frank Granton, Patrick Tryggestad, Erik eng Research Support, Non-U.S. Gov't Review England 2011/05/28 Phys Med Biol. 2011 Jun 21;56(12):R55-83. doi: 10.1088/0031-9155/56/12/R01. Epub 2011 May 26., R55–83. URL: https://www.ncbi.nlm.nih.gov/pubmed/21617291.

[221] D. Miles et al. "Dosimetric characterization of a rotating anode x-ray tube for FLASH radiotherapy research". In: *Med Phys* 51.2 (2024). 2473-4209 Miles, Devin Sforza, Daniel Wong, John Rezaee, Mohammad R01 CA262097/CA/NCI NIH HHS/United States Journal Article United States 2023/07/17 Med Phys. 2024 Feb;51(2):1474-1483. doi: 10.1002/mp.16609. Epub 2023 Jul 17., pp. 1474–1483.

[222] E Z Rothman, S L Hulbert, and N M Lazarz. *National synchrotron light source. [Annual report], October 1, 1992–September 30, 1993*. Report. Brookhaven National Lab. (BNL), Upton, NY (United States), 1994. URL: https://www.osti.gov/biblio/10169934%20https://www.osti.gov/servlets/purl/10169934.

[223] E. Bräuer-Krisch et al. "Effects of pulsed, spatially fractionated, microscopic synchrotron X-ray beams on normal and tumoral brain tissue". In: *Mutation Research/Reviews in Mutation Research* 704.1 (2010), pp. 160–166. URL: https://www.sciencedirect.com/science/article/pii/S138357420900074X%20https://www.sciencedirect.com/science/article/abs/pii/S138357420900074X?via%3Dihub.

[224] Rolf Behling. *Modern diagnostic X-ray sources : technology, manufacturing, reliability*. Electronic Book. 2020056866 Rolf Behling. illustrations Includes bibliographical references and index. Description based on online resource; title from PDF title page (Site, viewed 07/13/2022). 2021.

[225] P. G. Maxim, S. G. Tantawi, and Jr. Loo B. W. "PHASER: A platform for clinical translation of FLASH cancer radiotherapy". In: *Radiother Oncol* 139 (2019). Maxim, Peter G Tantawi, Sami G Loo, Billy W Jr eng Research Support, N.I.H., Extramural Research Support, Non-U.S. Gov't Research Support, U.S. Gov't, Non-P.H.S. Review Ireland Radiother Oncol. 2019 Oct;139:28-33. doi: 10.1016/j.radonc.2019.05.005. Epub 2019 Jun 6., pp. 28–33. URL: https://www.ncbi.nlm.nih.gov/pubmed/31178058%20https://www.thegreenjournal.com/article/S0167-8140(19)30404-9/fulltext.

[226] Brendan Whelan et al. "Bayesian optimization to design a novel x-ray shaping device". In: *Medical Physics* 49.12 (2022), pp. 7623–7637. URL: https://aapm.onlinelibrary.wiley.com/doi/abs/10.1002/mp.15887%20https://aapm.onlinelibrary.wiley.com/doi/pdfdirect/10.1002/mp.15887?download=true.

[227] Q. Lyu et al. "ROAD: ROtational direct Aperture optimization with a Decoupled ring-collimator for FLASH radiotherapy". In: *Phys Med Biol* 66.3 (2021), p. 035020.

[228] K. Shinohara et al. "Effects of single-pulse (< or = 1 ps) X-rays from laser-produced plasmas on mammalian cells". In: *J Radiat Res* 45.4 (2004), pp. 509–14.

[229] N. D. Powers et al. "Quasi-monoenergetic and tunable X-rays from a laser-driven Compton light source". In: *Nature Photonics* 8.1 (2014), pp. 28–31. URL: https://doi.org/10.1038/nphoton.2013.314.

[230] Marie Jacquet and Pekka Suortti. "Radiation therapy at compact Compton sources". In: *Physica Medica: European Journal of Medical Physics* 31.6 (2015). doi: 10.1016/j.ejmp.2015.02.010, pp. 596–600. URL: https://doi.org/10.1016/j.ejmp.2015.02.010.

[231] K. Burger et al. "Technical and dosimetric realization of in vivo x-ray microbeam irradiations at the Munich Compact Light Source". In: *Med Phys* 47.10 (2020), pp. 5183–5193. URL: https://aapm.onlinelibrary.wiley.com/doi/pdfdirect/10.1002/mp.14433?download=true.

[232] Benedikt Gunther et al. "The versatile X-ray beamline of the Munich Compact Light Source: design, instrumentation and applications". In: *Journal of Synchrotron Radiation* 27.5 (2020), pp. 1395–1414. URL: https://doi.org/10.1107/S1600577520008309%20https://journals.iucr.org/s/issues/2020/05/00/ok5018/ok5018.pdf.

[233] Feng Gao et al. "First demonstration of the FLASH effect with ultrahigh dose rate high-energy X-rays". In: *Radiotherapy and Oncology* (2021).

[234] N. M. Esplen et al. "Design optimization of an electron-to-photon conversion target for ultra-high dose rate x-ray (FLASH) experiments at TRIUMF". In: *Phys Med Biol* (2022). Esplen, Nolan Matthew Egoriti, Luca Paley, William Planche, Thomas Hoehr, Cornelia Gottberg, Alexander Bazalova-Carter, Magdalena eng England 2022/03/18 Phys Med Biol. 2022 Mar 17. doi: 10.1088/1361-6560/ac5ed6. URL: https://www.ncbi.nlm.nih.gov/pubmed/35299167%20https://iopscience.iop.org/article/10.1088/1361-6560/ac5ed6/pdf.

[235] Elke Bräuer-Krisch et al. "Medical physics aspects of the synchrotron radiation therapies: Microbeam radiation therapy (MRT) and synchrotron stereotactic radiotherapy (SSRT)". In: *Physica Medica* 31.6 (2015), pp. 568–583. URL: https://www.sciencedirect.com/science/article/pii/S1120179715001106.

[236] R. J. Griffin et al. "Understanding High-Dose, Ultra-High Dose Rate, and Spatially Fractionated Radiation Therapy". In: *Int J Radiat Oncol Biol Phys* 107.4 (2020), pp. 766–778.

[237] Y. Prezado et al. "Spatially fractionated radiation therapy: a critical review on current status of clinical and preclinical studies and knowledge gaps". In: *Phys Med Biol* 69.10 (2024).

[238] A. J. Johnsrud et al. "Evidence for Early Stage Anti-Tumor Immunity Elicited by Spatially Fractionated Radiotherapy-Immunotherapy Combinations". In: *Radiat Res* 194.6 (2020), pp. 688–697.

[239] G. Ferini et al. "Impressive Results after "Metabolism-Guided" Lattice Irradiation in Patients Submitted to Palliative Radiation Therapy: Preliminary Results of $\mathrm{LATTICE}_0 1 Multicenter Study$". In: *Cancers (Basel)* 14.16 (2022).

[240] Michael P. Grams et al. "Clinical aspects of spatially fractionated radiation therapy treatments". In: *Physica Medica* 111 (2023), p. 102616. URL: https://www.sciencedirect.com/science/article/pii/S1120179723000935%20https://www.physicamedica.com/action/showPdf?pii=S1120179723000935.

[241] Cole Billena and Atif J. Khan. "A Current Review of Spatial Fractionation: Back to the Future?" In: *International Journal of Radiation Oncology, Biology, Physics* 104.1 (2019). doi: 10.1016/j.ijrobp.2019.01.073, pp. 177–187. URL: https://doi.org/10.1016/j.ijrobp.2019.01.073%20https://pmc.ncbi.nlm.nih.gov/articles/PMC7443362/.

[242] I. Martínez-Rovira, J. Puxeu-Vaqué, and Y. Prezado. "Dose evaluation of Grid Therapy using a 6 MV flattening filter-free (FFF) photon beam: A Monte Carlo study". In: *Med Phys* 44.10 (2017), pp. 5378–5383.

[243] X. Zhang et al. "Application of Spatially Fractionated Radiation (GRID) to Helical Tomotherapy using a Novel TOMOGRID Template". In: *Technol Cancer Res Treat* 15.1 (2016), pp. 91–100.

[244] Mohammed Mohiuddin et al. "Spatially fractionated (GRID) radiation for palliative treatment of advanced cancer". In: *Radiation Oncology Investigations* 4.1 (1996), pp. 41–47. URL: https://onlinelibrary.wiley.com/doi/abs/10.1002/%28SICI%291520-6823%281996%294%3A1%3C41%3A%3AAID-ROI7%3E3.0.CO%3B2-M%20https://onlinelibrary.wiley.com/doi/10.1002/(SICI)1520-6823(1996)4:1%3C41::AID-ROI7%3E3.0.CO;2-M.

[245] S. Gholami et al. "Is grid therapy useful for all tumors and every grid block design?" In: *J Appl Clin Med Phys* 17.2 (2016), pp. 206–219.

[246] C. Buckey et al. "Evaluation of a commercially-available block for spatially fractionated radiation therapy". In: *J Appl Clin Med Phys* 11.3 (2010), p. 3163. URL: https://www.ncbi.nlm.nih.gov/pmc/articles/PMC5720442/pdf/ACM2-11-002.pdf.

[247] Hualin Zhang et al. "Photon GRID Radiation Therapy: A Physics and Dosimetry White Paper from the Radiosurgery Society (RSS) GRID/LATTICE, Microbeam and FLASH Radiotherapy Working Group". In: *Radiation Research* 194.6 (2020), pp. 665–677, 13. URL: https://doi.org/10.1667/RADE-20-00047.1.

[248] A. Nobah et al. "Effective spatially fractionated GRID radiation treatment planning for a passive grid block". In: *Br J Radiol* 88.1045 (2015), p. 20140363.

[249] W. Yan et al. "Spatially fractionated radiation therapy: History, present and the future". In: *Clin Transl Radiat Oncol* 20 (2020), pp. 30–38.

[250] Jonathan K. Ha et al. "Feasibility of delivering grid therapy using a multileaf collimator". In: *Medical Physics* 33.1 (2006), pp. 76–82. URL: https://aapm.onlinelibrary.wiley.com/doi/abs/10.1118/1.2140116.

[251] Geoffrey Neuner et al. "High-Dose Spatially Fractionated GRID Radiation Therapy (SFGRT): A Comparison of Treatment Outcomes With Cerrobend vs. MLC SFGRT". In: *International Journal of Radiation Oncology*Biology*Physics* 82.5 (2012), pp. 1642–1649. URL: https://www.sciencedirect.com/science/article/pii/S0360301611002525.

[252] A. S. Meigooni et al. "Dosimetric characteristics with spatial fractionation using electron grid therapy". In: *Medical Dosimetry* 27.1 (2002), pp. 37–42. URL: https://www.sciencedirect.com/science/article/pii/S0958394702000869%20https://www.meddos.org/article/S0958-3947(02)00086-9/fulltext.

[253] Mikoto Tamura et al. "Feasibility of tungsten functional paper in electron grid therapy: A Monte Carlo study". In: *Physics in Medicine and Biology* 62 (2017), pp. 878–889.

[254] Xiaodong Wu et al. "On Modern Technical Approaches of Three-Dimensional High-Dose Lattice Radiotherapy (LRT)". In: *Cureus* 2.3 (2010), e9. URL: http://dx.doi.org/10.7759/cureus.9%20https://assets.cureus.com/uploads/original_article/pdf/13/1613124192-20210212-24896-1qxak7q.pdf.

[255] Jayashree Np et al. "Feasibility planning study of lattice radiotherapy for palliation in bulky tumors". In: *Precision Radiation Oncology* 8.4 (2024), pp. 209–217. URL: https://doi.org/10.1002/pro6.1248.

[256] B. E. Amendola et al. "Safety and Efficacy of Lattice Radiotherapy in Voluminous Non-small Cell Lung Cancer". In: *Cureus* 11.3 (2019), e4263. URL: https://assets.cureus.com/uploads/original_article/pdf/17708/1612428561-1612428552-20210204-18203-1qc5k5h.pdf.

[257] M. P. Grams et al. "VMAT Grid Therapy: A Widely Applicable Planning Approach". In: *Pract Radiat Oncol* 11.3 (2021), e339–e347.

[258] L. Jiang et al. "Combined High-Dose LATTICE Radiation Therapy and Immune Checkpoint Blockade for Advanced Bulky Tumors: The Concept and a Case Report". In: *Front Oncol* 10 (2020), p. 548132. URL: https://pmc.ncbi.nlm.nih.gov/articles/PMC7907519/.

[259] Beatriz Amendola et al. "Lattice Radiotherapy with RapidArc for Treatment of Gynecological Tumors: Dosimetric and Early Clinical Evaluations". In: *Cureus* 2.9 (2010), e15. URL: http://dx.doi.org/10.7759/cureus.15%20https://assets.cureus.com/uploads/case_report/pdf/17/1613121632-20210212-19023-15ddxfk.pdf.

[260] J. M. Blanco Suarez et al. "The Use of Lattice Radiation Therapy (LRT) in the Treatment of Bulky Tumors: A Case Report of a Large Metastatic Mixed Mullerian Ovarian Tumor". In: *Cureus* 7.11 (2015), e389. URL: https://assets.cureus.com/uploads/case_report/pdf/3719/1613129390-20210212-13532-cnswze.pdf.

[261] L. Larrea et al. "Lattice Radiotherapy (LRT)-Spatially Fractionated Radiotherapy (SFRT): Advanced Non-Small Cell Lung Cancer (NSCLC): Early Experience". In: *International Journal of Radiation Oncology, Biology, Physics* 111.3 (2021). doi: 10.1016/j.ijrobp.2021.07.1253, e443. URL: https://doi.org/10.1016/j.ijrobp.2021.07.1253%20https://www.redjournal.org/action/showPdf?pii=S0360301621021234.

[262] P. Xu et al. "Spatially fractionated radiotherapy (Lattice SFRT) in the palliative treatment of locally advanced bulky unresectable head and neck cancer". In: *Clin Transl Radiat Oncol* 48 (2024), p. 100830.

[263] F. Iori et al. "Lattice Radiation Therapy in clinical practice: A systematic review". In: *Clin Transl Radiat Oncol* 39 (2023), p. 100569. URL: https://www.ctro.science/action/showPdf?pii=S2405630822001276.

[264] S. Tubin, H. H. Popper, and L. Brcic. "Novel stereotactic body radiation therapy (SBRT)-based partial tumor irradiation targeting hypoxic segment of bulky tumors (SBRT-PATHY): improvement of the radiotherapy outcome by exploiting the bystander and abscopal effects". In: *Radiat Oncol* 14.1 (2019), p. 21.

[265] Gianluca Ferini et al. *Lattice or Oxygen-Guided Radiotherapy: What If They Converge? Possible Future Directions in the Era of Immunotherapy.* Electronic Article. 2021.

[266] Chang W. Song et al. "Preferential Tumor Vascular Damage Is the Common Antitumor Mechanism of High-Dose Hypofractionated Radiation Therapy: SABR, Spatially Fractionated Radiation Therapy, and FLASH Radiation Therapy". In: *International Journal of Radiation Oncology, Biology, Physics* 117.3 (2023). doi: 10.1016/j.ijrobp.2023.05.015, pp. 701–704. URL: https://doi.org/10.1016/j.ijrobp.2023.05.015.

[267] D. N. Slatkin et al. "Microbeam radiation therapy". In: *Medical Physics* 19.6 (1992). Export Date: 04 October 2025; Cited By: 279, pp. 1395–1400. URL: https://www.scopus.com/inward/record.uri?eid=2-s2.0-0026482950&doi=10.1118%2f1.596771&partnerID=40&md5=b9faacfd66f71bf85222e88ec6054230.

[268] M. A. Grotzer et al. "Microbeam radiation therapy: Clinical perspectives". In: *Physica Medica* 31.6 (2015), pp. 564–567. URL: https://www.sciencedirect.com/science/article/pii/S1120179715000459.

[269] *Spatially Fractionated, Microbeam and FLASH Radiation Therapy.* Electronic Book. 2023. URL: https://dx.doi.org/10.1088/978-0-7503-4046-5.

[270] L. Samalens et al. “Innovative minimally invasive options to treat drug-resistant epilepsies”. In: *Rev Neurol (Paris)* 180.7 (2024), pp. 599–607. URL: https://www.ncbi.nlm.nih.gov/pubmed/37798162.

[271] Heng Li et al. “Overview and Recommendations for Prospective Multi-institutional Spatially Fractionated Radiation Therapy Clinical Trials”. In: *International Journal of Radiation Oncology*Biology*Physics* 119.3 (2024), pp. 737–749. URL: https://www.sciencedirect.com/science/article/pii/S0360301623082469.

[272] Gurdal Gokeri et al. “Monte Carlo simulation of stereotactic microbeam radiation therapy: evaluation of the usage of a linear accelerator as the x-ray source”. In: *Physics in Medicine & Biology* 58.13 (2013), p. 4621. URL: https://dx.doi.org/10.1088/0031-9155/58/13/4621.

[273] G. Cranmer-Sargison et al. “Medical linear accelerator mounted mini-beam collimator: design, fabrication and dosimetric characterization”. In: *Physics in Medicine & Biology* 60.17 (2015), p. 6991. URL: https://dx.doi.org/10.1088/0031-9155/60/17/6991.

[274] William Davis et al. “Dosimetric characterization of an accessory mounted mini-beam collimator across clinically beam matched medical linear accelerators”. In: *Biomedical Physics & Engineering Express* 3.1 (2017), p. 015014. URL: https://dx.doi.org/10.1088/2057-1976/aa586d%20https://iopscience.iop.org/article/10.1088/2057-1976/aa586d.

[275] V. Kundapur et al. “Is Mini Beam Ready for Human Trials? Results of Randomized Study of Treating De-Novo Brain Tumors in Canines Using Linear Accelerator Generated Mini Beams”. In: *Radiation Research* 198.2 (2022), pp. 162–171, 10. URL: https://doi.org/10.1667/RADE-21-00093.1.

[276] C. Stengl et al. “Development and characterization of a versatile mini-beam collimator for pre-clinical photon beam irradiation”. In: *Med Phys* 50.8 (2023), pp. 5222–5237.

[277] Y. Prezado and G. R. Fois. “Proton-minibeam radiation therapy: A proof of concept”. In: *Medical Physics* 40.3 (2013), p. 031712. URL: https://doi.org/10.1118/1.4791648.

[278] Ramon Ortiz, Ludovic De Marzi, and Yolanda Prezado. “Preclinical dosimetry in proton minibeam radiation therapy: Robustness analysis and guidelines”. In: *Medical Physics* 49.8 (2022), pp. 5551–5561. URL: https://aapm.onlinelibrary.wiley.com/doi/abs/10.1002/mp.15780.

[279] Hirsch Marks. “Clinical Experience with Irradiation Through a Grid”. In: *Radiology* 58.3 (1952), pp. 338–342. URL: https://doi.org/10.1148/58.3.338.

[280] Mohammed Mohiuddin et al. “Palliative treatment of advanced cancer using multiple nonconfluent pencil beam radiation: A pilot study”. In: *Cancer* 66.1 (1990), pp. 114–118. URL: https://acsjournals.onlinelibrary.wiley.com/doi/abs/10.1002/1097-0142%2819900701%2966%3A1%3C114%3A%3AAID-CNCR2820660121%3E3.0.CO%3B2-L%20https://acsjournals.onlinelibrary.wiley.com/doi/pdfdirect/10.1002/1097-

0142%2819900701%2966%3A1%3C114%3A%3AAID-CNCR2820660121%3E3.0.CO%3B2-L?download=true.

[281] M. Mohiuddin et al. "High-dose spatially-fractionated radiation (GRID): a new paradigm in the management of advanced cancers". In: *Int J Radiat Oncol Biol Phys* 45.3 (1999), pp. 721–7. URL: https://www.redjournal.org/article/S0360-3016(99)00170-4/fulltext.

[282] M. Kudrimoti et al. "Spatially fractionated radiation therapy (SFR) in the palliation of large bulky (>8 cm) melanomas". In: *International Journal of Radiation Oncology*Biology*Physics* 54.2, Supplement (2002), pp. 342–343. URL: https://www.sciencedirect.com/science/article/pii/S0360301602036465.

[283] Jeniffer L Huhn et al. "Spatially Fractionated GRID Radiation Treatment of Advanced Neck Disease Associated with Head and Neck Cancer". In: *Technology in Cancer Research & Treatment* 5.6 (2006), pp. 607–612. URL: https://journals.sagepub.com/doi/abs/10.1177/153303460600500608%20https://journals.sagepub.com/doi/pdf/10.1177/153303460600500608?download=true.

[284] G. A. Neuner et al. "High-dose Spatially-fractionated GRID Radiation Therapy (SFGRT): A Comparison of Outcomes of Treatment Delivered Through Cerrobend GRID versus MLC GRID". In: *International Journal of Radiation Oncology, Biology, Physics* 72.1 (2008). doi: 10.1016/j.ijrobp.2008.06.1435, S488. URL: https://doi.org/10.1016/j.ijrobp.2008.06.1435.

[285] X. Wu et al. "The Technical and Clinical Implementation of LATTICE Radiation Therapy (LRT)". In: *Radiat Res* 194.6 (2020), pp. 737–746. URL: https://www.ncbi.nlm.nih.gov/pubmed/33064814.

[286] S. Kanagavelu et al. "In vivo effects of lattice radiation therapy on local and distant lung cancer: potential role of immunomodulation". In: *Radiat Res* 182.2 (2014), pp. 149–62. URL: https://pmc.ncbi.nlm.nih.gov/articles/PMC7670883/.

[287] B. E. Amendola et al. "Improved outcome of treating locally advanced lung cancer with the use of Lattice Radiotherapy (LRT): A case report". In: *Clin Transl Radiat Oncol* 9 (2018), pp. 68–71. URL: https://www.ctro.science/action/showPdf?pii=S2405630817300666.

[288] A. Pollack et al. "Phase I Trial of MRI-Guided Prostate Cancer Lattice Extreme Ablative Dose (LEAD) Boost Radiation Therapy". In: *Int J Radiat Oncol Biol Phys* 107.2 (2020), pp. 305–315.

[289] J. I. Choi et al. "Clinical Outcomes of Spatially Fractionated GRID Radiotherapy in the Treatment of Bulky Tumors of the Head and Neck". In: *Cureus* 11.5 (2019), e4637. URL: https://assets.cureus.com/uploads/original_article/pdf/17769/1612428568-1612428561-20210204-18203-nbtaxc.pdf.

[290] James W. Snider et al. "Spatially Fractionated Radiotherapy (GRID) Prior to Standard Neoadjuvant Conventionally Fractionated Radiotherapy for Bulky, High-Risk Soft Tissue and Osteosarcomas: Feasibility, Safety, and Promising Pathologic Response Rates". In: *Radiation Research* 194.6 (2020), pp. 707–714. URL: https://doi.org/10.1667/RADE-20-00100.1.

[291] S. Tajiki et al. "Management of bulky high-grade pleomorphic sarcoma using grid therapy technique". In: *International Journal of Radiation Research* 19.1 (2021), pp. 239–242. URL: http://ijrr.com/article-1-3486-en.html.

[292] Sabapathi Sathishkumar et al. "The Impact of TNF-α Induction on Therapeutic Efficacy following High Dose Spatially Fractionated (GRID) Radiation". In: *Technology in Cancer Research & Treatment* 1.2 (2002), pp. 141–147. URL: https://journals.sagepub.com/doi/abs/10.1177/153303460200100207.

[293] Sabapathi Sathishkumar et al. "Elevated sphingomyelinase activity and ceramide concentration in serum of patients undergoing high dose spatially fractionated radiation treatment: Implications for endothelial apoptosis". In: *Cancer Biology & Therapy* 4.9 (2005). doi: 10.4161/cbt.4.9.1915, pp. 979–986. URL: https://doi.org/10.4161/cbt.4.9.1915.

[294] N. Somaiah et al. "High Dose Spatially Fractionated Radiotherapy (SFR) using a Megavoltage GRID in Advanced Lung Tumors: Preliminary Experience in UK". In: *International Journal of Radiation Oncology, Biology, Physics* 72.1 (2008). doi: 10.1016/j.ijrobp.2008.06.1439, S490. URL: https://doi.org/10.1016/j.ijrobp.2008.06.1439.

[295] M. Mohiuddin et al. "Spatially Fractionated Grid Radiation (SFGRT): A Novel Approach in the Management of Recurrent and Unresectable Soft Tissue Sarcoma". In: *International Journal of Radiation Oncology, Biology, Physics* 75.3 (2009). doi: 10.1016/j.ijrobp.2009.07.1200, S526. URL: https://doi.org/10.1016/j.ijrobp.2009.07.1200.

[296] Adeel Kaiser, Majid M. Mohiuddin, and Gilchrist L. Jackson. "Dramatic response from neoadjuvant, spatially fractionated GRID radiotherapy (SFGRT) for large, high-grade extremity sarcoma". In: *Journal of Radiation Oncology* 2.1 (2013), pp. 103–106. URL: https://doi.org/10.1007/s13566-012-0064-5.

[297] J. M. Edwards et al. "Definitive GRID and Fractionated Radiation in Bulky Head and Neck Cancer Associated With Low Rates of Distant Metastasis". In: *International Journal of Radiation Oncology*Biology*Physics* 93 (2015), E334.

[298] José A. Peñagarícano et al. "Evaluation of Spatially Fractionated Radiotherapy (GRID) and Definitive Chemoradiotherapy With Curative Intent for Locally Advanced Squamous Cell Carcinoma of the Head and Neck: Initial Response Rates and Toxicity". In: *International Journal of Radiation Oncology*Biology*Physics* 76.5 (2010), pp. 1369–1375. URL: https://www.sciencedirect.com/science/article/pii/S0360301609004684.

[299] Mohammed Mohiuddin et al. "Locally advanced high-grade extremity soft tissue sarcoma: Response with novel approach to neoadjuvant chemoradiation using induction spatially fractionated GRID radiotherapy (SFGRT)". In: *Journal of Clinical Oncology* 32.15$_s$*uppl* (2014), pp. 10575–10575. URL: https://ascopubs.org/doi/abs/10.1200/jco.2014.32.15_suppl.10575.

[300] M. Mohiuddin et al. "High-Dose Radiation as a Dramatic, Immunological Primer in Locally Advanced Melanoma". In: *Cureus* 7.12 (2015), e417.

[301] M. Kudrimoti et al. "Spatially fractionated radiation therapy (SFR) in the palliation of large bulky (>8 cm) melanomas". In: *International Journal of Radiation Oncology*Biology*Physics* 54.2, Supplement (2002), pp. 342–343. URL: https://www.sciencedirect.com/science/article/pii/S0360301602036465.

[302] B. E. Amendola et al. "Spatially Fractionated Radiation Therapy Using Lattice Radiation in Far-advanced Bulky Cervical Cancer: A Clinical and Molecular Imaging and Outcome Study". In: *Radiat Res* 194.6 (2020), pp. 724–736. URL: https://bioone.org/journals/radiation-research/volume-194/issue-6/RADE-20-00038.1/Spatially-Fractionated-Radiation-Therapy-Using-Lattice-Radiation-in-Far-advanced/10.1667/RADE-20-00038.1.pdf.

[303] D. Hannani et al. "Prerequisites for the antitumor vaccine-like effect of chemotherapy and radiotherapy". In: *Cancer J* 17.5 (2011), pp. 351–8.

[304] M. M. Wattenberg et al. "Unlocking the combination: potentiation of radiation-induced antitumor responses with immunotherapy". In: *Radiat Res* 182.2 (2014), pp. 126–38.

[305] Michael P. Grams et al. "Minibeam Radiation Therapy Treatment (MBRT): Commissioning and First Clinical Implementation". In: *International Journal of Radiation Oncology, Biology, Physics* 120.5 (2024). doi: 10.1016/j.ijrobp.2024.06.035, pp. 1423–1434. URL: https://doi.org/10.1016/j.ijrobp.2024.06.035.

[306] M. A. Jacobson et al. "Minibeam Radiation Therapy for Recurrent Mucosal Melanoma: An Eye-Opening Response". In: *Mayo Clin Proc Innov Qual Outcomes* 9.4 (2025), p. 100640.

[307] F. A. Dilmanian et al. "Response of avian embryonic brain to spatially segmented x-ray microbeams". In: *Cellular and molecular biology (Noisy-le-Grand, France)* 47.3 (2001). Export Date: 04 October 2025; Cited By: 103, pp. 485–493. URL: https://www.scopus.com/inward/record.uri?eid=2-s2.0-1242311446&partnerID=40&md5=9a4bc90a181f96b691db1859c23e2e6c.

[308] Jean Laissue et al. *Weanling piglet cerebellum: a surrogate for tolerance to MRT (microbeam radiation therapy) in pediatric neuro-oncology*. Vol. 4508. International Symposium on Optical Science and Technology. SPIE, 2001. URL: https://doi.org/10.1117/12.450774.

[309] R. Serduc et al. "In vivo two-photon microscopy study of short-term effects of microbeam irradiation on normal mouse brain microvasculature". In: *Int J Radiat Oncol Biol Phys* 64.5 (2006), pp. 1519–27. URL: https://www.ncbi.nlm.nih.gov/pubmed/16580502.

[310] Pantaleo Romanelli et al. "Microradiosurgical cortical transections generated by synchrotron radiation". In: *Physica Medica: European Journal of Medical Physics* 31.6 (2015). doi: 10.1016/j.ejmp.2015.05.007, pp. 642–646. URL: https://doi.org/10.1016/j.ejmp.2015.05.007.

[311] F. Avraham Dilmanian et al. “Tissue-sparing effect of x-ray microplanar beams particularly in the CNS: Is a bystander effect involved?” In: *Experimental Hematology* 35.4, Supplement (2007), pp. 69–77. URL: https://www.sciencedirect.com/science/article/pii/S0301472X07000173.

[312] J. A. Laissue et al. “Response of the rat spinal cord to X-ray microbeams”. In: *Radiother Oncol* 106.1 (2013), pp. 106–11. URL: https://www.ncbi.nlm.nih.gov/pubmed/23321495.

[313] J. A. Laissue et al. “Prospects for microbeam radiation therapy of brain tumours in children to reduce neurological sequelae”. In: *Dev Med Child Neurol* 49.8 (2007), pp. 577–81. URL: https://onlinelibrary.wiley.com/doi/pdfdirect/10.1111/j.1469-8749.2007.00577.x?download=true.

[314] J. A. Laissue et al. “Neuropathology of ablation of rat gliosarcomas and contiguous brain tissues using a microplanar beam of synchrotron-wiggler-generated X rays”. In: *International Journal of Cancer* 78.5 (1998). Export Date: 04 October 2025; Cited By: 262, pp. 654–660. URL: https://www.scopus.com/inward/record.uri?eid=2-s2.0-19244384949&doi=10.1002%2f%28SICI%291097-0215%2819981123%2978%3a5%3c654%3a%3aAID-IJC21%3e3.0.CO%3b2-L&partnerID=40&md5=d8be75f1219a4c213a2a25050f2aeca6.

[315] J. C. Crosbie et al. “Tumor cell response to synchrotron microbeam radiation therapy differs markedly from cells in normal tissues”. In: *Int J Radiat Oncol Biol Phys* 77.3 (2010), pp. 886–94.

[316] R. C. Priyadarshika et al. “Biodosimetric quantification of short-term synchrotron microbeam versus broad-beam radiation damage to mouse skin using a dermatopathological scoring system”. In: *Br J Radiol* 84.1005 (2011), pp. 833–42.

[317] E. Schültke et al. “A Mouse Model for Microbeam Radiation Therapy of the Lung”. In: *Int J Radiat Oncol Biol Phys* 110.2 (2021), pp. 521–525.

[318] S. Bazyar et al. “Immune-Mediated Effects of Microplanar Radiotherapy with a Small Animal Irradiator”. In: *Cancers (Basel)* 14.1 (2021).

[319] Laura Eling et al. “Ultra high dose rate Synchrotron Microbeam Radiation Therapy. Preclinical evidence in view of a clinical transfer”. In: *Radiotherapy and Oncology* 139 (2019), pp. 56–61. URL: https://www.sciencedirect.com/science/article/pii/S0167814019329706.

[320] A. Bouchet et al. “Chalcone JAI-51 improves efficacy of synchrotron microbeam radiation therapy of brain tumors”. In: *J Synchrotron Radiat* 19.Pt 4 (2012), pp. 478–82. URL: https://www.ncbi.nlm.nih.gov/pubmed/22713877.

[321] S. Sabatasso et al. “Transient and Efficient Vascular Permeability Window for Adjuvant Drug Delivery Triggered by Microbeam Radiation”. In: *Cancers (Basel)* 13.9 (2021).

[322] A. Bouchet et al. “Meloxicam can Potentiate the Therapeutic Effects of Synchrotron Microbeam Radiation Therapy on High-Grade Glioma Bearing Rats”. In: *Radiat Res* 197.6 (2022), pp. 655–661. URL: https://www.ncbi.nlm.nih.gov/pubmed/35245385.

[323] H. M. Smilowitz et al. “Synergy of gene-mediated immunoprophylaxis and microbeam radiation therapy for advanced intracerebral rat 9L gliosarcomas”. In: *J Neurooncol* 78.2 (2006), pp. 135–43. URL: https://link.springer.com/content/pdf/10.1007/s11060-005-9094-9.pdf.

[324] J. F. Adam et al. “Toward Neuro-Oncologic Clinical Trials of High-Dose-Rate Synchrotron Microbeam Radiation Therapy: First Treatment of a Spontaneous Canine Brain Tumor”. In: *Int J Radiat Oncol Biol Phys* 113.5 (2022), pp. 967–973.

[325] F. A. Dilmanian et al. “Response of rat intracranial 9L gliosarcoma to microbeam radiation therapy”. In: *Neuro-Oncology* 4.1 (2002). Export Date: 04 October 2025; Cited By: 252, pp. 26–38. URL: https://www.scopus.com/inward/record.uri?eid=2-s2.0-18344393248&doi=10.1215%2f15228517-4-1-26&partnerID=40&md5=7e5e3ef69a2006363ec2656fca5de1b4.

[326] D. A. Garcia et al. “Minibeam Radiation Therapy Valley Dose Determines Tolerance to Acute and Late Effects in the Mouse Oral Cavity”. In: *Int J Radiat Oncol Biol Phys* 123.1 (2025), pp. 262–269.

[327] S. Bazyar et al. “Minibeam radiotherapy with small animal irradiators; in vitro and in vivo feasibility studies”. In: *Phys Med Biol* 62.23 (2017), pp. 8924–8942.

[328] C. Koksal Akbas et al. “Preclinical photon minibeam radiotherapy using a custom collimator: Dosimetry characterization and preliminary in-vivo results on a glioma model”. In: *Phys Med* 124 (2024), p. 103420.

[329] Y. Prezado et al. “Increase of lifespan for glioma-bearing rats by using minibeam radiation therapy”. In: *J Synchrotron Radiat* 19.Pt 1 (2012), pp. 60–5. URL: https://www.ncbi.nlm.nih.gov/pubmed/22186645%20https://journals.iucr.org/s/issues/2012/01/00/hi5619/hi5619.pdf.

[330] M. Sotiropoulos et al. “X-rays minibeam radiation therapy at a conventional irradiator: Pilot evaluation in F98-glioma bearing rats and dose calculations in a human phantom”. In: *Clin Transl Radiat Oncol* 27 (2021), pp. 44–49. URL: https://www.ncbi.nlm.nih.gov/pubmed/33511291%20https://pmc.ncbi.nlm.nih.gov/articles/PMC7817429/.

[331] Y. Prezado et al. “Transfer of Minibeam Radiation Therapy into a cost-effective equipment for radiobiological studies: a proof of concept”. In: *Scientific Reports* 7.1 (2017), p. 17295. URL: https://doi.org/10.1038/s41598-017-17543-3.

[332] A. Bertho, L. Iturri, and Y. Prezado. “Radiation-induced immune response in novel radiotherapy approaches FLASH and spatially fractionated radiotherapies”. In: *Int Rev Cell Mol Biol* 376 (2023), pp. 37–68. URL: https://www.sciencedirect.com/science/article/abs/pii/S1937644822001435?via%3Dihub.

[333] Fardous Reaz et al. “Probing the therapeutic window of proton minibeam radiotherapy using dose-response curves in a mouse model”. In: *Radiotherapy and Oncology* 211 (2025). doi: 10.1016/j.radonc.2025.111050. URL: https://doi.org/10.1016/j.radonc.2025.111050.

[334] S. Potiron et al. “The significance of dose heterogeneity on the anti-tumor response of minibeam radiation therapy”. In: *Radiother Oncol* 201 (2024), p. 110577.

[335] Y. Prezado et al. "Proton minibeam radiation therapy widens the therapeutic index for high-grade gliomas". In: *Sci Rep* 8.1 (2018), p. 16479. URL: https://www.ncbi.nlm.nih.gov/pubmed/30405188%20https://www.nature.com/articles/s41598-018-34796-8.pdf.

[336] Y. Prezado et al. "Tumor Control in RG2 Glioma-Bearing Rats: A Comparison Between Proton Minibeam Therapy and Standard Proton Therapy". In: *Int J Radiat Oncol Biol Phys* 104.2 (2019), pp. 266–271. URL: https://www.ncbi.nlm.nih.gov/pubmed/30703513.

[337] C. Lamirault et al. "Spatially Modulated Proton Minibeams Results in the Same Increase of Lifespan as a Uniform Target Dose Coverage in F98-Glioma-Bearing Rats". In: *Radiat Res* 194.6 (2020), pp. 715–723. URL: https://www.ncbi.nlm.nih.gov/pubmed/32991712%20https://bioone.org/journals/radiation-research/volume-194/issue-6/RADE-19-00013.1/Spatially-Modulated-Proton-Minibeams-Results-in-the-Same-Increase-of/10.1667/RADE-19-00013.1.pdf.

[338] L. Iturri et al. "A first evaluation of the efficacy of minibeam radiation therapy combined with an immune check point inhibitor in a model of glioma-bearing rats". In: *Clin Transl Radiat Oncol* 51 (2025), p. 100911. URL: https://pmc.ncbi.nlm.nih.gov/articles/PMC11783053/.

[339] Lorea Iturri et al. "Proton FLASH Radiation Therapy and Immune Infiltration: Evaluation in an Orthotopic Glioma Rat Model". In: *International Journal of Radiation Oncology, Biology, Physics* 116.3 (2023). doi: 10.1016/j.ijrobp.2022.12.018, pp. 655–665. URL: https://doi.org/10.1016/j.ijrobp.2022.12.018.

[340] Tim Schneider et al. "Combining FLASH and spatially fractionated radiation therapy: The best of both worlds". In: *Radiotherapy and Oncology* 175 (2022), pp. 169–177. URL: https://www.sciencedirect.com/science/article/pii/S0167814022042268%20https://boris-portal.unibe.ch/entities/publication/9ca12ead-ad22-4551-9608-768b3e4a9df8.

[341] R. J. Griffin et al. "Microbeam radiation therapy alters vascular architecture and tumor oxygenation and is enhanced by a galectin-1 targeted anti-angiogenic peptide". In: *Radiat Res* 177.6 (2012), pp. 804–12.

[342] M. D. Wright et al. "Non-conventional Ultra-High Dose Rate (FLASH) Microbeam Radiotherapy Provides Superior Normal Tissue Sparing in Rat Lung Compared to Non-conventional Ultra-High Dose Rate (FLASH) Radiotherapy". In: *Cureus* 13.11 (2021), e19317.

[343] Loredana G. Marcu. *The Six Rs of Head and Neck Cancer Radiotherapy*. 1 online resource Summary: The Six Rs of Head and Neck Cancer Radiotherapy. sine loco: IntechOpen, 2015. URL: https://torl.biblioboard.com/content/79fad592-2433-43aa-94e4-98d6cd336f55?organizationId=1f7368e7-f10b-49a1-8ced-2d9476279974.

[344] S. Paillas et al. "Localized Irradiation of Cell Membrane by Auger Electrons Is Cytotoxic Through Oxidative Stress-Mediated Nontargeted Effects". In: *Antioxid Redox Signal* 25.8 (2016). 1557-7716 Paillas, Salomé Ladjohounlou, Riad Lozza, Catherine Pichard, Alexandre Boudousq, Vincent Jarlier, Marta Sevestre, Samuel Le Blay, Marion Deshayes, Emmanuel Sosabowski, Jane Chardès, Thierry Navarro-Teulon, Isabelle Mairs, Robert J Pouget, Jean-Pierre Journal Article Research Support, Non-U.S. Gov't United States 2016/05/26 Antioxid Redox Signal. 2016 Sep 10;25(8):467-84. doi: 10.1089/ars.2015.6309. Epub 2016 Jul 5., pp. 467–84.

[345] Matthew Peters et al. "Potential Utilization of Bystander / Abscopal-Mediated Signal Transduction Events in the Treatment of Solid Tumors". In: *Current Signal Transduction Therapy* 2 (2007), pp. 129–143.

[346] H. Nagasawa and J. B. Little. "Induction of sister chromatid exchanges by extremely low doses of alpha-particles". In: *Cancer Res* 52.22 (1992). Nagasawa, H Little, J B CA-47542/CA/NCI NIH HHS/United States ES-00002/ES/NIEHS NIH HHS/United States Journal Article Research Support, Non-U.S. Gov't Research Support, U.S. Gov't, P.H.S. United States 1992/11/15 Cancer Res. 1992 Nov 15;52(22):6394-6., pp. 6394–6.

[347] C. Shao et al. "Bystander effect induced by counted high-LET particles in confluent human fibroblasts: a mechanistic study". In: *Faseb j* 17.11 (2003), pp. 1422–7.

[348] N. Autsavapromporn et al. "Gap junction communication and the propagation of bystander effects induced by microbeam irradiation in human fibroblast cultures: the impact of radiation quality". In: *Radiat Res* 180.4 (2013). 1938-5404 Autsavapromporn, Narongchai Suzuki, Masao Funayama, Tomoo Usami, Noriko Plante, Ianik Yokota, Yuichiro Mutou, Yasuko Ikeda, Hiroko Kobayashi, Katsumi Kobayashi, Yasuhiko Uchihori, Yukio Hei, Tom K Azzam, Edouard I Murakami, Takeshi P01 CA049062/CA/NCI NIH HHS/United States Journal Article Research Support, Non-U.S. Gov't United States 2013/08/31 Radiat Res. 2013 Oct;180(4):367-75. doi: 10.1667/RR3111.1. Epub 2013 Aug 29., pp. 367–75. URL: https://pmc.ncbi.nlm.nih.gov/articles/PMC4058832/.

[349] Isheeta Seth et al. "Neutron Exposures in Human Cells: Bystander Effect and Relative Biological Effectiveness". In: *PLOS ONE* 9.6 (2014), e98947. URL: https://doi.org/10.1371/journal.pone.0098947.

[350] O. V. Belyakov et al. "Biological effects in unirradiated human tissue induced by radiation damage up to 1 mm away". In: *Proc Natl Acad Sci U S A* 102.40 (2005). 1091-6490 Belyakov, Oleg V Mitchell, Stephen A Parikh, Deep Randers-Pehrson, Gerhard Marino, Stephen A Amundson, Sally A Geard, Charles R Brenner, David J P01 CA049062/CA/NCI NIH HHS/United States P41 EB002033/EB/NIBIB NIH HHS/United States P01 CA-49062/CA/NCI NIH HHS/United States P41 EB002033-09/EB/NIBIB NIH HHS/United States Comparative Study Journal Article Research Support, N.I.H., Extramural Research Support, U.S. Gov't, Non-P.H.S. Research Support, U.S. Gov't, P.H.S. United States 2005/09/16 Proc Natl Acad Sci U S A. 2005 Oct 4;102(40):14203-8. doi: 10.1073/pnas.0505020102. Epub 2005 Sep 14., pp. 14203–8.

[351] R. W. Smith et al. "Irradiation of rainbow trout at early life stages results in trans-generational effects including the induction of a bystander effect in non-irradiated fish". In: *Environ Res* 145 (2016). 1096-0953 Smith, Richard W Seymour, Colin B Moccia, Richard D Mothersill, Carmel E Journal Article Research Support, Non-U.S. Gov't Netherlands 2015/12/01 Environ Res. 2016 Feb;145:26-38. doi: 10.1016/j.envres.2015.11.019. Epub 2015 Dec 6., pp. 26–38.

[352] M. D. Gow et al. "Effect of dose rate on the radiation-induced bystander response". In: *Phys Med Biol* 53.1 (2008). Gow, M D Seymour, C B Byun, Soo-Hyun Mothersill, C E Journal Article England 2008/01/10 Phys Med Biol. 2008 Jan 7;53(1):119-32. doi: 10.1088/0031-9155/53/1/008. Epub 2007 Dec 13., pp. 119–32. URL: https://iopscience.iop.org/article/10.1088/0031-9155/53/1/008.

[353] D. J. Craig et al. "The abscopal effect of radiation therapy". In: *Future Oncol* 17.13 (2021), pp. 1683–1694.

[354] S. Sabatasso et al. "Microbeam radiation-induced tissue damage depends on the stage of vascular maturation". In: *Int J Radiat Oncol Biol Phys* 80.5 (2011), pp. 1522–32.

[355] J. Denekamp. "Vascular endothelium as the vulnerable element in tumours". In: *Acta Radiol Oncol* 23.4 (1984), pp. 217–25.

[356] H. Fukunaga et al. "A Brief Overview of the Preclinical and Clinical Radiobiology of Microbeam Radiotherapy". In: *Clinical Oncology* 33.11 (2021). doi: 10.1016/j.clon.2021.08.011, pp. 705–712. URL: https://doi.org/10.1016/j.clon.2021.08.011.

[357] S. V. Jenkins et al. "Bystander Effects in Spatially Fractionated Radiation Therapy: From Molecule To Organism To Clinical Implications". In: *Semin Radiat Oncol* 34.3 (2024), pp. 284–291.

[358] Matthias Sammer et al. "Beam size limit for pencil minibeam radiotherapy determined from side effects in an in-vivo mouse ear model". In: *PLOS ONE* 14.9 (2019), e0221454. URL: https://doi.org/10.1371/journal.pone.0221454.

[359] Natasha L. Murphy et al. "A simple dosimetric approach to spatially fractionated GRID radiation therapy using the multileaf collimator for treatment of breast cancers in the prone position". In: *Journal of Applied Clinical Medical Physics* 21.11 (2020), pp. 105–114. URL: https://doi.org/10.1002/acm2.13040.

[360] Robert D. Zwicker, Ali Meigooni, and Mohammed Mohiuddin. "Therapeutic advantage of grid irradiation for large single fractions". In: *International Journal of Radiation Oncology, Biology, Physics* 58.4 (2004). doi: 10.1016/j.ijrobp.2003.07.003, pp. 1309–1315. URL: https://doi.org/10.1016/j.ijrobp.2003.07.003.

[361] E. Bräuer-Krisch et al. "New irradiation geometry for microbeam radiation therapy". In: *Physics in Medicine Biology* 50.13 (2005), p. 3103. URL: https://doi.org/10.1088/0031-9155/50/13/009.

[362] Pierrick Regnard et al. "Irradiation of intracerebral 9L gliosarcoma by a single array of microplanar x-ray beams from a synchrotron: balance between curing and sparing". In: *Physics in Medicine Biology* 53.4 (2008), p. 861. URL: https://doi.org/10.1088/0031-9155/53/4/003.

[363] Raphaël Serduc et al. "Synchrotron microbeam radiation therapy for rat brain tumor palliation—influence of the microbeam width at constant valley dose". In: *Physics in Medicine Biology* 54.21 (2009), p. 6711. URL: https://doi.org/10.1088/0031-9155/54/21/017.

[364] A. Uyama et al. "A narrow microbeam is more effective for tumor growth suppression than a wide microbeam: an in vivo study using implanted human glioma cells". In: *J Synchrotron Radiat* 18.Pt 4 (2011), pp. 671–8.

[365] M. Nakayama et al. "Dose Estimation of Normal Brain Tissue Tolerance for Microbeam Radiation Therapy". In: *International Journal of Radiation Oncology, Biology, Physics* 90.1 (2014). doi: 10.1016/j.ijrobp.2014.05.2321, S804. URL: https://doi.org/10.1016/j.ijrobp.2014.05.2321.

[366] Daniel Brönnimann et al. "Synchrotron microbeam irradiation induces neutrophil infiltration, thrombocyte attachment and selective vascular damage in vivo". In: *Scientific Reports* 6.1 (2016), p. 33601. URL: https://doi.org/10.1038/srep33601.

[367] A. Terahara et al. "Analysis of the relationship between tumor dose inhomogeneity and local control in patients with skull base chordoma". In: *Int J Radiat Oncol Biol Phys* 45.2 (1999), pp. 351–8.

[368] A. Niemierko. "Reporting and analyzing dose distributions: a concept of equivalent uniform dose". In: *Med Phys* 24.1 (1997), pp. 103–10.

[369] Hualin Zhang et al. "A Dosimetric Parameter Reference Look-Up Table for GRID Collimator-Based Spatially Fractionated Radiation Therapy". In: *Cancers* 14.4 (2022), p. 1037. URL: https://www.mdpi.com/2072-6694/14/4/1037%20https://mdpi-res.com/d_attachment/cancers/cancers-14-01037/article_deploy/cancers-14-01037-v2.pdf?version=1645608530.

[370] Danielle Anderson et al. "Evaluation of dose-volume metrics for microbeam radiation therapy dose distributions in head phantoms of various sizes using Monte Carlo simulations". In: *Physics in Medicine & Biology* 57.10 (2012), p. 3223. URL: https://dx.doi.org/10.1088/0031-9155/57/10/3223.

[371] J. Cotterill et al. "Challenges for the Implementation of Primary Standard Dosimetry in Proton Minibeam Radiation Therapy". In: *Cancers (Basel)* 16.23 (2024).

[372] Judith N. Rivera et al. "Conventional dose rate spatially-fractionated radiation therapy (SFRT) treatment response and its association with dosimetric parameters—A preclinical study in a Fischer 344 rat model". In: *PLOS ONE* 15.6 (2020), e0229053. URL: https://doi.org/10.1371/journal.pone.0229053.

[373] C. Fernandez-Palomo, S. Chang, and Y. Prezado. "Should Peak Dose Be Used to Prescribe Spatially Fractionated Radiation Therapy?-A Review of Preclinical Studies". In: *Cancers (Basel)* 14.15 (2022).

[374] Josie May McGarrigle, Kenneth Richard Long, and Yolanda Prezado. "On the significance of the different geometrical and dosimetric parameters in microbeam and minibeam radiation therapy a retrospective evaluation". In: *Frontiers in Oncology* Volume 14 - 2024 (2024). URL: https://www.frontiersin.org/journals/oncology/articles/10.3389/fonc.2024.1449293.

[375] Y. Prezado et al. "On the significance of peak dose in normal tissue toxicity in spatially fractionated radiotherapy: The case of proton minibeam radiation therapy". In: *Radiother Oncol* 205 (2025), p. 110769.

[376] H. Zhang et al. "Fractionated grid therapy in treating cervical cancers: conventional fractionation or hypofractionation?" In: *Int J Radiat Oncol Biol Phys* 70.1 (2008), pp. 280–8.

[377] C. Fernandez-Palomo et al. "Complete Remission of Mouse Melanoma after Temporally Fractionated Microbeam Radiotherapy". In: *Cancers (Basel)* 12.9 (2020).

[378] E.R.J.F Taylor et al. "Megavoltage photon FLASH for preclinical experiments". In: *Med Phys* 52.7 (2025), e17891. URL: https://www.ncbi.nlm.nih.gov/pubmed/40387520%20https://aapm.onlinelibrary.wiley.com/doi/pdfdirect/10.1002/mp.17891?download=true.

[379] Sergey V. Kutsaev et al. "Feasibility study of high-power electron linac for clinical X-ray ROAD-FLASH therapy system". In: *Frontiers in Medical Engineering* 2 (2024). URL: https://www.frontiersin.org/journals/medical-engineering/articles/10.3389/fmede.2024.1382025.

[380] K. H. Weber. "Eine einfache reichweite-energie-beziehung für elektronen im energiebereich von 3 keV bis 3 MeV". In: *Nuclear Instruments and Methods* 25 (1963), pp. 261–264. URL: https://www.sciencedirect.com/science/article/pii/0029554X63901964.

[381] W. Nakel. "The Elementary Process of Bremsstrahlung". In: *Physics Reports-Review Section of Physics Letters* 243.6 (1994), pp. 317–353. URL: %3CGo%20to%20ISI%3E://WOS:A1994PC24600001%20https://www.sciencedirect.com/science/article/pii/0370157394000689?via%3Dihub.

[382] F. H. Attix. *Introduction to radiological physics and radiation dosimetry*. New York: John Wiley & Sons, 1986.

[383] P Mayles, A Nahum, and J C Rosenwald, eds. *Handbook of radiotherapy physics*. Boca Raton, FL: CRC Press, June 2007.

[384] Martin Berger, J Coursey, and M Zucker. *ESTAR, PSTAR, and ASTAR: Computer Programs for Calculating Stopping-Power and Range Tables for Electrons, Protons, and Helium Ions (version 1.21)*. en. 1999-01-01 1999.

[385] F. H. Attix. *Introduction to radiological physics and radiation dosimetry*. New York: John Wiley & Sons, 1986.

[386] T. Tabata, R. Ito, and S. Okabe. "Generalized semiempirical equations for the extrapolated range of electrons". In: *Nuclear Instruments and Methods* 103.1 (1972), pp. 85–91. URL: https://www.sciencedirect.com/science/article/pii/0029554X72904636.

[387] M.J. Berger et al. *XCOM: Photon Cross Sections Database*. https://www.nist.gov/pml/xcom-photon-cross-sections-database. Online Multimedia. Accessed: 2022-28-6. 2010.

[388] Pedro Andreo et al. *Fundamentals of Ionizing Radiation Dosimetry*. Includes bibliographical references (pages 881-946) and index. Weinheim, Germany: Wiley-VCH, 2017.

[389] C. J. Karzmark and N. C. Pering. "Electron linear accelerators for radiation therapy: history, principles and contemporary developments". In: *Physics in Medicine and Biology* 18.3 (1973), pp. 321–354. URL: http://dx.doi.org/10.1088/0031-9155/18/3/001%20https://iopscience.iop.org/article/10.1088/0031-9155/18/3/001/pdf.

[390] T. Kawano et al. "IAEA Photonuclear Data Library 2019". In: *Nuclear Data Sheets* 163 (2020), pp. 109–162. URL: https://www.sciencedirect.com/science/article/pii/S0090375219300699%20https://www.sciencedirect.com/science/article/abs/pii/S0090375219300699?via%3Dihub.

[391] Rodolphe Antoni and Laurent Bourgois. *Applied Physics of External Radiation Exposure : Dosimetry and Radiation Protection*. Electronic Book. 2017.

[392] H. A. Nedaie et al. "Neutron dose measurements of Varian and Elekta linacs by TLD600 and TLD700 dosimeters and comparison with MCNP calculations". In: *J Med Phys* 39.1 (2014), pp. 10–7. URL: https://www.ncbi.nlm.nih.gov/pubmed/24600167%20https://www.ncbi.nlm.nih.gov/pmc/articles/PMC3931222/pdf/JMP-39-10.pdf.

[393] J Oosterkamp W. *The heat dissipation in the anode of an X-ray tube*. Report. Philips Research, Feb. 1948. URL: https://pearl-hifi.com/06_Lit_Archive/02_PEARL_Arch/Vol_16/Sec_53/Philips_Rsrch_Reports_1946_thru_1977/Philips%20Research%20Reports-03-1948.pdf.

[394] C. L. Briant. "The Properties and Uses of Refractory Metals and their Alloys". In: *MRS Online Proceedings Library* 322.1 (1993), pp. 305–314. URL: https://doi.org/10.1557/PROC-322-305.

[395] Xiaolei Ma et al. "High-temperature tensile and thermal shock characterization of low-temperature rolled tungsten". In: *Nuclear Materials and Energy* 34 (2023), p. 101353. URL: https://www.sciencedirect.com/science/article/pii/S2352179122002344.

[396] Muyuan Li et al. "Experimental and computational study of damage behavior of tungsten under high energy electron beam irradiation". In: *Engineering Fracture Mechanics* 135 (2015), pp. 64–80. URL: https://www.sciencedirect.com/science/article/pii/S0013794415000181.

[397] S. A. Korenev. *Target for production of x-rays*. Patent. 2002. URL: https://patents.google.com/patent/US6463123B1/en.

[398] William M. Haynes. *CRC handbook of chemistry and physics*. Ninety-seventh edition. Boca Raton: CRC Press, 2016. URL: http://whel-primo.hosted.exlibrisgroup.com/openurl/44WHELF_NLW/44WHELF_NLW_services_page?u.ignore_date_coverage=true&rft.mms_id=99955018402419%20https://tcdlibrary.ldls.org.uk/vdc_100044259106.0x000001.

[399] Simon Bonk et al. "Cold rolled tungsten (W) plates and foils: Evolution of the tensile properties and their indication towards deformation mechanisms". In: *International Journal of Refractory Metals and Hard Materials* 70 (2018), pp. 124–133. URL: https://www.sciencedirect.com/science/article/pii/S0263436817305036.

[400] Q. Wei and L. J. Kecskes. "Effect of low-temperature rolling on the tensile behavior of commercially pure tungsten". In: *Materials Science and Engineering: A* 491.1 (2008), pp. 62–69. URL: https://www.sciencedirect.com/science/article/pii/S0921509308000191%20https://www.sciencedirect.com/science/article/abs/pii/S0921509308000191?via%3Dihub.

[401] Philipp Lied et al. "Comparison of K-doped and pure cold-rolled tungsten sheets: Tensile properties and brittle-to-ductile transition temperatures". In: *Journal of Nuclear Materials* 544 (2021), p. 152664. URL: https://www.sciencedirect.com/science/article/pii/S0022311520312721.

[402] *Tungsten*. Web Page. URL: https://www.matweb.com/search/datasheet_print.aspx?matguid=41e0851d2f3c417ba69ea0188fa570e3.

[403] S. Panayotis et al. "Fracture modes of ITER tungsten divertor monoblock under stationary thermal loads". In: *Fusion Engineering and Design* 125 (2017), pp. 256–262. URL: https://www.sciencedirect.com/science/article/pii/S0920379617307779.

[404] J. Habainy et al. "Fatigue behavior of rolled and forged tungsten at 25°, 280° and 480 °C". In: *Journal of Nuclear Materials* 465 (2015), pp. 438–447. URL: https://www.sciencedirect.com/science/article/pii/S0022311515300568%20https://www.sciencedirect.com/science/article/pii/S0022311515300568?via%3Dihub.

[405] J. Habainy. "Characterisation of mechanical and thermal properties of tungsten for high power spallation target applications". Thesis. 2018.

[406] A. Giannattasio and S. G. Roberts. "Strain-rate dependence of the brittle-to-ductile transition temperature in tungsten". In: *Philosophical Magazine* 87.17 (2007). doi: 10.1080/14786430701253197, pp. 2589–2598. URL: https://doi.org/10.1080/14786430701253197.

[407] S. S. Manson. *Thermal stress and low-cycle fatigue*. 65025918 GB67-4002 [by] S.S. Manson. illus. 24 cm. Includes bibliographies. New York, McGraw-Hill, 1966, xi, 404 p.

[408] Jemila Habainy et al. "Tungsten as Spallation Material at the European Spallation Source". In: *Proceedings of the 14th International Workshop on Spallation Materials Technology*. Vol. 28. JPS Conference Proceedings. doi:10.7566/JPSCP.28.031004. Journal of the Physical Society of Japan, 2020. URL: https://doi.org/10.7566/JPSCP.28.031004%20https://journals.jps.jp/doi/pdf/10.7566/JPSCP.28.031004?download=true.

[409] J. Habainy et al. "Study of heavy ion beam induced damage in tungsten for high power target applications". In: *Nuclear Instruments and Methods in Physics Research Section B: Beam Interactions with Materials and Atoms* 439 (2019), pp. 7–16. URL: https://www.sciencedirect.com/science/article/pii/S0168583X18306633.

[410] Erik Lassner and Wolf-Dieter Schubert. *Tungsten : Properties, Chemistry, Technology of the Element, Alloys, and Chemical Compounds*. New York, NY, UNITED STATES: Springer, 1999. URL: http://ebookcentral.proquest.com/lib/oxford/detail.action?docID=3080907.

[411] Jemila Habainy et al. “Formation of oxide layers on tungsten at low oxygen partial pressures”. In: *Journal of Nuclear Materials* 506 (2018), pp. 26–34. URL: https://www.sciencedirect.com/science/article/pii/S0022311517301836.

[412] E. A. Gulbransen and K. F. Andrew. “Kinetics of the Oxidation of Pure Tungsten from 500° to 1300°C”. In: *Journal of The Electrochemical Society* 107.7 (1960), p. 619. URL: https://dx.doi.org/10.1149/1.2427787%20https://iopscience.iop.org/article/10.1149/1.2427787.

[413] S. C. Cifuentes, M. A. Monge, and P. Pérez. “On the oxidation mechanism of pure tungsten in the temperature range 600–800°C”. In: *Corrosion Science* 57 (2012), pp. 114–121. URL: https://www.sciencedirect.com/science/article/pii/S0010938X11006664.

[414] Norman E. Dowling. *Mechanical behavior of materials : engineering methods for deformation, fracture, and fatigue*. First edition. Prentice-Hall International editions. Englewood Cliffs, New Jersey ; London, England: Prentice Hall, 1993, xxiv, 773 pages : illustrations. URL: http://www.gbv.de/dms/bowker/toc/9780135790465.pdf.

[415] I. Uytdenhouwen et al. “Influence of recrystallization on thermal shock resistance of various tungsten grades”. In: *Journal of Nuclear Materials* 363-365 (2007), pp. 1099–1103. URL: https://www.sciencedirect.com/science/article/pii/S0022311507002292.

[416] G. E. Dieter. *Mechanical metallurgy*. 3rd edition. 23 cm. Kogakusha: McGraw-Hill, 1976, 798 pages.

[417] Michael Rieth et al. “Behavior of tungsten under irradiation and plasma interaction”. In: *Journal of Nuclear Materials* 519 (2019), pp. 334–368. URL: https://www.sciencedirect.com/science/article/pii/S002231151930025X.

[418] R. I. Stephens and H. O. Fuchs. *Metal fatigue in engineering*. 2nd. 00028972 by Ralph I. Stephens ... [et al.]. ill. ; 24 cm. Rev. ed. of: Metal fatigue in engineering / H.O. Fuchs, R.I. Stephens. c1980. "A Wiley-Interscience publication." Includes bibliographical references and indexes. New York: Wiley, 2001, xxi, 472 p. URL: Contributor%20biographical%20information%20http://www.loc.gov/catdir/bios/wiley042/00028972.html%20Publisher%20description%20http://www.loc.gov/catdir/description/wiley034/00028972.html%20Table%20of%20Contents%20http://www.loc.gov/catdir/toc/onix06/00028972.html.

[419] T. Hirai and G. Pintsuk. “Thermo-mechanical calculations on operation temperature limits of tungsten as plasma facing material”. In: *Fusion Engineering and Design* 82.4 (2007), pp. 389–393. URL: https://www.sciencedirect.com/science/article/pii/S0920379607001287%20https://www.sciencedirect.com/science/article/pii/S0920379607001287?via%3Dihub.

[420] Miao Qu et al. “Dependence of tungsten crack behaviors on heat source parameters under transient heat flow”. In: *Materials Science and Engineering: A* 874 (2023), p. 145079. URL: https://www.sciencedirect.com/science/article/pii/S0921509323005038.

[421] Changjun Li et al. "Theoretical analysis on the damages for tungsten plasma facing surface under superposition of steady-state and transient heat loads". In: *Fusion Engineering and Design* 132 (2018), pp. 99–106. URL: https://www.sciencedirect.com/science/article/pii/S0920379618304885%20https://www.sciencedirect.com/science/article/pii/S0920379618304885?via%3Dihub.

[422] Li Chen et al. "Computational study of tungsten cracking propagation under ELM-like high heat flux conditions". In: *Journal of Nuclear Materials* 605 (2025), p. 155567. URL: https://www.sciencedirect.com/science/article/pii/S0022311524006688.

[423] M. J. Berger and S. M. Seltzer. "Bremsstrahlung and photoneutrons from thick tungsten and tantalum targets". In: *Physical Review C* 2.2 (1970). Export Date: 16 July 2024; Cited By: 181, pp. 621–631. URL: https://www.scopus.com/inward/record.uri?eid=2-s2.0-0001351333&doi=10.1103%2fPhysRevC.2.621&partnerID=40&md5=4cc15356006e8e12ef1c1a930ddad035.

[424] K. Bertsche J, G. Asmerom, and M. Gutierrez. *Bremsstrahlung target for radiation therapy system*. Patent. 2020. URL: https://patents.google.com/patent/US10636609B1/en.

[425] L. H. Lanzl and A. O. Hanson. "Z Dependence and Angular Distribution of Bremsstrahlung from 17-Mev Electrons". In: *Physical Review* 83.5 (1951). PR, pp. 959–974. URL: https://link.aps.org/doi/10.1103/PhysRev.83.959%20https://journals.aps.org/pr/abstract/10.1103/PhysRev.83.959.

[426] A. Brahme and H. Svensson. "Radiation beam characteristics of a 22 MeV microtron". In: *Acta Radiol Oncol Radiat Phys Biol* 18.3 (1979). Brahme, A Svensson, H eng Sweden 1979/01/01 Acta Radiol Oncol Radiat Phys Biol. 1979;18(3):244-72. doi: 10.3109/02841867909128212., pp. 244–72. URL: https://www.ncbi.nlm.nih.gov/pubmed/118642%20https://www.tandfonline.com/doi/pdf/10.3109/02841867909128212.

[427] Ctovbun VI. *0,5-100 MeV electron accelerators as radiation sources*. Report. 1973. URL: https://inis.iaea.org/records/4ryds-q3h32.

[428] J Wang et al. "TU-H-BRC-06: Temperature Simulation of Tungsten and W25Re Targets to Deliver High Dose Rate 10 MV Photons". In: *Medical Physics* 43.6Part36 (2016), pp. 3767–3767. URL: https://aapm.onlinelibrary.wiley.com/doi/abs/10.1118/1.4957613%20https://aapm.onlinelibrary.wiley.com/doi/10.1118/1.4957613.

[429] J. Wang et al. "Thermal limits on MV x-ray production by bremsstrahlung targets in the context of novel linear accelerators". In: *Med Phys* 44.12 (2017), pp. 6610–6620. URL: https://www.ncbi.nlm.nih.gov/pubmed/28983960%20https://aapm.onlinelibrary.wiley.com/doi/pdfdirect/10.1002/mp.12615?download=true.

[430] N. Esplen et al. "Development of a Megavoltage Photon FLASH Radiotherapy Platform at TRIUMF". In: *Medical Physics* 47.6 (2020). Uv9xu Mo-Ef-Trac Times Cited:0 Cited References Count:0, E294–E294. URL: %3CGo%20to%20ISI%3E://WOS:000699823200126.

[431] Dandan Qu et al. “Mechanical characterization and modeling of brazed tungsten and Cu–Cr–Zr alloy using stress relief interlayers”. In: *Journal of Nuclear Materials* 455.1 (2014), pp. 130–133. URL: https://www.sciencedirect.com/science/article/pii/S0022311514002414.

[432] Taylan Tuğrul. “Effect of different target materials of LINAC head on photon spectrum”. In: *Journal of Radiation Research and Applied Sciences* 14.1 (2021), pp. 204–209. URL: https://www.sciencedirect.com/science/article/pii/S1687850722000206.

[433] R. Miller. *Electronic Irradiation of Foods: An Introduction to the Technology*. 2005.

[434] Gabriele Kragl et al. “Dosimetric characteristics of 6 and 10MV unflattened photon beams”. In: *Radiotherapy and Oncology* 93.1 (2009). 19592123 [PMID], pp. 141–146. URL: https://app.dimensions.ai/details/publication/pub.1003703574.

[435] P. J. Ebert, A. F. Lauzon, and E. M. Lent. “Transmission and Backscattering of 4.0 to 12.0 MeV Electrons”. In: *Physical Review* 183.2 (1969). PR, pp. 422–430. URL: https://link.aps.org/doi/10.1103/PhysRev.183.422.

[436] Stefan Bartzsch and Uwe Oelfke. “Line focus x-ray tubes—a new concept to produce high brilliance x-rays”. In: *Physics in Medicine & Biology* 62.22 (2017), p. 8600. URL: https://dx.doi.org/10.1088/1361-6560/aa910b.

[437] Martin Berger, J. Coursey, and M. Zucker. *ESTAR, PSTAR, and ASTAR: Computer Programs for Calculating Stopping-Power and Range Tables for Electrons, Protons, and Helium Ions (version 1.21)*. Personal Communication. 1999-01-01 1999.

[438] J. Winter et al. “Heat management of a compact x-ray source for microbeam radiotherapy and FLASH treatments”. In: *Med Phys* (2022).

[439] Dong-Hee Han et al. “Evaluation by thickness of a linear accelerator target at 6-20 MeV electron beam in MCNP6”. In: *Nuclear Engineering and Technology* 55.6 (2023), pp. 1994–1998. URL: https://www.sciencedirect.com/science/article/pii/S1738573323000967.

[440] J. Gaspar et al. “Emissivity measurement of tungsten plasma facing components of the WEST tokamak”. In: *Fusion Engineering and Design* 149 (2019), p. 111328. URL: https://www.sciencedirect.com/science/article/pii/S0920379619308245%20https://www.sciencedirect.com/science/article/pii/S0920379619308245?via%3Dihub.

[441] David J. Thomas. “ICRU report 85: fundamental quantities and units for ionizing radiation”. In: *Radiation Protection Dosimetry* 150.4 (2012), pp. 550–552. URL: https://doi.org/10.1093/rpd/ncs077.

[442] Hugo Palmans et al. “Dosimetry of small static fields used in external photon beam radiotherapy: Summary of TRS-483, the IAEA–AAPM international Code of Practice for reference and relative dose determination”. In: *Medical Physics* 45.11 (2018), e1123–e1145. URL: https://aapm.onlinelibrary.wiley.com/doi/abs/10.1002/mp.13208.

[443] D. Paynter et al. "Characterisation of flattening filter free (FFF) beam properties for initial beam set-up and routine QA, independent of flattened beams". In: *Physics in Medicine & Biology* 63.1 (2018), p. 015021. URL: https://dx.doi.org/10.1088/1361-6560/aa9a1f.

[444] Falk Pönisch et al. "Properties of unflattened photon beams shaped by a multileaf collimator". In: *Medical Physics* 33.6Part1 (2006), pp. 1738–1746. URL: https://aapm.onlinelibrary.wiley.com/doi/abs/10.1118/1.2201149%20https://aapm.onlinelibrary.wiley.com/doi/pdfdirect/10.1118/1.2201149?download=true.

[445] Antonella Fogliata et al. "Flattening filter free beams from TrueBeam and Versa HD units: Evaluation of the parameters for quality assurance". In: *Medical Physics* 43.1 (2016), pp. 205–212. URL: https://aapm.onlinelibrary.wiley.com/doi/abs/10.1118/1.4938060.

[446] KR Muralidhar. "Derivation of equations to define inflection point and its analysis in flattening filter free photon beams based on the principle of polynomial function". In: *Int J Cancer Ther Oncol* 3.1 (2015), p. 03015.

[447] G. Sahani et al. "Acceptance criteria for flattening filter-free photon beam from standard medical electron linear accelerator: AERB task group recommendations". In: *Journal of Medical Physics* 39.4 (2014). 25525307 [PMID] PMC4258727 [PMCID], pp. 206–211. URL: https://app.dimensions.ai/details/publication/pub.1033104076%20https://doi.org/10.4103/0971-6203.144482.

[448] R. Nath et al. "AAPM code of practice for radiotherapy accelerators: report of AAPM Radiation Therapy Task Group No. 45". In: *Med Phys* 21.7 (1994), pp. 1093–121. URL: https://www.ncbi.nlm.nih.gov/pubmed/7968843%20https://aapm.onlinelibrary.wiley.com/doi/pdfdirect/10.1118/1.597398?download=true.

[449] G. Budgell et al. "IPEM topical report 1: guidance on implementing flattening filter free (FFF) radiotherapy". In: *Phys Med Biol* 61.23 (2016). Budgell, Geoff Brown, Kirstie Cashmore, Jason Duane, Simon Frame, John Hardy, Mark Paynter, David Thomas, Russell eng England 2016/11/08 Phys Med Biol. 2016 Dec 7;61(23):8360-8394. doi: 10.1088/0031-9155/61/23/8360. Epub 2016 Nov 7., pp. 8360–8394. URL: https://www.ncbi.nlm.nih.gov/pubmed/27819253.

[450] S. Sharma et al. "A Simplified Approach for Determination of Inflection Points of Flattening Filter-Free Photon Beam Using In-House Developed Software and Derivation of Reference Levels". In: *J Med Phys* 48.3 (2023). 1998-3913 Sharma, Smriti Dixit, D K Sharma, S D Sharma, Amit Sahani, G Upreti, Ritu Raj Kinhikar, R A Sharma, P K Dash Journal Article India 2023/11/16 J Med Phys. 2023 Jul-Sep;48(3):259-267. doi: 10.4103/jmp.jmp$_5$0$_2$3.*Epub*2023*Sep*18., pp. 259–267.

[451] M. Hossain and J. Rhoades. "On beam quality and flatness of radiotherapy megavoltage photon beams". In: *Australas Phys Eng Sci Med* 39.1 (2016). 1879-5447 Hossain, Murshed Rhoades, Jeffrey P30 CA006927/CA/NCI NIH HHS/United States Journal Article Research Support, N.I.H., Extramural Netherlands 2015/12/05 Australas Phys Eng Sci Med. 2016 Mar;39(1):135-45. doi: 10.1007/s13246-015-0408-8. Epub 2015 Dec 3., pp. 135–45.

[452] A. Pichandi et al. "Analysis of physical parameters and determination of inflection point for Flattening Filter Free beams in medical linear accelerator". In: *Reports of Practical Oncology and Radiotherapy* 19.5 (2014), pp. 322–331. URL: https://doi.org/10.1016/j.rpor.2014.01.004.

[453] Diana M. Ghemiș et al. "Dosimetric characteristics of 6MV flattening filter free and flattened beams among beam-matched linacs: a three-institutional study". In: *Radiation Oncology* 18.1 (2023), p. 126. URL: https://doi.org/10.1186/s13014-023-02313-5.

[454] Pedro Andreo et al. *IAEA-398: Absorbed Dose Determination in External Beam Radiotherapy: An International Code of Practice for Dosimetry based on Standards of Absorbed Dose to Water*. Vol. 11. 2000.

[455] R. Sharma et al. "Evaluating the Impact of Ionization Chamber-Specific Beam Quality Correction Factor in Dosimetry of Filtered and Unfiltered Photon Beams". In: *J Med Phys* 47.2 (2022), pp. 159–165.

[456] T. Cheung, M. J. Butson, and P. K. Yu. "Independence of calibration curves for EBT Gafchromic films of the size of high-energy X-ray fields". In: *Appl Radiat Isot* 64.9 (2006), pp. 1027–30. URL: https://www.ncbi.nlm.nih.gov/pubmed/16774834.

[457] Kenneth R. Kase, Bengt E. Bjärngard, and Frank H. Attix. *The Dosimetry of ionizing radiation*. eng. Orlando: Academic Press, 1985 - 1990.

[458] Antony L. Palmer et al. "Evaluation of Gafchromic EBT-XD film, with comparison to EBT3 film, and application in high dose radiotherapy verification". In: *Physics in Medicine & Biology* 60.22 (2015), p. 8741. URL: https://iopscience.iop.org/article/10.1088/0031-9155/60/22/8741.

[459] M. J. Butson, T. Cheung, and P. K. Yu. "Weak energy dependence of EBT gafchromic film dose response in the 50 kVp-10 MVp X-ray range". In: *Appl Radiat Isot* 64.1 (2006), pp. 60–2. URL: https://www.ncbi.nlm.nih.gov/pubmed/16105740.

[460] M. P. Grams et al. "Technical Note: Initial characterization of the new EBT-XD Gafchromic film". In: *Med Phys* 42.10 (2015), pp. 5782–6.

[461] F. C. Su et al. "Dosimetry characteristics of GAFCHROMIC EBT film responding to therapeutic electron beams". In: *Appl Radiat Isot* 65.10 (2007), pp. 1187–92. URL: https://www.ncbi.nlm.nih.gov/pubmed/17590344.

[462] F. M. Khan et al. "TG-25: Clinical electron-beam dosimetry: report of AAPM Radiation Therapy Committee Task Group No. 25". In: *Med Phys* 18.1 (1991), pp. 73–109. URL: https://www.ncbi.nlm.nih.gov/pubmed/1901132%20https://aapm.onlinelibrary.wiley.com/doi/pdfdirect/10.1118/1.596695?download=true.

[463] L. Karsch et al. "Dose rate dependence for different dosimeters and detectors: TLD, OSL, EBT films, and diamond detectors". In: *Med Phys* 39.5 (2012). Karsch, L Beyreuther, E Burris-Mog, T Kraft, S Richter, C Zeil, K Pawelke, J eng Comparative Study Research Support, Non-U.S. Gov't 2012/05/09 Med Phys. 2012 May;39(5):2447-55. doi: 10.1118/1.3700400., pp. 2447–55. URL: https://www.ncbi.nlm.nih.gov/pubmed/22559615%20https://aapm.onlinelibrary.wiley.com/doi/10.1118/1.3700400.

[464] A. Niroomand-Rad et al. "Radiochromic film dosimetry: recommendations of AAPM Radiation Therapy Committee Task Group 55. American Association of Physicists in Medicine". In: *Med Phys* 25.11 (1998), pp. 2093–115. URL: https://aapm.onlinelibrary.wiley.com/doi/pdfdirect/10.1118/1.598407?download=true.

[465] G. Ataei et al. "Evaluation of Dose Rate and Photon Energy Dependence of Gafchromic EBT3 Film Irradiating with 6 MV and Co-60 Photon Beams". In: *J Med Signals Sens* 9.3 (2019), pp. 204–210.

[466] B. J. Gerbi et al. "TG-25: Recommendations for clinical electron beam dosimetry: supplement to the recommendations of Task Group 25". In: *Med Phys* 36.7 (2009), pp. 3239–79. URL: https://www.ncbi.nlm.nih.gov/pubmed/19673223%20https://aapm.onlinelibrary.wiley.com/doi/pdfdirect/10.1118/1.3125820?download=true.

[467] J. Dutreix and A. Dutreix. "FILM DOSIMETRY OF HIGH-ENERGY ELECTRONS". In: *Annals of the New York Academy of Sciences* 161.1 (1969), pp. 33–43. URL: https://nyaspubs.onlinelibrary.wiley.com/doi/abs/10.1111/j.1749-6632.1969.tb34039.x%20https://nyaspubs.onlinelibrary.wiley.com/doi/pdfdirect/10.1111/j.1749-6632.1969.tb34039.x?download=true.

[468] Indra Jeet Das. *Radiochromic film : role and applications in radiation dosimetry.* Imaging in medical diagnosis and therapy. Boca Raton, FL: CRC Press, Taylor & Francis Group, 2018, xxii, 387 pages.

[469] S. Devic, N. Tomic, and D. Lewis. "Reference radiochromic film dosimetry: Review of technical aspects". In: *Physica Medica-European Journal of Medical Physics* 32.4 (2016), pp. 541–556. URL: https://www.sciencedirect.com/science/article/pii/S112017971600510X?via%3Dihub.

[470] Slobodan Devic. "Radiochromic film dosimetry: Past, present, and future". In: *Physica Medica* 27.3 (2011), pp. 122–134. URL: https://www.sciencedirect.com/science/article/pii/S1120179710000578.

[471] W. L. McLaughlin et al. "Sensitometry of the response of a new radiochromic film dosimeter to gamma radiation and electron beams". In: *Nuclear Instruments and Methods in Physics Research Section A: Accelerators, Spectrometers, Detectors and Associated Equipment* 302.1 (1991), pp. 165–176. URL: https://www.sciencedirect.com/science/article/pii/016890029190506L%20https://www.sciencedirect.com/science/article/abs/pii/016890029190506L?via%3Dihub.

[472] S. Devic et al. "Precise radiochromic film dosimetry using a flat-bed document scanner". In: *Med Phys* 32.7 (2005), pp. 2245–53. URL: https://www.ncbi.nlm.nih.gov/pubmed/16121579%20https://aapm.onlinelibrary.wiley.com/doi/abs/10.1118/1.1929253.

[473] Indra J. Das et al. "Accelerator beam data commissioning equipment and procedures: Report of the TG-106 of the Therapy Physics Committee of the AAPM". In: *Medical Physics* 35.9 (2008), pp. 4186–4215. URL: https://aapm.onlinelibrary.wiley.com/doi/abs/10.1118/1.2969070%20https://aapm.onlinelibrary.wiley.com/doi/pdfdirect/10.1118/1.2969070?download=true.

[474] S. Vatnitsky and H. Järvinen. "Application of a natural diamond detector for the measurement of relative dose distributions in radiotherapy". In: *Phys Med Biol* 38.1 (1993). Vatnitsky, S Järvinen, H Comparative Study Journal Article England 1993/01/01 Phys Med Biol. 1993 Jan;38(1):173-84. doi: 10.1088/0031-9155/38/1/013., pp. 173–84. URL: https://iopscience.iop.org/article/10.1088/0031-9155/38/1/013.

[475] Indra J. Das et al. "Report of AAPM Task Group 155: Megavoltage photon beam dosimetry in small fields and non-equilibrium conditions". In: *Medical Physics* 48.10 (2021), e886–e921. URL: https://aapm.onlinelibrary.wiley.com/doi/abs/10.1002/mp.15030%20https://aapm.onlinelibrary.wiley.com/doi/pdfdirect/10.1002/mp.15030?download=true.

[476] H. K. Looe et al. "The role of radiation-induced charge imbalance on the dose-response of a commercial synthetic diamond detector in small field dosimetry". In: *Med Phys* 46.6 (2019). 2473-4209 Looe, Hui Khee Poppinga, Daniela Kranzer, Rafael Büsing, Isabel Tekin, Tuba Ulrichs, Ann-Britt Delfs, Björn Vogt, Dennis Würfel, Jan Poppe, Björn Journal Article United States 2019/04/12 Med Phys. 2019 Jun;46(6):2752-2759. doi: 10.1002/mp.13542. Epub 2019 May 2., pp. 2752–2759. URL: https://aapm.onlinelibrary.wiley.com/doi/pdfdirect/10.1002/mp.13542?download=true.

[477] Fabio Di Martino et al. "FLASH Radiotherapy With Electrons: Issues Related to the Production, Monitoring, and Dosimetric Characterization of the Beam". In: *Frontiers in Physics* Volume 8 - 2020 (2020). URL: https://www.frontiersin.org/journals/physics/articles/10.3389/fphy.2020.570697%20https://www.frontiersin.org/journals/physics/articles/10.3389/fphy.2020.570697/pdf.

[478] H. Benmakhlouf and P. Andreo. *Ten Years After: Impact of Recent Research in Photon and Electron Beam Dosimetry on the IAEA TRS-398 Code of Practice.* RADIATION PROTECTION AND DOSIMETRY RADIOLOGY AND NUCLEAR MEDICINE. International Atomic Energy Agency (IAEA): IAEA, 2011. URL: http://inis.iaea.org/search/search.aspx?orig_q=RN:43009114.

[479] IAEA. *Review of Data and Methods Recommended in the International Code of Practice for Dosimetry, The Use of Plane Parallel Ionization Chambers in High Energy Electron and Photon Beams, IAEA Technical Reports Series No. 381.* Report. INTERNATIONAL ATOMIC ENERGY AGENCY. IAEA, 2000. URL: https://www.iaea.org/publications/6054/review-of-data-and-methods-recommended-in-the-international-code-of-practice-for-dosimetry-iaea-technical-reports-series-no-381-the-use-of-plane-parallel-ionization-chambers-in-high-energy-electron-and-photon-beams.

[480] P. R. Almond et al. "TG-51: AAPM's TG-51 protocol for clinical reference dosimetry of high-energy photon and electron beams". In: *Medical Physics* 26.9 (1999), pp. 1847–1870. URL: %3CGo%20to%20ISI%3E://WOS:000082632200016%20https://aapm.onlinelibrary.wiley.com/doi/pdfdirect/10.1118/1.598691?download=true.

[481] J. R. Williams and D. I. Thwaites. *Radiotherapy physics : in practice*. 2nd. Includes bibliographical references and index. (Jerry R.) Oxford: Oxford University Press, 2000.

[482] H. Palmans. "Determination of the beam quality index of high-energy photon beams under nonstandard reference conditions". In: *Med Phys* 39.9 (2012). Palmans, Hugo Journal Article Research Support, Non-U.S. Gov't United States 2012/09/11 Med Phys. 2012 Sep;39(9):5513-9. doi: 10.1118/1.4745565., pp. 5513–9. URL: https://aapm.onlinelibrary.wiley.com/doi/pdfdirect/10.1118/1.4745565?download=true.

[483] Malcolm McEwen et al. "Addendum to the AAPMs TG-51 protocol for clinical reference dosimetry of high-energy photon beams". In: *Medical Physics* 41.4 (2014). 24694120 [PMID] PMC5148035 [PMCID], p. 041501. URL: https://app.dimensions.ai/details/publication/pub.1019606400%20https://aapm.onlinelibrary.wiley.com/doi/pdfdirect/10.1118/1.4866223%20https://www.ncbi.nlm.nih.gov/pmc/articles/PMC5148035/pdf/MPHYA6-000041-041501_1.pdf.

[484] David J. Eaton et al. "IPEM code of practice for high-energy photon therapy dosimetry based on the NPL absorbed dose calibration service". In: *Physics in Medicine & Biology* 65.19 (2020), p. 195006. URL: https://dx.doi.org/10.1088/1361-6560/ab99e3%20https://iopscience.iop.org/article/10.1088/1361-6560/ab99e3.

[485] H. Chung, B. Yi, and K. Prado. "SU-E-T-536: Is BJR Supplement 25 Recommendation for Megavoltage Energy Independent Scatter Factor Still Valid for Flattening Filter Free Photon Beams?" In: *Med Phys* 39.6Part18 (2012), p. 3829. URL: https://www.ncbi.nlm.nih.gov/pubmed/28518486%20https://aapm.onlinelibrary.wiley.com/doi/10.1118/1.4735625.

[486] Wolfgang Lechner et al. "Equivalent (uniform) square field sizes of flattening filter free photon beams". In: *Physics in Medicine & Biology* 62.19 (2017), p. 7694. URL: https://dx.doi.org/10.1088/1361-6560/aa83f5.

[487] David S. Followill et al. "An empirical relationship for determining photon beam quality in TG-21 from a ratio of percent depth doses". In: *Medical Physics* 25.7 (1998), pp. 1202–1205. URL: https://aapm.onlinelibrary.wiley.com/doi/abs/10.1118/1.598396.

[488] British Institute of Radiology. *Central Axis Depth Dose Data for Use in Radiotherapy: 1996*. Report Supplement 25. 1996.

[489] D.W.O. Rogers. "FUNDAMENTALS OF DOSIMETRY BASED ON ABSORBED-DOSE STANDARDS". In: *Teletherapy Physics, Present and Future*. 1996, pp. 319–356.

[490] S. J. Thomas et al. "Reference dosimetry on TomoTherapy: an addendum to the 1990 UK MV dosimetry code of practice". In: *Physics in Medicine & Biology* 59.6 (2014), p. 1339. URL: https://dx.doi.org/10.1088/0031-9155/59/6/1339.

[491] Zheng Chang et al. "Commissioning and dosimetric characteristics of TrueBeam system: Composite data of three TrueBeam machines". In: *Medical Physics* 39.11 (2012), pp. 6981–7018. URL: https://aapm.onlinelibrary.wiley.com/doi/abs/10.1118/1.4762682%20https://aapm.onlinelibrary.wiley.com/doi/10.1118/1.4762682.

[492] Katja M. Langen et al. "QA for helical tomotherapy: Report of the AAPM Task Group 148a)". In: *Medical Physics* 37.9 (2010), pp. 4817–4853. URL: https://aapm.onlinelibrary.wiley.com/doi/abs/10.1118/1.3462971%20https://aapm.onlinelibrary.wiley.com/doi/pdfdirect/10.1118/1.3462971?download=true.

[493] Otto A. Sauer. "Determination of the quality index for photon beams at arbitrary field sizes". In: *Medical Physics* 36.9Part1 (2009), pp. 4168–4172. URL: https://aapm.onlinelibrary.wiley.com/doi/abs/10.1118/1.3197062.

[494] D. I. Thwaites et al. "The IPEM code of practice for electron dosimetry for radiotherapy beams of initial energy from 4 to 25 MeV based on an absorbed dose to water calibration". In: *Phys Med Biol* 48.18 (2003). Thwaites, D I DuSautoy, A R Jordan, T McEwen, M R Nisbet, A Nahum, A E Pitchford, W G eng Guideline England 2003/10/08 Phys Med Biol. 2003 Sep 21;48(18):2929-70. doi: 10.1088/0031-9155/48/18/301., pp. 2929–70. URL: https://www.ncbi.nlm.nih.gov/pubmed/14529204%20https://iopscience.iop.org/article/10.1088/0031-9155/48/18/301/pdf.

[495] K. R. Hogstrom. "Treatment planning in electron beam therapy". In: *Front Radiat Ther Oncol* 25 (1991). Hogstrom, K R eng Review Switzerland 1991/01/01 Front Radiat Ther Oncol. 1991;25:30-52; discussion 61-3., 30–52, discussion 61–3. URL: https://www.ncbi.nlm.nih.gov/pubmed/1908420.

[496] I. J. Chetty et al. "Report of the AAPM Task Group No. 105: Issues associated with clinical implementation of Monte Carlo-based photon and electron external beam treatment planning". In: *Med Phys* 34.12 (2007), pp. 4818–53.

[497] D. Sheikh-Bagheri and D. W. O. Rogers. "Sensitivity of megavoltage photon beam Monte Carlo simulations to electron beam and other parameters". In: *Medical Physics* 29.3 (2002), pp. 379–390. URL: %3CGo%20to%20ISI%3E://WOS:000174408000015%20https://aapm.onlinelibrary.wiley.com/doi/pdfdirect/10.1118/1.1446109?download=true.

[498] G. X. Ding and D. W. Rogers. "Mean energy, energy-range relationships and depth-scaling factors for clinical electron beams". In: *Med Phys* 23.3 (1996). Ding, G X Rogers, D W eng R01 CA52692/CA/NCI NIH HHS/ Research Support, U.S. Gov't, P.H.S. 1996/03/01 Med Phys. 1996 Mar;23(3):361-76. doi: 10.1118/1.597788., pp. 361–76. URL: https://www.ncbi.nlm.nih.gov/pubmed/8815379%20https://aapm.onlinelibrary.wiley.com/doi/pdfdirect/10.1118/1.597788?download=true.

[499] Anders Brahme and Hans Svensson. "Specification of electron beam quality from the central-axis depth absorbed-dose distribution". In: *Medical Physics* 3.2 (1976), pp. 95–102. URL: https://aapm.onlinelibrary.wiley.com/doi/abs/10.1118/1.594210.

[500] D. W. Rogers and A. F. Bielajew. "Differences in electron depth-dose curves calculated with EGS and ETRAN and improved energy-range relationships". In: *Med Phys* 13.5 (1986), pp. 687–94. URL: https://aapm.onlinelibrary.wiley.com/doi/abs/10.1118/1.595831%20https://aapm.onlinelibrary.wiley.com/doi/10.1118/1.595831.

[501] IAEA. "The use of plane parallel ionization chambers in high energy electron and photon beams. An international code of practice for dosimetry". In: (1997).

[502] P. Andreo. "Monte Carlo techniques in medical radiation physics". In: *Physics in Medicine & Biology* 36.7 (1991), p. 861. URL: https://dx.doi.org/10.1088/0031-9155/36/7/001%20https://iopscience.iop.org/article/10.1088/0031-9155/36/7/001.

[503] Joao Seco and Frank Verhaegen. *Monte Carlo techniques in radiation therapy.* Imaging in medical diagnosis and therapy. Includes bibliographical references and index. Boca Raton: CRC Press, 2013.

[504] A. F. Bielajew, R. Mohan, and C. S. Chi. *Improved bremsstrahlung photon angular sampling in the EGS4 code system.* Report. 1989.

[505] F. Briesmeister Judith. *MCNP-A General Monte Carlo N-Particle Transport Code.* Online Multimedia. 1993.

[506] I. Kawrakow. "Accurate condensed history Monte Carlo simulation of electron transport. I. EGSnrc, the new EGS4 version". In: *Medical Physics* 27.3 (2000). Export Date: 23 November 2022; Cited By: 817, pp. 485–498. URL: https://www.scopus.com/inward/record.uri?eid=2-s2.0-0034104708&doi=10.1118%2f1.598917&partnerID=40&md5=dd9fbe27e033f9ffe072f2e0c0a11b3b.

[507] A. E. Nahum. "Simulation of Dosimeter Response and Interface Effects". In: *Monte Carlo Transport of Electrons and Photons.* Ed. by Theodore M. Jenkins, Walter R. Nelson, and Alessandro Rindi. Boston, MA: Springer US, 1988, pp. 523–547. URL: https://doi.org/10.1007/978-1-4613-1059-4_25.

[508] Alex F. Bielajew and David W. O. Rogers. "Electron Step-Size Artefacts and PRESTA". In: *Monte Carlo Transport of Electrons and Photons.* Ed. by Theodore M. Jenkins, Walter R. Nelson, and Alessandro Rindi. Boston, MA: Springer US, 1988, pp. 115–137. URL: https://doi.org/10.1007/978-1-4613-1059-4_5.

[509] D. W. O. Rogers. "How accurately can EGS4/PRESTA calculate ion-chamber response?" In: *Medical Physics* 20.2 (1993), pp. 319–323. URL: https://aapm.onlinelibrary.wiley.com/doi/abs/10.1118/1.597071.

[510] E. Poon, J. Seuntjens, and F. Verhaegen. "Consistency test of the electron transport algorithm in the GEANT4 Monte Carlo code". In: *Phys Med Biol* 50.4 (2005). Poon, Emily Seuntjens, Jan Verhaegen, Frank eng Comparative Study Evaluation Study Research Support, Non-U.S. Gov't Validation Study England 2005/03/19 Phys Med Biol. 2005 Feb 21;50(4):681-94. doi: 10.1088/0031-9155/50/4/008., pp. 681–94. URL: https://www.ncbi.nlm.nih.gov/pubmed/15773627%20https://iopscience.iop.org/article/10.1088/0031-9155/50/4/008.

[511] F Tessier. *Electron physics and parameters*. Online Multimedia. 2024.

[512] D. C; McGrath E.J; Irving. *Variance Reduction*. Report. Office of Naval Research (Code 462), Apr. 1975. URL: https://mcnp.lanl.gov/pdf_files/TechReport_1975_ORNL_ORNL-RSIC-38Vol.III_McGrathBasinEtAl.pdf.

[513] J. E. Cygler et al. "Evaluation of the first commercial Monte Carlo dose calculation engine for electron beam treatment planning". In: *Med Phys* 31.1 (2004), pp. 142–53.

[514] JCGM. *Evaluation of measurement data — Guide to the expression of uncertainty in measurement*. Report. Sept. 2008. URL: https://www.bipm.org/documents/20126/2071204/JCGM_100_2008_E.pdf/cb0ef43f-baa5-11cf-3f85-4dcd86f77bd6.

[515] B. R. B. Walters, I. Kawrakow, and D. W. O. Rogers. "History by history statistical estimators in the BEAM code system". In: *Medical Physics* 29.12 (2002), pp. 2745–2752. URL: https://aapm.onlinelibrary.wiley.com/doi/abs/10.1118/1.1517611%20https://aapm.onlinelibrary.wiley.com/doi/pdfdirect/10.1118/1.1517611?download=true.

[516] J. Sempau et al. "Monte Carlo simulation of electron beams from an accelerator head using PENELOPE". In: *Physics in Medicine & Biology* 46.4 (2001), p. 1163. URL: https://dx.doi.org/10.1088/0031-9155/46/4/318%20https://iopscience.iop.org/article/10.1088/0031-9155/46/4/318/pdf.

[517] J. Sempau and A. F. Bielajew. "Towards the elimination of Monte Carlo statistical fluctuation from dose volume histograms for radiotherapy treatment planning". In: *Phys Med Biol* 45.1 (2000), pp. 131–57. URL: https://www.ncbi.nlm.nih.gov/pubmed/10661588%20https://deepblue.lib.umich.edu/bitstream/handle/2027.42/48965/m00110.pdf?sequence=2.

[518] David W. O. Rogers, Iwan Kawrakow, and Ernesto Mainegra-Hing. *NRC User Codes for EGSnrc*. Technical Report PRS-702. Feb. 2023. URL: https://nrc-cnrc.github.io/EGSnrc/doc/pirs702-egsnrc-codes.pdf.

[519] I. Kawrakow, D. W. Rogers, and B. R. Walters. "Large efficiency improvements in BEAMnrc using directional bremsstrahlung splitting". In: *Med Phys* 31.10 (2004), pp. 2883–98. URL: https://www.ncbi.nlm.nih.gov/pubmed/15543798.

[520] M. Fragoso et al. "Fast, accurate photon beam accelerator modeling using BEAMnrc: a systematic investigation of efficiency enhancing methods and cross-section data". In: *Med Phys* 36.12 (2009), pp. 5451–66. URL: https://www.ncbi.nlm.nih.gov/pubmed/20095258%20https://www.ncbi.nlm.nih.gov/pmc/articles/PMC2787063/pdf/MPHYA6-000036-005451_1.pdf.

[521] T. Failing et al. "Enhancement of the EGSnrc code egs$_c$*hamberforfastfluencecalculationsofchargedparticles*". In: *Z Med Phys* 32.4 (2022), pp. 417–427.

[522] H. Bouchard. *Phase space files*. Online Multimedia. 2024.

[523] Walters B.R.B. "Application of efficient Monte Carlo photon beam simulations to dose calculations in voxellized human phantoms". Thesis. 2017.

[524] Gary S. Was. *Fundamentals of radiation materials science: metals and alloys*. Springer, 2016.

[525] R. W. K. Honeycombe. *The plastic deformation of metals*. 2nd. Includes bibliographical references (Robert William Kerr). London: Edward Arnold, 1984.

[526] Alberto Fasso et al. "FLUKA Realistic Modeling of Radiation Induced Damage". In: *Progress in NUCLEAR SCIENCE and TECHNOLOGY* 2 (2011), pp. 769–775.

[527] V. K. Bharadwaj et al. "Analysis of beam-induced damage to the SLC positron production target". In: *PACS2001. Proceedings of the 2001 Particle Accelerator Conference (Cat. No.01CH37268)*. Vol. 3, 2123–2125 vol.3.

[528] Abdallah Reza et al. "Thermal diffusivity degradation and point defect density in self-ion implanted tungsten". In: *Acta Materialia* 193 (2020), pp. 270–279. URL: https://www.sciencedirect.com/science/article/pii/S1359645420302214.

[529] Borivoj Vojnovic et al. "Monitoring beam charge during FLASH irradiations". In: *Frontiers in Physics* 11 (2023). URL: https://www.frontiersin.org/journals/physics/articles/10.3389/fphy.2023.1185237.

[530] A. Berne et al. "Monitoring electron energies during FLASH irradiations". In: *Physics in Medicine and Biology* 66.4 (2021). Qe3ds Times Cited:2 Cited References Count:46. URL: %3CGo%20to%20ISI%3E://WOS:000616090500001%20https://iopscience.iop.org/article/10.1088/1361-6560/abd672/pdf.

[531] A J Cohen and K F Koral. *BACKSCATTERING AND SECONDARY-ELECTRON EMISSION FROM METAL TARGETS OF VARIOUS THICKNESSES*. Report. 1965. URL: https://www.osti.gov/biblio/4625064.

[532] Veerle Kersemans et al. "A System-Agnostic, Adaptable and Extensible Animal Support Cradle System for Cardio-Respiratory-Synchronised, and Other, Multi-Modal Imaging of Small Animals". In: *Tomography* 7.1 (2021), pp. 39–54. URL: https://www.mdpi.com/2379-139X/7/1/4.

[533] PTW. *Advanced Markus® Chamber Type 34045*. Web Page. 2025. URL: https://www.ptwdosimetry.com/en/products/advanced-markus-electron-chamber.

[534] Kristoffer Petersson et al. "High dose-per-pulse electron beam dosimetry — A model to correct for the ion recombination in the Advanced Markus ionization chamber". In: *Medical Physics* 44.3 (2017), pp. 1157–1167. eprint: https://aapm.onlinelibrary.wiley.com/doi/pdf/10.1002/mp.12111. URL: https://aapm.onlinelibrary.wiley.com/doi/abs/10.1002/mp.12111.

[535] Indra Das, Y. Akino, and Paolo Francescon. "TU-F-BRE-05: Experimental Determination of K Factor in Small Field Dosimetry". In: *Medical Physics* 41 (2014), pp. 469–469. URL: https://aapm.onlinelibrary.wiley.com/doi/10.1118/1.4889313.

[536] M. Marinelli et al. "Experimental determination of the PTW 60019 microDiamond dosimeter active area and volume". In: *Med Phys* 43.9 (2016), p. 5205.

[537] V. De Coste et al. "Is the PTW 60019 microDiamond a suitable candidate for small field reference dosimetry?" In: *Phys Med Biol* 62.17 (2017), pp. 7036–7055.

[538] Marco Marinelli et al. "Design, realization, and characterization of a novel diamond detector prototype for FLASH radiotherapy dosimetry". In: *Medical Physics* 49.3 (2022), pp. 1902–1910. URL: https://aapm.onlinelibrary.wiley.com/doi/abs/10.1002/mp.15473.

[539] Luis Brualla-González et al. "Dose rate dependence of the PTW 60019 microDiamond detector in high dose-per-pulse pulsed beams". In: *Physics in Medicine & Biology* 61.1 (2016), N11. URL: https://dx.doi.org/10.1088/0031-9155/61/1/N11.

[540] E. Y. Leon-Marroquin et al. "Response characterization of EBT-XD radiochromic films in megavoltage photon and electron beams". In: *Medical Physics* 46.9 (2019). Ix9ps Times Cited:15 Cited References Count:38, pp. 4246–4256. URL: %3CGo%20to%20ISI%3E://WOS:000480028700001%20https://aapm.onlinelibrary.wiley.com/doi/pdfdirect/10.1002/mp.13708?download=true.

[541] Azam Niroomand-Rad et al. "Report of AAPM Task Group 235 Radiochromic Film Dosimetry: An Update to TG-55". In: *Medical Physics* 47.12 (2020), pp. 5986–6025. URL: https://aapm.onlinelibrary.wiley.com/doi/abs/10.1002/mp.14497.

[542] Ashland. *gafchromicTM ebt-xd films*. Web Page. 2021. URL: https://www.ashland.com/file_source/Ashland/Documents/PHA21-011_Gafchromic%20EBT-XD%20Protocol.pdf.

[543] S. Khachonkham et al. "Characteristic of EBT-XD and EBT3 radiochromic film dosimetry for photon and proton beams". In: *Phys Med Biol* 63.6 (2018), p. 065007. URL: https://www.ncbi.nlm.nih.gov/pubmed/29474189.

[544] F. Guan et al. "Dosimetric response of Gafchromic(™) EBT-XD film to therapeutic protons". In: *Precis Radiat Oncol* 7.1 (2023), pp. 15–26.

[545] Felix Hofmann, Michael P. Short, and Cody A. Dennett. "Transient grating spectroscopy: An ultrarapid, nondestructive materials evaluation technique". In: *MRS Bulletin* 44.5 (2019), pp. 392–402. URL: https://doi.org/10.1557/mrs.2019.104%20https://link.springer.com/content/pdf/10.1557/mrs.2019.104.pdf.

[546] Abdallah Reza et al. "Non-contact, non-destructive mapping of thermal diffusivity and surface acoustic wave speed using transient grating spectroscopy". In: *Review of Scientific Instruments* 91.5 (2020). URL: https://doi.org/10.1063/5.0003742%20https://pubs.aip.org/aip/rsi/article-abstract/91/5/054902/360128/Non-contact-non-destructive-mapping-of-thermal?redirectedFrom=fulltext.

[547] Cody A. Dennett and Michael P. Short. "Time-resolved, dual heterodyne phase collection transient grating spectroscopy". In: *Applied Physics Letters* 110.21 (2017). URL: https://doi.org/10.1063/1.4983716.

[548] M.R. Mitchell and ASM Handbook Committee. "Fundamentals of Modern Fatigue Analysis for Design". In: *Fatigue and Fracture*. Vol. 19. ASM International, 1996, p. 0. URL: https://doi.org/10.31399/asm.hb.v19.a0002364.

[549] Dan Wilcox et al. "Stress levels and failure modes of tantalum-clad tungsten targets at ISIS". In: *Journal of Nuclear Materials* 506 (2018), pp. 76–82. URL: https://www.sciencedirect.com/science/article/pii/S0022311516312041%20https://www.sciencedirect.com/science/article/pii/S0022311516312041?via%3Dihub.

[550] S. S. Manson. "A simple procedure for estimating high-temperature low-cycle fatigue". In: *Experimental Mechanics* 8.8 (1968), pp. 349–355. URL: https://doi.org/10.1007/BF02326037%20https://link.springer.com/content/pdf/10.1007/BF02326037.pdf.

[551] Muyuan Li and Jeong-Ha You. "Interpretation of the deep cracking phenomenon of tungsten monoblock targets observed in high-heat-flux fatigue tests at 20MW/m2". In: *Fusion Engineering and Design* 101 (2015), pp. 1–8. URL: https://www.sciencedirect.com/science/article/pii/S0920379615302775.

[552] Shuming Wang et al. "Numerical analysis of fatigue behaviors for tungsten armor of ITER divertor". In: *Nuclear Materials and Energy* 25 (2020), p. 100815. URL: https://www.sciencedirect.com/science/article/pii/S2352179120300909.

[553] H. Leggett and H. Parechanian. *Mechanical Properties of Wrought Tungsten*. Report ASD-TDR-63-585. AF materials laboratory, research and technology division, air force systems command, Nov. 1963.

[554] J.A. Collins. *Failure of Materials in Mechanical Design: Analysis, Prediction, Prevention*. Wiley, 1993. URL: https://books.google.co.uk/books?id=TNvwS0ZqyzEC.

[555] Inc. eFunda. *Fatigue*. Web Page. URL: https://www.efunda.com/formulae/solid_mechanics/fatigue/fatigue_lowcycle.cfm.

[556] N. Jaksic, A. Herrmann, and H. Greuner. "Transient Thermal and Structural Mechanics Investigation of the New Solid Tungsten Divertor Tile for Special Purposes at ASDEX Upgrade". In: *IEEE Transactions on Plasma Science* 42.6 (2014), pp. 1790–1795.

[557] Milton A. Miner. "Cumulative Damage in Fatigue". In: *Journal of Applied Mechanics* 12.3 (1945), pp. 159–164. URL: https://doi.org/10.1115/1.4009458.

[558] U. Muralidharan and S. S. Manson. "A Modified Universal Slopes Equation for Estimation of Fatigue Characteristics of Metals". In: *Journal of Engineering Materials and Technology* 110.1 (1988), pp. 55–58. URL: https://doi.org/10.1115/1.3226010%20https://asmedigitalcollection.asme.org/materialstechnology/article-abstract/110/1/55/385195/A-Modified-Universal-Slopes-Equation-for?redirectedFrom=fulltext.

[559] S. S. Manson. "Fatigue: A complex subject—Some simple approximations". In: *Experimental Mechanics* 5.4 (1965), pp. 193–226. URL: https://doi.org/10.1007/BF02321056.

[560] Y. B. Cho and P. Munro. "Kilovision: Thermal modeling of a kilovoltage x-ray source integrated into a medical linear accelerator". In: *Medical Physics* 29.9 (2002). 595ec Times Cited:10 Cited References Count:28, pp. 2101–2108. URL: %3CGo%20to%20ISI%3E://WOS:000178093000018%20https://aapm.onlinelibrary.wiley.com/doi/pdfdirect/10.1118/1.1501142?download=true.

[561] Vinod K. Arya and Gary R. Halford. *FLAPS (Fatigue Life Analysis Programs): Computer Programs to Predict Cyclic Life Using the Total Strain Version of Strainrange Partitioning and Other Life Prediction Methods*. Report NASA/CR-2003-212530,NAS 1.26:212530,E-14092. NASA, Aug. 2003.

[562] Muyuan Li, Ewald Werner, and Jeong-Ha You. "Low cycle fatigue behavior of ITER-like divertor target under DEMO-relevant operation conditions". In: *Fusion Engineering and Design* 90 (2015), pp. 88–96. URL: https://www.sciencedirect.com/science/article/pii/S0920379614006401%20https://www.sciencedirect.com/science/article/pii/S0920379614006401?via%3Dihub.

[563] J. Allison et al. "Recent developments in GEANT4". In: *Nuclear Instruments & Methods in Physics Research Section a-Accelerators Spectrometers Detectors and Associated Equipment* 835 (2016), pp. 186–225. URL: %3CGo%20to%20ISI%3E://WOS:000386057800022.

[564] Yann Perrot. "Evaluation of the dose deposited by electron beams in radiotherapy in voxelized phantoms using the Monte Carlo GATE simulation platform based on GEANT4 in a grid environment Evaluation de la dose déposée par des faisceaux d'électrons en radiothérapie dans des fantômes voxelisés en utilisant la plateforme de simulation Monte Carlo GATE fondée sur GEANT4 dans un environnement de grille". Alain Baldit [Président] Sébastien Incerti [Rapporteur] Manuel Bardiès [Rapporteur] David Sarrut Lydia Maigne Physics [physics]/Condensed Matter [cond-mat]/Other [cond-mat.other]Theses. Thesis. 2011. URL: https://theses.hal.science/tel-00721940.

[565] V. Ivanchenko. "Simulation of Multiple and Single Scattering in GEANT4". In: *International Workshop The evaluation of Leading Hadron Contributions to the Muon Anomalous Magnetic Moment*. URL: https://indico.mitp.uni-mainz.de/event/128/contributions/405/attachments/311/323/Ivantchenko.pdf.

[566] P. Arce et al. *An optimized Geant4 physics list for gamma radiotherapy*. Report. Sept. 2019. URL: https://indico.cern.ch/event/825306/contributions/3561756/attachments/1916239/3168136/RTphyslist.G4WS2019_arce.pdf.

[567] P. Arce et al. “Results of a Geant4 benchmarking study for bio-medical applications, performed with the G4-Med system”. In: *Med Phys* (2025).

[568] J. F. Carrier et al. “Validation of GEANT4, an object-oriented Monte Carlo toolkit, for simulations in medical physics”. In: *Med Phys* 31.3 (2004). Carrier, J F Archambault, L Beaulieu, L Roy, R Journal Article Research Support, Non-U.S. Gov’t United States 2004/04/09 Med Phys. 2004 Mar;31(3):484-92. doi: 10.1118/1.1644532., pp. 484–92.

[569] J. Torres et al. “Dosimetry characterization of 32P intravascular brachytherapy source wires using Monte Carlo codes PENELOPE and GEANT4”. In: *Med Phys* 31.2 (2004). Torres, Javier Buades, Manuel J Almansa, Julio F Guerrero, Rafael Lallena, Antonio M eng Research Support, Non-U.S. Gov’t 2004/03/06 Med Phys. 2004 Feb;31(2):296-304. doi: 10.1118/1.1637970., pp. 296–304. URL: https://www.ncbi.nlm.nih.gov/pubmed/15000615.

[570] B. A. Faddegon et al. “Benchmarking of Monte Carlo simulation of bremsstrahlung from thick targets at radiotherapy energies”. In: *Medical Physics* 35.10 (2008), pp. 4308–4317. URL: %3CGo%20to%20ISI%3E://WOS:000259591800005%20https://www.ncbi.nlm.nih.gov/pmc/articles/PMC2736754/pdf/MPHYA6-000035-004308_1.pdf.

[571] B. Askri. “Optimization of a photoneutron source based on 10 MeV electron beam using Geant4 Monte Carlo code”. In: *Nuclear Instruments & Methods in Physics Research Section B-Beam Interactions with Materials and Atoms* 360 (2015), pp. 1–8. URL: %3CGo%20to%20ISI%3E://WOS:000361859500001%20https://www.sciencedirect.com/science/article/pii/S0168583X15007211?via%3Dihub.

[572] S. Chauvie et al. “Validation of Geant4 Bremsstrahlung models: first results”. In: *2006 IEEE Nuclear Science Symposium Conference Record*. Vol. 3, pp. 1511–1515. URL: https://ieeexplore.ieee.org/stampPDF/getPDF.jsp?tp=&arnumber=4179298&ref=.

[573] Luciano Pandola. *Geant4 Intro*. 2022.

[574] S. Agostinelli et al. “Geant4—a simulation toolkit”. In: *Nuclear Instruments and Methods in Physics Research Section A: Accelerators, Spectrometers, Detectors and Associated Equipment* 506.3 (2003), pp. 250–303. URL: https://www.sciencedirect.com/science/article/pii/S0168900203013688.

[575] L. Maigne et al. “Comparison of GATE/GEANT4 with EGSnrc and MCNP for electron dose calculations at energies between 15 keV and 20 MeV”. In: *Physics in Medicine & Biology* 56.3 (2011), p. 811. URL: https://dx.doi.org/10.1088/0031-9155/56/3/017.

[576] Deae-eddine Krim et al. “Monte Carlo simulation of a novel medical linac concept for highly conformal x-ray FLASH cancer radiotherapy”. In: *Scientific Reports* 15.1 (2025), p. 17604. URL: https://doi.org/10.1038/s41598-025-02150-4.

[577] E. Poon and F. Verhaegen. “Accuracy of the photon and electron physics in GEANT4 for radiotherapy applications”. In: *Med Phys* 32.6 (2005). Poon, Emily Verhaegen, Frank eng Research Support, Non-U.S. Gov’t 2005/07/15 Med Phys. 2005 Jun;32(6):1696-711. doi: 10.1118/1.1895796., pp. 1696–711. URL: https://www.ncbi.nlm.nih.gov/pubmed/16013728.

[578] V. N. Ivanchenko et al. "Geant4 models for simulation of multiple scattering". In: *Journal of Physics: Conference Series* 219.3 (2010), p. 032045. URL: https://dx.doi.org/10.1088/1742-6596/219/3/032045.

[579] S. Elles et al. "Geant4 and Fano cavity test: where are we?" In: *Journal of Physics: Conference Series* 102.1 (2008), p. 012009. URL: https://dx.doi.org/10.1088/1742-6596/102/1/012009.

[580] J. Deng et al. "Photon beam characterization and modelling for Monte Carlo treatment planning". In: *Physics in Medicine and Biology* 45.2 (2000). Deng, J Jiang, SB Kapur, A Li, JS Pawlicki, T Ma, CM Deng, Jun/0000-0003-2619-8054, pp. 411–427. URL: %3CGo%20to%20ISI%3E://WOS:000085410400013.

[581] Joao Seco and Frank Verhaegen. *Monte Carlo techniques in radiation therapy.* Second. Imaging in Medical Diagnosis and Therapy. Boca Raton: CRC Press, 2021.

[582] Andrea Dotti et al. "Extending Geant4 parallelism with external libraries (MPI, TBB) and its use on HPC resources". In: (2016). URL: http://dx.doi.org/10.48550/ARXIV.1605.01792.

[583] A. Dotti. *Geant4 on HPC systems.* Online Multimedia. URL: https://indico.cern.ch/event/658060/contributions/2890755/attachments/1624233/2585853/HSF_Naples_1.pdf.

[584] I Kawrakow et al. "The EGSnrc C++ class library". In: *NRC Report PIRS-898 (rev A)* (2009).

[585] W. R. Nelson, H. Hirayama, and D. W. O. Rogers. *EGS4 code system.* Report. 30 1985. URL: https://www.osti.gov/biblio/6137659.

[586] J. Wulff, J. T. Heverhagen, and K. Zink. "Monte-Carlo-based perturbation and beam quality correction factors for thimble ionization chambers in high-energy photon beams". In: *Phys Med Biol* 53.11 (2008), pp. 2823–36. URL: https://www.ncbi.nlm.nih.gov/pubmed/18460747.

[587] J. Wulff, K. Zink, and I. Kawrakow. "Efficiency improvements for ion chamber calculations in high energy photon beams". In: *Med Phys* 35.4 (2008), pp. 1328–36. URL: https://www.ncbi.nlm.nih.gov/pubmed/18491527%20https://aapm.onlinelibrary.wiley.com/doi/10.1118/1.2874554.

[588] H. Bouchard, J. Seuntjens, and I. Kawrakow. "A Monte Carlo method to evaluate the impact of positioning errors on detector response and quality correction factors in nonstandard beams". In: *Phys Med Biol* 56.8 (2011), pp. 2617–34. URL: https://www.ncbi.nlm.nih.gov/pubmed/21454927.

[589] F. Crop et al. "The influence of small field sizes, penumbra, spot size and measurement depth on perturbation factors for microionization chambers". In: *Phys Med Biol* 54.9 (2009). Crop, F Reynaert, N Pittomvils, G Paelinck, L De Wagter, C Vakaet, L Thierens, H eng Research Support, Non-U.S. Gov't England 2009/04/23 Phys Med Biol. 2009 May 7;54(9):2951-69. doi: 10.1088/0031-9155/54/9/024. Epub 2009 Apr 21., pp. 2951–69. URL: https://www.ncbi.nlm.nih.gov/pubmed/19384005.

[590] Kawrakow I. *Monte Carlo transport parameters.* Online Multimedia. 2024.

[591] Rogers D.W.O. et al. *NRC User Codes for EGSnrc*. Report NRCC Report PIRS-702(revC). Jan. 2025.

[592] Andrew Richards. "University of Oxford Advanced Research Computing". In: (2015). URL: https://doi.org/10.5281/zenodo.22558%20http://dx.doi.org/10.5281/zenodo.22558.

[593] B Wood. "Improved Alloy or Metallic Composi tion Suitable for a Metallic Cement in the Manufacture of Tin, Pewter, and Other Metals; Also Useful for Casting and Other Purposes". In: *J. Franklin Inst.* 40 (Third Series) (1860), pp. 125–128.

[594] F. Trompier et al. "Minimum reporting standards should be expected for preclinical radiobiology irradiators and dosimetry in the published literature". In: *Int J Radiat Biol* 100.1 (2024), pp. 1–6.

[595] Y. Poirier et al. "Minimum Reporting Standards Should be Expected for Preclinical Radiobiology Irradiators and Dosimetry in the Published Literature". In: *Radiat Res* 200.3 (2023). 1938-5404 Poirier, Yannick DeWerd, Larry A Trompier, François Santos, Morgane Dos Sheng, Ke Kunugi, Keith Satyamitra, Merriline M DiCarlo, Andrea L Winters, Thomas A Z99 AI999999/ImNIH/Intramural NIH HHS/United States Journal Article United States 2023/08/17 Radiat Res. 2023 Sep 1;200(3):217-222. doi: 10.1667/RADE-23-00119.1., pp. 217–222.

[596] M. Desrosiers et al. "The Importance of Dosimetry Standardization in Radiobiology". In: *J Res Natl Inst Stand Technol* 118 (2013), pp. 403–18.

[597] Y. S. Kim et al. "Estimation of photoneutron yield in linear accelerator with different collimation systems by Geant4 and MCNPX simulation codes". In: *Physics in Medicine and Biology* 61.7 (2016), pp. 2762–2779. URL: %3CGo%20to%20ISI%3E://WOS:000374016800011%20https://iopscience.iop.org/article/10.1088/0031-9155/61/7/2762/pdf.

[598] Bhushankumar Jagnnath Patil. "Studies on (i) characterization of bremsstrahlung spectra from high Z elements and (ii) development of neutron source using MEV pulsed electron beam and their applications". Thesis. 2010. URL: http://hdl.handle.net/10603/3833.

[599] Xiao Yu et al. "Numerical optimization of transmission bremsstrahlung target for intense pulsed electron beam". In: *Nuclear Engineering and Technology* 54.2 (2022), pp. 666–673. URL: https://www.sciencedirect.com/science/article/pii/S173857332100509X.

[600] Z H Wang et al. "Damage Behavior of Tungsten Targets for 6 MeV Linear accelerators". In: *Proceedings, 10th International Particle Accelerator Conference (IPAC 2019): Melbourne, Australia* (2019), pp. 3934–3936.

[601] Sanford T.W.L. Halbleib J. A. *Predicted Flash X-Ray Environments Using Standard Converter Configurations*. Report. Sandia National Laboratories, Sept. 1985. URL: https://www.osti.gov/servlets/purl/5291181.

[602] R. Svensson and A. Brahme. "Effective source size, yield and beam profile from multi-layered bremsstrahlung targets". In: *Physics in Medicine and Biology* 41.8 (1996). Va701 Times Cited:20 Cited References Count:30, pp. 1353–1379. URL: %3CGo%20to%20ISI%3E://WOS:A1996VA70100008.

[603] P. Williams Jacqueline et al. “Animal Models for Medical Countermeasures to Radiation Exposure”. In: *Radiation Research* 173.4 (2010), pp. 557–578. URL: https://doi.org/10.1667/RR1880.1.

[604] A. Hart et al. “High-throughput, low-cost FLASH: irradiation of Drosophila melanogaster with low-energy X-rays using time structures spanning conventional and ultrahigh dose rates”. In: *J Radiat Res* 65.6 (2024), pp. 836–844.

[605] AJ Mundt, JC Roeske, and TD Chung. *Physical Basis of Radiation Therapy*. Ed. by DW Kufe, RE Pollock, RR Weichselbaum, et al. 6th. Hamilton (ON): BC Decker, 2003. URL: https://www.ncbi.nlm.nih.gov/books/NBK13943/.

[606] Nolan Esplen et al. “Dosimetric characterization of a novel UHDR megavoltage X-ray source for FLASH radiobiological experiments”. In: *Scientific Reports* 14.1 (2024), p. 822. URL: https://doi.org/10.1038/s41598-023-50412-w%20https://www.nature.com/articles/s41598-023-50412-w.pdf.

[607] Y. Yang et al. “FLASH radiotherapy using high-energy X-rays: Current status of PARTER platform in FLASH research”. In: *Radiother Oncol* (2023), p. 109967.

[608] B. Singers Sorensen et al. “In vivo validation and tissue sparing factor for acute damage of pencil beam scanning proton FLASH”. In: *Radiother Oncol* 167 (2022), pp. 109–115. URL: https://www.ncbi.nlm.nih.gov/pubmed/34953933%20https://www.sciencedirect.com/science/article/pii/S0167814021090708?via%3Dihub.

[609] Per Rugaard Poulsen et al. “Oxygen Enhancement Ratio-Weighted Dose Quantitatively Describes Acute Skin Toxicity Variations in Mice After Pencil Beam Scanning Proton FLASH Irradiation With Changing Doses and Time Structures”. In: *International Journal of Radiation Oncology*Biology*Physics* 120.1 (2024), pp. 276–286. URL: https://www.sciencedirect.com/science/article/pii/S0360301624003584.

[610] Nina A. Mayr et al. “Practice Patterns of Spatially Fractionated Radiation Therapy: A Clinical Practice Survey”. In: *Advances in Radiation Oncology* 9.2 (2024), p. 101308. URL: https://www.sciencedirect.com/science/article/pii/S2452109423001367.

[611] Beatriz E. Amendola et al. “An International Consensus on the Design of Prospective Clinical–Translational Trials in Spatially Fractionated Radiation Therapy for Advanced Gynecologic Cancer”. In: *Cancers* 14.17 (2022), p. 4267. URL: https://www.mdpi.com/2072-6694/14/17/4267.

[612] S. Paillas et al. “Quantifying the FLASH effect and its dependence on average dose rate in-vivo for 6 MeV electron and 6 MV photon beams”. Unpublished Work. Clinical and Translational Radiation Oncology [Manuscript under review], 2025. URL: http://dx.doi.org/10.2139/ssrn.5310282.

[613] Melody Liu et al. “Electron Spatially Fractionated Radiation Therapy for Mycosis Fungoides”. In: *Blood* 144.Supplement 1 (2024), pp. 6260–6260. URL: https://doi.org/10.1182/blood-2024-208820.

[614] Kuei-Hua Lin et al. “Surface dose with grids in electron beam radiation therapy”. In: *Applied Radiation and Isotopes* 56.3 (2002), pp. 477–484. URL: https://www.sciencedirect.com/science/article/pii/S0969804301002494.

[615] Stefan Bartzsch et al. “A preclinical microbeam facility with a conventional x-ray tube”. In: *Medical Physics* 43.12 (2016), pp. 6301–6308. URL: https://aapm.onlinelibrary.wiley.com/doi/abs/10.1118/1.4966032.

[616] S. K. Ahmed et al. “Spatially Fractionated Radiation Therapy in Sarcomas: A Large Single-Institution Experience”. In: *Adv Radiat Oncol* 9.3 (2024), p. 101401. URL: https://www.advancesradonc.org/action/showPdf?pii=S2452109423002294.

[617] Nathan Clements, Magdalena Bazalova-Carter, and Nolan Esplen. “Monte Carlo optimization of a GRID collimator for preclinical megavoltage ultra-high dose rate spatially-fractionated radiation therapy”. In: *Physics in Medicine & Biology* 67.18 (2022), p. 185001. URL: https://dx.doi.org/10.1088/1361-6560/ac8c1a.

[618] Leyla Moghaddasi et al. *Radiobiological and Treatment-Related Aspects of Spatially Fractionated Radiotherapy*. Electronic Article. 2022. URL: https://mdpi-res.com/d_attachment/ijms/ijms-23-03366/article_deploy/ijms-23-03366-v2.pdf?version=1647914764.

[619] Carmen Kut, Harry Quon, and Xuguang S. Chen. *Emerging Radiotherapy Technologies for Head and Neck Squamous Cell Carcinoma: Challenges and Opportunities in the Era of Immunotherapy*. Electronic Article. 2024.

[620] V. Trappetti et al. “Towards melanoma in situ vaccination with multiple ultra-narrow X-ray beams”. In: *Cancer Lett* 608 (2025), p. 217326.

[621] Austin Sloop et al. “Rapid Switching of a C-Series Linear Accelerator Between Conventional and Ultrahigh-Dose-Rate Research Mode With Beamline Modifications and Output Stabilization”. In: *International Journal of Radiation Oncology*Biology*Physics* 119.4 (2024), pp. 1317–1325. URL: https://www.sciencedirect.com/science/article/pii/S0360301624002992.

[622] J. Apostolakis et al. “Geometry and physics of the Geant4 toolkit for high and medium energy applications”. In: *Radiation Physics and Chemistry* 78.10 (2009), pp. 859–873. URL: https://www.sciencedirect.com/science/article/pii/S0969806X09001650.

[623] P. Arce et al. “Report on G4-Med, a Geant4 benchmarking system for medical physics applications developed by the Geant4 Medical Simulation Benchmarking Group”. In: *Medical Physics* 48.1 (2021), pp. 19–56. URL: https://aapm.onlinelibrary.wiley.com/doi/abs/10.1002/mp.14226.

[624] RS. *RS PRO Type K Thermocouple 1m Length, 0.3mm Diameter*. Web Page. URL: https://uk.rs-online.com/web/p/thermocouples/4094920?gb=s.

[625] Inc. Thorlabs. *WG41010 - Ø1" UVFS Broadband Precision Window, Uncoated, t = 1 mm*. Web Page. URL: https://www.thorlabs.com/thorproduct.cfm?partnumber=WG41010.

[626] *EVAL-AD8497*. Web Page. URL: https://www.analog.com/en/resources/evaluation-hardware-and-software/evaluation-boards-kits/eval-ad8497.html#eb-overview.

[627] A. Y. Lee and Donald R. Burgess. *NIST Temperature Scale Database Version 3.0*. Dataset. 16th August 2025 2016.

[628] R Malik. *AN-1087: Thermocouple Linearization When Using the AD8494/AD8495/AD8496/AD8497*. Web Page. URL: https://www.analog.com/en/resources/app-notes/an-1087.html.

[629] Joseph B. Tipton Jr. *Uncertainty Quantification of Monolithic Tungsten Target Block Fatigue*. Report. Jan. 2022. URL: https://www.osti.gov/biblio/2394723%20https://www.osti.gov/servlets/purl/2394723.

[630] Nikola Jaksic et al. "Results of high heat flux tests and structural analysis of the new solid tungsten divertor tile for ASDEX Upgrade". In: *Fusion Engineering and Design* 98-99 (2015), pp. 1333–1336. URL: https://www.sciencedirect.com/science/article/pii/S0920379615001891.

[631] John W. Arblaster. *Selected Values of the Crystallographic Properties of Elements*. Materials Park, UNITED STATES: A S M International, 2018. URL: http://ebookcentral.proquest.com/lib/oxford/detail.action?docID=5515132.

[632] R. W. Powell et al. *Thermal conductivity of selected materials*. NSRDS-NBS 8 16. [Main author] (Cho Yen) 1 online resource (2 volumes) Title from title screen (viewed on May 19, 2009). "Issued November 25, 1966"–[Pt. 1] "Issued February, 1968"–Pt. 2 "Category 5: thermodynamic and transport properties." Digital reproduction; no longer available for sale by the Supt. of Docs. Includes bibliographical references. Contents: [pt. 1]. Thermal conductivity of metals – Thermal conductivity of nonmetallic solids – Thermal conductivity of liquids – thermal conductivity ofgases – pt. 2. Thermal conductivity of metallic elements – Thermal conductivity of graphites – Thermal conductivity of gases. Washington, D.C: U.S. Dept. of Commerce, National Bureau of Standards : For sale by the Supt. of Docs., U.S. G.P.O, 1966. URL: http://hdl.handle.net/2027/mdp.39015086492306%20http://hdl.handle.net/2027/mdp.39015086492314%20http://hdl.handle.net/2027/uc1.l0065512907.

[633] Jr. Chase M. W. *NIST-JANAF thermochemical tables, monograph 9*. Fourth Edition. Vol. 9. Washington DC: American Chemical Society, 1998, pp. 1–1951. URL: http://www.nist.gov/srd/monogr.cfm.

[634] Y. S. Touloukian. *Thermophysical properties of matter*. Vol. 7. The TPRC data series. Includes bibliographies and index. New York, N.Y.: IFI/Plenum, 1970.

[635] G. S. Pisarenko, V. A. Borisenko, and Yu A. Kashtalyan. "The effect of temperature on the hardness and modulus of elasticity of tungsten and molybdenum (20–2700‡)". In: *Soviet Powder Metallurgy and Metal Ceramics* 1.5 (1964), pp. 371–374. URL: https://doi.org/10.1007/BF00774121.

[636] Asanka Weerasinghe, Brian D. Wirth, and Dimitrios Maroudas. "Elastic Properties of Plasma-Exposed Tungsten Predicted by Molecular-Dynamics Simulations". In: *ACS Applied Materials & Interfaces* 12.19 (2020). doi: 10.1021/acsami.0c01381, pp. 22287–22297. URL: https://doi.org/10.1021/acsami.0c01381.

[637] Gordon R. Johnson and W. Howard Cook. "A Constitutive Model and Data for Metals Subjected to Large Strains, High Strain Rates, and High Temperatures." In: *7th International Symposium on Ballistics*, pp. 541–547.

[638] A. M. Lennon and K. T. Ramesh. "The thermoviscoplastic response of polycrystalline tungsten in compression". In: *Materials Science and Engineering: A* 276.1 (2000), pp. 9–21. URL: https://www.sciencedirect.com/science/article/pii/S0921509399005171%20https://www.sciencedirect.com/science/article/pii/S0921509399005171?via%3Dihub.

[639] GP Skoro, JRJ Bennett, and TR Edgecock. "Experimental results and constitutive modelling for tungsten and tantalum at high strain rates and very high temperatures". In: *arXiv preprint arXiv:1105.5514* (2011).

[640] Jin Wang et al. "A comparative study of several constitutive models for powder metallurgy tungsten at elevated temperature". In: *Materials & Design* 90 (2016), pp. 91–100. URL: https://www.sciencedirect.com/science/article/pii/S0264127515306924.

[641] Raul E. Munoz. "Finite Element Modelling (Including Material Grain Refinement Prediction) when Turning Advanced Aerospace Alloys". Thesis. 2014. URL: https://etheses.bham.ac.uk//id/eprint/5844/1/Munoz15PhD%5B1%5D.pdf.

[642] Muyuan Li, Ewald Werner, and Jeong-Ha You. "Cracking behavior of tungsten armor under ELM-like thermal shock loads: A computational study". In: *Nuclear Materials and Energy* 2 (2015), pp. 1–11. URL: https://www.sciencedirect.com/science/article/pii/S2352179114200044.

[643] M. Wirtz et al. "Transient heat load challenges for plasma-facing materials during long-term operation". In: *Nuclear Materials and Energy* 12 (2017), pp. 148–155. URL: https://www.sciencedirect.com/science/article/pii/S2352179116302320.

[644] J. Linke et al. "Performance of different tungsten grades under transient thermal loads". In: *Nuclear Fusion* 51.7 (2011), p. 073017. URL: https://dx.doi.org/10.1088/0029-5515/51/7/073017.

[645] M. Roedig et al. "Investigation of tungsten alloys as plasma facing materials for the ITER divertor". In: *Fusion Engineering and Design* 61-62 (2002), pp. 135–140. URL: https://www.sciencedirect.com/science/article/pii/S0920379602001138.

[646] J. F. Salavy et al. "Analysis of high heat flux testing of mock-ups". In: *Fusion Engineering and Design* 66-68 (2003), pp. 277–281. URL: https://www.sciencedirect.com/science/article/pii/S0920379603001479.

[647] Paolo Dondero et al. "Electron backscattering simulation in Geant4". In: *Nuclear Instruments and Methods in Physics Research Section B: Beam Interactions with Materials and Atoms* 425 (2018), pp. 18–25. URL: https://www.sciencedirect.com/science/article/pii/S0168583X18302301.

[648] ABAQUS. *ABAQUS Documentation*. Vol. 6.6. ABAQUS Analysis User's Manual. Online, 2009. URL: https://classes.engineering.wustl.edu/2009/spring/mase5513/abaqus/docs/v6.6/books/popups/usb-pre.html.

[649] T. P. Lin. "Estimation of Temperature Rise in Electron Beam Heating of Thin Films". In: *Ibm Journal of Research and Development* 11.5 (1967). A0188 Times Cited:28 Cited References Count:32, pp. 527–&. URL: %3CGo%20to%20ISI%3E://WOS:A1967A018800005%20https://ieeexplore.ieee.org/document/5391961/?arnumber=5391961&tag=1.

[650] L. G. Pittaway. "Temperature Distributions in Thin Foil + Semi-Infinite Targets Bombarded by Electron Beam". In: *British Journal of Applied Physics* 15.8 (1964). 7448a Times Cited:96 Cited References Count:4, pp. 967–&. URL: %3CGo%20to%20ISI%3E://WOS:A19647448A00015%20https://iopscience.iop.org/article/10.1088/0508-3443/15/8/314/pdf.

[651] K. Roll. "The Temperature Distribution in a Thin Metal-Film Exposed to an Electron-Beam". In: *Applied Surface Science* 5.4 (1980). Ks717 Times Cited:21 Cited References Count:12, pp. 388–397. URL: %3CGo%20to%20ISI%3E://WOS:A1980KS71700004.

[652] Richard A. Perkins, W. L. Price, and Donald D. Crooks. "Oxidation of Tungsten at Ultra-High Temperatures". In: 1962.

[653] Muyuan Li. "A fracture mechanics study of tungsten failure under high heat flux loads". PLASMA PHYSICS AND FUSION TECHNOLOGY MATERIALS SCIENCE. Thesis. 2015. URL: http://inis.iaea.org/search/search.aspx?orig_q=RN:46109510.

[654] I. Bobin-Vastra et al. "Activity of the European high heat flux test facility: FE200". In: *Fusion Engineering and Design* 75-79 (2005), pp. 357–363. URL: https://www.sciencedirect.com/science/article/pii/S0920379605004072.

[655] T. Hirai et al. "Use of tungsten material for the ITER divertor". In: *Nuclear Materials and Energy* 9 (2016), pp. 616–622. URL: https://www.sciencedirect.com/science/article/pii/S2352179115301046%20https://www.sciencedirect.com/science/article/pii/S2352179115301046?via%3Dihub.

[656] F.F. Schmidt, Battelle Memorial Institute. Defense Metals Information Center, and H.R. Ogden. *The Engineering Properties of Tungsten and Tungsten Alloys*. Defense Metals Information Center, Battelle Memorial Institute, 1963. URL: https://books.google.co.uk/books?id=BW1kAAAAMAAJ.

[657] Youyun Lian et al. "Thermal shock performance of CVD tungsten coating at elevated temperatures". In: *Journal of Nuclear Materials* 455.1 (2014), pp. 371–375. URL: https://www.sciencedirect.com/science/article/pii/S0022311514004607.

[658] M. Fursdon, J. H. You, and M. Li. "Towards reliable design-by-analysis for divertor plasma facing components – Guidelines for inelastic assessment (part 1: Unirradiated)". In: *Fusion Engineering and Design* 147 (2019), p. 111234. URL: https://www.sciencedirect.com/science/article/pii/S0920379619307124.

[659] K. Sato et al. "Investigation of mechanical properties of stress-relieved and electron-irradiated tungsten after hydrogen charging". In: *Nuclear Materials and Energy* 17 (2018), pp. 29–33. URL: https://www.sciencedirect.com/science/article/pii/S2352179117301758.

[660] L. F. Coffin. "The effect of frequency on the cyclic strain and low cycle fatigue behavior of cast Udimet 500 at elevated temperature". In: *Metallurgical Transactions* 2.11 (1971), pp. 3105–3113. URL: https://doi.org/10.1007/BF02814962.

[661] Graham Bass et al. “A prototype low-cost secondary standard calorimeter for reference dosimetry with ultra-high pulse dose rates”. In: *The British Journal of Radiology* 96 (2022).

[662] Sergey Kutsaev et al. *Linear Accelerator for Demonstration of X-ray Radiotherapy With FLASH Effect*. Conference Paper. 28 August-02 September 2022.

[663] J. Haimson. “Some Aspects of Electron Beam Optics and X-Ray Production with the Linear Accelerator”. In: *IRE Transactions on Nuclear Science* 9.2 (1962), pp. 32–49.

[664] Canan Koksal Akbas et al. “Preclinical photon minibeam radiotherapy using a custom collimator: Dosimetry characterization and preliminary in-vivo results on a glioma model”. In: *Physica Medica* 124 (2024), p. 103420. URL: https://www.sciencedirect.com/science/article/pii/S1120179724002151.

[665] L. Yeomans et al. “Adaptation of a small animal radiation research platform for pre-clinical microbeam irradiations”. In: *Med Phys* 52.12 (2025), e70162.

[666] Judith Noemi Rivera. “Exploring Potential Therapeutic Benefits of Spatially Fractionated Radiation Therapy”. Thesis. 2020.

[667] Nolan M. Esplen et al. “Monte Carlo optimization of a microbeam collimator design for use on the small animal radiation research platform (SARRP)”. In: *Physics in Medicine Biology* 63.17 (2018), p. 175004. URL: https://doi.org/10.1088/1361-6560/aad7e2.

[668] Steven Herchko, Sridhar Yaddanapudi, and C. K. Chris Wang. “Design and validation of a minibeam treatment delivery system for use with a radiation therapy research platform”. In: *Biomedical Physics Engineering Express* 11.4 (2025), p. 047001. URL: https://doi.org/10.1088/2057-1976/adcf2c.

[669] Emily Poon and Frank Verhaegen. “A CT-based analytical dose calculation method for HDR brachytherapy”. In: *Medical Physics* 36.9Part1 (2009), pp. 3982–3994. URL: https://aapm.onlinelibrary.wiley.com/doi/abs/10.1118/1.3184695.

[670] Stefan Bartzsch and Uwe Oelfke. “A new concept of pencil beam dose calculation for 40–200 keV photons using analytical dose kernels”. In: *Medical Physics* 40.11 (2013), p. 111714. URL: https://doi.org/10.1118/1.4824150.

[671] Charlotte Debus, Uwe Oelfke, and Stefan Bartzsch. “A point kernel algorithm for microbeam radiation therapy”. In: *Physics in Medicine Biology* 62.21 (2017), p. 8341. URL: https://doi.org/10.1088/1361-6560/aa8d63.

[672] S. Tubin et al. “Shifting the Immune-Suppressive to Predominant Immune-Stimulatory Radiation Effects by SBRT-PArtial Tumor Irradiation Targeting HYpoxic Segment (SBRT-PATHY)”. In: *Cancers (Basel)* 13.1 (2020).

[673] Philip Mayles. *Physics aspects of quality control in radiotherapy*. Report ; no. 81. Includes bibliographical references and index. York: Institute of Physics and Engineering in Medicine, 1999.

[674] D. C; McGrath E.J; Irving. *Selecting Probability Distributions*. Report. Office of Naval Research (Code 462), 1975. URL: https://mcnp.lanl.gov/pdf_files/TechReport_1975_ORNL_ORNL-RSIC-38Vol.I_McGrathBasinEtAl.pdf.

[675] John R. Taylor. *An introduction to error analysis : the study of uncertainties in physical measurements*. A series of books in physics. 81051269 (John Robert), John R. Taylor. ill. ; 25 cm. Bibliography: p. 253. Includes index. Mill Valley, Calif.: University Science Books, 1982, x, 270 p.

[676] Standards National Research Council of Canada. Metrology Research Centre. Ionizing Radiation. *EGSnrc: software for Monte Carlo simulation of ionizing radiation*. Computer Program. 2021 2021. URL: https://github.com/nrc-cnrc/EGSnrc.

[677] B. A. Faddegon et al. "The accuracy of EGSnrc, Geant4 and PENELOPE Monte Carlo systems for the simulation of electron scatter in external beam radiotherapy". In: *Physics in Medicine and Biology* 54.20 (2009). 503to Times Cited:48 Cited References Count:33, pp. 6151–6163. URL: %3CGo%20to%20ISI%3E://WOS:000270563300008%20https://iopscience.iop.org/article/10.1088/0031-9155/54/20/008/pdf.

[678] D. Sheikh-Bagheri et al. "Comparison of measured and Monte Carlo calculated dose distributions from the NRC linac". In: *Medical Physics* 27.10 (2000). 367yg Times Cited:71 Cited References Count:51, pp. 2256–2266. URL: %3CGo%20to%20ISI%3E://WOS:000090089500008%20https://aapm.onlinelibrary.wiley.com/doi/pdfdirect/10.1118/1.1290714?download=true.

[679] Ioannis Sechopoulos et al. "RECORDS: improved Reporting of montE CarlO RaDiation transport Studies: Report of the AAPM Research Committee Task Group 268". In: *Medical Physics* 45.1 (2018), e1–e5. URL: https://aapm.onlinelibrary.wiley.com/doi/abs/10.1002/mp.12702.

[680] Jemila Habainy et al. "Fatigue properties of tungsten from two different processing routes". In: *Journal of Nuclear Materials* 506 (2018), pp. 83–91. URL: https://www.sciencedirect.com/science/article/pii/S0022311516312028.

[681] Ph Mertens et al. "Bulk tungsten in the JET divertor: Potential influence of the exhaustion of ductility and grain growth on the lifetime". In: *Journal of Nuclear Materials* 438 (2013), S401–S405. URL: https://www.sciencedirect.com/science/article/pii/S0022311513000883%20https://www.sciencedirect.com/science/article/pii/S0022311513000883?via%3Dihub.

[682] R. E. Schmunk and G. E. Korth. "Tensile and low-cycle fatigue measurements on cross-rolled tungsten". In: *Journal of Nuclear Materials* 104 (1981), pp. 943–947. URL: https://www.sciencedirect.com/science/article/pii/0022311582907218%20https://www.sciencedirect.com/science/article/pii/0022311582907218?via%3Dihub.

[683] J. R. Davis and ASM International. Handbook Committee. *Metals handbook*. Desk. 98045866 edited by J.R. Davis ; prepared under the direction of the ASM International Handbook Committee. ill. ; 28 cm. Includes bibliographical references and index. Materials Park, Oh.: ASM International, 1998, xiv, 1521 p.